Aerodynamic Performance and Self-Starting Analysis of Darrieus Wind Turbines with J-Shaped Airfoils

A Thesis

Submitted in Partial Fulfilment of the Requirements

for the Award of the Degree of

DOCTOR OF PHILOSOPHY

By

Kabita Naik

Under the Guidance of

Prof. Niranjan Sahoo

School of Energy Science and Engineering

Indian Institute of Technology Guwahati

Guwahati-781039, India

March 2026

Dedicated to….

My beloved son, Krishna

My beloved husband Sunil

&

My Parents

Mr. Radhakanta Naik

Mrs. Rama Naik

School of Energy Science and Engineering
Indian Institute of Technology Guwahati
Guwahati-781039, Assam, India

DECLARATION

I hereby certify that the work compiled in this dissertation entitled **'Aerodynamic Performance and Self-Starting Analysis of Darrieus Wind Turbines with J-Shaped Airfoils'** is the outcome of the research work performed by myself in partial fulfilment of the requirements for the award of the Degree of Doctor of Philosophy and submitted to the School of Energy Science and Engineering, Indian Institute of Technology Guwahati under the guidance of **Prof. Niranjan Sahoo** in the Department of Mechanical Engineering, Indian Institute of Technology Guwahati, Assam, India.

Any part of this work has not earlier been submitted for the award of any degree, diploma, associate fellowship, fellowship or its equivalent to any university or institution.

Date: 24th March, 2026

Kabita Naik
Registration No. 186151102
School of Energy Science and Engineering
Indian Institute of Technology Guwahati
Guwahati-781039, Assam, India

School of Energy Science and Engineering
Indian Institute of Technology Guwahati
Guwahati-781039, Assam, India

CERTIFICATE

It is certified that the work contained in the thesis entitled **'Aerodynamic Performance and Self-Starting Analysis of Darrieus Wind Turbines with J-Shaped Airfoils'** submitted by **Kabita Naik,** a student, to the Indian Institute of Technology Guwahati for the award of the degree of Doctor of Philosophy has been carried out under my supervision in the School of Energy Science and Engineering, Indian Institute of Technology Guwahati. This work has not been submitted elsewhere for any other degree or diploma award.

Date: 24th March, 2026

Prof. Niranjan Sahoo
Department of Mechanical Engineering
Indian Institute of Technology Guwahati
Guwahati-781039, Assam, India

ACKNOWLEDGMENTS

I would like to offer my deepest gratitude to all those who encouraged and guided me throughout this research journey. This dissertation would not have been achievable without the professional, intellectual, and individual support of many people and my institutions. First and foremost, I would like to express my deepest gratitude to my supervisor, **Prof. Niranjan Sahoo**, for his valuable guidance, patience, encouragement, mentorship, support, and cooperation throughout my research work. I would also like to thank my Doctoral Committee members, **Prof. Sisir Kumar Nayak**, **Prof. Poonam Kumari**, and **Dr. E S N Raju P**, for continuously monitoring the progress of my work, dedicating their time and providing their expertise to this work, along with valuable suggestions, recommendations and encouragement. Your interesting questions and positive criticism significantly contributed to this work. I am profoundly grateful to **Prof. Vinayak Kulkarni** and **Prof. U. K. Saha** for their valuable guidance, suggestions, and recommendations provided for completing these investigations.

I am thankful to the **School of Energy Science and Engineering** and the **Department of Mechanical Engineering**, **Indian Institute of Technology Guwahati**, for providing the necessary assistantship, institutional support, and access to the resources that were essential to the execution of my experiments and computational analysis. I also express my gratitude to the **Technology Innovation and Development Foundation, IITG,** for the financial support.

I thank my lab seniors, PhD colleagues and friends in the wind tunnel and gas dynamic lab. I am thankful to **Dr. Anil K. Rout**, **Dr. Saibal Kanchan**, **Dr. Santosh Hotta** and **Dr. Ojing Siram**, who have given me guidance, suggestions, and much-needed encouragement in my PhD journey. I would also like to acknowledge my lab mates: **Dr. Anand Verma, Dr. Umang Rathod, Dr. Bastav Borah, Mr. Abhishek Kamal, Mr. Amit Kumar, Mr. Ravi Kumar, Miss. Suchita Barhate, Miss. Sima Nayak, Mr. Pankaj Kumar, Dr. Mridusmita Borah** and **Mr. Rishi Purohit**. They were my first family at IITG, and without their support, affection and encouragement, my research journey would have been less delightful.

Finally, I deeply thank God and my beloved family for their unconditional love, affection, support, blessing and continuous encouragement to pursue my academic desires. I am profoundly grateful to my husband, **Sunil Kumar Biswal**, for his unconditional love, emotional support, guidance, motivation and patience during the most challenging periods of my PhD

research journey. This journey would not have been possible without him. I express my love to my beloved son, **Sanmay Kritarth Biswal**, who came into my life during the last phase of my PhD journey and made this journey enjoyable. I am grateful to my parents, **Radhakanta Naik, Rama Naik, Surath Chandra Biswal,** and **Nalini Prabha Biswal** for their love, support and encouragement during my research journey.

Kabita Naik

Indian Institute of Technology Guwahati

March 2026

ABSTRACT

To meet the challenges of the impending energy crisis, greenhouse gases, global warming, and pollution from fossil fuels, it is essential to incorporate different types of renewable energy technologies. From this perspective, wind energy is one of the most abundant and highly contributing renewable sources among other technologies. The Darrieus-type straight-bladed vertical axis wind turbines (SB-VAWTs) have immense potential to extract wind energy as a standalone system, particularly in remote locations. The increasing enthusiasm toward the advancement of Darrieus-type SB-VAWTs can offer a potential remedy for addressing power shortage and the unpredictability of climate conditions. The SB-VAWTs provide distinct advantages over their counterparts due to their linear blade design and uncomplicated structure. However, the aerodynamic performance of SB-VAWTs is not as good as that of horizontal axis wind turbines (HAWTs). Further, the starting characteristics of the SB-VAWTs are poor, which limits their applicability in low wind speed environments for small-scale power generation. In that context, the present study is focused on analyzing the aerodynamic performance and starting characteristics of Darrieus-type SB-VAWTs with J-shaped airfoils.

The present thesis investigates the uppercut and lowercut J-shaped airfoils with various opening ratios (ORs) through two-dimensional (2D) computational fluid dynamics (CFD) simulations in the preliminary stage. The J-shaped airfoils are created by removing a portion toward the trailing edge of the conventional cambered NACA 4415 airfoils. The J-shaped airfoils are called uppercut and lowercut when a part is removed from the upper and lower surfaces of the conventional cambered airfoils. This study revealed that the SB-VAWTs depicted superior performance when they employed the uppercut J-shaped airfoils. Furthermore, the present study demonstrates that the power and torque coefficient of SB-VAWTs improve by about 31% when the ORs of the uppercut J-shaped airfoil are varied from 0.1 to 0.8. In addition, the J-shaped airfoils contributes to the SB-VAWTs to generate torque during the critical starting conditions, which enhanced the self-starting characteristics.

Numerical investigations are conducted on small-scale Darrieus-type SB-VAWTs with a series of cambered airfoils and their J-shaped airfoils to obtain an optimum airfoils to improve the aerodynamic performance and starting torque. Based on the outcomes of the numerical study, experimental tests are conducted to systematically analyze the influence of the uppercut J-shaped airfoil with various ORs. In this test, the J-shaped blade profile is designed using a

conventional cambered NACA 4418 airfoil. The numerical study disclosed that the J-shaped NACA 4418 airfoil outperforms its alternative conventional cambered airfoil designs. The performance of SB-VAWTs improves by about 25% with the J-shaped NACA 4418 airfoil with an OR of 70%. Moreover, the self-starting torque of SB-VAWTs increases due to the contribution of the drag force developed by the J-shaped airfoil configurations.

Furthermore, the present work investigated the effect of J-shaped blade numbers (N_b) (i.e. 2,3 and 4) on the aerodynamic performance and starting characteristics of small-scale Darrieus-type SB-VAWTs. The J-shaped N_b with ORs of 30%, 50% and 70% are experimented in a wind tunnel to determine the overall performance of SB-VAWTs at lower tip speed ratio (λ) ranging between 0.4 and 1.5. This study uses a conventional cambered NACA 4418 airfoil for the creation of J-shaped N_b. Also, numerical simulations have been performed to understand the aerodynamic and self-starting behaviour of the SB-VAWTs. The results demonstrated that the J-shaped blades performed better compared to the conventional blades in terms of aerodynamic performance and starting ability. The 4-bladed J-shaped SB-VAWTs depicted better performance at lower λ values while the 2-bladed J-shaped SB-VAWTs performed better at larger λ values. Moreover, the 3-bladed J-shaped SB-VAWTs generated more consistent performance at low to medium λ values. The J-shaped blades with OR of 70% depicted superior performance with an improvement of 25%, 23% and 43% for the case of 2-bladed, 3-bladed and 4-bladed SB-VAWTs, respectively compared to the alternative conventional blades.

CONTENTS

Nomenclature

English Symbols

A	Swept or projected area (product of H and D) (m^2)
A_{wt}	Test section area of the wind tunnel
AC_P	Average power coefficient
$AC_{P,max}$	Maximum average power coefficient
$AC_{P,opt}$	Optimum average power coefficient
AC_T	Average torque coefficient
$AC_{T,\ max}$	Maximum average torque coefficient
$AC_{T,\ opt}$	Optimum average torque coefficient
c	Chord length of airfoil (m)
C_D	Drag coefficient
C_L	Lift coefficient
C_P	Power coefficient
C_{Pm}	Power coefficient of model
$C_{P,\ max}$	Maximum power coefficient
C_R	Resultant coefficient
C_{ST}	Static torque coefficient
C_T	Torque coefficient
D	Wind turbine rotor diameter (m)
D_P	Diameter of bracking pulley (m)
D_{RR}	Diameter of rotating zone (m)
D_{shaft}	Shaft diameter (m)
F_D	Drag force (N)
F_L	Lift force (N)
F_N	Normal force (N)
F_T	Tangential force (N)
F_X	Net force in x direction (N)
F_T	Net force in y direction (N)
H	Height of wind turbine (m)
IC_T	Instantaneous torque coefficient
$IC_{T,\ max}$	Maximum instantaneous torque coefficient

IC_{Ts}	Instantaneous static torque coefficient
L	Domain length (m)
N	RPM, rotation per minute
N_b	Blade number
P	Power (W)
$P_{available}$	Available wind power (W)
$P_{turbine}$	Actual power of wind turbine (W)
R	Radius of wind turbine (m)
Re	Reynolds number
Re_c	Chord based Reynolds number
S	Spring balance reading (N)
$SOIC_{Ts}$	Summation of instantaneous static torque coefficient
$SOIC_{Ts,\,max}$	Maximum value of summation of instantaneous static torque coefficient
t	time (s)
T	Torque of the blade (Nm)
u_i	Velocity component along x_i direction (m/s)
$\overline{u_i' u_j'}$	Specific Reynolds stress component
u_j	Velocity component along x_j direction (m/s)
V	Free stream velocity of air (m/s)
V_c	Chord line velocity (m/s)
V_i	Induced velocity (m/s)
V_m	Inlet velocity with the model (m/s)
V_r	Relative velocity (m/s)
W	Domain width (m)
W_L	Measured load or dead weight (kg)
X_c	Opening Length (m)
X_c/c	Opening ratio
x_i	Coordinates along i^{th} direction
x_j	Coordinates along j^{th} direction
y^+	Normalized wall distance

Greek Symbols

α	Angle of attack
θ	Azimuth angle (deg)
ρ	Density of air (kg/m^3)
λ_{opt}	Optimum tip speed ratio
ν	Kinematic viscosity (m^2/s)
κ	Kinetic energy of turbulent fluctuations (m^2/s^2)
δ_{jj}	Kronecker delta
Ω	Rotational velocity (rad/s)
σ	Solidity
ω	Specific turbulence dissipation energy rate (m^{-1})
λ	Tip speed ratio
λ_m	Tip speed ratio of the model

Abbreviations

2D	Two dimensional
3D	Three dimensional
AOA	Angle of attack
AR	Aspect ratio
BC	Boundary condition
BCMs	Blockage correction methods
BF	Blockage factor
BL	Boundary layer
BR	Blockage ratio
BSR	Blade speed ratio
CFD	Computational fluid dynamics
CB-VAWT	Curved-bladed vertical axis wind turbine
EIA	Energy information administration
FVM	Control volume method
FDM	Fused deposition modelling

GR	Growth rate
HAWT	Horizontal axis wind turbine
LE	Leading edge
LS	Lower surface
OR	Opening ratio
PLA	Polylactic acid
SB-VAWT	Straight-bladed vertical axis wind turbine
SIMPLE	Semi implicit method for pressure linked equation
SMM	Sliding moving mesh
SST	Shear stress transport
TE	Trailing edge
TI	Turbulent intensity
TSR	Tip speed ratio
URANS	Unsteady Reynolds-averaged Navier-Stokes equations
uc	Upper cut
US	Upper surface
VAWT	Vertical axis wind turbine
WT	Wind turbine

List of Figures and Tables

List of Figures

List of Tables

CHAPTER 1

Introduction

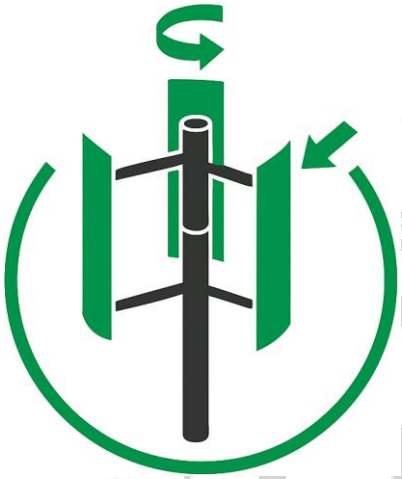

Chapter Layout

Overview

This chapter highlights wind energy as a leading and cost-effective, one of the most abundant and significant contributors among various renewable energy options. The comprehensive overview of the current energy scenario is explored from both global and Indian perspectives. The growing importance of wind power in the future and the substantial growth in wind energy installation are emphasised in this chapter. The types of wind turbines and their classification are discussed. The current applications of wind turbines are elaborated. It is identified that small-scale vertical axis wind turbines (VAWTs) have significant future potential, although off-shore and on-shore horizontal axis wind turbines, including floating turbines are more dominant. The small-scale Darrieus-type straight-bladed vertical axis wind turbines (SB-VAWTs) and their aerodynamics are demonstrated. The selection of J-shaped blade profiles for small-scale Darrieus-type SB-VAWTs is explained as the research focus. Finally, the chapter concludes by presenting a concise survey of the organization of the current thesis work.

1.1. Motivation

Energy is one of the most important contributing sources for humanity, as it is a necessity in all fields of our economy. The existence of energy in nature is available in several forms and humankind has harnessed this natural energy by utilizing the basic principle of energy conservation for centuries. The most widely used and accessible energy sources are fossil fuels, where energy is derived through coal, petroleum and natural gas combustion. Since the initiation of industrial development, fossil fuels have been used in many fields such as transport, manufacturing, domestic devices, and complex facilities. However, fossil fuels are non-renewable energy sources that have significantly declined over the past few decades due to their limited supply. Further, the uncontrolled usage of fossil fuels results in carbon dioxide emissions, which are the main cause of global warming and climate change (Mackay, 2009). The continuous depletion of fossil fuels and other non-renewable energy sources may create a global energy crisis in the future energy market.

From this perspective, the energy sectors seek alternative energy sources for power generation. In accordance with this, renewable energy sources such as solar, wind, hydro, geothermal and biofuels have become practical and sustainable solutions to address the growing energy deficit globally. Solar energy is the primary natural source, where photovoltaic technology converts sunlight directly to electricity. Solar energy delivers the largest share of the energy to the market among other renewable energy sources. But it is low-grade and unconcentrated, which relies on sophisticated and high-cost semiconducting materials. On the other hand, a more consistent energy supply is obtained from other sources, such as hydro, tidal and geothermal energy, but they require costly infrastructure. Further, since ancient history, biofuels processing and production have been used but have required considerable time and labour-intensive methods. Finally and most importantly, renewable energy that has attracted significant research attention is wind energy due to its several ways of extraction. Wind energy is a promising and economical energy source, one of the most abundant and fastest emerging renewable energy. Wind energy is extracted through multiple ways, such as wind turbines, flying kites, airborne wind energy systems, floating wind turbines, oscillating objects based on vortex-induced vibrations, hybrid turbines, multirotor systems and diffuser augmented wind turbines (Watson et al., 2019). Moreover, the aforementioned wind energy systems are implemented in two ways: either centralized installation or as standalone units. In this collection, the wind turbines (WTs) are the most prevalent technology. The WTs are renewable power-generating devices that convert the kinetic energy in the air stream into electricity. The WTs consist of one or several rotor blades

and are equipped with rotors to extract the wind power. The extracted wind power generates rotation and is converted into mechanical power at the rotor shaft. At the shaft, the mechanical power is taken up in the form of a moment at a certain rotation and then transferred to a machine (such as a generator) to generate electricity. Thus, the entire wind power station consists of a wind turbine, a mechanical gearbox, a generator, electricity storage, and transmission devices (Fig. 1.1). The WTs are connected to some electrical networks, and these networks include battery charging circuits, residential-scale power systems, isolated networks, and large utility grids to supply the generated electricity.

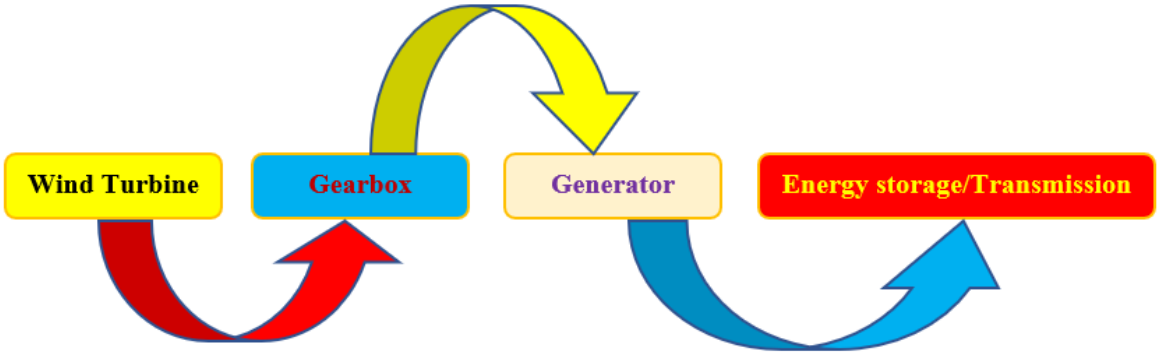

Fig. 1.1. Schematic of a basic conversion system of wind power

Considering the preceding discussions, the author of the current PhD thesis has decided to perform research in the WTs field. The designs of WTs vary widely to account for the distinct operating conditions and energy needs of different regions or nations. Therefore, the current energy scenario is evaluated (Section 1.2) and based on that, an appropriate WT is chosen from the many available types (Section 1.3).

1.2. Present Energy Scenario

The consumption of energy in the form of electricity has consistently risen faster over the last two decades, as illustrated in Fig. 1.2 (IEA, 2022; Jung et al., 2018). According to IEA (International Energy Agency) report, the global electricity net consumption in 2021 increased to 5.4% from the previous year, while it was about 0.7% in 2020 because of the crisis of COVID-19 (Buechler et al., 2022). Moreover, the electrical growth was lifted by about 40% with an annual increment rate of 1.7% after 2000 (Siram et al., 2022c). Every year, the world meets the growing demand for electrical energy by installing more and more wind power capacity.

Renewable energy provides about 12% of the total energy, where 10% is contributed by the wind power sector. On the other hand, the universal share extended between 20% and 40% towards energy expenditure from occupational and inhabited buildings in the evolved countries (Pérez-Lombard et al., 2008).

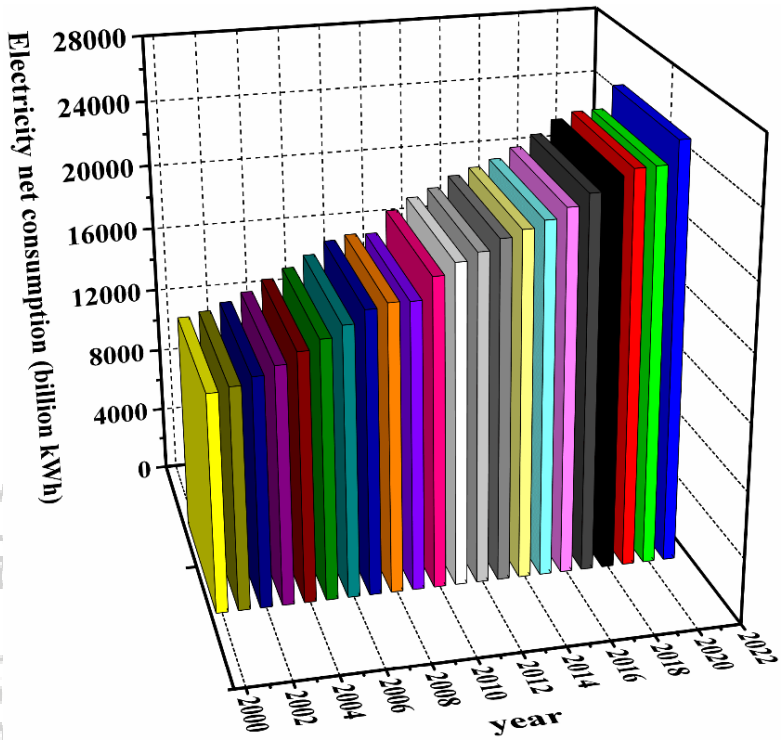

Fig. 1.2. Schematic of the world electricity net consumption (IEA, 2022)

As per the U.S. Energy Information Administration (EIA) assessment from 2008 to 2035, occupational and inhabited energy exploitation per year is rising at a mean rate of 1.1% and 1.5% (Chen et al., 2015). According to the IEA, the wind energy contribution is expected to double by 2050 as per the net-zero emissions scenario. Based on the data published by the GWEC (Global Wind Energy Council), the global cumulative wind power capacity has become 1136 GW due to the new installation of about 117 GW, presenting a year-over-year growth of 11% compared to last year (2024) (GWEC, 2025). The global cumulative wind power installation (i.e., total installations) in 2024 is 73%, which is 1% higher than the previous year (GWEC, 2025). Furthermore, the global installed wind power capacity (i.e., new installations) became 81% in 2024, which is 1% higher compared to last year. The growth in global cumulative and installed wind power capacities is primarily due to the world's top five markets, such as China, United States, Germany, India and Brazil. The global cumulative and installed wind energy capacity over the last 24 years is demonstrated in Fig. 1.3. Moreover, as per WWEA

(World Wind Energy Association), the global growth rate showed to 11,5% in 2024 due to the addition of volume of wind capacity which is significantly less than to13,0% growth observed in 2023 (WWEA, 2025).

The total energy expenditure from an Indian perspective was approximately 27 EJ (1 EJ = 10^{18} J), accounting for 6% of the world's total energy consumption (IEA, 2022). The energy consumption in India per capita remains significantly lower currently as well as historically compared to the developed nations (IEA, 2022; Mackay, 2009). India used renewable energy sources specifically for electricity production and supplied 21% of the nation's total electricity intake of 1583 TWh (1 TWh = 10^{12} Wh) as stated by 2019 reports (IEA, 2021). In 2019, half of the country's electricity was generated by hydro-sources, accompanied by wind at 20% up to now onwards, which is expected to be reversed by 2040 according to the Indian state policy predictions. This emphasised a rising indication in wind energy for future electricity generation. As per the Ministry of New and Renewable Energy (MNRE), the total installed wind energy capacity has reached to 41.93 GW by the end of 2022 (MNRE, 2023). The majority of the electricity production in the wind sector is controlled by onshore wind farms. The MNRE has identified various potential sites for developing wind farms in India on the basis of wind speed distribution. The average wind speed of India is 6.5 m/s at 100 meter height (for 10% of windiest areas) as per the global wind atlas (DTU, 2023). Moreover, the average wind speed for most of states like Tamilnadu, Gujarat and Jammu & Kashmir is 7-9 m/s. While the mean wind velocity is 4 m/s for the North-eastern states, along with Assam, it is generally very low. The WT types are chosen according to the aforementioned wind energy potential and energy needs, which are categorized in Section 1.3.

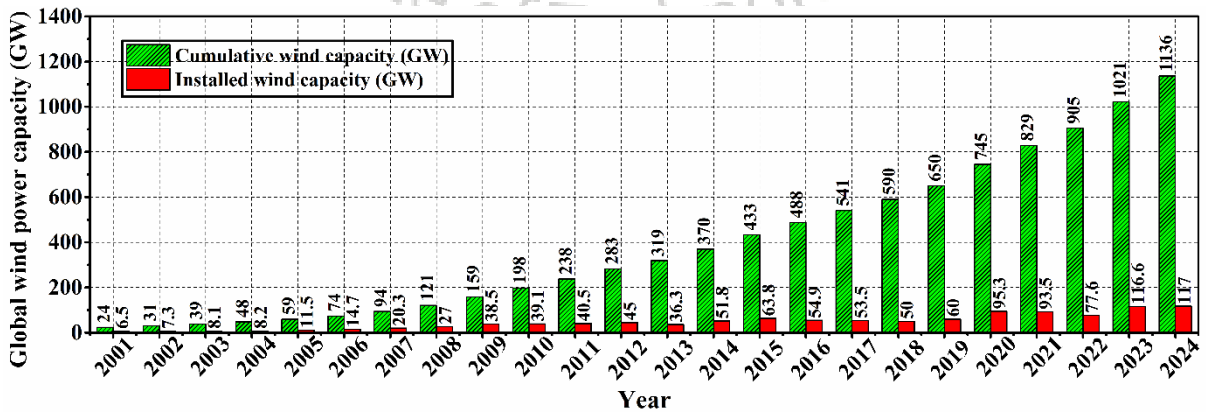

Fig. 1.3. Global cumulative and installed wind energy capacity (GWEC, 2025)

1.3. Classification of Wind Turbines

There are many ways of classifying WTs to take advantage of wind power based on the principle of aerodynamics. Basically, WTs are classified according to the turbine capacity, turbine diameter, standard power rating and the orientation of the axis of rotation (Yan Li, 2019). The classification of WTs is depicted in Fig. 1.4. Among them, the main classification is the orientation of the rotation axis. Depending on the orientation of the rotation axis, WTs are of two types: horizontal axis wind turbines (HAWTs) and vertical axis wind turbines (VAWTs). The rotational axis of HAWTs is parallel to the ground and the direction of the wind stream. On the other hand, the rotational axis of VAWTs is oriented vertically and perpendicular to the wind direction.

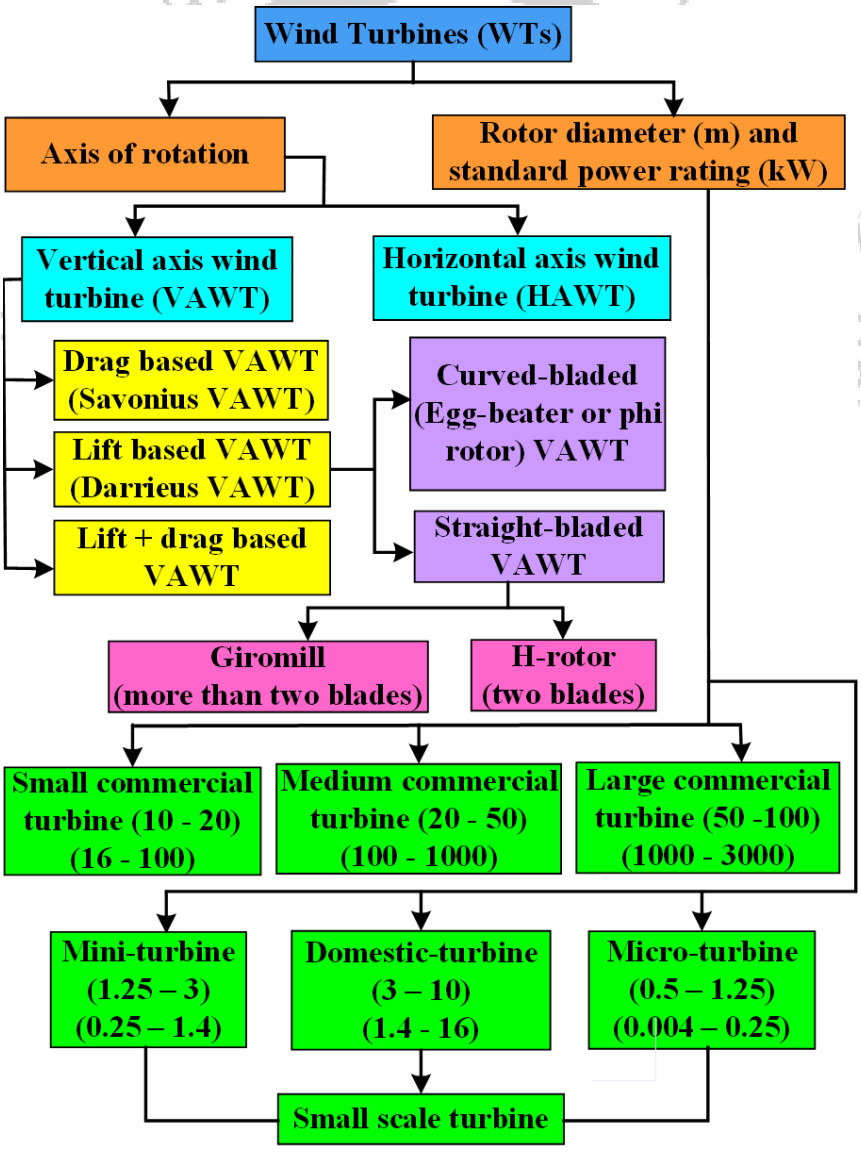

Fig. 1.4. Schematic of WTs classification

The HAWTs are operated based on the lift generation principle, while the VAWTs are either lift-based or drag-based turbines. The energy output of HAWTs depends mainly on wind turbulence and the site's average wind speed. The HAWTs are currently used in large to medium-scale wind farm applications at offshore locations and remote areas where undisturbed and clean wind is obtainable due to their advantages, such as the highest efficiencies and grid linking ability (Roy and Ducoin, 2016). The rotors of HAWTs should always face towards the direction of the wind. Therefore, a self-starter and yaw system are usually equipped in the HAWTs to turn the blades towards the wind. Further, these HAWTs generate poor performance in urban areas where flow is difficult to maintain and highly unsteady (Toja-Silva et al., 2013). This is due to their large value of cut-in wind speed, the disordered nature of wind, and public insight against these large machines. The VAWTs produce electricity by capturing winds from any direction; thus, these are omnidirectional. Compared to the HAWTs, the VAWTs are simpler in design, using limited space for installation, produced lower noise and easier to manufacture. The HAWTs need to be placed at a larger height above the ground level to acquire high velocity winds and avoid atmospheric boundary layers. Thus, these required a tall tower, which increases the overall capital cost. However, VAWTs function within lower wind velocity and atmospheric wind shear layers. The generator and other auxiliary equipment of VAWTs are placed at ground level, making installation and maintenance of VAWTs easier.

Under steady wind, the ideal aerodynamic efficiency of HAWTs is reported in the range of 40-55% at higher rotational speeds (Kumar et al., 2018). In contrast to this, VAWTs are still preferred choices over HAWTs because of the aforementioned benefits. The efficiency of an effective VAWT lies below 40% (Eriksson et al., 2008). The above characteristics of VAWTs have facilitated their implementation as small-scale power generators in regions such as highways, offshore oil fields, public places, communication base-stations, city streets or on high-rise rooftop buildings in urban areas, border areas, islands and many isolated locations (Li et al., 2022). Figure 1.5 depicts various applications of VAWTs, such as the installation of 200 Quiet Revolution VAWTs at RWE stadium Essen, a 14 kW helical-type VAWT for charging an electric vehicle in Spain, implementations of VAWTs at Paris as a wind tree for providing heat to the home and VAWTs powering the tiny light as a kinetic sculpture at Singapore (Liu et al., 2019). Most of the small VAWTs are designed attractively in such a way for dual-purpose utilization. That means their structures look like kinetic sculptures installed in a public art display, which provides heat to the home and powers tiny lights as presented in Fig. 1.5 (c) &

(d). According to the geometry, the VAWTs have many distinct variants. The most prevalent and extensively studied types of VAWTs are the Darrieus and Savonius rotors among their different configurations. The Savonius-type wind rotors are drag-based type VAWTs, while Darrieus-type wind rotors come under lift-based VAWTs. The Savonius-type wind rotors consist of two or three scoops; their performance is poor compared to Darrieus rotors. The Savonius-type wind rotors normally generate efficiency below 25% (Akwa et al., 2012).

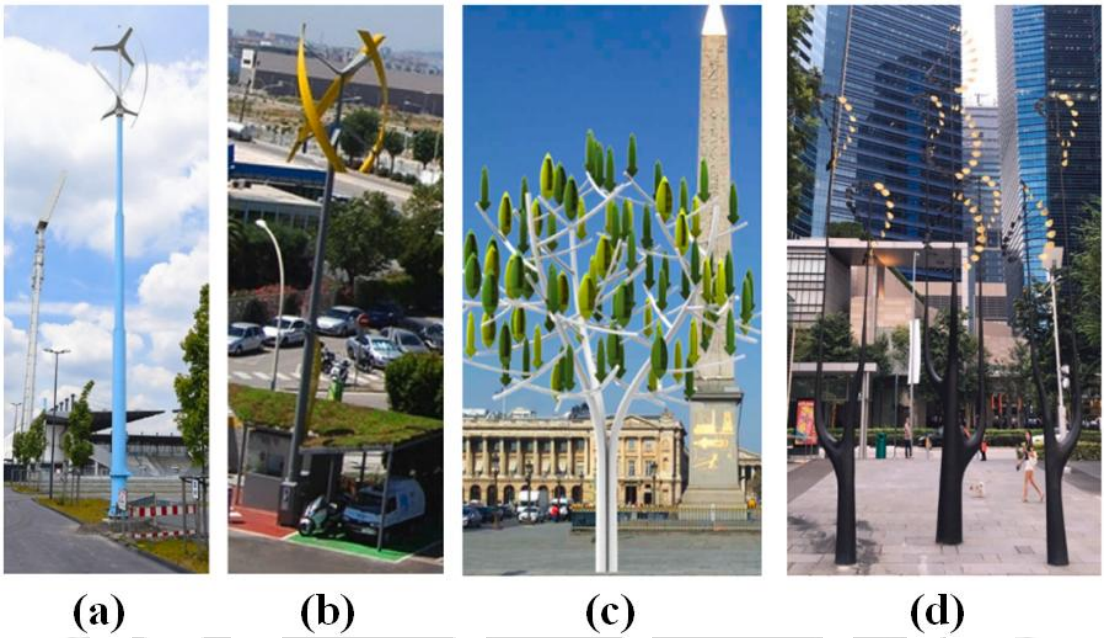

Fig. 1.5. (a) VAWT installed at RWE stadium Essen, (b) VAWT integrated in an electric vehicle charging station, (c) Drag-based VAWTs as a wind tree, (d) Drag-based VAWTs for powering tiny lights (Liu et al., 2019)

The Darrieus-type wind rotors consist of two or more blades attached to the central vertical shaft and can be used in single or multi-staged arrangements. Even though the Darrieus-type wind rotors face self-starting issues, these are more beneficial for small-scale power production due to their higher performance at urban locations where wind speed is lower, inconsistent and highly turbulent (Benedict et al., 2016). A French aeronautical engineer, Georges Jean Marie Darrieus, invented the first lift-based VAWT by adopting an airfoil profile for the blades during the 1920s (Kumar et al., 2019). He patented the Darrieus-type VAWTs design in 1925 in France and 1931 in the U.S. (Liu et al., 2019; Tjiu et al., 2015). According to this patent, the Darrieus-type VAWTs are categorized into curved-bladed vertical axis wind turbines (CB-VAWTs) and straight-bladed vertical axis wind turbines (SB-VAWTs), as shown in Fig. 1.6. As per the identical look, the CB-VAWTs configurations are also called egg-beater or phi-rotor (Tjiu et al.,

2015). Among the various configurations of SB-VAWTs, H-rotor and Giromil configurations are more favourable designs because of their simpler look. When SB-VAWTs consist of two blades, it is referred to as H-rotor, and when it has more than two blades, they are called a Giromill (Tjiu et al., 2015). The bending stress in blades of CB-VAWTs is lower. Still, it requires a higher fabrication cost due to the more complex design than that of SB-VAWTs. However, the Darrieus-type SB-VAWTs are the most attributed turbines among all types of VAWTs for small-scale power production because of their more straightforward design, fabrication and lower expenditure (Kumar et al., 2019). Due to these peculiar attributes of the Darrieus-type SB-VAWTs, the author of the present thesis selected it for PhD research investigations.

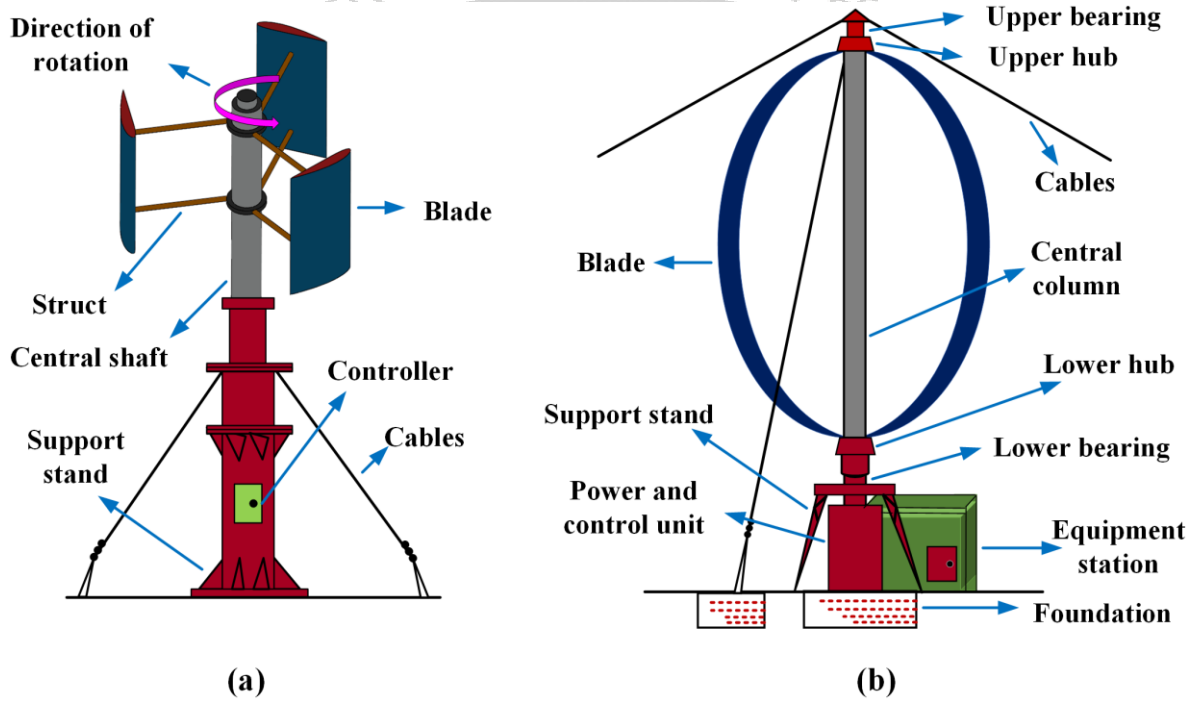

Fig. 1.6. Schematic of Darrieus rotors: (a) SB-VAWT, (b) CB-VAWT

1.4. Darrieus-type Straight-Bladed Vertical Axis Wind Turbines

The Darrieus-type SB-VAWTs are the most common types of VAWTs, which can extract more energy from the wind per unit swept area and are based on lift force. Mainly two or more numbers of airfoil-shaped blades are attached to the central shaft of the SB-VAWTs with the help of structs, as demonstrated in Fig. 1.6 (a). The working principle of the Darrieus-type SB-VAWTs during starting is mainly based on biomimicry, specifically the birds wings. During the design of the blades, a streamlined section is provided similar to a birds wings. That means the blades provide minimal resistance towards forward movement. In this design, the blades allow

the conversion of the maximum amount of available fluid energy into mechanical energy by the available component of the traverse thrust (Tjiu et al., 2015).

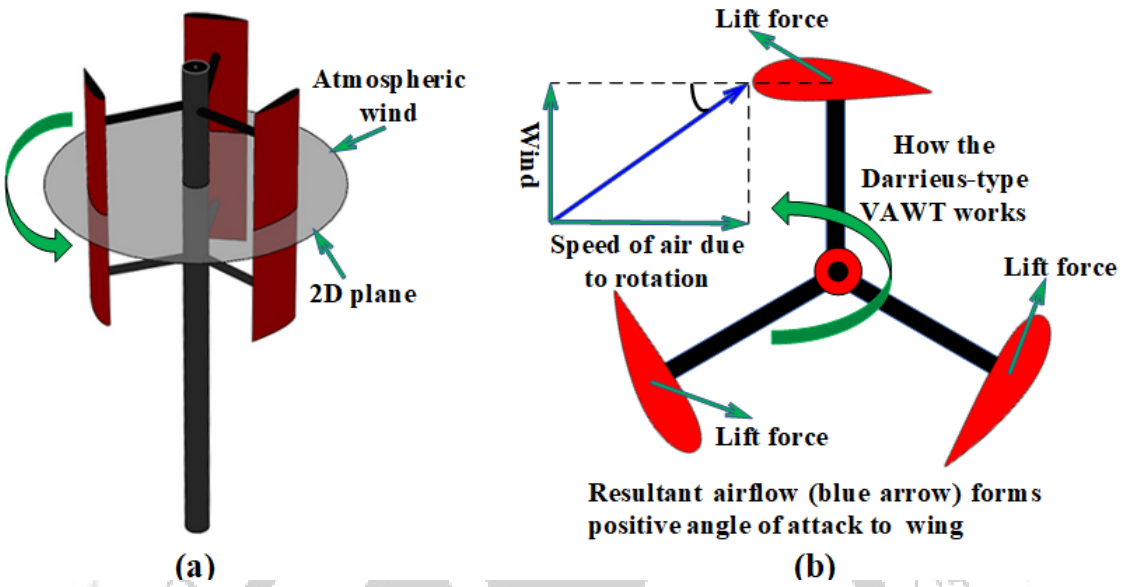

Fig. 1.7. Operational principle of Darrieus-type SB-VAWT: (a) 3D model and (b) 2D view

The airfoils of the Darrieus-type SB-VAWTs move forward in a circular path in the air during the rotation, as presented in Fig. 1.7. The incoming airflow combines with the wind to develop a resultant airfoil that creates a small positive angle of attack (AOA) relative to the blade. This produces a net force on the Darrieus-type SB-VAWTs, which pushes towards the forward, generating a positive torque on the shaft (Jin et al., 2015). Additionally, the forces on the blades of Darrieus-type SB-VAWTs are primarily due to tension, which helps to lessen the bending stress on the blade supports. These SB-VAWTs have several advantages compared to other WTs, but still, they face several issues (Mohamed, 2019): (i) poor aerodynamic efficiency and output torque; (ii) inferior self-starting ability. The above concerns create obstacles for Darrieus-type SB-VAWTs when used primarily for small-scale wind energy development. The aerodynamics of the airfoil configurations, new blade designs and blade numbers play an essential role in the improvement of the aerodynamic performance as well as the starting torque of Darrieus-type SB-VAWTs (Al Hamad et al., 2022). The SB-VAWTs may fail to generate self-starting torque unless the proper types of airfoils, freestream wind speed and rotor solidity (σ, the ratio of blade area to rotor swept area) are chosen. In steady conditions, although the Darrieus WT or rotor is competent in developing a low quantity of forward torque, it may generate a net quantity of torque per revolution at the initial state. Furthermore, the rotor may

create negative torque beneath certain conditions over a tip speed ratio (λ, the ratio of rotational blade speed to wind speed) ranging between 0.5 and 2.0, depending on the blade configuration. The negative torque zone is stated as a 'dead band' (J R Baker, 1983). The WTs with the above characteristic may just start, but they will not have sufficient ability to evade the dead band to accomplish their maximum operating speed. It confines the usage and its miscellaneous applications of the SB-VAWTs, especially for those utilized for small-scale energy production. Therefore, researchers have proposed several ways not only to enhance the start-up ability of the SB-VAWTs but also to improve the performance of SB-VAWTs, such as a new blade profile, unsymmetrical/cambered airfoils, variable pitch blades, flexible blades, Turby/helical Darrieus, Savonius-Darrieus hybrid turbine, augmentation techniques, airfoil with opening ratios, experimental and numericval investigations and so on.

1.5. Aerodynamics of Darrieus-type Straight-Bladed Vertical Axis Wind Turbines

The Darrieus-type SB-VAWT rotates on the basis of lift force (F_L) perpendicular to the flow direction of the wind and this force is generated due to the incoming wind (Fig. 1.8). The blade profile (or airfoil) of the Darrieus-type SB-VAWT produces useful power and torque when the wind flows over the airfoil. Figure 1.8 depicts a rotating airfoil with flow velocities and several induced aerodynamic forces at different azimuthal angular positions. The velocity triangle shown in Fig. 1.8 is formed because of the airfoil rotation at every point. This triangle consists of a relative velocity (V_r) generated due to the chordal or tangential velocity (V_c) variation concerning the wind flow direction (V) (Mohamed, 2019). The angle of attack (α) is the angle between the V_r and V_c. The α of blades consistently changes as a function of their azimuthal position due to the rotation of Darrieus-type SB-VAWT and generating many aerodynamic forces. The F_L and F_D (drag force) are the forces perpendicular and aligned to the V_r component, respectively. The normal or perpendicular force (F_N) and tangential force (F_T) are manifested by resolving the aerodynamic forces (Mohamed, 2019). The cyclic variations of blades created large variations in the α and induced a non-linear unsteady phenomenon called dynamic stall (Schuerich and Brown, 2011). This type of phenomenon is noticed in various turbo-machines, such as helicopter rotor blades, insect wings and compressor blades of jet engines. The existence of dynamic stalls may raise the power generation of Darrieus-type SB-VAWTs even if at lower λ values. On the other hand, it causes several unfavourable impacts, such as blade life reduction, vibrations, and noise.

Multiple essential parameters, such as λ, σ, α and performance pointer viz., lift coefficient (C_L), drag coefficient (C_D), torque coefficient (C_T) and power coefficient (C_P) must be taken into

consideration while designing the Darrieus-type SB-VAWTs. All these essential parameters are described in Eqs. (1.1) to (1.10). The dynamic performance parameters of Darrieus-type SB-VAWTs are determined based on an experimental observation by applying Eqs. (1.1) and (1.6) - (1.10). The aerodynamic torque of the SB-VAWTs is calculated from the measured load (W_L) and spring balance readings (S) by using Eq. (1.10).

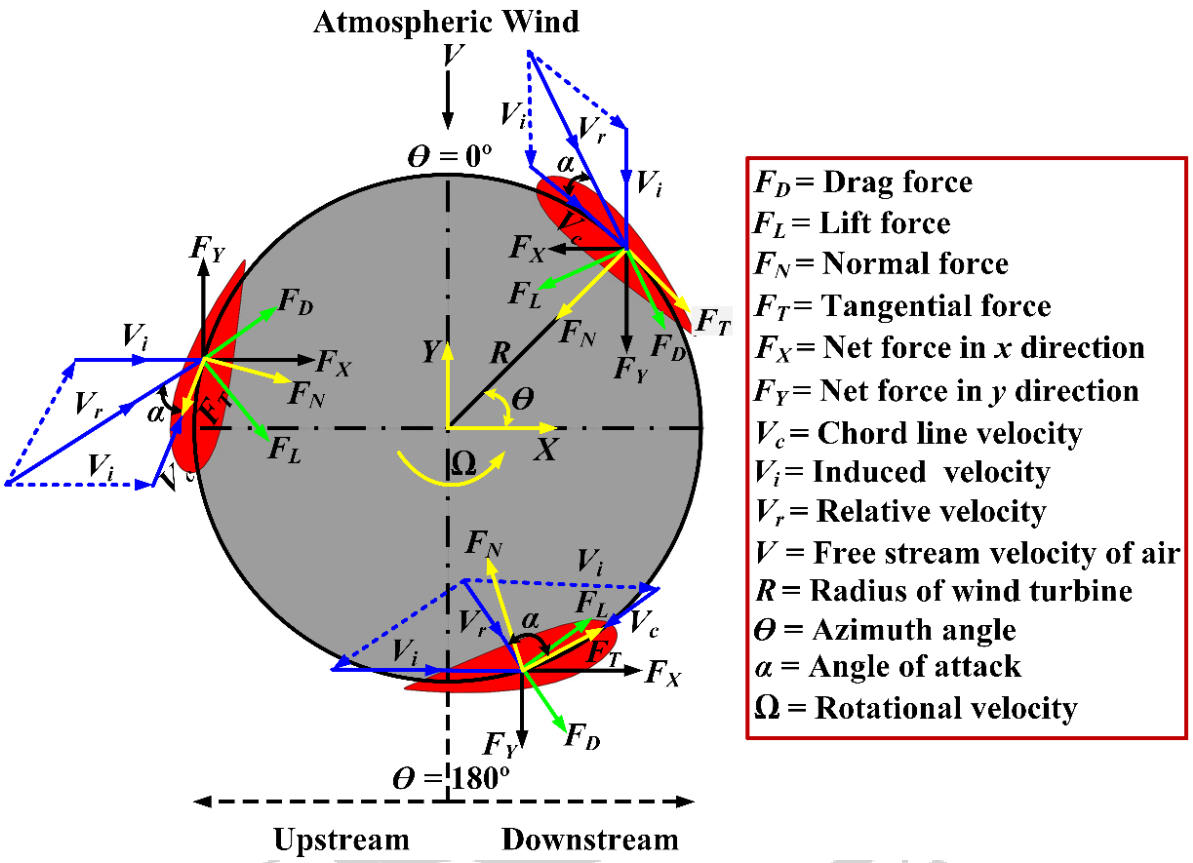

Fig. 1.8. Schematic diagram of flow velocities and forces on a 2D plan view at different azimuthal angle positions

$$\lambda = \frac{\Omega R}{V} = \frac{2\pi N}{60V} \times \frac{D}{2} \tag{1.1}$$

$$\sigma = \frac{N_b c}{D} \tag{1.2}$$

$$\alpha = \tan^{-1}\left(\frac{\sin\theta}{\lambda + \cos\theta}\right) \tag{1.3}$$

$$C_L = \frac{F_L}{0.5\rho A V^2} \tag{1.4}$$

$$C_D = \frac{F_D}{0.5\rho AV^2} \tag{1.5}$$

$$C_T = \frac{T}{0.5\rho ARV^2} \tag{1.6}$$

$$C_P = \frac{P_{turbine}}{P_{available}} = C_T \times \lambda \tag{1.7}$$

$$P_{turbine} = T \times \Omega = \frac{2\pi NT}{60} \tag{1.8}$$

$$P_{available} = 0.5\rho AV^3 \tag{1.9}$$

$$T = \left(\frac{W_L - S}{1000}\right) \times 9.81 \times \left(\frac{D_P}{2}\right) \tag{1.10}$$

Where T is the torque, W_L means measured weight/load, S is the spring balance readings and D_P is the braking pulley diameter. The $P_{turbine}$ means the actual power of WT and $P_{available}$ determines the available wind power. The Ω is the rotor rotational velocity, N means rotation per minute (rpm), ρ is the density, R is the rotor radius, V means free stream velocity of air and A (product of H and D) is used to calculate the swept or projected area of the WT. The H and D signify the height and diameter of WT.

The static characteristics of the Darrieus-type SB-VAWTs are expressed through the static torque coefficient (C_{ST}) and the azimuthal angle (θ). These parameters are computed using Eqs. (1.11) and (1.12).

$$T_S = 0.5 \times F_T \times D_P \tag{1.11}$$

$$C_{ST} = \frac{T_S}{0.5\rho AV^2 \times R} \tag{1.12}$$

1.6. Aerodynamic Configurations of J-shaped Blade Profiles

The J-shaped airfoil structure is formed by removing some portion of the conventional airfoil either from the upper or lower surfaces close to the trailing edge (TE), as illustrated in Fig. 1.9 (a-c). The conventional airfoil shape is similar to a locked bag-like design as identical to the

wing of an aeroplane (Fig. 1.9 (a)); thus, its performance is not better compared to the J-shaped airfoil because of the smooth surface on each side of the airfoil. The removed portion from the upper surface of the conventional airfoil is called an uppercut J-shaped airfoil, as displayed in Fig. 1.9 (b). The lowercut J-shaped airfoil is presented in Fig. 1.9 (c) and formed by removing a portion from the lower surface of the conventional airfoil. The Darrieus-type SB-VAWT with uppercut J-shaped airfoils is shown in Fig. 1.9 (d).

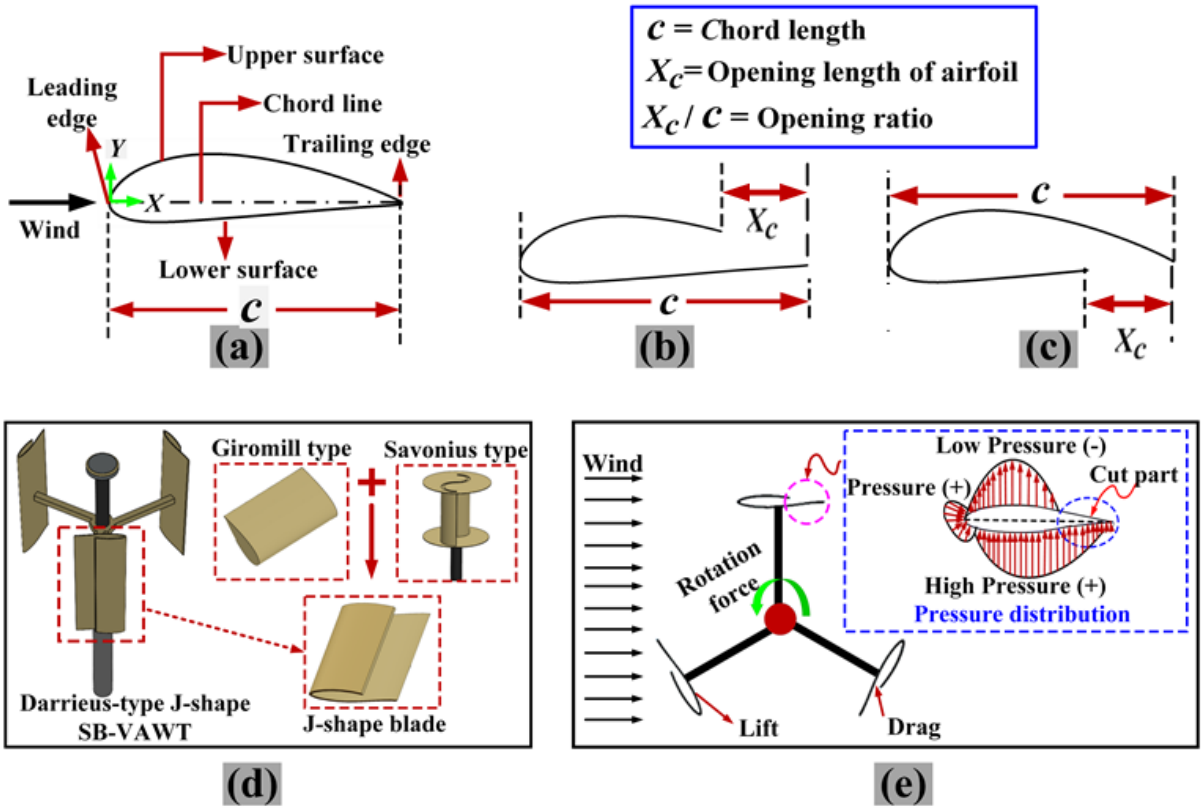

Fig. 1.9. Schematic of airfoil design and J-shaped models: (a) Conventional airfoil, (b) Uppercut J-shaped airfoil, (c) Lowercut J-shaped airfoil, (d) Three-dimensional J-shaped model and (e) Two-dimensional J-shaped model

The laminar flow over the smooth surface (convex or upper surface) of a J-shaped airfoil generates a pressure differential as with conventional blades to create aerodynamic lift (Fig. 1.9 (e)). Further, the notch at the TE of the J-shaped airfoil easily catches the wind at its back side and develops a higher drag coefficient during rotation. Therefore, these airfoils function due to the simultaneous effect of both F_L and F_D. The J-shaped airfoils are referred to as resistive type airfoils as it operates like Savonius-type VAWTs, in which the wind resistance is the dominant mechanism for generating torque on the blade surface. The J-shaped airfoil of Darrius-type SB-VAWT rotated because of the lift action when the wind blew from the left side. Further, the

airfoil profile towards its leading edge facing the incoming wind acts as a conventional airfoil that starts to rotate at the cut-in speed due to the F_L. Simultaneously, the F_D of the J-shaped airfoil further helps them to maintain their rotation due to the notch (Fig. 1.9 (e)). In this way, it generates more torque as the J-shaped airfoil utilises the same wind more than once. Thus, it can enhance the rotational efficiency and wind energy capture rate of Darrius-type SB-VAWTs (Zamani et al., 2016b, 2016a). The combined force (F_L and F_D) of the J-shaped airfoil can help the SB-VAWTs to operate faster at low wind speeds, specifically at low λ values, which can improve their self-starting and make them rotate even in a gentle wind (Earnest and Rachel, 2019). The design of the J-shaped blade is a hybrid type of blade as it works by the combination of lift-based (Giromill type) and drag-based (Savonius type) blades, as shown in Fig. 1.9 (d).

1.7. Summary

The renewable energy sector is expected to grow fast due to the reduction of technological costs and specific policies to promote and support a transition towards clean and sustainable energy production. In the next few years, wind power will play a pivotal role in the world's energy supply. It can buy us by providing huge amounts of clean, affordable power to fight against global warming during revolutions in energy efficiency and solar power gain momentum. In this scenario, the VAWTs are more appropriate for urban environments due to their simple construction, small operation space, low noise, and low cut-in speed. The VAWTs can be used environmentally for a range of applications, including the generation of electricity, water pumping, purifying and/or desalinating water by reverse osmosis, cooling and heating using vapour compression heat pumps, aerating and mixing water bodies and heating water by fluid turbulence. Among the many configurations of VAWTs, the Darrieus-type SB-VAWTs are the most prevalent configurations for low wind applications. However, the Darrieus-type SB-VAWTs face difficulty in self-starting and low efficiency. As per the earlier studies, these machines produce little or no torque and are unable to self-start (J. R. Baker, 1983). On the other hand, other investigations have demonstrated that the Darrieus-type SB-VAWTs can self-start by carefully selecting airfoils, blade configurations, and blade numbers (Dominy et al., 2007; Hill et al., 2009a). The J-shaped airfoils have the capability to self-start the SB-VAWTs because they take the benefits of both lift force and drag force simultaneously, as clearly described in Section 1.6. Further, these designs augmented the efficiency of Darrieus-type SB-VAWTs.

1.8. Objective of the Thesis and Roadmap

The Darrieus-type SB-VAWTs are a promising option for small-scale off-grid energy conversion for confined space and low wind speed applications where the counterpart of these VAWTs cannot operate effectively. However, a key challenge for these SB-VAWTs is their ability to self-start. The lack of research has focused on this topic, leading to a significant knowledge gap regarding aerodynamics and self-starting performance of SB-VAWTs, particularly for low Reynolds number (*Re*) and low tip speed ratio (λ) conditions. This thesis provides an in-depth analysis to address the knowledge gap in SB-VAWTs to enhance the self-startup and aerodynamic performance at low *Re* and λ. Although the current literature survey presents the use of various methods and airfoils in Darrieus-type SB-VAWTs to improve their starting characteristics and performance, very limited investigations have been conducted to examine the influence of resistive airfoils, such as J-shaped airfoils. Further, previous literature primarily reported the numerical performance assessment of J-shaped VAWT blades at higher *Re* and higher λ. The systematic aerodynamic performance trend analyses and self-starting torque analyses of J-shaped VAWT blades under clearly defined conditions particularly at lower *Re* and lower λ using numerical and experimental investigations have not been documented for small-scale applications. In view of this, **the objective of the present study is to analyze a novel type of airfoil known as the "J-shaped airfoil" for the blade of the small-scale Darrieus-type SB-VAWTs to enhance the starting characteristics and aerodynamic performance**. This study identified an operating regime at lower λ at which J-shaped configurations offer measurable performance benefits over conventional designs. From this perspective, the following key objectives of the present work are mentioned below. The road map of the present research is depicted in Fig. 1.10.

- Performing the thorough 2D numerical analysis on J-shaped airfoils (uppercut and lowercut) with various opening ratios (ORs) to determine the optimal J-shaped airfoils.
- Investigating the uppercut J-shaped airfoils with different ORs experimentally and numerically on the performance and starting characteristics of the small-scale Darrieus-type SB-VAWTs for lower *Re* and λ conditions and comparative analysis between conventional cambered airfoils and their uppercut J-shaped airfoils.
- Conducting in-depth experimental and numerical analysis of uppercut J-shaped blade numbers to study their effect on overall performance and starting behaviours of the small-scale Darrieus-type SB-VAWTs for low wind regimes.

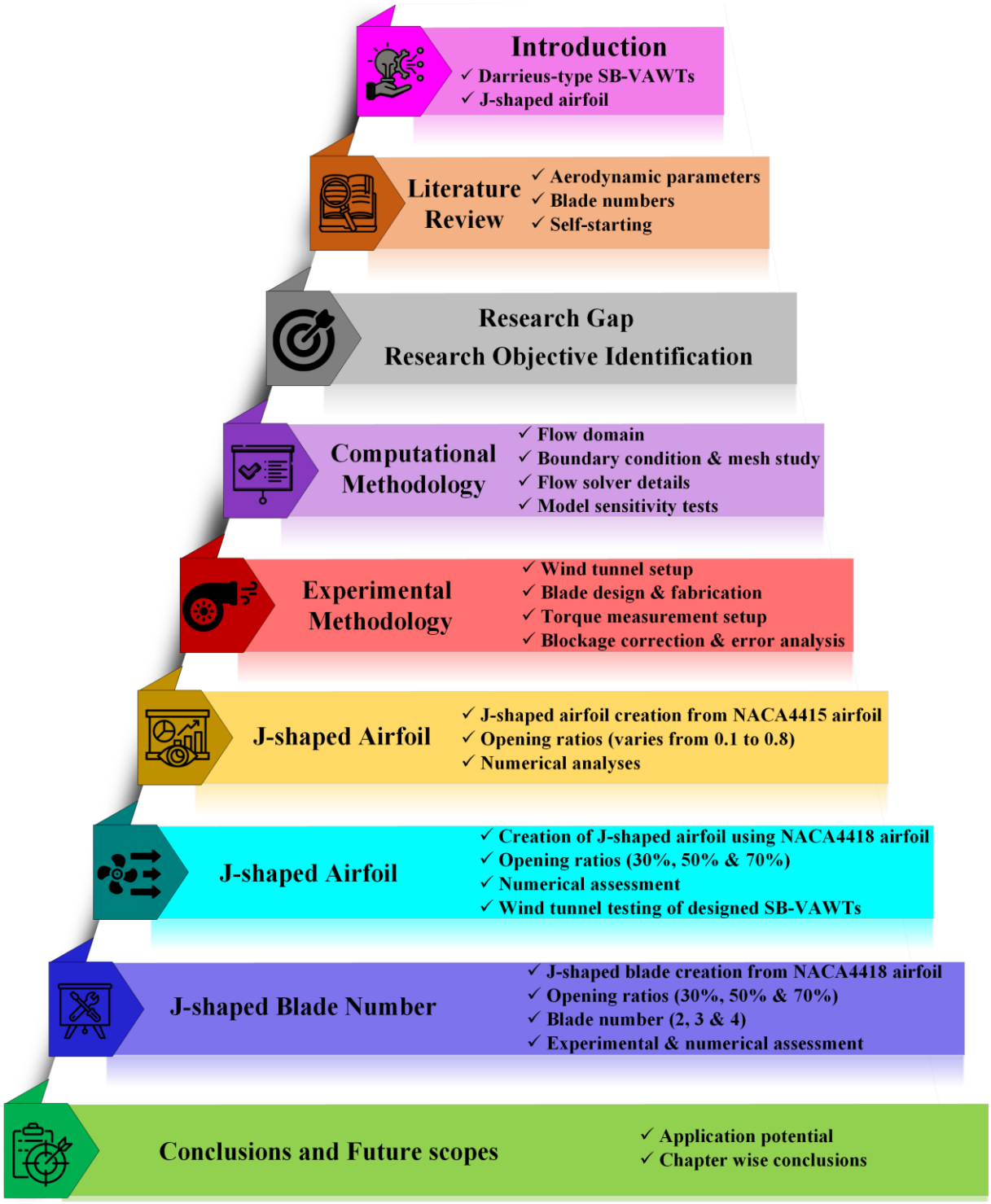

Fig. 1.10. Road map of the present investigation

1.9. Organization of the Thesis

The present thesis has been organized into eight chapters by focusing on the improvement of the Darrieus-type SB-VAWTs to address the objectives of this study. **Chapter 1** presented the motivation for this research as well as a brief introduction to the current energy scenario and wind turbine classification. This chapter describes the Darrieus-type SB-VAWTs and their aerodynamics. In addition, the aerodynamic configurations on J-shaped airfoils are presented. The chapter concludes with a summary and outlines the objectives of the thesis. **Chapter 2** demonstrates the comprehensive literature reviews on Darrieus-type SB-VAWTs addressing different aerodynamic parameters. This chapter also discussed existing literature relevant to the blade numbers and self-starting ability. The chapter wraps up by summarizing the literature. **Chapter 3** discusses the computational methodology adopted in the present investigations. This chapter elaborately describes the computational domain and various independent studies relevant to the numerical simulations. **Chapter 4** presents the experimental setup and methodology to carry out the wind tunnel experimentation. The experimental facility as well as the instruments used are described in this chapter. **Chapter 5** exhibits the numerical investigation of J-shaped airfoils on the performance of Darrieus-type SB-VAWTs. **Chapter 6** elaborates on the experimental tests of the Darrieus-type SB-VAWTs with J-shaped airfoils and conventional airfoils. This chapter also presents the adopted numerical assessment of the experimental design models. **Chapter 7** focuses on wind tunnel tests and numerical studies of the blade numbers used on Darrieus-type SB-VAWTs. **Chapter 8** summarizes the outcome of the present research work and presents the final conclusion. This chapter highlights the applications and the possible future scopes for further studies.

CHAPTER 2

Literature Review

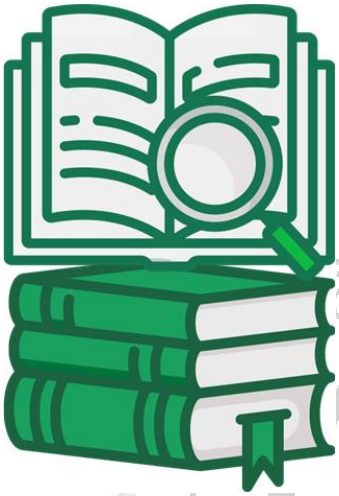

Chapter Layout

Overview

Since the commencement of the Darrieus-type VAWTs, a host of researchers have conducted experimental and numerical investigations to examine and enhance the aerodynamic performance and self-starting ability. The research interest in the VAWTs has been increasing than the other WTs due to the various inherent benefits of the VAWTs. This chapter demonstrated a comprehensive survey of available literature concerning the parameters that influence the aerodynamic performance and self-starting ability of VAWTs. The present chapter is divided into different sections to discuss the performance parameters, such as types of airfoils, tip speed ratio, solidity, Reynolds numbers, and wind speed. The effect of wake characteristics and blade numbers on the performance of the VAWTs is also described. In addition, viable solution approaches to improve the self-starting ability of the Darrieus-type VAWTs along with earlier investigations on starting torque have been discussed. This chapter highlights the current research trends for identifying the key research gaps. Based on these identified gaps, a summary of the whole literature survey is briefly outlined.

2.1. Effect of Airfoils on VAWTs

The SB-VAWTs produce higher efficiency than all types of VAWTs but suffer from starting problems. These VAWTs usually develop minimal starting torque and may be unsuccessful in speeding up beyond a dead band even if they start to move (Lazauskas and Kirke, 1992). It confines the usage and application of the SB-VAWTs, especially for those utilized for small-scale energy production. The aerodynamics of the airfoil configurations and new blade designs play an essential role in the improvement of the aerodynamic performance as well as the starting torque of Darrieus-type SB-VAWTs (Al Hamad et al., 2022). The SB-VAWTs may fail to generate self-starting torque unless the proper types of airfoils, freestream wind speed and rotor solidity are chosen. Therefore, researchers have proposed several ways not only to enhance the start-up ability of the SB-VAWTs but also to improve the performance of SB-VAWTs, such as a new blade profile, unsymmetrical/cambered airfoils, variable pitch blades, flexible blades, Turby/helical Darrieus, Savonius-Darrieus hybrid turbine, airfoil with opening ratios and so on.

The usage of various types of airfoils is one of the feasible ways to overcome the issue of the starting torque in Darrieus-type SB-VAWTs, among all the possible solutions, as it can substantially affect the starting torque and overall performance of those SB-VAWTs (Celik et al., 2022). An optimum airfoil shape is expected to have some desirable features during various operating conditions, mainly at a low λ, to acquire the optimum self-starting ability for SB-VAWTs. Thus, several numerical and experimental studies have been carried out on the impact of airfoil profiles to enhance the aerodynamic performance and self-starting of SB-VAWTs (Gupta et al., 2008; B K Kirke and Lazauskas, 1991; Wang et al., 2016). Batista et al. (2011) employed a new type of blade profile in the Darrieus-type VAWT to improve its starting ability at the low speed of the wind. They used the EN0005 airfoil as a new blade profile and observed that it provides the self-starting capability to the WT at low λ and low velocities. Beri and Yao (2011) studied the effect of a cambered airfoil of NACA2415 on the self-startup of the Darrieus-type VAWT and found that the cambered airfoil has the potential to self-start the VAWT with a lowered C_P. Similarly, other researchers (Bausas and Danao, 2015; Healy, 1978; Qamar and Janajreh, 2017a; Singh et al., 2015) have also used multiple cambered or unsymmetrical blade airfoils to develop the self-starting capability in the Darrieus-type VAWT. The symmetrical designs of the blade are another major drawback of the SB-VAWT due to its poor self-start-up traits (Bausas and Danao, 2015). A better lift is generated by the unsymmetrical blades than by symmetrical blades, mainly in the downwind pass (Bausas and Danao, 2015). The starting performance of the Darrieus rotors is also improved by the flexible blades (Lazauskas and Kirke,

1992), Turby/helical Darrieus rotors (Wang et al., 2018), Savonius-Darrieus hybrid rotor (Roshan et al., 2020) and variable pitch blades (Schönborn and Chantzidakis, 2007). The hybrid Darrieus-Savonius WTs have generated better self-starting ability in an urban atmosphere and developed a maximum C_P than the conventional VAWT (Roshan et al., 2020). This C_P value is much less than that of an ordinary Darrieus VAWT (Bedon et al., 2014). Further, Kyozuka (2008) reported that the C_P of the Darrieus-Savonius combined turbines is decreased to 70% of the solo Darrieus WT.

However, these problems can be resolved by an alternative approach by utilizing a J-shaped airfoil. A limited number of researchers have studied the J-shaped airfoil (Celik et al., 2022; Naik and Sahoo, 2023; Zamani et al., 2016a, 2016b) and applied it to the Darrieus-type SB-VAWTs. The J-shaped airfoil is made by eliminating some portion from the conventional airfoil either from its upper surface (US) or lower surface (LS) towards the trailing edge (TE), as shown in Figs. 1.9 (b) and (c). Zamani et al. (2016a, 2016b) investigated the J-shaped of DU-06-W-200 and NACA 0015 airfoils and reported that the Darrieus-type VAWT performance can be enhanced using the above airfoil at low wind speed. Further, the outcomes indicate that the aerodynamic performance is improved significantly at the first half revolution ($0^{\circ} <$ azimuthal angle (θ) $< 180^{\circ}$) of the turbine. The wake area behind the rotor with a J-shaped airfoil is independent of the slow vorticity dissipation and possesses very less turbulence. Mohamed (2019) criticised the J-shaped Darrieus VAWT with NACA 0015, NACA 0021 and S1046 airfoils in terms of performance and noise generation. The author reported that the J-shaped blade profiles reduce the performance and noise of the turbine at a high λ range (2 to 6). However, many authors (Celik et al., 2022; Ghazalla et al., 2019; Naik and Sahoo, 2023; Zamani et al., 2016a, 2016b) stated that J-shaped airfoils perform better at low λ values due to their innovative blade profile design. Blade structure improvement can be a significant way for offshore wind turbine analysis. In accordance with this, Pan et al. (2021) numerically analysed the impact of a J-shaped blade profile on offshore VAWT at low λ values. They demonstrated that the optimized J-shaped blade structure significantly increases the upwind torque and capture rate of wind energy. A numerical analysis is examined by Chen et al. (2015) for improving the self-starting issue of Darrieus VAWT with a J-shaped symmetric NACA 0015 airfoil. The findings revealed that the inner opening (0.48 and 0.60) and outer opening (0.72 and 0.84) display desirable VAWT performance. Some researchers (Al Hamad et al., 2022; Celik et al., 2022; Naik and Sahoo, 2023) have studied the effect of several openings at the upper or lower surface on a J-shaped airfoil to augment the aerodynamic performance and starting torque of the

Darrieus-type SB-VAWT. The J-shaped airfoils with an opening at their lower surface (inner surface) do not bring any benefits to Darrieus-type SB-VAWT compared to the opening on its upper surface (outer surface) (Naik and Sahoo, 2023). Better performance is observed at low λ values when using a J-shaped airfoil with the largest opening ratio (the ratio of opening length (X_c) to the chord length of an airfoil (c)) on its upper surface. Hill et al. (2009b) have investigated the physics of the self-starting ability of the small-scale Darrieus rotors. The starting problem of the Darrieus rotor can be resolved by using a blade profile constructed in such a way that it can use the advantages of both F_L and F_D (Celik et al., 2022; Ghazalla et al., 2019; Mohamed, 2019; Zamani et al., 2016a, 2016b). The benefit of this blade profile is the good start-up torque as it functions due to a drag-based mechanism like Savonius rotor blades and simultaneously enhances the overall C_P of the VAWT because it's a lift-based like the Darrieus rotor (Earnest and Rachel, 2019).

2.2. Effect of Tip Speed Ratios on VAWTs

A thorough literature survey has been carried out on the effect of tip speed ratio (λ) on the performance of the Darrieus-type SB-VAWTs. The λ is the linear velocity of the tip of the blades normalized by the incoming wind velocity. Various investigations have been undertaken in this research field, which are discussed in this section. Zanforlin and Deluca (2018) investigated the effect of λ on the optimal aspect ratio (AR) of SB-VAWT. Three different λ values (i.e., 3.5, 3.75, and 4) are simulated to verify the influence of λ on the performance of the SB-VAWT. The increased value of λ is the only way to avoid flow separation in blades characterized by high AR. On the outer part of the blade, an increase in λ worsens performance due to an excessive reduction of attack angle. The flow separation is mitigated by a small increment in λ values for larger AR, mainly in the central part of the blade. Parker and Leftwich (2016) studied the influence of three different λ (λ_{low} = 0.9, λ_{mid} = 1.3 and λ_{high} = 2.2) on VAWT at high *Re* and noticed that the structure of the wake is far more sensitive to λ as compared to *Re*. Further, they reported that the vortices convect within the wake downstream at middle λ (λ_{mid} = 0.9), whereas vortices pair shed towards the wake shear layer at high λ (λ_{high} = 2.2). They demonstrated that λ strongly depends on the wake structure during small variations in *Re*. A backflow region is seen along the streamwise direction at λ_{high} and observed fine wake boundaries on both sides. At the λ_{low}, the backflow region is not found. Further, a highly asymmetric profile with much steeper transitions was obtained on one side of the wake region, generally for λ_{mid}. Moreover, two pairs of vortices are developed by every blade at the downstream for λ_{mid}. These vortices are convected directly along the downstream area. Contrastingly, only one pair of vortices is generated at λ_{high},

which convects in the wake edge. The effect of different λ on the performance of a VAWT has been investigated by Rezaeiha et al. (2018a). In this work, the λ values vary between 1.5 and 5.5 for different azimuthal increments ($d\theta$) varying between 0.05° and 1.0°. At high λ values of 4.5 and 5.5, results are negligible for $d\theta \leq 0.5°$. Mostly attached flow is found along the regime for the moderate to high λ values of 4.5 and 5.5. Less complex flow physics is obtained at lower λ without blade wake-blade interactions and dynamic stall. On the other hand, the blade wake-blade interactions and dynamic stall are present for the low to moderate λ values. The wind tunnel tests are carried out by Li et al. (2016b) to investigate the effect of λ on power performance for SB-VAWT with NACA0021 airfoil profile. Larger values of C_P were obtained in the field test than in the wind tunnel experiments at low and high λ values. In contrast, smaller values of C_P are found from the field test at optimum λ compared to the wind tunnel results. Slight changes are seen in C_P values for different turbulence intensities at low λ. The increment in turbulence intensity reduced C_P at high λ. Joo et al. (2015) have studied the effect of λ on the performance of a 2-bladed H-Darrieus at various σ values. When the σ value decreases, the interaction and blockage impact can be decreased. The features of self-starting are lost due to the negative torque at a lower λ value. At larger $\lambda \geq 3.7$, a deep decrement in torque is seen due to the weak free stream towards the downwind revolution because of blockage. During the upwind revolution for low $\lambda \leq 2.2$ and $\sigma = 0.5$, the AOA achieve its critical angle (stall). It does not reach a high value of $\lambda \geq 3.7$ and $\sigma = 0.5$, but suddenly decreases the torque and becomes small due to its small AOA. The lower operation point of λ is found when the σ increases. Sun et al. (2014) have studied the effect of λ on the aerodynamic performance of VAWTs. The C_P of the Darrieus turbine increases with the increase of λ until a maximum point is achieved. Further increment in λ and σ decreases the C_P. For optimal λ, the C_P increases initially and decreases thereafter when the σ increases. Posa (2020) manifested that the wake characteristics strongly depend on λ. A larger momentum deficit is generated in the wake with increasing λ, but recovery of the wake is done in a faster manner.

2.3. Effect of Solidity on VAWTs

The appropriate selection of solidity (σ) for the design configurations of the VAWT can potentially enhance the self-starting capability and the aerodynamic performance of the VAWT. In this background, extensive research has been conducted on the σ effect on λ, *Re*, self-starting capability and the aerodynamic performance of the Darrieus-type VAWTs. Bel Mabrouk and EI Hami (2019) studied the effect of σ on the aerodynamic performance of two, three, and four-bladed Darrieus-type VAWT configurations at several values of λ. This study used various σ

values, such as 0.33, 0.5, and 0.66 for all rotor configurations. For a given R and c, the σ values drastically increase if the blade number (N_b) increases, but this degrades the performance of WT. The decrement is observed in maximum efficiency with a decrease in σ values with one or two blades due to the reduction in F_L. Both numerical and wind tunnel investigations were conducted by Edwards et al. (2008) to study the σ effect on the performance of a Small VAWT. A significant improvement is observed in the performance coefficient for rotors with larger σ values. According to the reports (Edwards et al., 2008; Howell et al., 2010), the machines with high σ are better for high torque, low-speed operation, while machines with lower σ are good for low torque, high-speed operation. Moreover, Howell et al. (2010) reported that the higher σ values dictated the lower λ and efficiency for a Small VAWT. Further, two-bladed turbines maxima lie at a low value of λ because of lower σ. An increment in N_b substantially increases the σ values without reducing their blades' chord. Roh & Kang (2013) investigated the effect of σ varying from 0.08333 to 0.5 at Re of 3,60,000 on the performance of SB-VAWT by adopting the NACA0015 airfoil. The increment in σ produced a marked reduction in the power production. When the BSR (blade-speed ratio zone) < 3, a steep variation is obtained in power values around their peak for high σ > 0.3. They mentioned that the self-starting problem of a straight-type Darrieus VAWT can be overcome by improvement in torque with increasing the σ for the low-speed range (BSR < 2). The VAWT with high σ reduced both peak efficiency and λ. Furthermore, when σ increases, considerably different behaviour is observed in the power of the straight-type Darrieus VAWT and the eggbeater-type Darrieus VAWT. Zhu et al. (2019) used the NACA0021 airfoil as the base profile to study the σ impacts on the SB-VAWT with the Gurney flap (GF). In this work, many σ values are investigated, such as 0.175, 0.25, 0.333, 0.416, and 0.5, using six types of GF and dimple GF (i.e., inboard, outboard, two sides, and dimple). The C_P of SB-VAWT is enhanced at low λ by outboard GF and dimple GF for different values of σ. The SB-VAWT blades with high σ are preferred choices for the requirement of initial self-starting torque. The flow structure complexity increases when σ increases. Due to the greater flow blockage, the 3-bladed H-Darrieus VAWT can self-start faster with a high turbine σ than low σ turbines (Du et al., 2019)**.** Furthermore, the self-starting ability of VAWT is reduced when σ decreases because of decreased blockage effect and torque. The influence of σ on SB-VAWT is investigated by Li and Li (2010) using NACA0012 and NACA 0018 airfoils. When the σ increases, the average static C_T also increases, which augments the starting performance of the SB-VAWT. The aerodynamic performance of Darrieus H-type VAWTs has been investigated by varying the σ range of 0.09-0.36 (Rezaeiha et al., 2018b)**.** A shift is observed in optimal λ from 4.5 to 2.0 by increasing the σ from 0.09 to 0.36. This increment in σ increased

the maximum C_P by 22.5%. Further, C_T produces asymptotically with the increase of σ. For a given airfoil chord-based Reynolds number (Re_c) value, the maximum F_L increases and the maximum F_D decreases for the lower λ values due to the increment in σ values. Li et al. (2017b) have studied the impact of rotor σ on SB-VAWTs in the 3D analysis by the panel method. As per the study, the C_P peak increases for the fixed σ of 0.064 due to the increased value of the diameter and blade span length ratio. Thus, it is expected that the optimal λ will be increased. Subramanian et al. (2017) used a 3D CFD model to study the σ impact on the performance of small-scale VAWT. The 2-bladed VAWTs produce more power compared to 3-bladed VAWTs, which states that better performance is found at high λ values for VAWTs with lower σ. Moreover, the thinner airfoils dissipate the shed vortex much faster than that of thicker airfoils for larger values of λ. Li et al. (2016a) reported that the maximum C_P of VAWTs depends on the σ of the rotor and the σ depends on R, c and N_b. The pressure differences decrease substantially with an increment in σ and a decrement in Re. It is found that the C_P decreases and the C_T increases with an increase in σ. Eboibi et al. (2016) mentioned that the poor performance regions decrease for a VAWT when σ, wind speed and Re increase. It is observed that the VAWT with larger σ achieved an identical maximum C_P than the VAWT with lower σ, but it presented a narrower performance curve (C_P –λ). The VAWT with lower σ limits the rotor efficiency compared to the VAWT with larger σ. This happens as the generation and shedding of stall vortices are initiated earlier. Superior performance has been obtained in the performance of a cross-flow turbine with NACA 0015 airfoil due to the high σ (Consul et al., 2009). On the other hand, the larger σ reduces the overall lift, which decreases streamwise velocity and resultant flow velocity. At higher λ, the decrement in total T has been offset because of the additional T from additional blades with larger σ. Whereas at lower λ, the VAWT with higher σ may increase the turbine's power take-off. Qamar and Janajreh (2017b) have investigated turbine σ for cambered Darrieus VAWTs with NACA4312 airfoil. Lower performance coefficient is obtained from the VAWTs with lower σ for higher λ ranges and higher performance coefficient is found at lower λ by the VAWTs with σ close to unity. The operating range is greater for the low σ VAWTs at the cost of low overall performance, while the high σ VAWTs have obtained much greater performance. Mohamed et al. (2013) stated that the maximum C_P of the H-rotor Darrieus turbine begins to fall after the σ of 0.4. The peaks in the maximum C_P are observed at a σ between 0.3 and 0.4; thereafter, it begins to fall. A good self-start capability has been obtained from the SB-VAWT with high σ, as the generated total T is positive with a relatively large value (Peng et al., 2019). The C_P increases by increasing the σ in the variable pitch angle VAWT (Sagharichi et al., 2018). At medium and high σ values, the F_D and the flow separation are reduced by the

variable pitch angle VAWT. Mohamed et al. (2019) studied the effect of σ on the performance of the J-shaped Darrieus VAWT with a 3-bladed rotor. They demonstrated that the T and power output coefficients have reduced for all σ values (such as 0.1, 0.15, and 0.2). Islam et al. (2011) have studied the effect of σ varied between 0.1 and 1 on the performance of a small-capacity VAWT. They presented that the blade chord increases and the turbine height increases from the design approach when the σ value increases, but the turbine diameter decreases. Joo et al. (2015) have stated that the performance of the H-Darrieus does not improve by increasing the value of σ alone. The blockage and interaction also increase as σ increases, even though an increment in the peak value of T. The highest C_P of VAWTs occurs at the σ of 0.5. Sun et al. (2014) have found that optimal λ is higher for the smaller value of σ. When the σ increases, the C_P increases at low λ values. Further, the C_P increases initially and then decreases for optimum λ with the increase of σ. On the other hand, the C_P decreases at high λ and increases at low λ with increasing σ.

2.4. Effect of Reynolds Numbers and Wind Speed on VAWTs

The Reynolds number (Re) is an effective key factor for increasing power production in Darrieus-type VAWTs. It is one of the significant parameters that influences the rotational and inflow velocity at which the turbine achieves its maximum performance coefficient. A vast research review has been conducted on Re to study its effect on VAWTs. Roh & Kang (2013) investigated the effect of Re on the performance of SB-VAWT with NACA0015 airfoil by varying the BSR range from 1 to 12. In this work, the power (P) has been estimated by varying Re from 8.0×10^4 to 7.0×10^5 at different BSR and a fixed σ of 0.08333. The increment in Re rapidly reduces the improvement in P. Further, a very steep variation pattern is observed around the peak of P at BSR < 3 and high $\sigma > 0.3$. Brusca et al. (2014) studied the effect of Re on the turbine performance of VAWTs and found an improvement in the performance of VAWTs by increasing Re values. The Re values strongly influence the aerodynamic performance of the SB-VAWTs (Zanforlin and Deluca, 2018). The $Re_c > 1 \times 10^6$ produces a larger lift-to-drag (L/D) ratio. When the wind speed and turbine size decrease for $Re_c < 1 \times 10^6$, the drag and flow separation play a significant role. They reported that the production of P is not dependent on high values of Re. Parker and Leftwich (2016) studied the impacts of higher Re on VAWTs. Asymmetric wakes behind the VAWT model are observed for each Re (i.e., 60,000, 120,000, and 180,000). Negligible changes in the flow surrounding the turbine are obtained when changes in Re. Naik and Sahoo (2024) experimented on Darrieus-type SB-VAWTs to study the effect of Re on the aerodynamic performance. An improvement in aerodynamic performance is

obtained when the *Re* values are increased. Wind tunnel experiments have been conducted by Li et al. (2016c) to investigate the effect of *Re* on the performance of SB-VAWT with NACA0021 airfoil. These tests discuss the C_P curves for *Re* values that vary between 1.62×10^5 and 2.89×10^5. Enhancement in *P* production is obtained at $0.5 < \lambda < 3.0$ when *Re* increases. At the highest *Re*, the WT attained the highest C_P and the lowest optimum λ. Further, a larger *T* is produced on the rotor due to the increase in the value of C_L at higher *Re*. Thus, better performance is accomplished by the rotor for larger *Re*. The performance of SB-VAWT is improved by increasing the *Re*. The *Re* of the blade increases as the wind velocity increases.

Wind tunnel experiments have been conducted by Li et al. (2016b) to investigate the effect of wind speed on the power performance of SB-VAWT with NACA0021 airfoil profile. The Laser Doppler Velocimeter (LDV) system is used to measure the wind velocity, from which the flow field characteristics of WTs. Smaller values of maximum C_P are found in the range of low wind velocity, ranging between 3 m/s and 7 m/s for the case of low wind speed. In comparison, these values are increased for the case of larger wind speeds. During larger wind speeds, optimum λ becomes smaller. The performance of VAWTs is enhanced when the wind velocity increases. The effect of wind speed (i.e., 6 to 10 m/s) on a micro VAWT is studied by Elkhoury et al. (2015) numerically and experimentally. The lift generation from the blades relies on *Re*, which depends on wind speed. The C_P curve displayed the highest value with a maximum C_P of 0.21 at λ of 1.3 for the lowest wind speed equal to 6 m/s. According to the outcomes of laminar separation transition, it is deduced that the increment in drag of the NACA 0018 airfoil is higher than the lift increment for wind speeds ranging between 8 m/s and 10 m/s. This phenomenon is not observed for a lower velocity of 6 m/s. When the wind speed is equal to 4 m/s, the highest C_P is generated from the fixed pitch NACA 63_4-221 blade. Thereafter, the experimental values decrease for 8 m/s and 10 m/s. Mo et al. (2013) studied the changes in wind speed of a WT using large eddy simulation in a virtual wind tunnel. A larger velocity deficit has been noticed for the smaller wind speed and the deficit decreases with wind speed. The turbulent intensity (TI) reduces for a wind speed of 7 m/s and is constant for higher wind speeds. They reported that the downstream distance where wake instability and vortex breakdown occur is a function of upstream wind speed.

2.5. Effect of Wake Characteristics on VAWTs

Mo et al. (2013) investigated the influence of wind speed on the wake instability of a WT within a virtual wind tunnel. The flow is attached to the blade surface throughout the pre-stall state,

while it is completely separated from the total blade span for the post-stall state. Moreover, separation in the flow is observed close to the root region and attached around the tip region for the transitional state at a wind speed of 10 m/s. An intense and stable vortex of helical type is obtained in the wake at the back side of WTs. Furthermore, an unstable vortex structure is found in the wake, which breaks down and streamwise vortices patterns are developed in far wake areas. Sørensen and Shen (2002) have presented the numerical modeling of WT wakes to study the 3D flow field. The shed vortices are observed during the near wake as distinct vortex tubes and are diffused into the continuous vortex tubes after two turns. Experimental tests have been conducted by Adaramola and Krogstad (2011) to investigate the effect of wake on the performance of downstream WT. The C_P and thrust coefficient decrease due to the low velocity during the WT operated in the wake. The velocity recovers slowly in the wake when the distance between the WT increases and produces an improvement in power. The characteristics of wake structure are studied by Posa et al. (2016) behind the single VAWT by particle imaging velocimetry (PIV) and large-eddy simulation (LES). The upwind stall from the blades generates higher turbulence and coherence along the leeward side of the wake. Meanwhile, the coherence towards the downwind stall in the wake core decays quickly. The wake structure dependence displayed higher asymmetry and bigger vortices at the lower rotational speed because of the dynamic stall phenomena. Lam and Peng (2016) have investigated the wake characteristics of VAWTs through 2D and 3D CFD simulations. The zones for the near and far wakes are decided according to the maximum velocity deficit. A drastic deficit of about 85% suffered in the velocity within the near wake. However, maximum velocity recovery happened as per the average streamwise velocity, which achieved approximately 75% in the far wake. The wake asymmetry is observed when the downstream distance increases. Elkhoury et al. (2015) investigated the numerical and experimental effect of vortex interaction on a micro-VAWT with variable pitch. A complex flow structure occurs around the blades when the VAWT undergoes dynamic stall during high AOA and low λ. The dynamic stall produces large recirculation separated flow zones that form vortices shed towards downstream and impinge on other blades. As a result of the vortex interaction on blades, VAWT generates P at low λ. A deep dynamic stall occurs on blades inducing hysteresis lift and drag loops at lower λ (Amet et al., 2009). Further, these blades represent an attached boundary layer at higher λ. Simão Ferreira et al. (2009) have analyzed dynamic stall at different λ of a VAWT by particle image velocimetry (PIV). During the lower λ values, the dynamic stall phenomenon impacts both loads and the P of a VAWT. Generally, the dynamic stall is commonly obtained when the AOA can vary over a wider range. Buchner et al. (2015) have studied the effect of the dynamic stall in VAWTs and

reported that the dynamic stall is the primary obstacle for VAWTs to achieve higher aerodynamic efficiency. Li et al. (2017a) have investigated the behaviour of the stall of SB-VAWT through numerical and experimental studies. The predominant vortex-shedding flow structure is clearly observed by numerical simulation. The importance of the stall phenomenon and the separation vortex interaction with blades are displayed through the flow separation behavior of the airfoil. Parker and Leftwich (2016) found that the wake structure is considerably more sensitive to λ than to *Re*. The J-shaped blade profiles has the inherent ability that traps the generated vorticities and releases the backside of the SB-VAWTs (Naik and Sahoo, 2024, 2023; Zamani et al., 2016b, 2016a). Further, the wake area behind the SB-VAWTs with J-shaped blade profiles are free from the slow moving vorticities dissipation and produces much lesser turbulency.

2.6. Effect of Blade Numbers on VAWTs

The complex flow phenomena are caused by the geometrical and operational characteristics of the SB-VAWTs (Rezaeiha et al., 2018b). The SB-VAWTs are influenced by operational characteristics such as λ, TI and Re_c (Rezaeiha et al., 2018c). On the other hand, the geometrical characteristics involve σ, airfoil shape, blade numbers (N_b) and so on (Rezaeiha et al., 2018b, 2018c). For a SB-VAWT, σ relies on the *c*, *R* and N_b. Different geometrical and operational parameters affect the aerodynamic behaviour of the Darrieus-type SB-VAWTs (Edwards et al., 2008), among which N_b plays a significant role (Li et al., 2015). The amount of power extracted from the wind is determined by the blade's characteristics (Li et al., 2015). As a result, improvements in blade design and aerodynamics can directly translate to a significant boost in the efficiency of the wind power plant. Several authors (Castelli et al., 2012; Li et al., 2015; Wang and Chen, 2008) have studied the influence of the N_b on the aerodynamic performance of SB-VAWTs experimentally and numerically. Mabrouk and Hami (2019) have investigated the N_b (2, 3 and 4) effect on the aerodynamic performance of a Darrieus turbine and reported that the 3-bladed turbine configuration shows the best aerodynamic performance compared to the others in terms of efficiency and torque production. As per their demonstration, the 4-bladed turbine displays smoother torque behaviour; thus, it forms the lowest dynamic vibration in the bearings. A similar type of investigation conducted by Castelli et al. (2012) revealed that 3-bladed VAWT performs better than 4 and 5-bladed VAWT configurations. They also stated that a larger N_b enhances the C_P values at lower angular velocities. A more N_b incorporated with WTs performs best at lower λ values when they use longer *c* and higher height to diameter ratio and this trend is reversed at higher λ values (Ghiasi et al., 2022). In contrast, Saad and Ahmed

(2023) revealed that the 3-bladed Darrieus rotor with helical blades shows higher C_P at higher ranges of λ than the 2 and 4-bladed rotors. According to Kuang et al. (2023), a 3-bladed design is more beneficial at higher σ, while the 2-bladed design attains a higher C_P peak at lower σ. They further mentioned that Re_c affects the impacts of N_b. Rezaeiha et al. (2018b) reported that the smaller N_b with a higher c displayed a higher K (reduced frequency) for a given σ and thus, a larger C_P. M. EI-Samanoudy et al. (2010) have pointed out that the maximum C_P decreases when N_b decreases from 4 to 2 blades and found 25% improvement in the C_P of a 4-bladed Giromill VAWT. Meanwhile, Howell et al. (2010) stated that the 2-bladed rotor produces higher C_P than a 3-bladed rotor. Some earlier studies reported that the C_P values of small SB-VAWT decrease by increasing the N_b (Edwards et al., 2008; Li et al., 2015). It happens because of the interference between them, as per Tirkey et al. (2014). Moreover, the advantages of incorporating more blades (Bedon et al., 2017) rely on finding a balance between the various necessary performance traits and manufacturing expenses. According to Bedon et al. (2017), the N_b equivalent to 2 or 3 is a good alternative equally for enhancing the performance of Darrieus VAWT as per the load. In applications of offshore environments, N_b always remain a primary consideration during the design of a VAWT. Cheng et al. (2017) investigated the influence of N_b on floating SB-VAWTs. They illustrated that the fluctuations in bending moment decrease more notably at the tower base when the N_b rises from 2 to 3, compared to using the N_b from 3 to 4. The N_b also affects the wind speed (Bel Mabrouk and El Hami, 2019) of the Darrieus-type SB-VAWT. Wang and Chen (2008) studied the impact of N_b and exhibited that a higher speed in flow is achieved with less N_b, whereas more torque is generated with a larger N_b. Further, the 3-bladed VAWT has a greater mean C_P at high wind velocity (V > 9 m/s), while the 5-bladed VAWT display a higher mean C_P at low wind velocity (V < 6 m/s) (Sun et al., 2021). The impact of N_b ranging from 2 to 5 is investigated by Reddy and Bhosale (2024) on performance and wake recovery for a helical hydrokinetic VAWT and obtained the highest C_P for a 4-bladed rotor with σ of 0.3. They also mentioned that TI and velocity deficit increase when the N_b increases.

2.7. Effect of Self-Starting on VAWTs

The self-starting capability of Darrieus-type SB-VAWTs has always been a strong research topic among researchers (Celik et al., 2022). It plays an essential role during the installation of Darrieus-type SB-VAWTs. A mechanical or electrical mechanism is employed to initiate the SB-VAWTs (Auyanet et al., 2022). However, this procedure makes the entire system expensive. Previous investigations (Al Hamad et al., 2022; Naik and Sahoo, 2023; Zamani et al., 2016a)

manifested the trouble in Darieus-type SB-VAWTs to self-initiate. Most of the research in this field focuses on demonstrating and enhancing the VAWTs self-starting capability. A strong correlation between self-starting performance and N_b has been found in earlier studies (Liu et al., 2019; Sun et al., 2022). Sun et al. (2022) examined the start-up performance of tidal current VAWT with various N_b and achieved a good starting performance with 4-bladed VAWT for θ positions from 100º to 120º. Delafin et al. (2016) found an increment in the starting performance of a 4-bladed VAWT at low λ because of better torque ripple. Further, these torque ripples reduce when N_b increases from 2 to 3. However, Dominy et al. (2007) reported that the 3-bladed Darrieus rotor with minimal load always has the ability to self-start under steady winds. They also obtained that the 2-bladed rotor relies on its starting orientation to start up. Feng et al. (2021) investigated the N_b impacts of lift-type VAWT with a novel device called the lift-drag combined stater (LDCS) to enhance the starting ability of VAWT. In this analysis, the 3-bladed LDCS displayed better static starting characteristics among the 2 and 4-bladed LDCS VAWT. Changing the blade design is an alternative technique that can also improve the self-starting and blade aerodynamics of Darrieus-type SB-VAWTs (Kuang et al., 2023). A very few number of authors (Celik et al., 2022; Zamani et al., 2016b, 2016a) employed the J-shaped blade design instead of conventional straight blades in the SB-VAWTs and found improvement in aerodynamic performance and startup torque results. Celik et al. (2022) analyzed the self-starting of H-type 3-bladed VAWT with J-shaped NACA 0018 airfoils and presented that the self-startup capability of 3-bladed VAWT increases when the OR of J-shaped airfoils increases. Further, Zamani et al. (2016b, 2016a) studied the 3-bladed J-shaped VAWT and demonstrated that this design intensified the turbine performance and self-starting ability. Moreover, Naik and Sahoo (2023) suggested that the 3-bladed VAWT with J-shaped profile enhanced the starting torque and performance of Darrieus-type SB-VAWTs at low λ when this blade design is created by removing some part of the conventional airfoil from its upper surface.

2.8. Summary

The Darrieus-type SB-VAWTs can be a sustainable solution for small, simple, low-cost and easy-to-maintain wind energy systems, especially for urban and rural settings. The Darrieus-type SB-VAWTs are one of the simplest and most cost-effective renewable energy machines, but face self-starting issues and generate lower power output. These configurations are suitable for small-scale applications where the benefits of limited installation space, lower wind velocity, lower cost, decentralized power production and omnidirectional operation are the prime

concerns. This chapter provides insightful information about the Darrieus-type SB-VAWTs and the different parameters that affect the properties of these turbines. A major part of the chapter is involved in selecting the airfoil shape for the blades, N_b and self-starting ability of the Darrieus-type SB-VAWTs. The effect of λ, σ, *Re* and wind speed and wake characteristics on the performance of SB-VAWTs is illustrated. There is a significant opportunity for further research and investigation within this area. The survey also concentrated on determining the gaps in existing literature, which are analyzed and summarized below:

- Numerous experimental and numerical investigations have been carried out on Darrieus-type SB-VAWTs with symmetrical airfoils. The symmetrical airfoils possess poor self-starting features, even if they help SB-VAWTs produce better C_P. The symmetrical airfoils have a lower C_L than cambered airfoils for the same AOA. In accordance with this, many researchers proposed various ways to overcome these problems. The airfoil with ORs is one of the possible solutions to improve self-starting ability and power output. Due to their design structure, these airfoils with ORs are also called J-shaped airfoils. The lack of information on the J-shaped airfoils motivates researchers to do further research to understand their applications in various areas. Usually, the small-scale SB-VAWTs use blades with a constant profile. Therefore, careful airfoil selection is required for the SB-VAWTs taking into account lower *Re* and λ.
- The SB-VAWTs performance is highly dependent on λ. In the middle part of the blade, a small increase in λ values mitigates flow separation for high AR. The C_P of Darrieus-type SB-VAWTs increases with the increase of λ values and then, the C_P decreases with further increases in the λ values.
- The σ significantly increases if the N_b is increased while keeping R and c constant, but it leads to a degradation in the overall performance of the Darrieus-type SB-VAWTs. The complexity in the flow structure increases as the σ increases. The VAWTs with a high σ manifest superior performance at low λ, while those with low σ perform better at high λ. Generally, the maximum C_P of VAWT mainly depends on the σ of the rotor, and it depends on the R, c and the N_b. Selecting an appropriate value of σ is vital for the design configurations of the SB-VAWTs to achieve optimum performance.
- The *Re* is a key parameter that dictates the inflow and rotational velocity at which SB-VAWTs achieve their maximum performance coefficient. The *Re* is affected by the ratio between H and R. The structure of the wake varies slightly with *Re*. The C_P of the SB-VAWTs is strongly influenced by the *Re* values. The increment in wind velocity increases the *Re* of the blade. The performance of SB-VAWTs is enhanced at higher

wind speeds as the lift generation increases. In these conditions, the reduction in rotational speed of SB-VAWTs ensures their safety.

- The structures of flow in the wake mainly depend upon the operating state of the SB-VAWTs. In the far wake, the complex flow structures are closely related to the local increase in the TI. These flow structures develop gradually around the blades of the SB-VAWTs at high AOA and low λ, undergoing dynamic stall. The blades with innovative vortex trapping designs can trap the vortex shedding, thus improving the efficiency and self-starting capability of SB-VAWTs. Further, these designs release the trapped vortices slowly and lessen the turbulence behind the SB-VAWTs. The dynamic stall is the principal impediment of SB-VAWTs to achieving enhanced aerodynamic efficiency.
- The N_b is one of the most important parameters that influences the performance of Darrieus-type SB-VAWTs. According to the literature survey, higher N_b produces more power but reduces the efficiency of SB-VAWTs because of interferences between them. However, the higher N_b appears to be promising for applications with lower λ. Generally, the benefits of adding more blades involve a trade-off between the various required performance characteristics and manufacturing costs. Thus, an appropriate N_b must be employed on SB-VAWTs to generate optimal overall performance and efficiency. There is a lack of comprehensive research on J-shaped N_b employed in the Darrieus-type SB-VAWTs for low λ.
- Self-starting plays an essential role in the installation of Darrieus-type SB-VAWTs. During the steady wind conditions, the 3-bladed SB-VAWTs can produce starting torque under minimal load conditions. Better torque is obtained at low λ from the 4-bladed SB-VAWTs. The conventional symmetrical blade profiles face self-startup issues compared to the conventional cambered blade profiles. Changing the configurations of the blade structure can be an alternative technique to enhance the self-starting. A very limited number of research studies are available that focus on self-starting issues.

CHAPTER 3

Computational Methodology

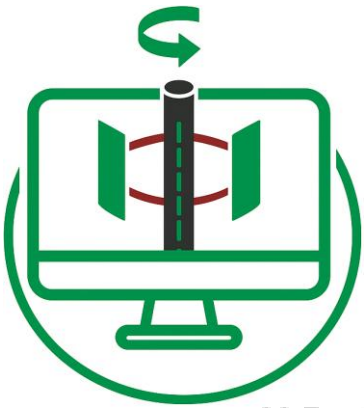

Chapter Layout

Overview

This chapter discussed the numerical setup used on the Darrieus-type SB-VAWTs with conventional and J-shaped blade profiles. After completing the accuracy checks, the numerical simulations are used as a modelling approach to achieve high fidelity analysis, which is reasonably accurate and computationally efficient. The different evaluation methods of the numerical setup, such as flow domain, boundary conditions, mesh strategy, flow solver setup, domain independence test, grid independent test, time independent test and validation are described in this chapter. The computational methodology is demonstrated for two cases with two different domain sizes. In the first case, a suitable domain of dimension 12D ×8D (length×Width) is selected for Darrieus-type SB-VAWTs. The rotor diameter (D) of 2.5m and airfoil chord length (c) of 0.4m are used for these SB-VAWTs. This case is employed in order to conduct a series of numerical simulations on SB-VAWTs with J-shaped airfoils with various opening ratios (ORs) and conventional airfoils. The numerical simulation results are validated with existing numerical data and experimental data. In the second case, the numerical setup utilizes a domain of length 48D and width of 32D. This case chose the D and c of 0.25m and 0.1m, respectively. The second case dimensions are selected based on the experimentation conducted in the wind tunnel. The second case investigates the series of cambered airfoils and their J-shaped airfoils with ORs and J-shaped blade numbers effect on Darrieus-type SB-VAWTs.

3.1. Computational Methodology (Case: I)

The computational fluid dynamics (CFD) study on Darrieus-type SB-VAWTs is getting much attention in the current scenario due to the rapid increase of computer processing ability. Further, the CFD provides easier and more accurate predictions than other methods (Celik et al., 2022). The 2D CFD models necessitate less computational time, are budget-friendly computationally and maintain the same level of computational accuracy compared to the 3D model simulation. As per earlier studies (Abraham et al., 2012; Elsakka et al., 2019; Rezaeiha et al., 2018a), the results from the 2D simulation models are comparable to the 3D simulation models. Researchers can achieve satisfactory results by utilizing 2D simulation models and obtaining valuable insights about critical factors that control the overall performance and flow behaviour near the WT blades (Rezaeiha et al., 2018a; Sun et al., 2020). The numerical simulations are investigated by using a 2D solver for the Darrieus-type SB-VAWTs with J-shape and conventional airfoils. This section includes the computational domain description, governing equations, mesh setting, boundary conditions (BCs), solver settings, model sensitivity test, and model validation.

3.1.1. Flow Domain Description

The Darrieus-type SB-VAWTs operate in open field conditions; therefore, it is necessary to consider a large domain to avoid solid blockage. Accordingly, a numerical model is produced in order to generate a solution independent of the BCs with several advisable model conditions, timestep size, and convergence details to acquire the essential aerodynamic force coefficients. In view of this, additional independence tests and model validation are carried out in a straightforward improving manner for distinct reasons.

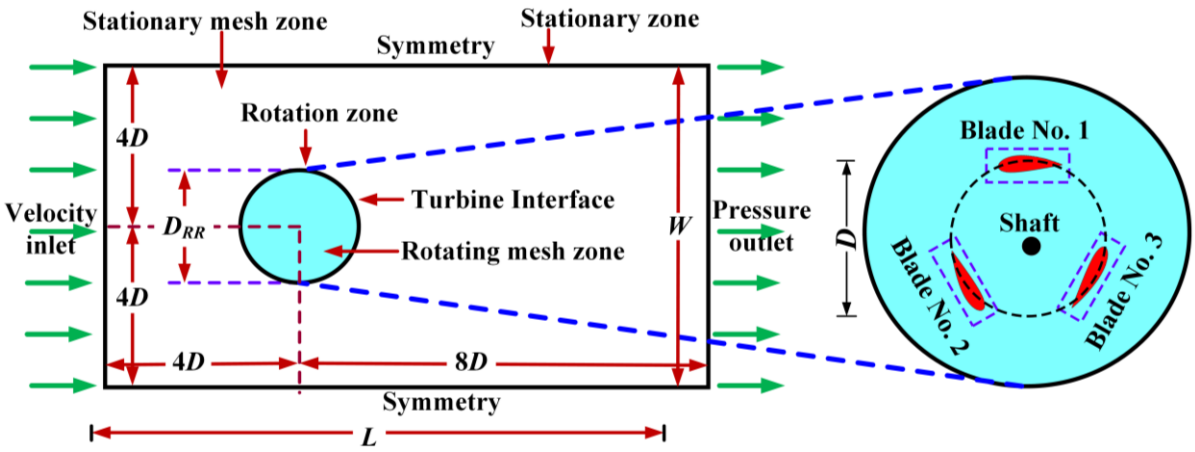

Fig. 3.1. Geometrical features and BCs of the flow domain

A rectangular shape 2D flow domain with suitable dimensions has been used to simulate the fluid flow with a large ratio between the turbine diameter (D) and the rectangular domain length (L), as shown schematically in Fig. 3.1. This ratio is 12D towards the length and 8D towards the width. The figure displays the geometrical characteristics of the main computational flow domain and its BCs. The computational domain consists of two separate zones: the stationary and rotation zones. The circular shape rotation zone of diameter D_{RR} is located at (0, 0) acts as a turbine and is placed in a rectangular domain positioned at 4D from the inlet and 8D from the outlet. Further, it is established 4D distance from the upper and lower parts to reduce the lateral wall distance. Thus, the domain boundaries are kept at a suitably far distance from the turbine to reduce the boundary effects, like blockage conditions and insufficient wake development. Three blades are placed in the rotation zone of the computational domain at an azimuth angle of 120° relative to each other. The flow domain shown in Fig. 3.1 is used for numerical simulations of SB-VAWTs employing a total of sixteen configurations of J-shaped airfoils (Table 5.1, Section 5.2), along with the conventional airfoil with no cutting.

Table 3.1 Main geometrical and flow field features of the Darrieus-type SB-VAWTs

Denomination	Value
Blade profile	NACA 4415
Number of blades, N [-]	3
Wind turbine diameter, D [m]	2.5
Rotating zone diameter, D_{RR}	1.2D
Wind turbine height, H [m]	1
Shaft diameter, D_{Shaft} [m]	0.115
Chord length of blade, c [m]	0.4
Rotor solidity, σ [-]	0.48
Tip speed ratio, λ [-]	0.1-3
Pressure [Pa]	101325
Density (ρ) [kg/m3]	1.225
Inlet velocity (V_∞) [m/s]	10
Domain 1 (L×W) [m×m]	15×9
Domain 2 (L×W) [m×m]	22×13
Domain 3 (L×W) [m×m]	29×17
Domain 4 (L×W) [m×m]	36×21
Domain 5 (L×W) [m×m]	43×25

The main geometrical and flow field features for the tested Darrieus-type SB-VAWTs of the present investigation are illustrated in Table 3.1. Simulations are performed to investigate the flow field characteristics for several values of λ at different rotational speeds for a constant wind speed of 10 m/s. The turbine performance is evaluated by varying the angular velocity of the turbine. The rotational zone is named as a turbine zone and set as an interface to provide mesh linkage between the turbine and the domain. This zone is characterized through a sliding moving mesh (SMM) and rotates at the same angular velocity as the rotor (Mohamed, 2019). The main assumptions taken in the current work are as follows:

- The problem geometry is assumed to be two-dimensional, and the flow is turbulent.
- The flowing fluid (air) is considered to be incompressible.
- The flow is independent of temperature as it is taken to be constant.
- The effects of volumetric forces and gravitational acceleration are ignored.

3.1.2. Mesh Study

One of the most crucial parts of numerical simulations is the meshing strategy of the computational domain because of its effect on the numerical model precision. This strategy of the whole computational domain consists of both structured and hybrid grid topologies, as illustrated in Fig. 3.2. A structured mesh is used for the stationary part of the above domain, as depicted in Fig. 3.2 (a), while the hybrid mesh is used in the rotating area, which is a conjunction of triangular cells and quadrangular cells, as shown in Fig. 3.2 (b). Additionally, the inflation layer grid is used on the leading edge (LE), trailing edge (TE) and airfoil surface to hold the boundary layer (BL) flow above the turbine surface, as displayed in Fig. 3.2 (c-e) (Ghazalla et al., 2019). Generally, this mesh is selected to reduce the computational time and increase accuracy despite increasing the CFD simulations preparation time. Approximately identical mesh cell size has been chosen to obtain faster convergence on both sides of the interface (rotating and stationary domain) (Ghazalla et al., 2019).

Furthermore, great attention is given to the area being close to the blade surfaces, where CFD grids have been built from lower topologies to higher ones and adopting appropriate sizes. The clustering grid points of the blade profiles near the LE and TE capture the physics and improve the CFD code ability. The mesh near the blade airfoil wall is well refined so as to ensure the non-dimensional normal distance from the wall, i.e., $y+$, falls under the permissible range. In order to get a normalized wall distance $y+ < 1$, 40 inflation layers with a growth rate (GR) of

1.1 have been selected on the airfoils wall boundaries. The 40 inflation layers has been chosen to ensures that the simulation captures finer flow details near the airfoil surfaces, such as turbulence structures and boundary layer separation points and transition. Furthermore, it matches experimental data closely and provides greater confidence in the accuracy of the simulation. Also, keeping the wall function to $y+ < 1$ during the flow field simulation with the constant wind velocity of 10 m/s has been fixed in all simulations in the present paper.

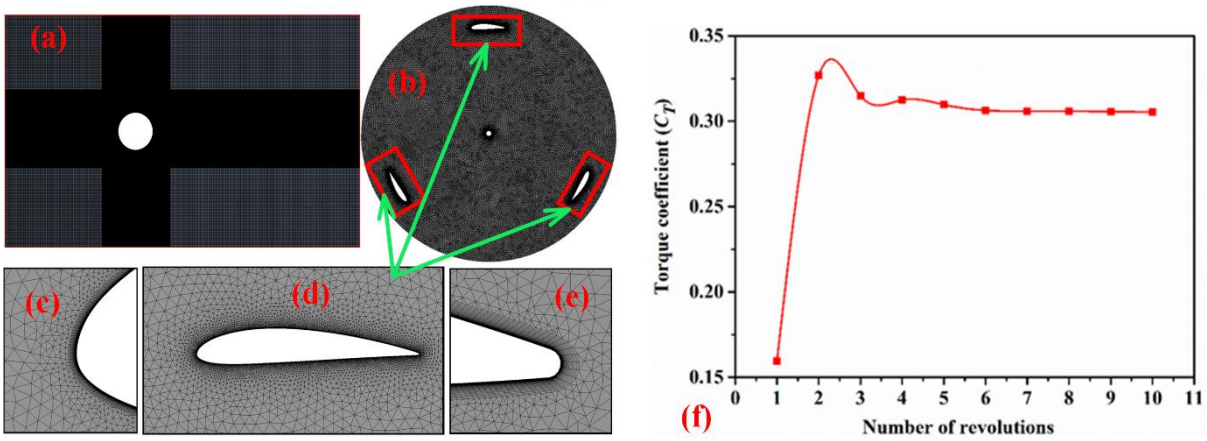

Fig. 3.2. Computational grids and convergence history: (a) Stationary region, (b) Rotating region, (c) LE, (d) Airfoil, (e) TE and (f) C_T variation over more than 10 revolutions

3.1.3. Boundary Condition

The BCs of the computational domain are presented in Fig. 3.1 and they are defined appropriately for the simulations to acquire relevant results. The left and right vertical lines of the rectangular domain are set as velocity inlet and pressure outlet type BCs and reside at a sufficiently great distance from the turbine blades because the result is independent of the domain shape. The free stream velocity of wind in the inlet type BC is taken as 10 m/s in the current simulation and the consequent chord-based Reynolds number (Re_c) resulting on the basis of the above velocity is 0.27×10^6. The pressure value is equivalent to the atmospheric pressure in the pressure outlet BC (Zamani et al., 2016a, 2016b). The pressure gradient is taken as zero in the inlet BC and a zero velocity gradient is used in the outlet type BC (Zamani et al., 2016a, 2016b). The symmetry type BC is utilized for the horizontal upper and lower lateral lines of the above domain. This BC is helpful for the simulation as it permits the solver to consider the wall as a free shear slip wall and, in this manner, avoids the effects of the wall (Jain and Saha, 2020a, 2020b). A moving wall (No-slip) type BC is used for the shaft and the blade surfaces, as

illustrated in Fig. 3.1. Moreover, the contact region between the two domains is fixed as interface type BC to maintain consistency in the flow field (Mohamed, 2019).

3.1.4. Flow Solver Setup Details

In this work, the multigrid commercial CFD software, FLUENT 2020 R1 solver, has been used to solve all numerical simulations through a control-volume method (FVM) with appropriate BCs. The shear stress transport (SST) *k- ω* turbulence model is utilized to simulate the current numerical simulations due to its prophecy ability for transient fluid flow problems (Rathod et al., 2019). It is a two-equation eddy-viscosity hybrid type of model, which is very popular and combines two models to analyze the flow near the wall region. This turbulence model has become directly usable down to the wall through the viscous sub-layer due to the *k–ω* formulation usage in the BL inner parts, which is unsatisfactory by the *k–ε* turbulence model with adverse pressure gradients. This system uses the *k–ε* turbulence model for turbulent BL and the wake areas (Menter, 1994). In some cases, SST k–*ω* formulation also switches to a standard *k–ε* behaviour to avoid the common *k–ω* problem and obtain flow properties in the free stream (Menter, 1994). The y+ value should be < 1, which is an important requirement for fluid flow simulations that use the SST k–ω turbulence model to accurately capture the separation of flow and turbulence calculations.

The URANS equations are solved using the Semi Implicit Method for Pressure-Linked equation (SIMPLE) algorithm (Almohammadi et al., 2015). Further, this algorithm is employed to couple the velocity and pressure terms in the pressure correction equation, which is more stable and takes less time to compute with respect to other schemes. The second-order scheme is utilized to discretize all the parameters, including momentum, turbulent kinetic energy and turbulent dissipation rate (Mohamed, 2012). However, a standard scheme is employed to discretize the pressure. The convection terms are discretized to a first-order upwind scheme for a trial convergence and then switched over to second-order upwind for the final converged solution, which is more accurate than the first-order upwind scheme. The second-order implicit scheme is employed to solve the transient formulation. The least-square cell-based gradient is used for spatial discretization in this simulation. The 2D unsteady Reynolds-Averaged Navier-Stokes equations (URANS) simulate the incompressible flow field around the Darrieus-type SB-VAWTs. The following URANS equation for the present investigations is mentioned in Eqs.

(3.1) and (3.2) for unsteady incompressible flow. The continuity and momentum equations in tensorial form is expressed in Eqs. (3.1) and (3.2).

$$\frac{\partial u_i}{\partial x_i} = 0 \tag{3.1}$$

$$\frac{\partial u_i}{\partial t} + u_j \frac{\partial u_i}{\partial x_j} = -\frac{1}{\rho}\frac{\partial P}{\partial x_i} + \frac{\partial}{\partial x_j}\left[\nu\left(\frac{\partial u_i}{\partial x_j} + \frac{\partial u_j}{\partial x_i}\right) - \overline{u_i' u_j'}\right] \tag{3.2}$$

This simulation work has achieved two convergence checks: the first one is the convergence criterion of the C_T, which should be less than 1%, and the second check is the residuals for every time step that must be lower than 10^{-5}. Each simulation has been run according to a global convergence criterion until C_T values have shown a deviation of less than 1% compared to the previous period relative value, equivalent to a rotation of 120°. For every simulation, ten revolutions are required to obtain the quasi-steady state, as shown schematically in Fig. 3.2 (f). The convergence history in Fig. 3.2 (f) is presented in terms of the number of revolutions (N) which describes the normalized measure of time (t) for transient rotating flow simulations. If the rotational speed of SB-VAWT is constant, the N is directly proportional to t. Therefore, the convergence history plotted with respect to the N, which directly signifies convergence with respect to t. In the present work, ten revolutions are set for each simulation to get the C_T result and save the computation time. Approximately 360 number of steps are required for one revolution, so the number of steps for ten revolutions is 3600, with 20 maximum number of iterations. The averaged C_T values are determined over the last three revolutions, as these show less deviation than those from the previous period. Therefore, these averaged C_T values have been multiplied by λ to compute the final C_P values (C_P = averaged $C_T \times \lambda$). In the present study, the simulations are carried out on seven processors, 2.60 GHz PC with 32-GB RAM, which requires a total CPU time of about four hours for every simulation.

3.1.5. Computational Model Sensitivity Tests

3.1.5.1. Domain Size Independent Study

The checking of the domain size should be done not to influence the simulation results before proceeding with the simulation operation. A sensitivity study is analyzed to obtain the suitable size of the computational domain whose BCs have a minimum effect on the model force coefficient. In this computational domain-independent study, five different domains are tested by varying their length and width (i.e., $L \times W$) and their values are mentioned in Table 3.1. The influence of change in the stationary zone dimensions of the computational domains at λ of 1.6

is presented in Fig. 3.3 (a). A considerable increment is observed in the C_T for "Domain 1" on the upwind and downwind areas of the rotation.

Researchers have reported that the domains introduce a high variation on the rotor coefficient with the smaller dimensions (Mohamed et al., 2011). However, "Domain 3, Domain 4 and Domain 5" show a less than 2% change in the maximum C_T. Additionally, the outcomes of these domains are matched closely to each other than "Domain 1 and Domain 2". However, the large size domain gives approximately constant values of the C_P less than 1.1% with relative deviations (Mohamed et al., 2011). Therefore, the computational domain should not be too small to produce the flow correctly around the wind turbine. The BCs affect the results in a domain of a smaller size in an inappropriate manner. Further, the domain should not be too large; otherwise, it will increase the grid cell number and computation time. Therefore, a suitable computational domain (Fig. 3.1) of dimension between "Domain 3 and Domain 4" is chosen for the present investigation to reproduce the rotation of the rotor adequately.

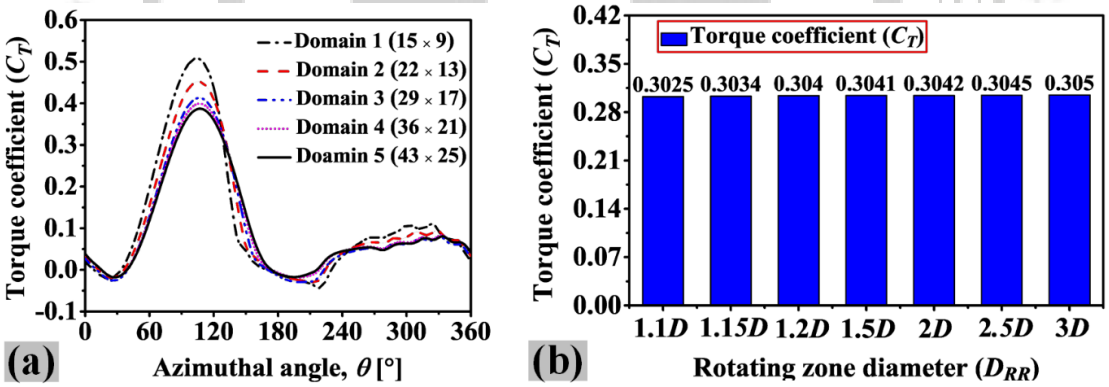

Fig. 3.3. (a) Computational domain test and (b) Domain independent study

Furthermore, the effect of different rotating or circulating zone diameters (D_{RR}) has been investigated in a chosen computational domain (Fig. 3.1) and the results are shown here in Fig. 3.3 (b). Different circulating zone diameters are tested computationally (Rathod et al., 2019; Satrio et al., 2018) at Re =1.7 × 10^6 and λ = 1.6, and their C_T values are compared. As seen in Fig. 3.3 (b), when the D_{RR} is increased from 1.1D to 3D, a negligible change is observed in the C_T values. Therefore, the D_{RR} of 1.2D (Satrio et al., 2018) is selected for the current numerical investigation as it seems appropriate in terms of its minimal dependence on domain size increment and computational cost (Rathod et al., 2019).

3.1.5.2. Mesh and Time Step Independent Study

The mesh independent study is one of the essential methods for the numerical model in order to check the refinement and quality of the mesh size. As a first step to obtain precise numerical work, the mesh independent study is done for the geometrical design with a standard blade profile (Fig. 3.1) to check the number of nodes that influence the solution. This study is carried out in this investigation at λ =1.6, as depicted in Fig. 3.4 (a). A fine quality of structured and hybrid grid topologies is chosen for the entire computational flow domain. A similar number of mesh element sizes is used on both sides of the interface BCs to obtain a faster convergence, especially in the continuity equation. The quality and density of grid topologies are investigated in a 2D computational domain and inspected within several grid size values within a range of approximately between 240,000 and 460,000 cells. The study discloses that over 330,000 cells lead to relative deviations of the C_T of less than 1.15% (Fig. 3.4 (a)). Hence, the grid size of 360,000 cells is retained for further calculations to decrease the computation time. The element size is substantially increased to 200,000 elements in the case of using a J-shaped blade.

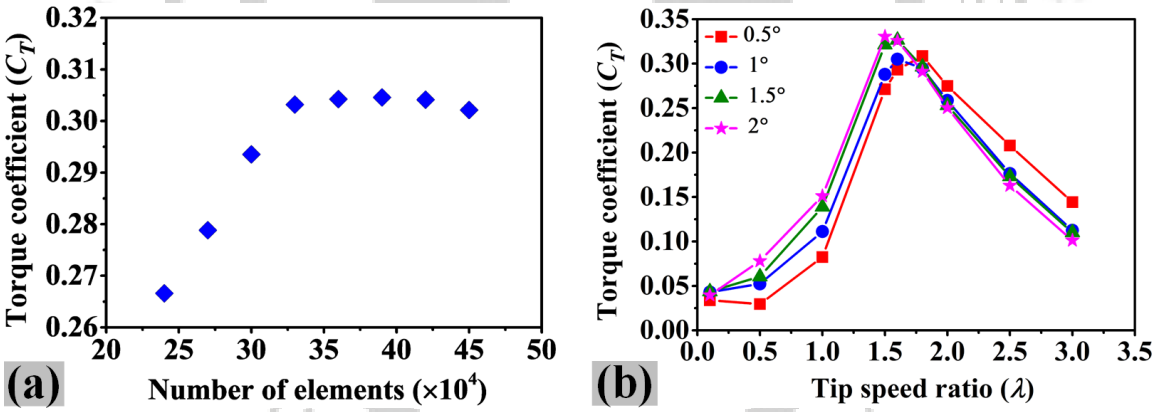

Fig. 3.4. (a) Mesh independent study and (b) Time-step sizes effect on the C_T

The time step independent study is performed on the computational domain displayed in Fig. 3.1 with the conventional blade profile to obtain an adequate solution for the simulation results. The reliable result is obtained by selecting a proper time step size (Δt). Also, a longer time is required by a small time step size for a complete revolution. Therefore, the time independent study is carried out for time step sizes corresponding to four different azimuthal increments of 0.5°, 1°, 1.5° and 2° (at each step) in the present investigation to check its effect on the C_T values. Figure 3.4 (b) displays the effect of time step sizes on the C_T value at different λ. The difference between the C_T values for the azimuthal increments of 1°, 1.5° and 2°are not significantly large at all λ. It is observed from the figure that a small relative error is obtained in the C_T result for

these three azimuthal increments at the higher value of λ. Further, the C_T for the azimuthal increments of 1.5° and 2° is higher than the 1° and 0.5° at lower λ. The azimuthal increment of 0.5° shows higher C_T than others at the λ, ranging from 1.8 to 3 and displays lower C_T at the lower λ. Therefore, the time step size corresponding to an azimuthal increment of 1° is selected for each simulation of this study in order to save computational time and avoid reliability problems.

3.1.5.3. Validation of CFD Model

The numerical simulation of the current work is validated with the experimental published result achieved by Bravo et al. (2007). Therefore, the present computational investigation uses the same turbine configurations as employed by that author (Bravo et al., 2007). The SST k–ω model is chosen for the CFD simulation to properly capture the separation of flow from blade surfaces and the effect of airfoils on Darrieus-type SB-VAWTs (Menter, 1994).

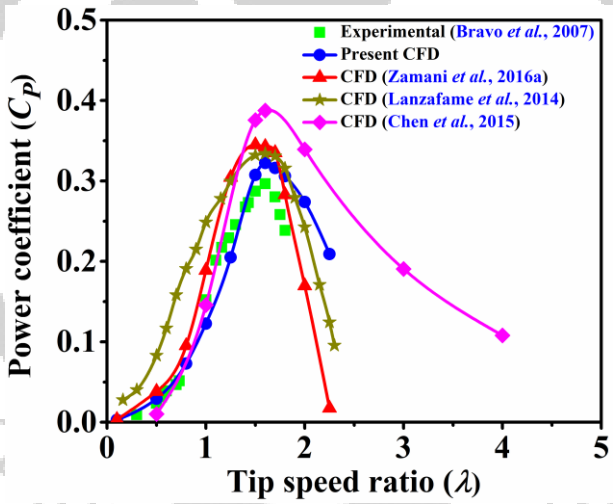

Fig. 3.5. Validation of present CFD results with experimental data (Bravo et al., 2007) and the other CFD results for a Darrieus-type VAWTs (Chen et al., 2015; Lanzafame et al., 2014; Zamani et al., 2016a)

The numerical result presents a satisfactory agreement with the experimental work and follows a similar pattern to the experimental curve (Fig. 3.5). It is found from the above figure that the C_P value of the present CFD simulation for λ lower than 1.5 is almost matched with the experimental results and displays a slightly higher C_P value than that results when λ is higher than 1.5. These differences occurred between the two curves, as it is a 2D model that considers only the aerodynamic forces and does not consider the mechanical losses. Further, the

experimental C_P values are lower than the present numerical values because wall effects, blockage effects and aerodynamic losses due to support struts. The losses due to struts are absent in numerical simulations because their effects are not included, as they generate additional drag force, strong vortices, and complex flow interactions in the wind turbine (Zamani et al., 2016a; Howell et al., 2010). Analogous to this study, the same discrepancies are observed between the numerical and experimental results from previous research (Chen et al., 2015; Mohamed, 2019). The main important point is that it accurately captured the maximum C_P at λ =1.6 and the experimental work also showed maximum C_P at the same λ value. It has been clear from this comparison that the current CFD strategy is an accurate methodology to simulate and predict the performance of the Darrieus-type SB-VAWTs. Therefore, all present CFD investigations use the same rotor characteristics as considered by the researcher (Bravo et al., 2007).

3.2. Computational Methodology (Case: II)

The computational fluid dynamics (CFD) study on Darrieus-type SB-VAWTs is getting much attention in the current scenario due to the rapid increase of computer processing ability. Further, the CFD provides easier and more accurate predictions than other methods (Celik et al., 2022). The 2D CFD models necessitate less computational time, are budget-friendly computationally and maintain the same level of computational accuracy compared to the 3D model simulation. As per earlier studies (Abraham et al., 2012; Elsakka et al., 2019; Rezaeiha et al., 2018a), the results from the 2D simulation models are comparable to the 3D simulation models. Researchers can achieve satisfactory results by utilizing 2D simulation models and obtaining valuable insights about critical factors that control the overall performance and flow behaviour near the WT blades (Rezaeiha et al., 2018a; Sun et al., 2020).

2D CFD simulations have been conducted on a Darrieus-type SB-VAWTs at different λ values to obtain the optimum J-shaped cambered airfoil from the selected conventional cambered airfoils. The geometrical and flow features of the tested numerical model are depicted in Table 3.2. The details of computational domains, boundary conditions (BCs), mesh study and flow solver employed in the present investigation are described below. The “XX” denotes the maximum thickness as a percentage (%) of the c from the LE (leading edge). The “YY” mean the upper cut (uc) and “OR” is the opening ratio. This methodology first investigates the various cambered airfoils and their uppercut J-shaped airfoils on the performance and starting torque of 3-bladed Darrieus-type SB-VAWTs. Furthermore, it is employed to studies the effect of J-

shaped blade numbers with various ORs on the overall performance and self-starting of Darrieus-type SB-VAWTs.

Table 3.2. Geometrical and flow field characteristics of the Darrieus-type SB-VAWTs

Denomination	Value
Blade profile	NACA 44XX, J_{YY}- N_{XX} (OR)
Blades number, N [-]	2, 3 and 4
WT diameter, D [m]	0.25
Rotating zone diameter, D_{RR}	$3D$
WT height, H [m]	1 (2D)
Shaft diameter, D_{Shaft} [m]	0.0122
Airfoil chord length, c [m]	0.1
Rotor solidity, $\sigma = Nc/D$ [-]	0.8, 1.2 and 1.6
Tip speed ratio, λ [-]	0.55-1.2
Pressure [Pa]	101325
Density (ρ) [kg/m3]	1.225
Freestream velocity (V) [m/s]	10

3.2.1. Computational domain description

A 2D rectangular computational domain has been constructed, as shown in Fig. 3.6. The domain is split into the rotation zone (rotor) and the stationary zone (stator). The three blades are positioned at 120º azimuthal angle from each other in the rotation zone. The boundaries of the computational domain are placed far away from the rotor, which minimizes the blockage conditions and unsatisfactory wake formation (Ghazalla et al., 2019). An interface between the rotor and stator is created to employ the sliding moving mesh (SMM). The velocity inlet BC is used with a freestream velocity of 10 m/s at the left vertical line of a rectangular domain to maintain the Re_c of 0.68×10^5. The right vertical line of the rectangular domain is set as a pressure outlet BC with a pressure value equal to atmospheric pressure. The symmetry BCs are used for the top and bottom horizontal lines of the rectangular domain, where the faces are considered as free shear slip walls to ignore the wall effect (Naik and Sahoo, 2023). The wall of blades and shafts is employed as a no-slip (moving wall) BC. An interface BC is used for the contact region

between the two rectangular domains, which maintains the flow field consistency. The same domain size is used for conventional cambered and J-shaped blades.

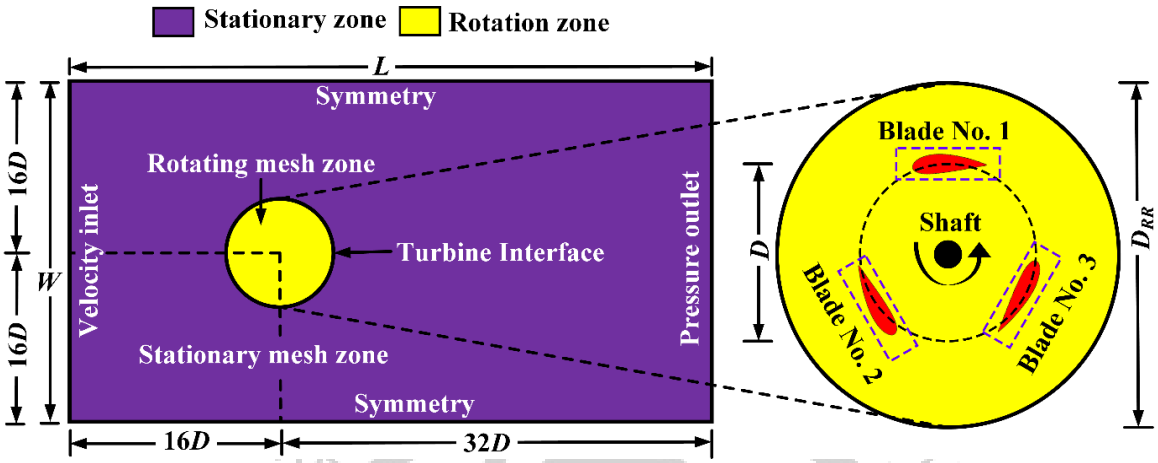

Fig. 3.6. Schematic of computational domain and BCs

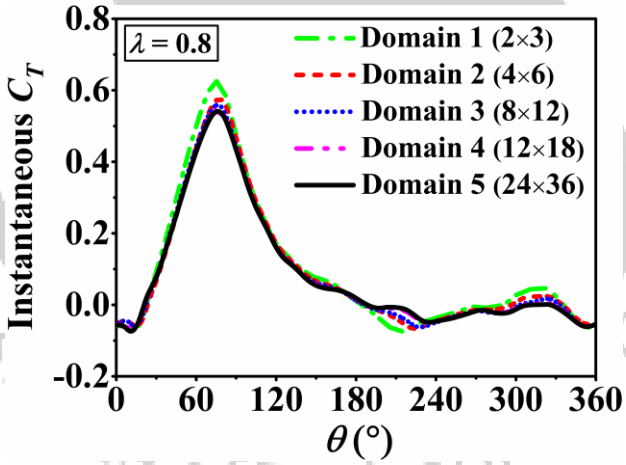

Fig. 3.7. Schematic of domain independent test

A suitable domain structure is chosen for the simulation of Darrieus-type SB-VAWTs by performing domain independent study of five different domains, as illustrated in Fig. 3.7. This test is conducted by varying the width and length of the domain ($W \times L$) at λ = 0.8 and Re = 1.71×10^5. It is observed from Fig. 3.7 that smaller domain sizes (domain 1 and domain 2) displayed a larger instantaneous C_T variation compared to the larger domain sizes (domain 3, domain 4 and domain 5). Thus, a moderate size domain (domain 3) is used for CFD simulation with a $W = 32D$ and $L = 48D$, as it provides lower relative deviations in instantaneous C_T values

and requires less computation time than the larger domain structures. Moreover, the D_{RR} of 3D is selected for this work due to the negligible effect found in its average C_T values (Naik and Sahoo, 2023) by varying the D_{RR} sizes.

3.2.2. Mesh strategy and grid independent test

The present simulation employed structure and hybrid grid topologies to mesh the whole CFD domain. The CFD domain of SB-VAWTs consisting of conventional and J-shaped airfoils used an identical type of grid, as demonstrated in Fig. 3.8. A structure quadrangular type grid is used to mesh the stationary zone, as depicted in Fig. 3.8 (a). The circular rotation zone uses a hybrid grid, which is a combination of triangular and quadrangular cells, as shown in Fig. 3.8 (b) and (d). The surfaces of airfoils (N_{18} and J_{uc}-N_{18} (70%)) utilized the inflation layer (structure quadrangular grid) to measure the boundary layer (BL) flow along the normal direction (Fig. 3.8 (c, and e-i)). To acquire the normalized wall distance (y+) < 1, 40 number of BLs are employed around the airfoil walls with a growth rate of 1.1. The BL numbers have been selected based on earlier research (Balduzzi et al., 2016a; Jain and Saha, 2020b). It is chosen to measure the more accurate data related to flow around the airfoil surface, which includes the BL separation point and transition and turbulence structures. Furthermore, it strengthens the confidence level in the simulation accuracy by presenting a close match with the experimental results (Jain and Saha, 2020b). Both faces of the interface use the same grid size for faster convergence. The above mesh details are mainly chosen to reduce the computation time and increase the simulation accuracy.

A grid independent test is crucial to obtain the suitable mesh size and mesh accuracy for the numerical simulation models. It also checked the quality and refinement of the mesh size. The present work conducted this test on a 3-bladed Darrieus-type SB-VAWTs with conventional N_{18} and J_{uc}-N_{18} (70%) blade profiles at λ = 0.8 and Re = 1.71×10^5, as illustrated in Fig. 3.8 (j) and (k). In the grid independent test of SB-VAWT with conventional N_{18} blade profile, five different mesh sizes (from M1 to M5) are examined by varying mesh sizes from 500,000 to 750,000. It is observed from Fig. 3.8 (j) that the trend of the instantaneous C_T (IC_T) curve of all mesh configurations follows an almost similar trend. The M1 and M2 mesh configurations display a larger reduction of IC_T values than other mesh configurations. However, M3, M4 and M5 mesh configurations show IC_T values that remain pretty consistent with each other.

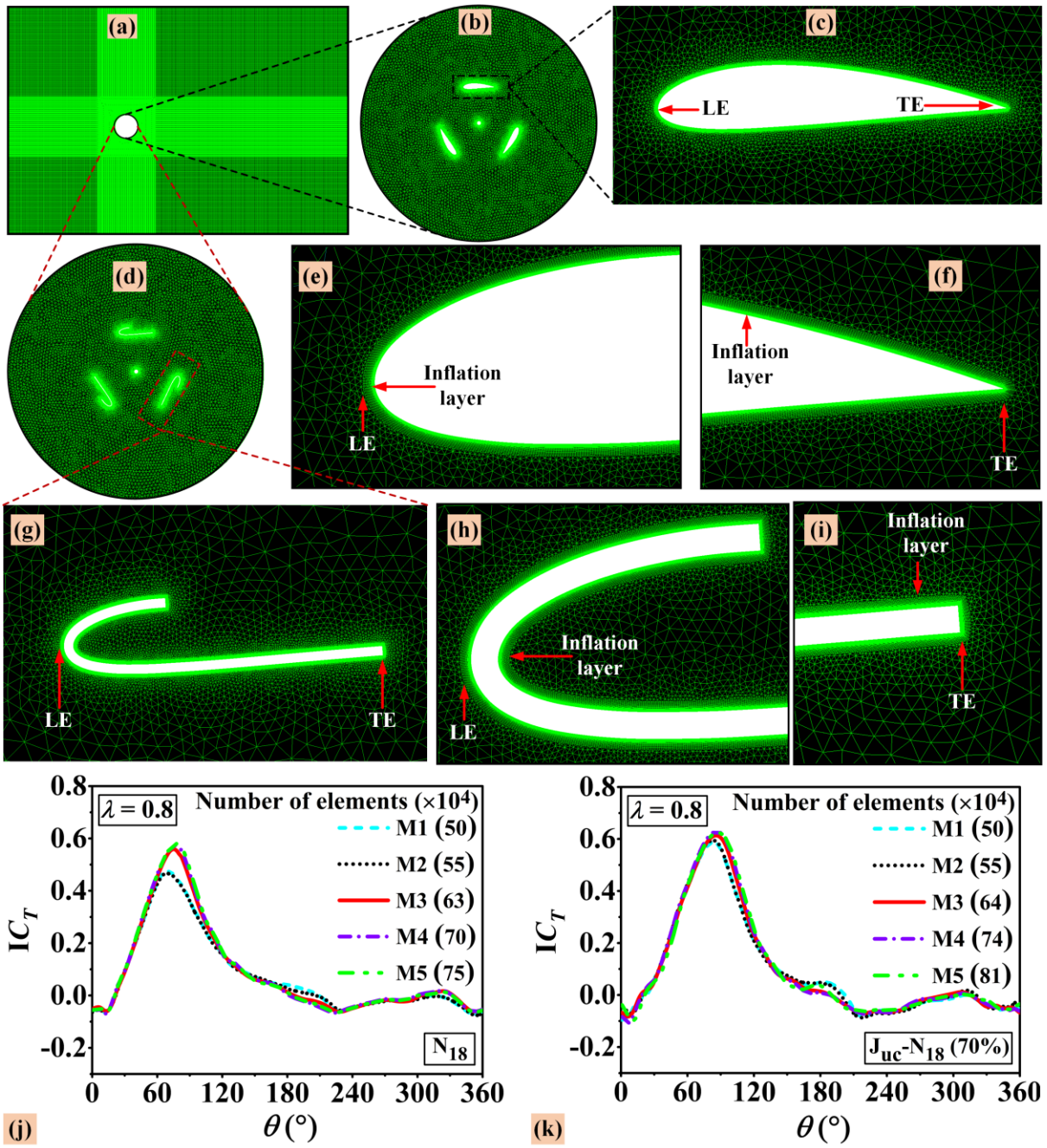

Fig. 3.8. Mesh details: (a) stationary zone, (b) rotation zone (N_{18}), (c) N_{18} airfoil, (d) rotation zone (J_{uc}-N_{18} (70%), (e) leading edge (LE) of N_{18}, (f) trailing edge (TE) of N_{18}, (g) J_{uc}-N_{18} (70%) airfoil, (h) LE of J_{uc}-N_{18} (70%, (i) TE of J_{uc}-N_{18} (70%), (j) grid independent test (N_{18}) and (k) grid independent test (J_{uc}-N_{18} (70%))

Figure 3.8 (k) displayed the grid independent test of SB-VAWT with J_{uc}-N_{18} (70%) blade profile. This study also conducted for five different mesh sizes (from M1 to M5) varying from 500,000 to 815,000. Same elements sizes are employed for both conventional N_{18} and J_{uc}-N_{18} (70%) blade profiles. But, the number of elements is increased for J_{uc}-N_{18} (70%) blade profile

due to its design structure. The M1 and M2 mesh configurations for J_{uc}-N_{18} (70%) blade profile presented a reduction of IC_T values compared to its M3, M4 and M5 mesh configurations. Further this reduction is not as much as in case of conventional N_{18} blade profile. Moreover, quite consistent IC_T values are noticed for the M3, M4 and M5 mesh configurations, as displayed in Fig. 3.8 (k). The M3 mesh configuration is selected for numerical simulation of 2, 3 and 4-bladed Darrieus-type SB-VAWTs with conventional N_{18} and J-shaped blade profiles as it needs a lower computation time due to the smaller mesh size than other configurations (M4 and M5). Further, when this configuration is utilized for other J-shaped bladed profiles, such as J_{uc}-N_{18} (30%) and J_{uc}-N_{18} (50%), the mesh size increases compared to the conventional N_{18} blade profile because of the design of J-shaped blades. The maximum cell skewness and average orthogonal quality of 3-bladed Darrieus-type SB-VAWT with conventional N_{18} and J_{uc}-N_{18} (70%) blade profiles are 0.66 and 0.97, respectively.

3.2.3. Flow Solver Setup

The current investigations use the commercial CFD software package ANSYS Fluent 2020 R1 for the incompressible URANS simulations. The URANS equations are solved by the SIMPLE algorithm because this algorithm is more stable and computes the pressure velocity coupling within less time. Temporal and spatial discretizations utilize the second-order scheme to discretize all the equations. All numerical simulation employs a TI of 0.3% to account for incoming flow turbulence (Siram et al., 2022a, 2022c). This value ensures that the computational simulations remain consistent with the physical experimental environment for a valid comparison of aerodynamic performance. The SST k-ω turbulence model is selected as the turbulence model due to their significantly better capability for transient fluid flow problems (Balduzzi et al., 2016b). This model combines the turbulent kinetic energy (k) and specific turbulent dissipation rate (ω) to analyse the flow crossing near the wall region and capture the flow separation near the blade profiles (Menter, 1994). Further, the SST k-ω turbulence model is more stable, reliable and provides a closer alignment with experimental data (Balduzzi et al., 2016b; Menter, 1994). Thus, this model is well suited for this simulation as it precisely describes the boundary layer and captures stall during the profile rotation (Balduzzi et al., 2016b). The y+ (non-dimensional wall distance value) value is kept below 1. It is a necessary condition for 2D numerical computation, which uses the SST k-ω turbulence model (Naik and Sahoo, 2024).

Two convergence checks are conducted in this study to ensure the accuracy of the simulation work. The first convergence check is the residuals of every simulation, which are kept below 10^{-5} to achieve the convergence criterion. The second convergence check is based on the difference between the average C_T (AC_T) values of two consecutive revolutions. Thus, the IC_T values versus θ for a 3-bladed Darrieus-type SB-VAWT with conventional blade profiles are plotted in Fig. 3.9 at λ = 0.8 and Re = 1.71×10^5. Fig. 3.9 shows that convergence is achieved after the fifth revolution and an AC_T difference between the two revolutions is obtained < 1% from the fifth to the tenth. Therefore, each simulation is run for ten rotational cycles before determining their AC_T values to provide reliability. The AC_T values are calculated by averaging the IC_T values of the last three rotational cycles. In every simulation, the θ value is used 1° for calculating the time step size (Δt) and is selected according to research done by Naik and Sahoo (2023). The computation time is increased when too small θ values are chosen and does not produce enough precision when too large θ values are used in the simulations (Naik and Sahoo, 2023). In accordance with this, the present work determines the Δt ($\Delta t = \pi\theta/180\Omega$) for each λ value by using θ = 1° and thus not only saves the time for computation but also minimizes the reliability issues. All numerical computations are performed on a PC with 12 cores processor and 64 GB RAM.

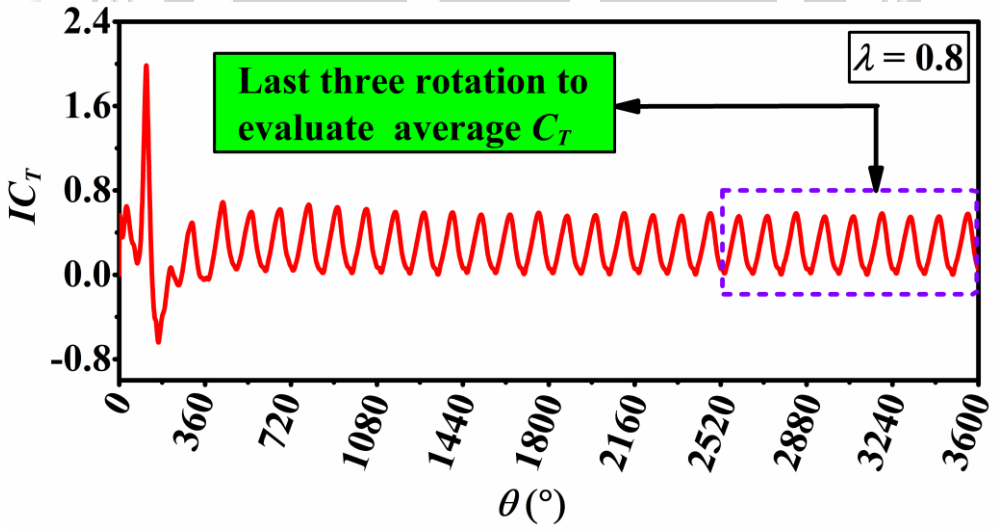

Fig. 3.9. Instantaneous C_T variation versus azimuthal angle (θ) over more than 10

3.3. Summary

The computational methodology is described in this chapter. A series of 2D numerical simulations are conducted to find out the optimum blade profile, opening ratios of J-shaped blade profiles and blade numbers for Darrieus-type SB-VAWTs. This chapter discusses the computational domain, mesh study, boundary conditions, and flow solver setup. The computational model sensitivity tests, such as the domain size independent test, mesh independent test and time independent test are described in order to develop a proper domain size, mesh size and time step for numerical simulations. The numerical simulation of the current work is validated with the experimental results published by the researchers. The numerical result presents a satisfactory agreement with the experimental work and follows a similar pattern to the experimental curve. In this chapter, two different cases are numerically analyzed with two different computational domain sizes. In the first case, numerical simulations are carried out on Darrieus-type SB-VAWTs with conventional cambered and J-shaped airfoils. The selected chord length of the airfoil (c) and the diameter of the rotor (D) are 0.4m and 2.5m, respectively. A domain size with a length (L) and width (W) of $12D \times 8D$ is chosen for simulation in this case. While the second case chose a moderate sized domain for CFD simulation with a $W = 32D$ and $L = 48D$. The second domain size has been selected based on the experimental investigations. The c and D of the Darrieus-type rotor are 0.1m and 0.25m, respectively. The effect of blade profiles, opening ratios of J-shaped airfoils and blade numbers are examined in the second case. The results of these numerical simulations build a platform for conducting further investigations on Darrieus-type SB-VAWTs using wind tunnel experiments.

CHAPTER 4

Experimental Setup and Methodology

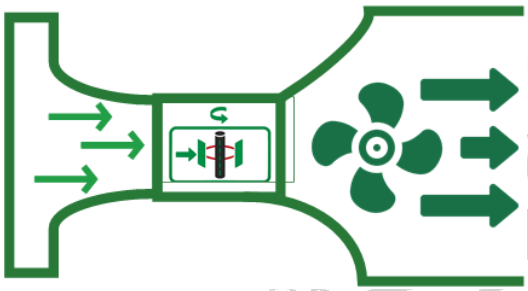

Chapter Layout

Overview

The experimental investigations are carried out based on the outcome of the computational studies. The experimental tests have been conducted in an open-circuit subsonic wind tunnel. The wind tunnel facility has been established at the Mechanical Engineering Department of IITG. This chapter discussed the key features of this facility, the experimental setup, the blades design of SB-VAWTs, the fabrication of blades, and the dynamic and static torque measurement setups. Moreover, the uncertainty analysis and blockage corrections of the wind tunnel setup are calculated in this chapter to determine the reliability of the current experimental setup. The experimental investigations are conducted for two different cases. In the first case, only 3-bladed Darrieus-type SB-VAWTs are tested in the wind tunnel with conventional and uppercut J-shaped blade profiles with different opening ratios. In the second case, the effect of blade numbers (such as 2-bladed, 3-bladed, and 4-bladed) for Darrieus-type SB-VAWTs is experimented with in the wind tunnel. This case includes both conventional and uppercut J-shaped blade profiles with various opening ratios.

4.1. Wind Tunnel Setup

The experiments are conducted on Darrieus-type SB-VAWTs with conventional and J-shaped straight blades in an open circuit-type subsonic wind tunnel, as displayed in Fig. 4.1. A three-phase induction motor of 30 hp supplies power to this wind tunnel facility. This tunnel has a square shape test section of 2000 mm × 600 mm × 600 mm × and its range of wind velocity is 0–50 m/s. The detailed specifications of the subsonic wind tunnel are illustrated in Table 4.1. The Darrieus-type SB-VAWTs are tested by mounting their shaft on the top and bottom of this tunnel with the help of a bearing, as illustrated in Fig. 4.1. The primary function of the bearing is to absorb the fluctuating axial loads and radial loads of the rotating Darrieus-type SB-VAWTs. The actual experimental setup with arrangement of instruments, such as Darrieus rotor mounting, data acquisition system (DAQ), hot wire system, personal computer (PC), electronic manometer, pitot tube, mechanical rope brake dynamometer, spring balance, braking pulley and proximity RPM (rotation per minute) sensor are displayed in Fig. 4.2 (a-c).

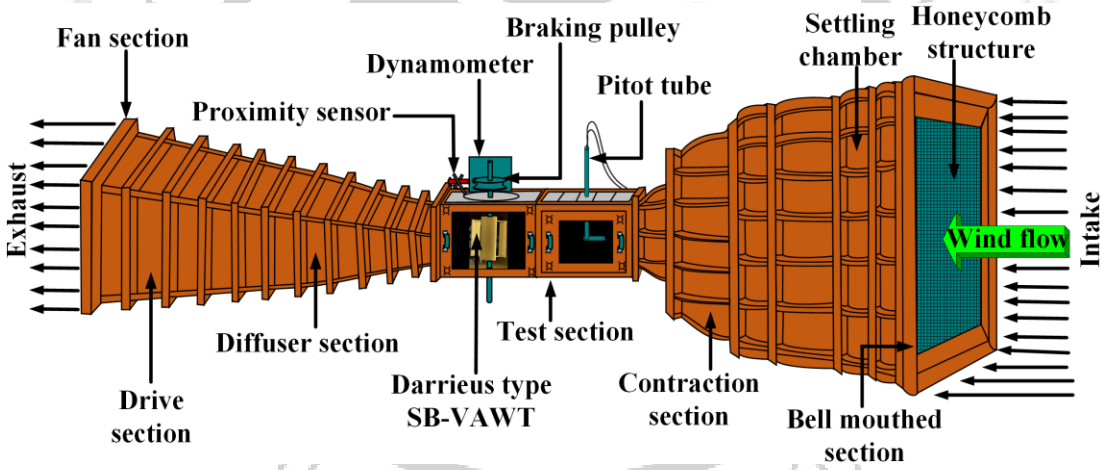

Fig. 4.1. Schematic of subsonic open circuit-type wind tunnel facility

The tunnel wind velocity (V) is correlated with the rotational speed of the wind tunnel fan. A single-channel electric manometer measures this velocity, which senses the differential tunnel pressure by a pitot-static tube mounted on the rotor upstream in the test section. The rotor RPM is measured by a proximity sensor, which is a non-contact type. This speed is calibrated by mounting a small magnet on the rotational periphery of the braking pulley and placing the proximity sensor close to the magnet's rotational path in such a manner that it can show the changes of magnetic flux in the RPM sensor display. The relative position of the RPM sensor with respect to the braking pulley for experimentation is demonstrated in Fig. 4.2.

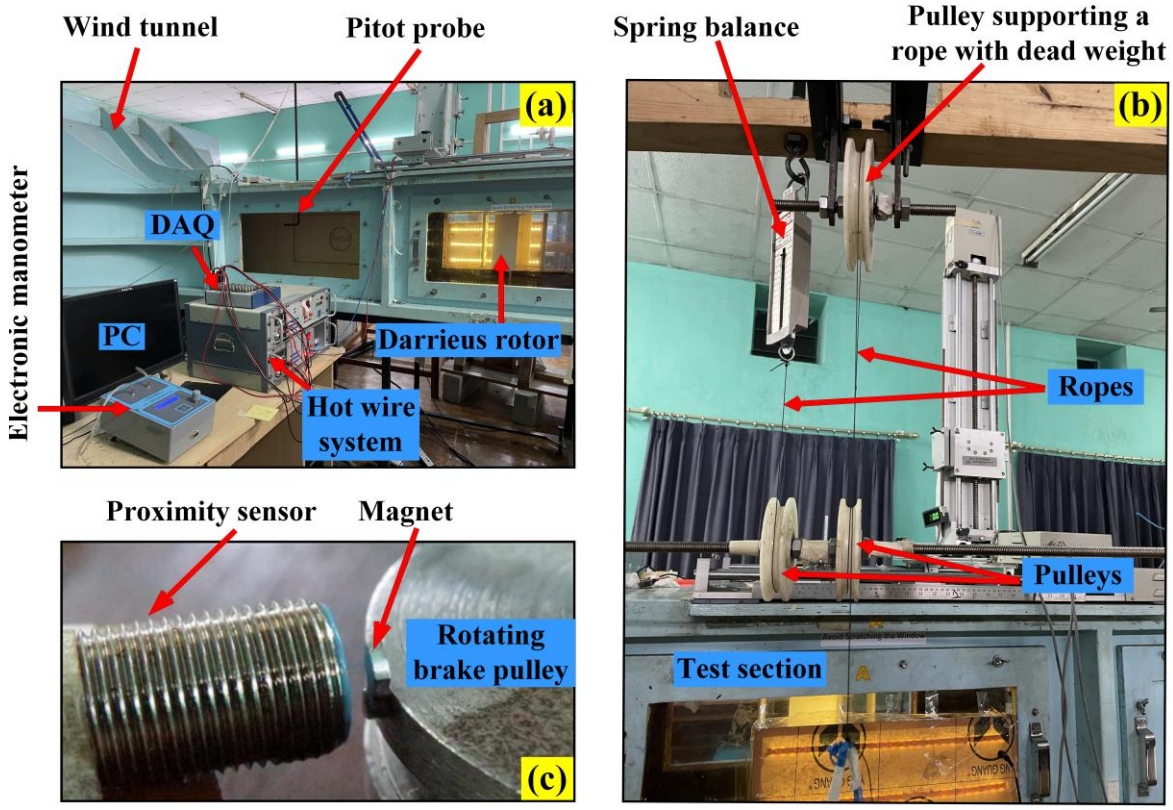

Fig. 4.2. Schematic of actual experimental setup: (a) Arrangement of instruments, (b) Rope-brake dynamometer with pulley configuration and (c) Proximity sensor

Table 4.1 Specifications of wind tunnel

Parameters	Details
Tunnel type	Open loop suction type
Test section size	2000 mm × 600 mm× 600 mm
Wind speed range	0.1 – 50 m/s
Fan RPM range	0 – 1450 RPM
Contraction ratio	9:1
Settling chamber size	1.8 m × 1.8 m
Overall tunnel length	9.4 m
Motor power	30 HP
Turbulent intensity	< 0.35%

In the current study, the experimental tests are carried out for two different cases. In the first case, 3-bladed Darrieus-type rotors are experimented with conventional and uppercut J-shaped straight blades in the wind tunnel, as demonstrated in Fig. 4.3 (a-d). Four different models of 3-bladed Darrieus rotors were tested for comparison in terms of performance in this case. In the second case, Darrieus-type rotors with varying N_b (e.g. 2-bladed, 3-bladed and 4-bladed) are examined in the wind tunnel. The varying N_b fitted inside the wind tunnel test section are presented in Fig. 4.3 (e-g). Furthermore, a thorough comparison between the conventional and uppercut J-shaped Darrieus-type rotors is carried out for each blade number in the second case.

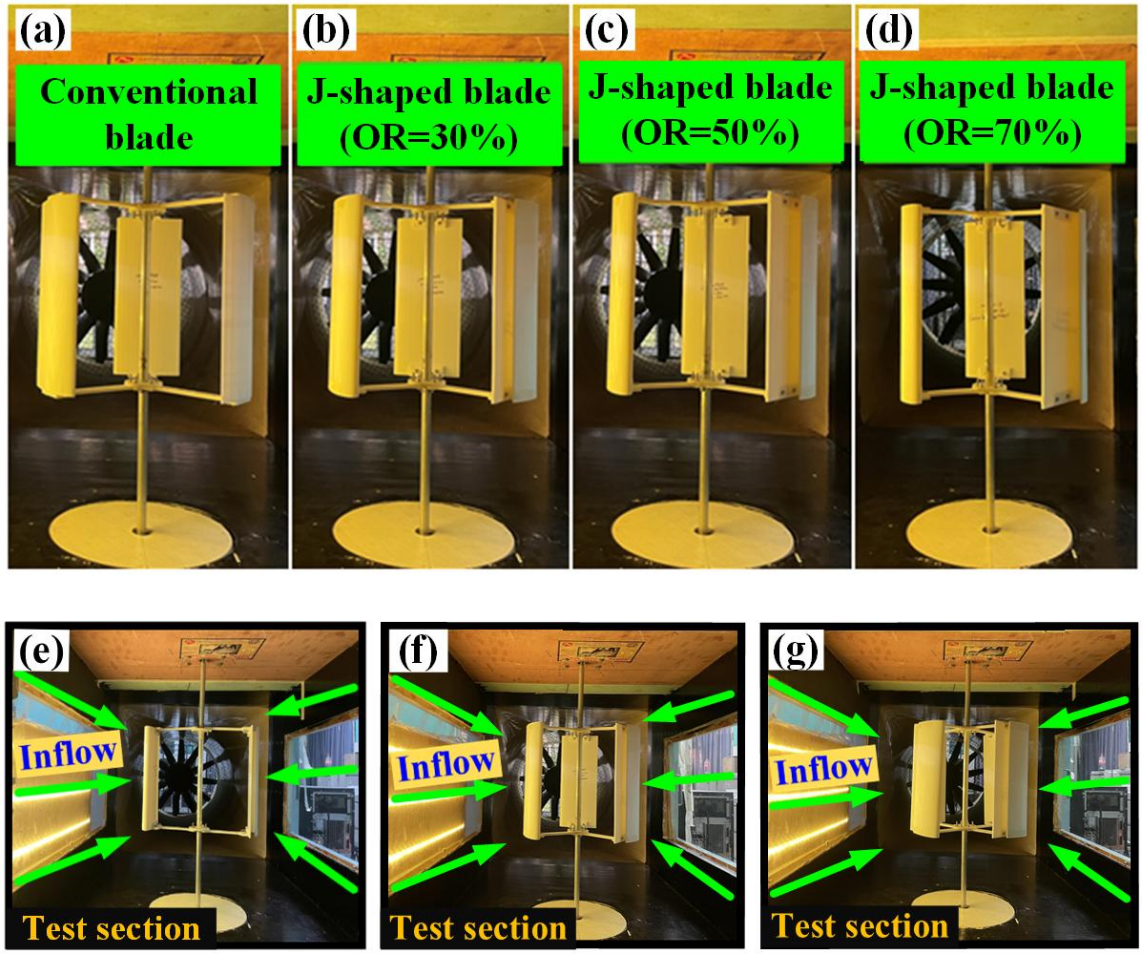

Fig. 4.3. Darrieus-type rotor models mounted inside the test section of the wind tunnel: (a) 3-bladed conventional rotor, (b) 3-bladed J-shaped rotor with OR=30%, (c) 3-bladed J-shaped rotor with OR=50%, (d) 3-bladed J-shaped rotor with OR=70%, (e) 2-bladed J-shaped rotor, (f) 3-bladed J-shaped rotor and (g) 4-bladed J-shaped rotor

4.2. Blade Design and Fabrication Procedure

The different types of blades for the Darrieus-type SB-VAWTs are fabricated on a 3D printing machine of fused deposition modelling (FDM) type. This printer has a large printing area of dimensions 305 mm × 305 mm × 605 mm and has two extruders (left and right), which work for printing technology of fuse filament to fabricate the parts of the turbine prototype models. The polylactic acid (PLA) material is used to print the blades. This material is eco-friendly and biodegradable. Fig. 4.4 (a) shows the various types of 3D-printed blades. During printing, the nozzle and bed maintain a temperature of 210 ─ 235ºC and 60 ─ 70ºC, respectively. Additionally, 60 ─ 80% of the infill density is kept at the printing time, which is obtained to be better enough to assure the structural consistency of the SB-VAWT. The blade fabrication procedure followed step by step is presented in Fig. 4.4 (b). The third step illustrated in Fig. 4.4 (b) is the ideamaker tool, a slicing program which translates the computer-aided 3D model into a format suitable for 3D printing. Slicing is a conversion process that generates a set of instructions that a printer can follow to build the model layer by layer. The dimensions of *c* and *H* for the 3D-printed blades are set as 100 mm and 250 mm, respectively. These blades are attached to a central circular aluminium shaft of diameter 12.20 mm with the help of six 3D-printed structs on the top and bottom surfaces of Darrieus-type rotors, as shown in Fig. 4.3.

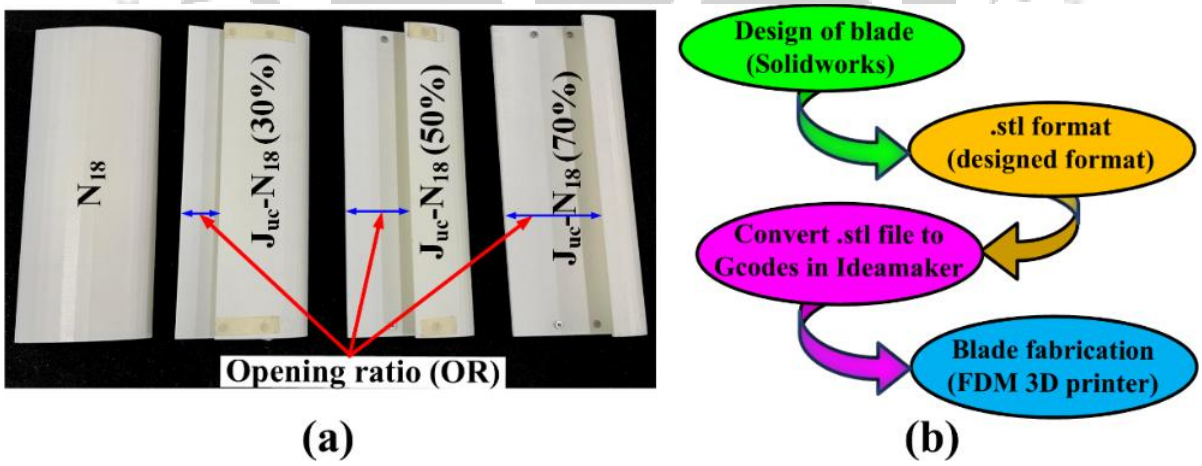

Fig. 4.4. (a) Various types of 3D printed blades and (b) Blade fabrication procedure

4.3. Torque Measurement Setup and Measurement Procedure

The arrangements of dynamic and static torque measurements for the Darrieus-type SB-VAWTs are illustrated in Fig. 4.5 (a) and (b). The dynamic torque is calculated when the SB-VAWT is rotating. These tests are conducted on SB-VAWT models under several applied mechanical

loading conditions by utilizing the spring balance and a braking pulley fitted to the central shaft. A weighing pan is attached to the central shaft of SB-VAWT through a rope and is also connected to the spring balance, braking pulley and tight and slack side pulley set, as shown in Fig. 4.5 (a). At first, the SB-VAWT is allowed to rotate from the zero-load condition until it reaches its maximum rotational speed. Then, the weighing pan is gradually loaded with a gradual weight/load (W_L), which acts as a braking load and shows corresponding reading values in the rpm display and spring balance (Kamoji et al., 2008; Naik and Sahoo, 2024). From this procedure, RPM (N) and spring balance (S) reading values are noted. This process is repeated multiple times under many loading conditions to collect a series of reading values (W_L, N and S).

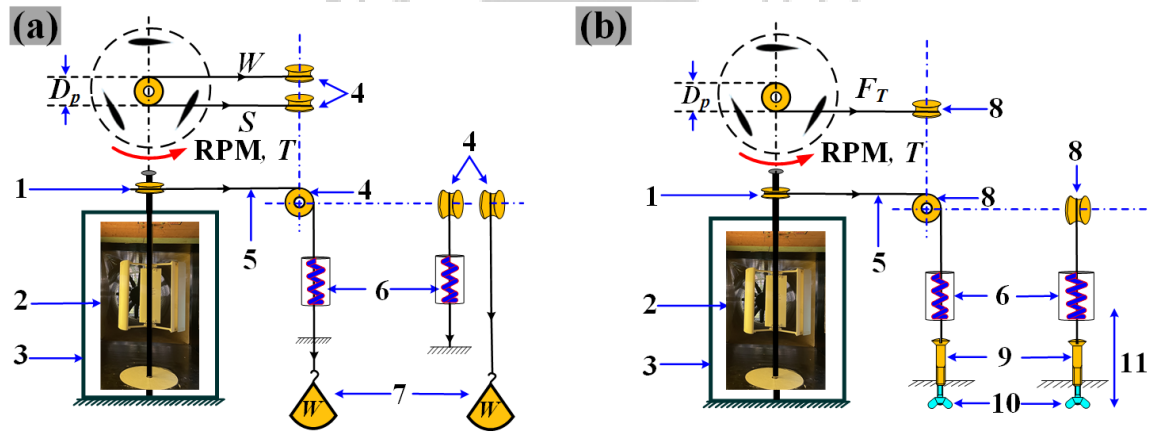

1. Braking pulley, 2. Darrieus-type SB-VAWT, 3. Wind tunnel, 4. Tight and slack side pulley set, 5. Rope, 6. Spring balance, 7. Weighing pan, 8. Pully, 9. Screw, 10. Wing nut, and 11. Up-down movement of screw by wing nut

Fig. 4.5. Setup for torque measurement: (a) Dynamic torque and (b) Static torque

The experimental dynamic T (Eq. (1.10)) is determined by using these values (W_L and S) and a braking pulley diameter (D_P = 67 mm). This dynamic T is used to determine the other dimensionless parameters, such as C_T and C_P, as expressed in Eqs. (1.6) and (1.7). The performance of the Darrieus-type rotor designs is compared by considering the C_P vs. λ characteristics. The mechanical $P_{turbine}$ is calculated utilizing the mechanical dynamic T and Ω by Eq. (1.8). The static torque is measured during the stationary mode of SB-VAWT. The same procedure is followed in this as used in the dynamic torque measurement technique, except for the weighing pan. In the static torque measurement, one side of the rope is connected to a screw and a wing nut and the other side is wound around the central shaft of SB-VAWT through a braking pulley, as depicted in Fig. 4.5 (b). The SB-VAWT is placed at a particular θ through the use of the translating movement of the screw and wing nut (Tabassum and Probert, 1987). At a

particular SB-VAWT rotational angle, the C_{ST} (Eq. (1.11)) is evaluated by means of F_T (Eq. (1.12)) from the rope, which is coupled to the spring balance. This static torque measurement methodology is repeated for each interval of θ = 10º, starting from θ = 0º to 180º.

The TI is one of the essential indicators in wind tunnel testing, and it is used to calculate the fluctuation of wind velocity intensity (Belabes and Paraschivoiu, 2021). It is the ratio between the vector norm of the fluctuating part and the average of the mean wind speed value. The TI of the wind tunnel is measured by the hot-wire anemometry (HWA). The present work selected the TI value of 0.3% for the experimental test. This value has been adopted from prior experimental tests (Siram et al., 2022a, 2022c) that used the same wind tunnel configuration as the present one. It is acceptable for all aerodynamic model characterization and flow physics phenomena (Bruun and H, 1996). This TI level ensures that the minimum errors are obtained in all fundamental investigations tested in a wind tunnel and guarantees that the calculated values are meaningful (Bruun and H, 1996). Furthermore, the above mentioned TI value is good enough for validation and comparison (Bruun and H, 1996; Siram et al., 2022a).

4.4. Uncertainty Analysis

Uncertainty in measurements expresses the range of inaccuracy which may exist in a calculated and measured quantity. This uncertainty arises due to the restrictions of the instruments, environmental variations and errors introduced in the measurement techniques. The uncertainty (Moffat, 1988) related to the experimental C_P and λ is determined by the error propagation method utilizing the Eqs. (4.1) and (4.2). This analysis is examined by taking the accuracy values of different instruments used for the measurements. Table 4.2 displays the considering accuracy values of various instruments. An overall uncertainty value of ±0.858% and ±0.58% are found using Eqs. (4.1) and (4.2) for C_P and λ, respectively. The uncertainty associated with experimental T is estimated by Eq. (4.3).

$$\frac{\partial C_P}{C_P} = \sqrt{\left(\frac{\partial T}{T}\right)^2 + \left(\frac{\partial \lambda}{\lambda}\right)^2 + \left(2\frac{\partial V}{V}\right)^2} \tag{4.1}$$

$$\frac{\partial \lambda}{\lambda} = \sqrt{\left(\frac{\partial V}{V}\right)^2 + \left(\frac{\partial N}{N}\right)^2} \tag{4.2}$$

$$\frac{\partial T}{T} = \frac{\partial S}{S} \tag{4.3}$$

The experiments are repeated several times to calculate the standard deviation of the experimental samples and estimate their standard errors. Fig.4.6 presented the mean C_P variation along with their standard error bars for 3-bladed SB-VAWT configurations with N_{18} and J_{uc}-N_{18} (70%) blade profiles. The length of the maximum error bar for SB-VAWT with J_{uc}-N_{18} (70%) blade profile is ±0.283%, while it is ±0.318% for the case of the N_{18} blade profile. The error bars are very small and do not overlap with each other for both configurations because of sufficient differences between their C_P values. Therefore, the determination of the mean C_P and comparison of power characteristics for experimental samples can be considered by these SB-VAWT configurations. This analysis is adopted in the present study to represent the experimental performance data for all SB-VAWTs.

Table 4.2 Accuracy values of measuring instruments

Measuring instruments	Accuracy values
Electronic manometer (V)	±0.3%
Proximity rpm sensor (N)	±0.5%
Spring balance (S)	±0.2%

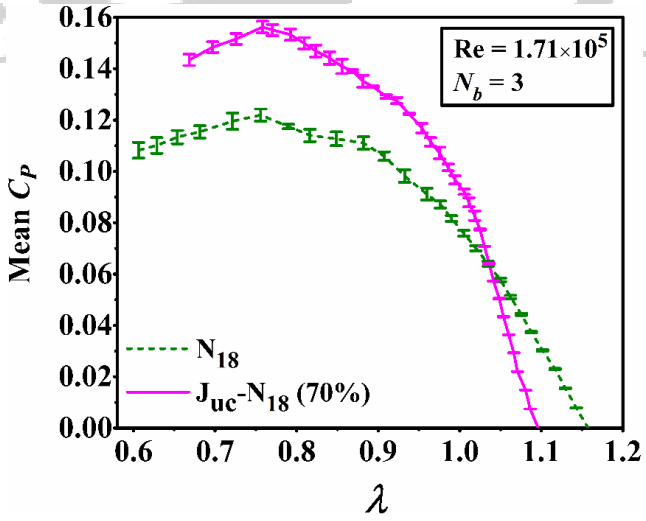

Fig. 4.6. Schematic of mean C_P variation with error bars

4.5. Blockage Correction

In the wind tunnel test, the blockage effect is one of the essential issues caused by the model being experimentally tested. Various discrepancies can originate due to the high blockage on the calculated data, which can decrease the performance of other corresponding parameters (Van Treuren, 2015). The experimental model that caused the blockage is often defined as the blockage ratio (BR). It is defined as the ratio between the projected or swept area (A) of the tested model and the test section area (A_{wt}) of the wind tunnel (Van Treuren, 2015). The BR effect on the average C_P (AC_P) of the present work is examined by adopting two different blockage correction methods (BCMs), such as Chen and Liou (2011) and Pope and Harper (1966). The BCM implemented by Chen and Liou (2011) is mainly used for small-scale WTs and in this method, the measured data is presented based on the blockage factor (BF). The BF signifies the ratio of V with and without the model inside the wind tunnel (Eq. (4.4)). Eqs. (4.5) and (4.6) are used to determine the corrected C_P (C_{Pc}) and the corrected λ (λ_c), where subscript 'm' means the model.

$$\mathrm{BF} = \frac{\text{inlet velocity with the model}}{\text{inlet velocity without the model}} = \frac{V_m}{V} \tag{4.4}$$

$$\lambda_c = \lambda_m \times \mathrm{BF} = \frac{R\Omega}{V_m} \times \mathrm{BF} = \frac{R\Omega}{V} \tag{4.5}$$

$$C_{Pc} = C_{Pm} \times \mathrm{BF}^3 = \frac{T\Omega}{0.5\rho A V_m^{\,3}} \times \mathrm{BF}^3 = \frac{T\Omega}{0.5\rho A V^3} \tag{4.6}$$

The other most commonly used BCM in wind tunnel testing is the Pope and Harper (1966) method. In this method, they described the corrected velocity (V_c) in the way of the correction factor (ε_t), which is expressed in Eq. (4.7). The C_{Pc} and λ_c are calculated by employing Eq. (4.8).

$$V_c = V\left[1 + 0.25(\mathrm{BR})\right] = V\left(1 + \varepsilon_t\right); \text{ and } \mathrm{BR} = \left(\frac{A}{A_{wt}}\right) \tag{4.7}$$

$$C_{Pc} = \frac{T\Omega}{0.5\rho A V_c^3} = \frac{C_P}{(1+\varepsilon_t)^3}; \text{ and } \lambda_c = \frac{R\Omega}{V_c} = \frac{\lambda}{(1+\varepsilon_t)} \tag{4.8}$$

The performance of Darrieus-type SB-VAWT configurations are estimated based on the Chen and Liou (2011) and Pope and Harper (1966) BCM. Both the BCM are utilized for the case study on performance of 3-bladed Darrieus-type SB-VAWTs with conventional blade (N_{18}) and J-shaped blades (J_{uc}-N_{18} (30%), J_{uc}-N_{18} (50%) and J_{uc}-N_{18} (70%)) for V= 10 m/s. Figure 4.7 illustrates the comparative analysis between the uncorrected C_P and C_{Pc} at $Re = 1.71\times10^5$ for 3-bladed Darrieus-type SB-VAWT configurations with different blade profiles. It has been observed that the Pope and Harper (1966) method displays lower C_{Pc} values than other methods. However, the Chen and Liou (2011) method shows a smaller reduction in C_{Pc} values for all blade profiles compared to the uncorrected C_P. Furthermore, the relative performance trend remains the same for all SB-VAWT configurations, regardless of whether their power characteristics utilized these BCMs, as depicted in Fig. 4.7. The same analogy is adopted for all the case studies of SB-VAWT configurations.

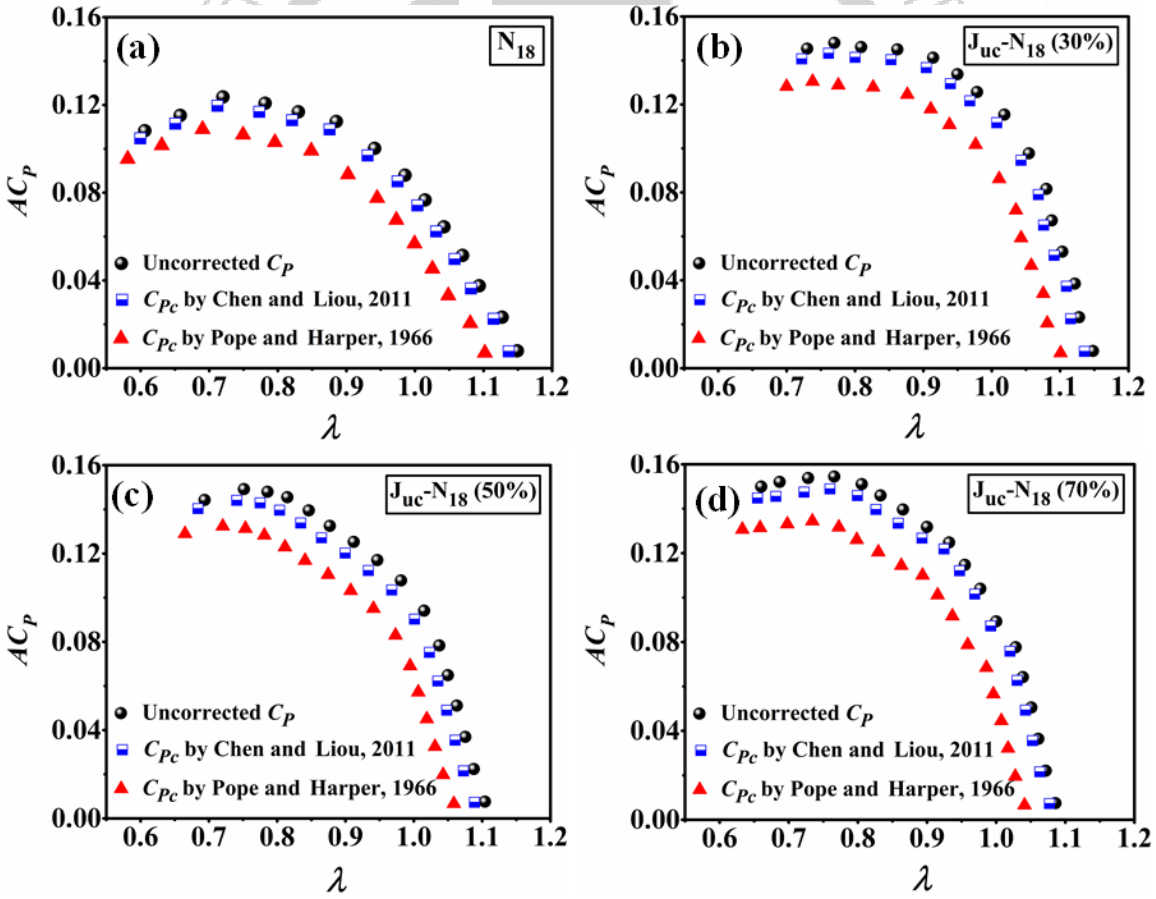

Fig. 4.7. Comparative analysis of blockage correction effect: (a) N_{18}, (b) J_{uc}-N_{18} (30%), (c) J_{uc}-N_{18} (50%) and (d) J_{uc}-N_{18} (70%)

4.6. Summary

This chapter describes the details of the experimental facility and the instruments used for the experimental tests. For this investigation, an open-type subsonic wind tunnel is used, which is installed at the Mechanical Engineering Department of IITG. Furthermore, the experimental setup and experimental procedure are elucidated. The experiments are conducted for different wind speeds and Reynolds numbers. The fabrication of blades is done on a fuse deposition modelling (FDM) 3D printer. Polylactic acid (PLA) material is used for blade fabrication by keeping 70% of the filament infill density, which ensures the turbine's structural stability at various RPMs. The prototype design models of Darrieus-type SB-VAWTs are used with these fabricated blades for experimental tests. The torque calculation method utilizes two different types of torque measurement setups: a dynamic torque measurement setup and a static torque measurement setup. The error analysis has been carried out, presenting standard error bars of the experiments and they do not overlap for the mean C_P vs λ trend. Thus, it is considered that the experimental setup is reliable for the collection of data. The present wind tunnel investigations implemented this analysis to represent the experimental rotor performance data. The blockage effect of the experimentally tested model is one of the important factors in the wind tunnel study. Several distortions can be generated in measured values when there is a high blockage and can reduce the other relevant parameters. Thus, the blockage corrections are calculated for four different types of Darrieus-type rotor models and the uncorrected C_P values are compared with the corrected C_P values used by previous researchers. Two different cases are examined in this experiment. The 3-bladed Darrieus-type SB-VAWTs with conventional and uppercut J-shaped blade profiles are experimented with in the first case. In the second case, the impacts of different blade numbers on Darrieus-type SB-VAWTs are tested in the wind tunnel. Both cases used conventional blades and uppercut J-shaped blades with various ORs.

CHAPTER 5

Numerical Investigations of J-shaped airfoils on the Performance of Darrieus-Type SB-VAWTs

Chapter Layout

Overview

This chapter discussed the numerical investigations on the Darrieu-type SB-VAWTs with conventional and J-shaped airfoils. The airfoil is one of the very significant parameters used to design the Darrieus-type SB-VAWTs. Proper selection of airfoils enhances aerodynamic performance and improves the starting ability of SB-VAWTs. Thus, a conventional cambered airfoil is selected for the creation of J-shaped airfoils. Two categories of J-shaped airfoils are used: uppercut and lowercut. The main focus of this study is to augment the performance and starting capability of the SB-VAWTs. In accordance with this, a series of numerical simulations are carried out on Darrieu-type SB-VAWTs using both conventional cambered and J-shaped airfoils with various opening ratios. Further, this chapter described the effect of uppercut and lowercut J-shaped airfoils on various performance parameters. Further, their flow field analysis is also illustrated comprehensively to make a comparative evaluation. Finally, a comparison is presented between the conventional and J-shaped

5.1. Introduction

In this study, the effect of a new type of blade profile (J-shaped airfoil) with different opening ratios (ORs) on Darrieus-type SB-VAWTs has been investigated through numerical analysis. This study's primary goal is to find the optimum J-shaped airfoils to improve the aerodynamic performance and self-starting ability of the Darrieus-type SB-VAWTs. In doing so, an extensive literature review has been performed on self-starting and aerodynamic performance outlined in Chapter 2 (Sections 2.1-2.5 and 2.7). This work has chosen a non-symmetric airfoil (NACA 4415 airfoil) for the J-shaped blade design due to its several advantages, such as high lift-drag ratios, more suitable stall features and start-up ability in the low to medium λ range (B. K. Kirke and Lazauskas, 1991). The conventional Darrius-type SB-VAWTs generate low torque and aerodynamic performance at low λ values because of the standard airfoils (Celik et al., 2022; Zamani et al., 2016a, 2016b). The lower lift forces of these SB-VAWTs are not sufficient to overcome the starting friction at low λ values because of the low rotational speed. In this case, J-shaped airfoils can overcome this problem due to the cut on their surface. With this viewpoint, numerical simulations are carried out on Darrieus-type SB-VAWTs with a conventional airfoil and its J-shaped airfoils with different ORs. The effect of ORs on the J-shaped airfoils is discussed and their aerodynamic performance is compared with that of the conventional airfoil. The details of the computational methodology have been discussed in Chapter 3 (Section 3.1). The typical methodological process of this work is displayed in the flowchart (Fig. 5.1).

5.2. J-shaped Airfoil Configurations

The conventional NACA 4415 airfoil is selected for the creation of the J-shaped airfoil in the present investigation due to its better performance and smooth WTs operation (López et al., 2016). This cambered (or non-symmetric) airfoil has increased lift-drag ratios, more desirable stall characteristics and self-start ability (B. K. Kirke and Lazauskas, 1991). In addition, it is a suitable profile to obtain good starting features in the low to medium λ range. Usually, the conventional blade with NACA 4415 airfoil is a locked bag-like design similar to that of an aircraft wing. The conventional straight blade performance is not good compared to the J-shaped blade due to its smooth surface on each side of the blade (Zamani et al., 2016b). The J-shaped airfoil is constructed by removing some portion of the conventional NACA 4415 airfoil either from the upper or lower surfaces close to the trailing edge (TE), as shown in Fig. 1.9 (b) and (c). The laminar flow over the smooth surface of a J-shaped airfoil causes aerodynamic lift. Further, the notch of this airfoil easily catches the wind at its back side. Therefore, these airfoils function

due to the simultaneous effect of both F_L and F_D. The aerodynamics of J-shaped airfoils are discussed in Chapter 1 (Section 1.6). When a portion is removed from the upper surface of the NACA 4415 airfoil, it is called an uppercut J-shaped airfoil and designated as a J_{uc} (X_c/c) airfoil, as displayed in Fig. 1.9 (b). Moreover, the lowercut J-shaped airfoil is formed by removing a portion from the lower surface of the NACA 4415 airfoil and is defined as a J_{lc} (X_c/c) airfoil, as depicted in Fig. 1.9 (c). The "J" stands for J-shaped, "uc" means uppercut and "lc" defines the lowercut. The opening ratios (ORs) of J-shaped airfoils are denoted as "X_c/c". Where "X_c" is the opening length and "c" is the chord length of the airfoil.

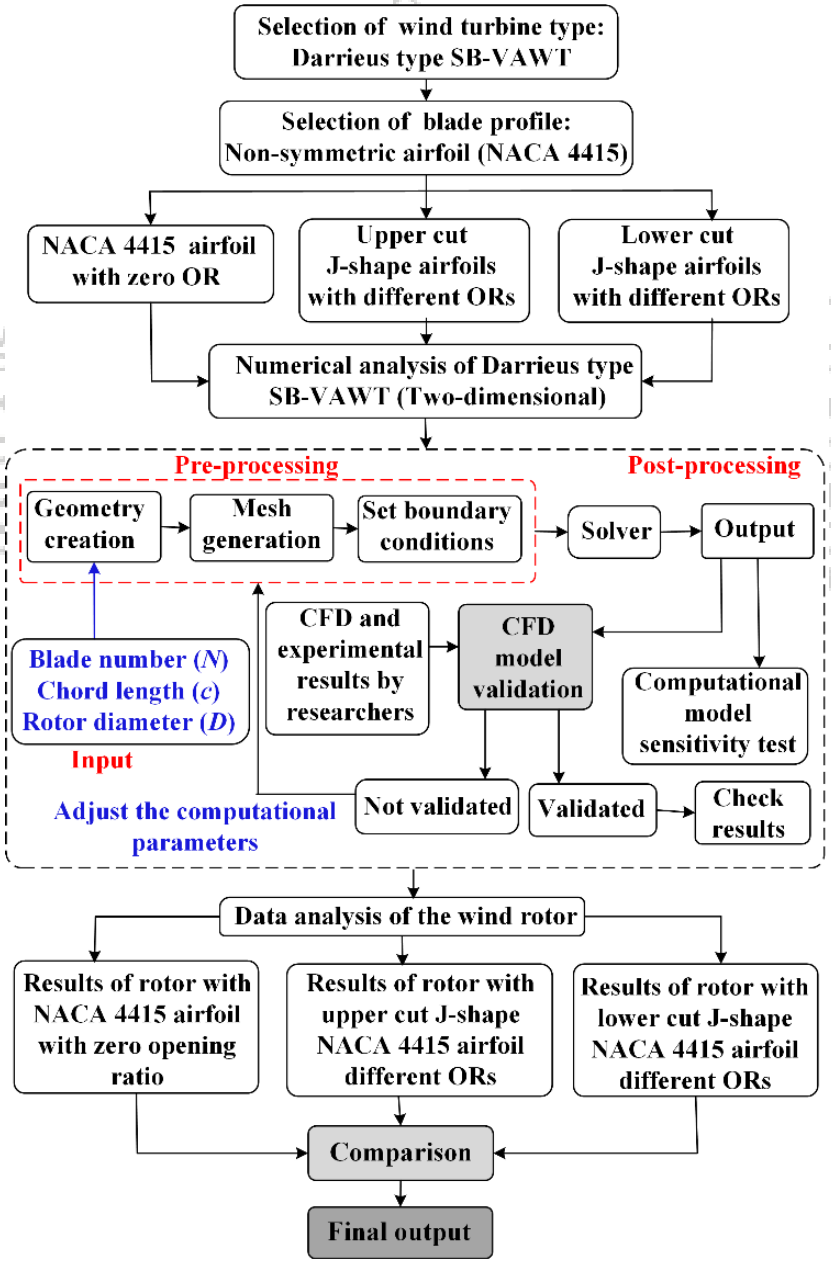

Fig. 5.1. Flowchart depicting the methodology of numerical simulation

Table 5.1 Abbreviations for the J-shaped NACA 4415 airfoil

ORs	J-shaped airfoils named with ORs	
(X_c /c)	Uppercut profile	Lowercut profile
0.8	J_{uc} (OR = 0.8)	J_{lc} (OR = 0.8)
0.7	J_{uc} (OR = 0.7)	J_{lc} (OR = 0.7)
0.6	J_{uc} (OR = 0.6)	J_{lc} (OR = 0.6)
0.5	J_{uc} (OR = 0.5)	J_{lc} (OR = 0.5)
0.4	J_{uc} (OR = 0.4)	J_{lc} (OR = 0.4)
0.3	J_{uc} (OR = 0.3)	J_{lc} (OR = 0.3)
0.2	J_{uc} (OR = 0.2)	J_{lc} (OR = 0.2)
0.1	J_{uc} (OR = 0.1)	J_{lc} (OR = 0.1)

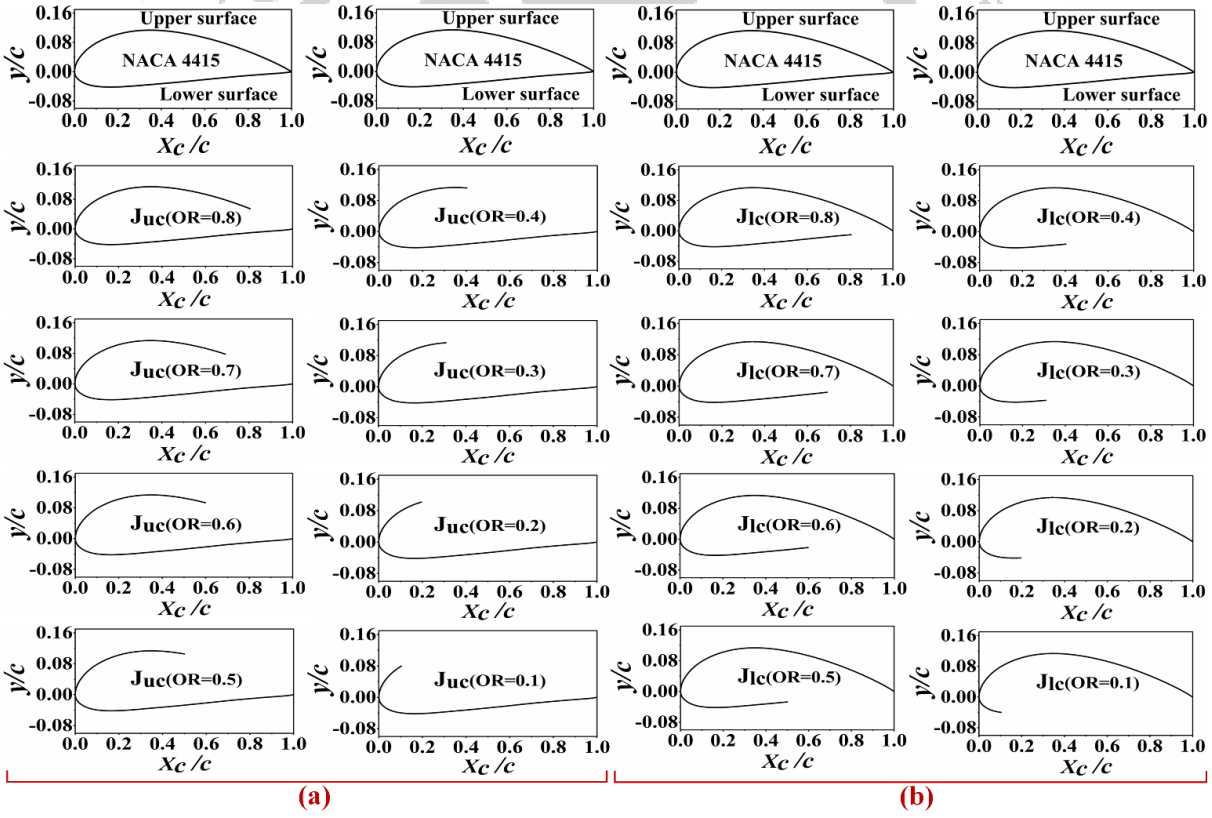

Fig. 5.2. Configuration of J-shape airfoils: (a) Uppercut profiles, (b) Lowercut profiles

Sixteen configurations of J-shaped airfoils have been examined critically, including eight from the uppercut and the remaining eight from the lowercut, as illustrated in Table 5.1. Therefore, the eight different ORs have been chosen and the specifications of the J-shaped airfoils are

represented in Fig. 5.2 (a) and (b). The J-shaped airfoils are adjacent to the rotational shaft as they are fitted in Darrieus-type SB-VAWTs in such a way that their faces are towards the rotational shaft.

5.3. Results and Discussion

This section is mainly divided into two portions: the uppercut J-shaped airfoils and the lowercut J-shaped airfoils. The effect of both airfoils with different ORs on the Darrieus-type SB-VAWTs is described in this part. Further, their C_P, C_T, instantaneous torque coefficient (IC_T), and summation of instantaneous static torque coefficient ($SOIC_{Ts}$) values of both J-shaped airfoils are compared with the conventional NACA 4415 airfoil. The pressure and vorticity fields for the conventional NACA 4415 airfoil and its J-shaped airfoils (uppercut and lowercut) are also presented comprehensively to make a comparative evaluation.

5.3.1. Uppercut J-shaped Airfoils with Different Opening Ratios

5.3.1.1. Effect of the Upper Openings on the C_P

The C_P curves address the influence of the uppercut J-shaped airfoils with various ORs (Fig. 5.3). The C_P values of uppercut J-shaped airfoils at low λ values (up to λ of 1.0) increase slowly due to the gradual increment in the lift by the rotational speed. Further, these airfoils show a sharp increment in C_P values after the λ of 1.0. The growth in the C_P happens because of the substantial increment in the period of the dynamic stall peak (Almohammadi et al., 2015; Zamani et al., 2016a) above the upstream areas of the Darrieus-type SB-VAWTs. At an optimum λ of 1.6, the uppercut J-shaped airfoils generate the highest C_P performance (Fig. 5.3) due to the larger torque. This happens as the rotor blade is close to its stall angle. The increment in the lift value is because of the higher pressure difference produced by the uppercut of the J-shaped airfoil. The C_P value begins to drop after attaining a maximum value at the determined λ due to the reduction of the amplitude peak of dynamic stall (Almohammadi et al., 2015; Zamani et al., 2016a). The gradual decrement in C_P values is due to the flow separation towards its TE. For this reason, more drag is produced, which decreases the performance of the C_P at high λ values (Peng, 2018). A similar type of trend in the C_P performance curve has also been observed in previous research (Celik et al., 2022; Zamani et al., 2016a, 2016b). On the other hand, the conventional NACA 4415 airfoil depicted a larger C_P value at high λ values. This airfoil exhibits higher lift characteristics at higher λ values ($\lambda > 2.0$) and thus, produces higher torque during the high rotational speed. Therefore, the C_P value of the conventional NACA 4415 airfoil is better

at high λ values compared to the uppercut J-shaped airfoils. Moreover, the Darrieus-type SB-VAWTs performance with a conventional NACA 4415 airfoil is mainly due to the lift, as this is a lift-based turbine. For these SB-VAWTs, the drag force may have a favourable effect on its output torque when λ is less than 1.0 (Celik et al., 2022).

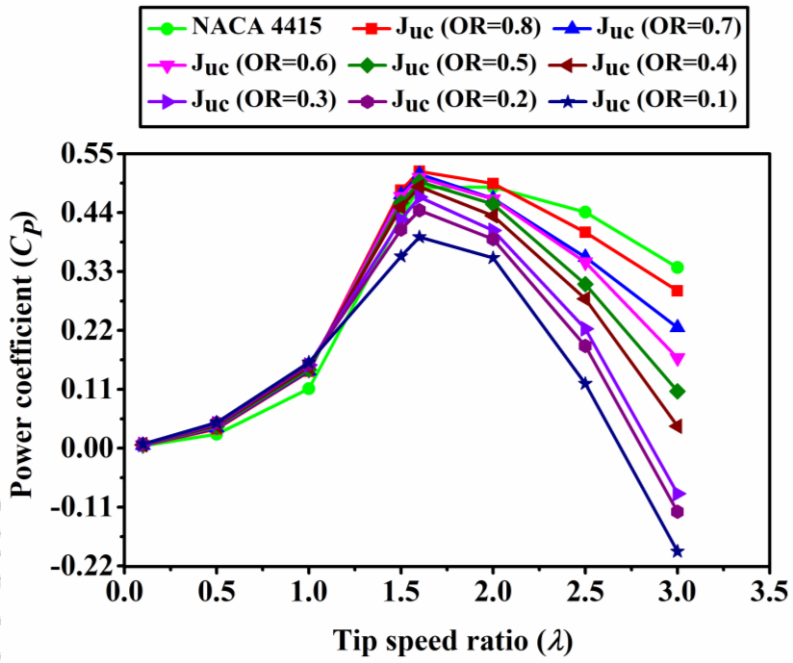

Fig. 5.3. Power coefficient variation of the J-shaped airfoils with upper openings

Furthermore, the J_{uc}(OR=0.8), J_{uc}(OR=0.7), J_{uc}(OR=0.6) and J_{uc}(OR=0.5) airfoils displayed better C_P results in the upstream area for the λ range of 1.5 to 1.6 as compared to other airfoils. The conventional NACA 4415 airfoil exhibits improved C_P in the downwind region compared with all uppercut J-shape profiles except for the J_{uc}(OR=0.8) airfoil at a λ of 2.0. A maximum power coefficient ($C_{P,max}$) of 0.517 is obtained at an optimum λ of 1.6 by the J_{uc}(OR=0.8) airfoil. The $C_{P,max}$ value of J_{uc}(OR=0.7), J_{uc}(OR=0.6), J_{uc}(OR=0.5) and J_{uc}(OR=0.5) airfoil at λ =1.6 are 0.512, 0.506, 0.498 and 0.488, respectively. The conventional NACA 4415 airfoil displayed a $C_{P,max}$ value of 0.486 at the same λ, but it is lower compared to the above mentioned $C_{P,max}$ value. The Darrieus-type SB-VAWTs performance increases when the ORs of the uppercut J-shaped profiles are increased. Further, the uppercut J-shaped airfoils with larger ORs generate higher C_P as they form a complete arc airfoil that can produce more F_L compared to the smaller ORs. This higher F_L sustains a relatively larger C_T that is less influenced by the vorticity generated in the TE. It is the main reason of the uppercut J-shaped airfoils to enhance the aerodynamic performance of the Darrieus-type SB-VAWTs. Furthermore, the uppercut J-shaped airfoils

generate superior C_P results than the lowercut. The above benefits show that flow separation and dynamic stall are lower for upper openings than lower ones.

5.3.1.2. Effect of the Upper Openings on the C_T

The variation of the C_T of uppercut J-shaped airfoils with various ORs at different λ values is illustrated in Fig. 5.4. The C_T is calculated by the average of the sum of the instantaneous C_T and is evaluated by adding the instantaneous C_T of three blades. At the low λ values, the uppercut J-shaped airfoils depicted higher C_T performance because of the larger torque production as compared to the conventional NACA 4415 airfoil. This is because of more lift generation and the benefits of both lift and drag forces. The uppercut J-shaped airfoils produce the $C_{T,max}$ at the optimum λ due to the highest lift and its near to stall angle. After the optimum λ, their C_T values decrease gradually due to the flow separation at their TE. The reduction in C_T value is related to the dynamic stall effects (Celik et al., 2022; Zamani et al., 2016a, 2016b). Thus, it increases the drag, which declines the C_T performance after the optimum λ values. For this reason, the uppercut J-shaped airfoils depicted lower C_T at higher λ values. On the other hand, higher torque is generated by the conventional NACA 4415 airfoil at higher λ values ($\lambda > 2.0$). As the rotational speed of this airfoil increases, its lift also increases. In this way, it raises the torque of the rotor. The increment in lift value is higher for the conventional NACA 4415 airfoil than the uppercut J-shaped airfoils at high λ values. Therefore, the C_T performance of the uppercut J-shaped airfoils is not good at high λ values.

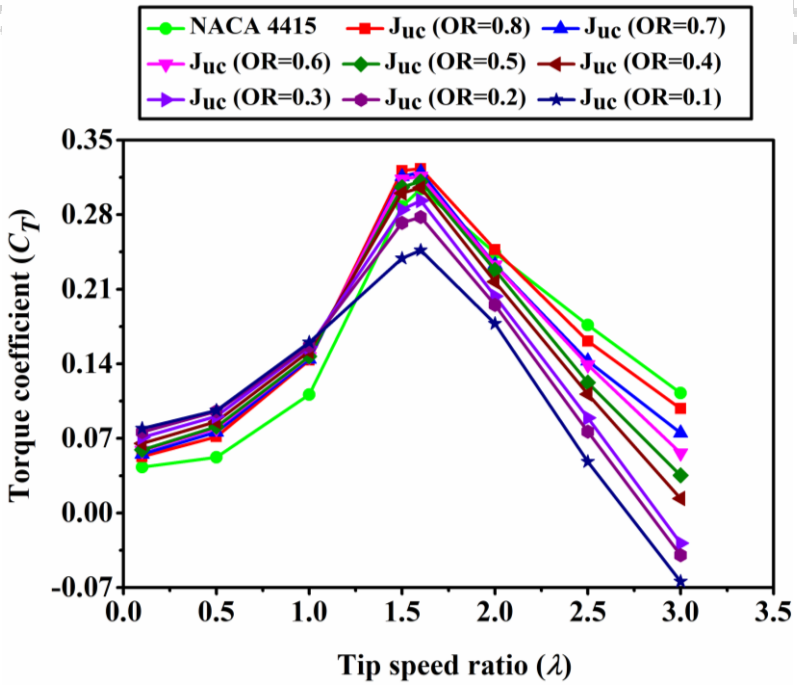

Fig. 5.4. Torque coefficient variation of the J-shaped airfoils with upper openings

The uppercut J-shaped airfoils, such as J_{uc}(OR=0.8), J_{uc}(OR=0.7), J_{uc}(OR=0.6), J_{uc}(OR=0.5) and J_{uc}(OR=0.4) airfoils demonstrate better C_T for the $1.5 \leq \lambda \leq 1.6$ than the rest of the airfoils. Moreover, the conventional NACA 4415 airfoil displays a greater C_T value than all uppercut J-shaped airfoils with ORs for $2.0 \leq \lambda \leq 3.0$ except for the J_{uc}(OR=0.8) airfoil at λ of 2.0. The J_{uc}(OR=0.8) airfoil exhibits a maximum C_T ($C_{T,max}$) of 0.323 at the optimum λ of 1.6, whereas the conventional NACA 4415 airfoil shows an $C_{T,max}$ of 0.304 at the same λ. The λ for the $C_{T,max}$ is nearly constant for all airfoils, which means the uppercut J-shaped airfoils have a minor influence on the λ of the $C_{T,max}$. From the above discussions, there is an enhancement in the C_T of the Darrieus-type SB-VAWTs when using J_{uc}(OR=0.8), J_{uc}(OR=0.7), J_{uc}(OR=0.6), J_{uc}(OR=0.5) and J_{uc}(OR=0.4) airfoils as compared to the conventional NACA 4415 airfoil. Generally, a very significant torque is produced by the non-zero C_T, which helps in the rotation of Darrieus-type SB-VAWTs by suppressing the friction and losses during the starting time. In such a situation, these SB-VAWTs have the capability to self-start. It is to be noted that, the startup capability in real-world application also relies on the inertia, friction and angular acceleration, as it is a transient process. In accordance to this, the actual start-up characteristics not only depends on positive static torque, but also considering the mechanical and inertial dynamics to generate fully dynamic start-up. Referring to Fig. 5.4, the self-starting ability of the uppercut J-shaped airfoils is higher compared to the conventional NACA 4415 airfoil. Thus, these airfoils can self-start the Darrieus-type SB-VAWTs more easily than the conventional NACA 4415 airfoil.

5.3.1.3. Effect of the Upper Openings on the Instantaneous C_T

Figure 5.5 (a-g) depicts the IC_T variation as a function of azimuth angles for blade No. 1 with different ORs at $0.1 \leq \lambda \leq 3.0$. It is observed that the variation patterns of IC_T for blade No. 1 are quite identical in the upwind region at each λ and their maximum instantaneous torque coefficient ($IC_{T,max}$) values are obtained at the same azimuthal angle. It demonstrates that the ORs have minor effects on the location of the $IC_{T,max}$. The IC_T values for the same λ are pretty close to one another in the upwind region. In the downwind side, the IC_T variation curves are adjacent to each other for $\lambda < 1.0$ and the spacing in each curve increases for $\lambda > 1.0$. Further, the IC_T variation patterns of the NACA 4415 airfoil in the upwind region also show similarities to the uppercut J-shaped airfoils with ORs. In the downwind region, the variation patterns of each airfoil display dissimilarity at all λ values.

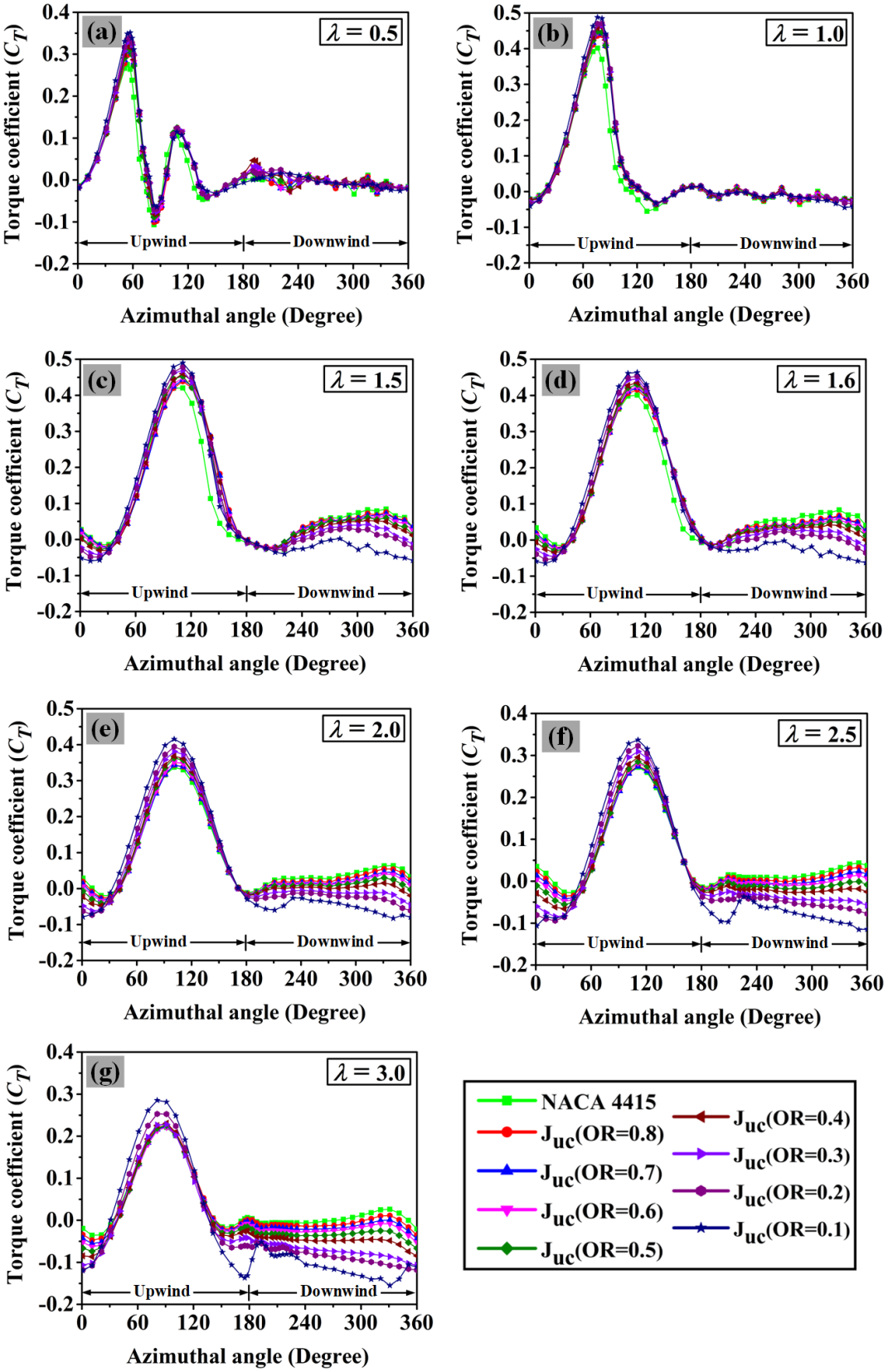

Fig. 5.5. Instantaneous C_T variation of the blade No. 1 with upper openings: (a) λ = 0.5, (b) λ =1.0, (c) λ =1.5, (d) λ =1.6, (e) λ =2.0, (f) λ =2.5 and (g) λ =3.0

Moreover, the IC_T values of the NACA 4415 airfoil in the upwind region are lower compared to all uppercut J-shaped airfoils at an azimuthal angle varying from 30° to 180° for λ ranging from 0.5 to 2.5. This observation also holds at λ = 3.0 for the azimuthal angle range of 30° to 150°. However, the NACA 4415 airfoil exhibits IC_T values comparable to those of uppercut J-shaped airfoils, particularly at lower λ of 0.5, 1.0, and 1.5, for azimuthal angles ranging from 0 - 30°. For the same azimuthal angles range, higher IC_T values are obtained by the NACA 4415 airfoil compared to the uppercut J-shaped airfoils for higher λ of 1.6, 2.0, 2.5 and 3.0. On the other hand, the NACA 4415 airfoil in the downwind region displayed higher IC_T values for each azimuth angle ranging between 180° to 360°.

Generally, the IC_T values are less affected by the upper openings, mainly in the upwind region and are substantially influenced in the downwind region. The reason behind this matter is the large torque generation by the blade in the upwind region compared to the downwind region. A similar analogy for IC_T variation can also be made for other blades thoroughly as a function of azimuth angles with different ORs.

5.3.1.4. Effect of the Upper Openings on the $SOIC_{Ts}$

The variation of the $SOIC_{Ts}$ for three blades of Darrieus-type SB-VAWTs as a function of azimuth angle is presented in Fig. 5.6 at an optimum λ of 1.6. The maximum values of summation of instantaneous static C_T ($SOIC_{Ts,max}$) of three blades are observed in the azimuth angle range of 105° to 110°, 225° to 230° and 345° to 355° with different blades airfoils. On the other hand, the minimum values of summation of instantaneous static C_T ($SOIC_{Ts,min}$) are found at the azimuth angle of 46°, 166° and 286° for three blades with various uppercut J-shaped blade airfoils. The three blades with the conventional NACA 4415 airfoil show its $SOIC_{Ts,min}$ at the azimuth angle of 41°, 161° and 281°. The variation patterns of $SOIC_{Ts,max}$ and $SOIC_{Ts,min}$ are quite similar for three blades with all airfoils.

It is noticed from Fig. 5.6 that the $SOIC_{Ts,max}$ values of NACA 4415 airfoil, J_{uc}(OR=0.8) airfoil and J_{uc}(OR=0.7) airfoil are nearer to each other. There are a few differences for the rest of the uppercut J-shaped airfoils. Further, the J_{uc}(OR=0.8), J_{uc}(OR=0.7), J_{uc}(OR=0.6), J_{uc}(OR=0.5), J_{uc}(OR=0.4), J_{uc}(OR=0.3), and J_{uc}(OR=0.2) airfoil displays higher $SOIC_{Ts,min}$ as compared to the NACA 4415 airfoil. All uppercut J-shaped airfoils except J_{uc}(OR=0.1) airfoil enhance the starting torque of Darrieus-type SB-VAWTs compared to the NACA 4415 airfoil. On the other hand, the minimum values of summation of instantaneous static C_T ($SOIC_{Ts,min}$) are found at the

azimuth angle of 46°, 166° and 286° for three blades with various uppercut J-shaped blade airfoils. The three blades with the conventional NACA 4415 airfoil show their $SOIC_{Ts,min}$ at the azimuth angles of 41°, 161° and 281°. The variation patterns of $SOIC_{Ts,max}$ and $SOIC_{Ts,min}$ are quite similar for three blades with all airfoils.

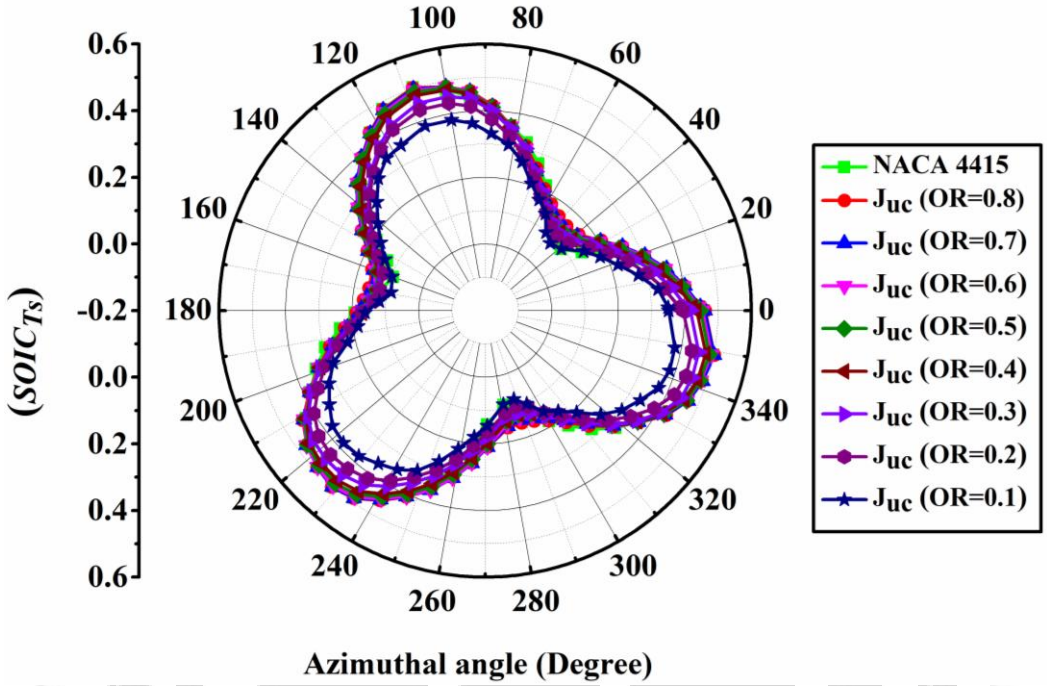

Fig. 5.6. Summation of instantaneous static C_T variation of three blades with upper openings at optimum λ

5.3.1.5. Effect of the Upper Openings on the Pressure and Vorticity Field

The pressure and vorticity contour of blade No. 1 for the NACA 4415 airfoil and J_{uc}(OR=0.7) airfoil at optimum λ = 1.6 for upwind and downwind regions is presented in Figs. 5.7. These contour plots are represented at an optimum λ of 1.6 at six different azimuth angles, such as 0°, 60°, 120°, 180°, 240° and 300°. The pressure difference between the upper and lower surfaces of the blades in the upwind region (up to 120°) is higher than in the downwind region (180° to 300°), as shown in the pressure contour plot. Thus, more lift is generated by J_{uc}(OR=0.7) airfoil than the NACA 4415 airfoil. Therefore, the F_L generated in the downwind region is smaller compared to the upwind region, which is indicated by the above difference. Moreover, it is the reason for the generation of higher IC_T in the upwind zone and lower IC_T in the downwind zone, as shown in Fig. 5.5 (a-g). It is observed that the difference in pressure between LE and TE

increases by J_{uc}(OR=0.7) airfoil and thus, the F_D improves. Therefore, this airfoil develops a better start-up torque due to its Savonius-type drag-based blades.

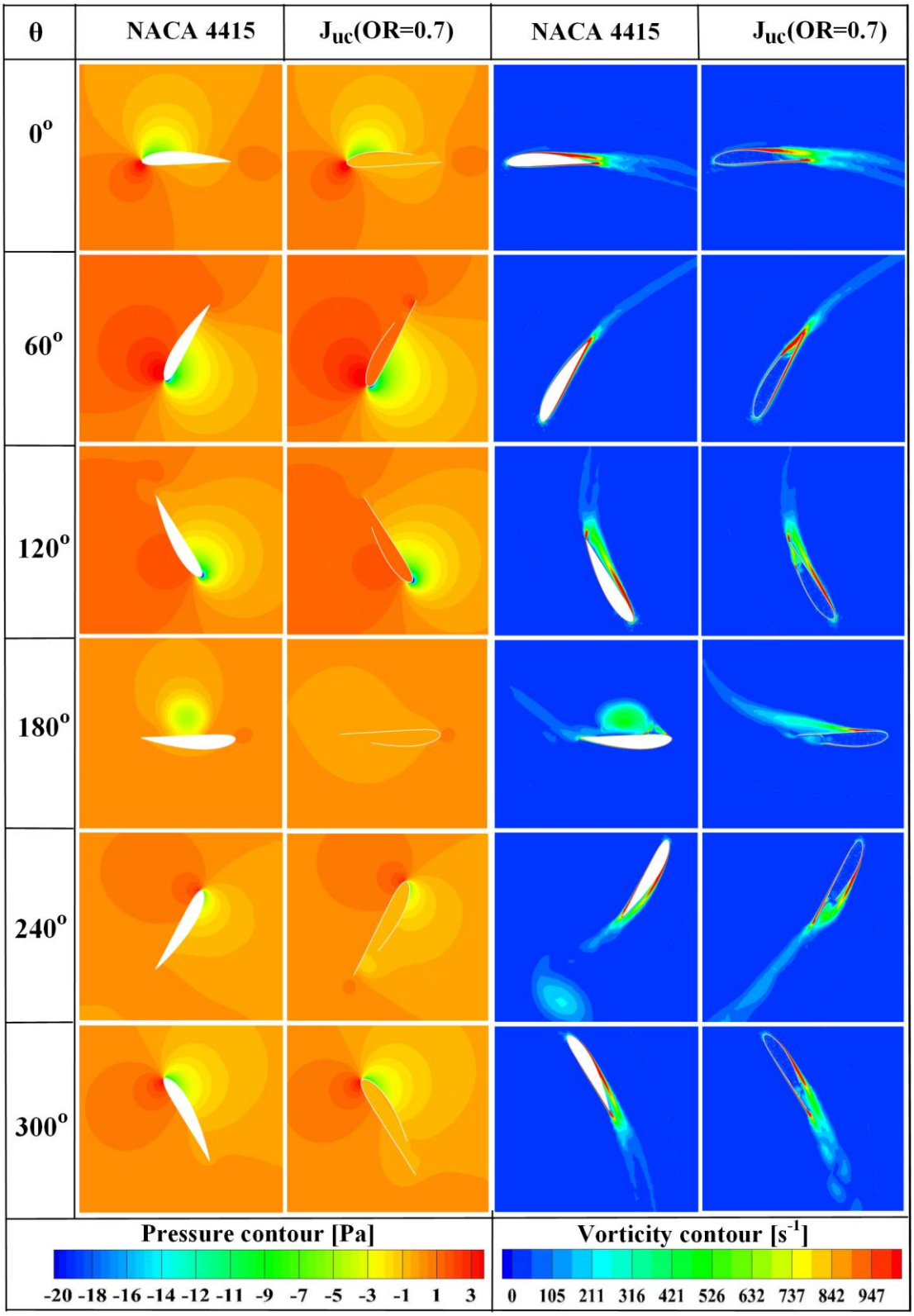

Fig. 5.7. Pressure and vorticity contour of the blade No. 1 with upper opening at an optimum λ

Figure 5.7 depicts that a large number of shed vortices are being convected due to their low-pressure cores towards the downstream side. Moreover, the vortex structures with large shapes are developed in the blade upwind region and transferred to the downwind region at a speed which is pretty equal to the blade speed. The above figure displayed that the J_{uc}(OR=0.7) airfoil generated much fewer separated vortices than the NACA 4415 airfoil. Accordingly, the flow all over the turbine vicinity turns more stable, which helps to lessen the vibrations acting on its several parts. In this study, the contour profiles of blade No.1 have been thoroughly examined. At any instant, the aerodynamic behaviour of the three blades will be different due to their polar position. In order to understand the aerodynamic influence at those positions, the case study of a single blade has been undertaken for a full rotation. Thus, one can understand the influence on the individual blade.

5.3.2. Lowercut J-shaped Airfoils with different Opening Ratios

5.3.2.1. Effect of the Lower Openings on the C_P

The impact of the lower opening on the C_P of the Darrieus-type SB-VAWTs is illustrated in Fig. 5.8. As noticed in the above figure, the C_P values of all airfoils first increase up to the λ =1.6 and then those values decrease when $\lambda \geq 1.6$ except for the J_{lc}(OR=0.1) airfoil and the conventional NACA 4415 airfoil. The J_{lc} (OR=0.1) airfoil shows higher C_P up to λ =1.5, while the conventional NACA 4415 airfoil shows up to λ =2.0. Furthermore, Fig. 5.8 also shows the comparison between the lowercut J-shaped airfoils with a conventional NACA 4415 airfoil. The above comparison displays that the C_P value of the J_{lc} (OR=0.8) airfoil and J_{lc} (OR=0.7) airfoil is larger than all other airfoils in the upwind region.

On the other hand, the conventional NACA 4415 airfoil in the downwind region depicts better C_P performance for the λ range of 2.0 to 3.0 compared to the rest of the airfoils. Further, the J_{lc} (OR=0.8) airfoil displays the $C_{P,max}$ of 0.514 at optimum λ = 1.6, while the conventional NACA 4415 airfoil shows 0.486 at the same λ. Moreover, the C_P values of all lowercut J-shaped airfoils increase at each λ when their lower openings increase.

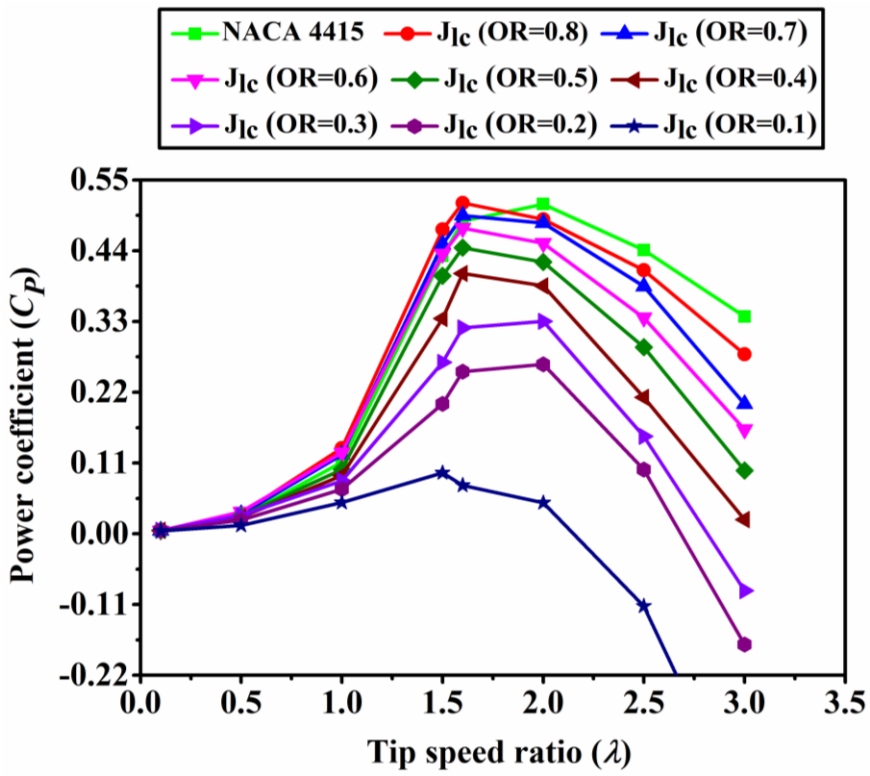

Fig. 5.8. Power coefficient variation of the J-shaped airfoils with lower openings

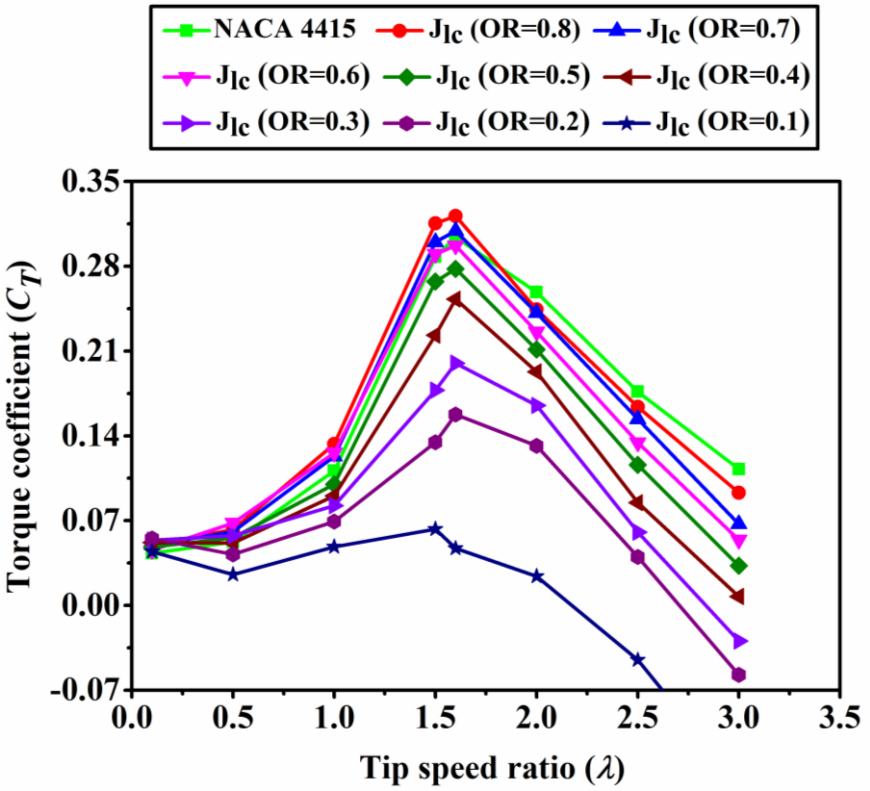

Fig. 5.9. Torque coefficient variation of the J-shaped airfoils with lower openings

5.3.2.2. Effect of the Lower Openings on the C_T

Figure 5.9 demonstrates the variation of C_T as a function of λ for the conventional NACA 4415 airfoil and the lowercut J-shaped airfoils. It is observed that the C_T of all airfoils increases up to a λ = 1.6 and then decreases gradually. Moreover, the conventional NACA 4415 airfoil and the lowercut J-shaped airfoils displayed their C_T peak at the same λ, while the J_{lc} (OR=0.1) airfoil showed its C_T peak at a λ of 1.5. A higher C_T is found by the J_{lc} (OR=0.8) airfoil and J_{lc} (OR=0.7) airfoil at the optimum λ = 1.6 compared with other airfoils. The conventional NACA 4415 airfoil displayed higher C_T only after the λ value of 2.0, compared to all lowercut J-shaped airfoils. A $C_{T,max}$ is found by the J_{lc} (OR=0.8) airfoil at an optimum λ =1.6. Further, the C_T value increases when the lower openings increase, but not at the same rate as the upper openings. However, the lowercut J-shaped airfoils display lower C_T values when compared to the uppercut. That means the Darrieus-type SB-VAWTs generated lower C_T values if they used the lowercut J-shaped airfoils compared to the uppercut J-shaped airfoil.

5.3.2.3. Effect of the Lower Openings on the Instantaneous C_T

The influence of blade No. 1 with lowercut J-shaped airfoils and conventional NACA 4415 airfoil on the IC_T variation is observed in Fig. 5.10 (a-g) at different λ values. The IC_T variation curves are close to each other in the downwind region when λ < 1.0 and lots of fluctuations are also noticed for λ. The closeness starts to decrease in each IC_T curve when λ > 1.0 for both upwind and downwind regions. Further, the distance between each IC_T variation curve of blade No. 1 with the lower opening is higher for the azimuth angle range of 0° to 180° compared to the upper opening. The IC_T curve of the J-shaped airfoil with various lower ORs exhibited different shapes on the downwind side. The $IC_{T,max}$ value of all airfoils is found at different azimuth angles in the upwind region for λ < 1.6. However, these values are obtained at a constant azimuth angle for λ > 1.6 except for the J_{lc} (OR=0.1) airfoil. The conventional NACA 4415 airfoil shows a higher IC_T value in the upwind region than the lowercut J-shaped airfoils for λ =2.0, 2.5 and 3.0. It is noticed that the IC_T values increase when lower openings increase in the upwind area, but these values are lower compared to upper openings. That means the J-shaped airfoils with lower ORs displayed poor IC_T values for blade No.1 compared to upper ORs. A comparable analogy for IC_T variation can also be produced for blade No.2 and blade No.3 thoroughly as a function of azimuth angles with different ORs.

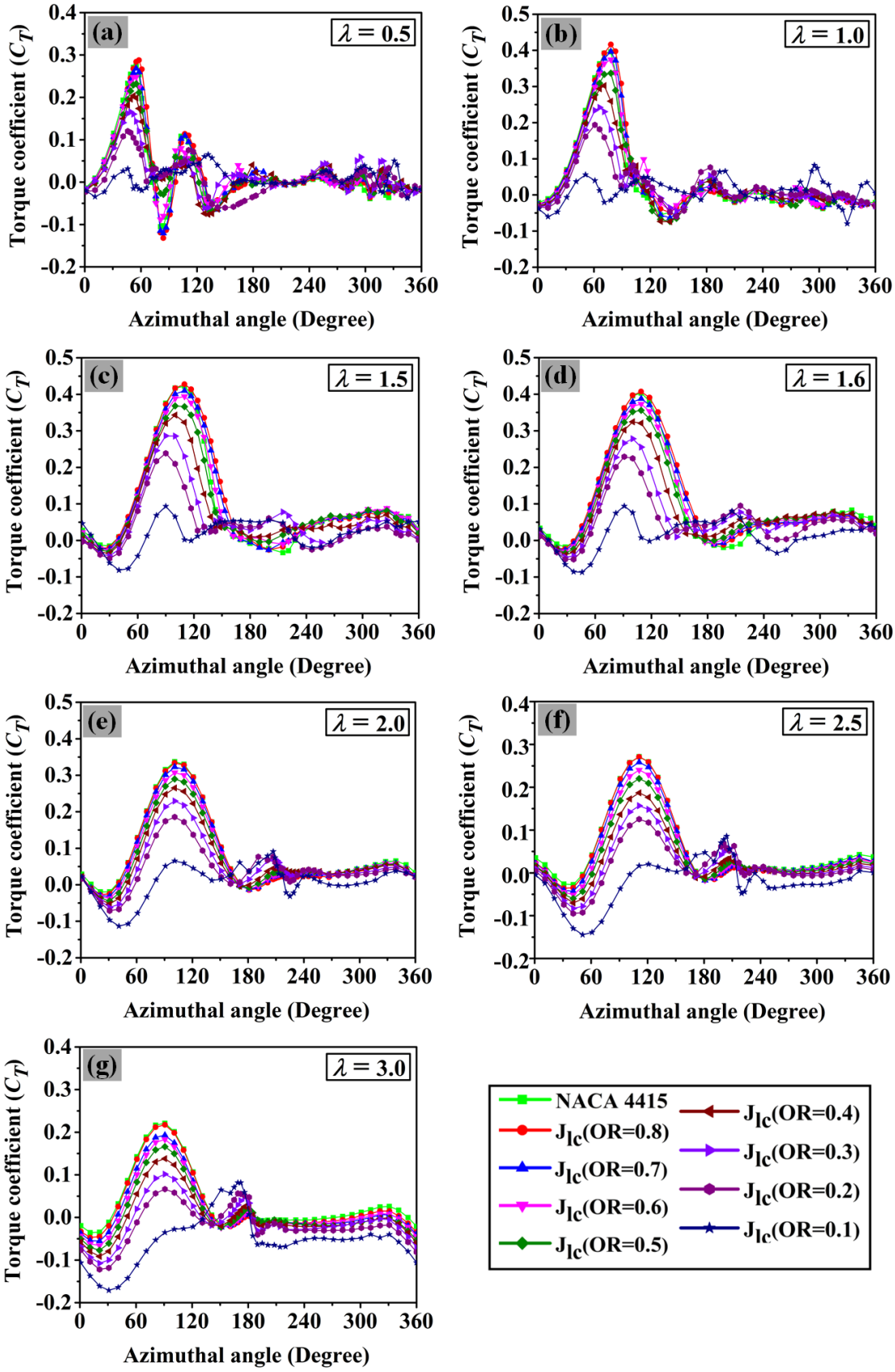

Fig. 5.10. Instantaneous C_T variation of the blade No. 1 with lower openings: (a) λ = 0.5, (b) λ =1.0, (c) λ =1.5, (d) λ =1.6, (e) λ =2.0, (f) λ =2.5 and (g) λ =3.0

5.3.2.4. Effect of the Lower Openings on the $SOIC_{Ts}$

The $SOIC_{Ts}$ variation of three blades with lowercut J-shaped airfoils and conventional NACA 4415 airfoil for optimum λ of 1.6 is shown in Fig. 5.11 at a different azimuth angle. Three maximum peaks in the $SOIC_{Ts}$ values for three blades of all configurations are observed at different azimuth angle ranges such as 80° to 120°, 200° to 240° and 320° to 360°. Further, the $SOIC_{Ts,min}$ for all configurations is obtained at an azimuth angle range of 20° to 60°, 140° to 180° and 260° to 300°. The conventional NACA 4415 airfoil depicted a higher $SOIC_{Ts}$ value at azimuth angles of 40°, 160° and 280°. On the contrary, it is viewed that the J_{lc} (OR=0.8), J_{lc} (OR=0.7) and J_{lc} (OR=0.6) airfoils illustrated superior $SOIC_{Ts}$ results compared to the NACA 4415 airfoil with zero lower ORs. The $SOIC_{Ts}$ plots for all airfoils displayed in Fig. 5.11 presented closeness in each curve at an azimuth angle range of 60° to 90°, 180° to 200° and 300° to 320° except the J_{lc}(OR=0.1) airfoil. The three blades with lower ORs show a large gap in each $SOIC_{Ts}$ curve at an azimuth angle of 0° to 60°, 90° to 180°, 200° to 300° and 320° to 360°. The lower ORs of the three blades displayed poor $SOIC_{Ts}$ values when it is compared with the $SOIC_{Ts}$ values of the blade with upper ORs.

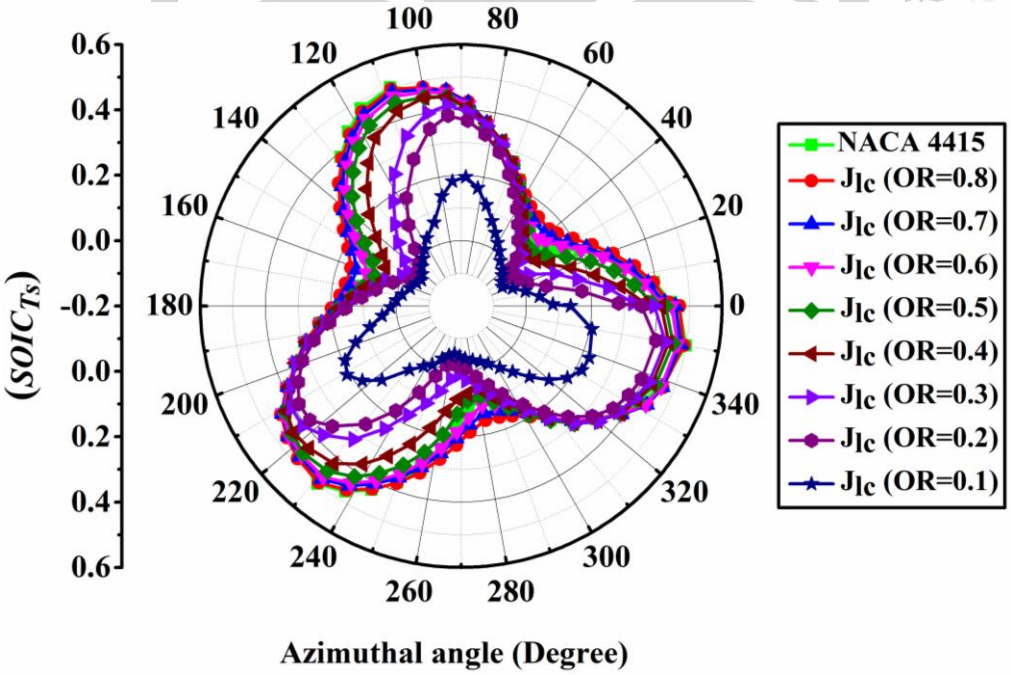

Fig. 5.11. Summation of instantaneous static C_T variation of three blades with lower openings at optimum λ

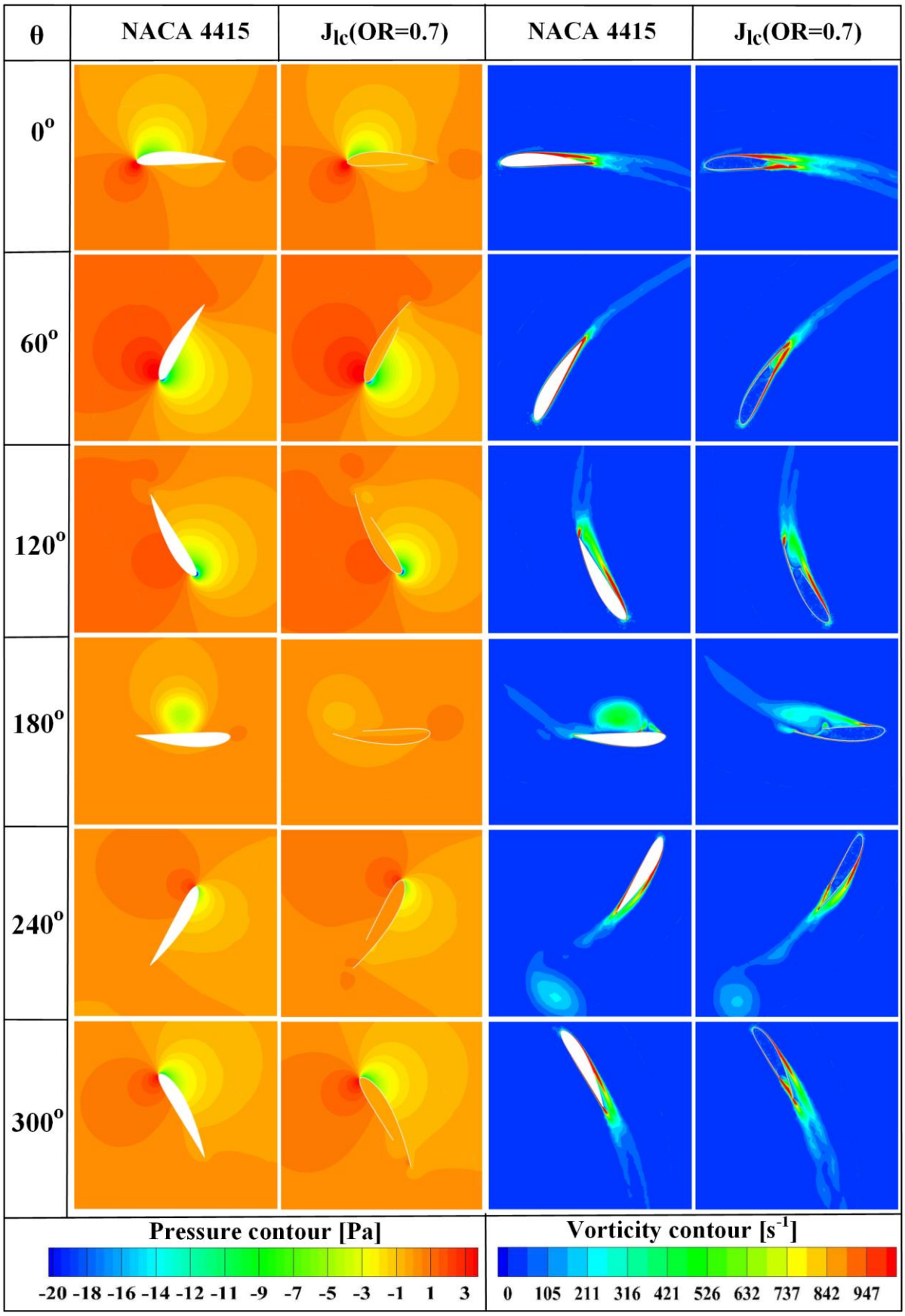

Fig. 5.12. Pressure and vorticity contour of the blade No. 1 with lower opening at an optimum λ

5.3.2.5. Effect of the Lower Openings on the Pressure and Vorticity Field

Figures 5.12 illustrate the pressure and vorticity contour plot of blade No. 1 with the NACA 4415 airfoil and the J_{lc} (OR=0.7) airfoil for upwind and downwind regions. These plots are presented at optimum λ =1.6 at six different azimuth angles such as 0°, 60°, 120°, 180°, 240° and 300°. Among these six angles, azimuth angles (0°, 60° and 120°) show the contour plots for the upwind region and the azimuth angles (180°, 240° and 300°) display these plots for the downwind region. The differences in pressure between the two surfaces of blades are not very high, as shown in the pressure contour profile with lower ORs compared to blades with upper ORs. Thus, J-shaped blades with lower openings generate less F_D and F_L than blades with upper openings, which means that they have less self-starting ability. Based on the above reason, the IC_T value of lowercut J-shaped airfoils is lower in both upwind and downwind regions compared to the uppercut J-shaped airfoils (Fig. 5.10 (a-g)). However, the J-shaped blades with lower ORs produce better self-start ability compared to the standard blade due to their bag configuration. It is noticed from the above plots that several shed vortices, which have lower pressure cores are convecting in the downwind region. Moreover, the vortex structures with large sizes formed in the blade upwind region are moving to the downwind region at nearly the same rate as the turbine blades.

The vortexes from the J-shaped blade surfaces are less separated than the standard blade, as observed in Fig. 5.12. Therefore, a more stable flow is generated around the turbine, decreasing the vibrations and fatigue stress of the wind rotor and its shaft. Further, these blades with lower ORs generate more vortices than those with upper ORs. In this investigation, the contour profiles of blade No.1 have been thoroughly examined. A similar comparison can also be made for the other two blades.

5.3.3. Comparison between Conventional and J-shape Airfoils with ORs

Figure 5.13 displays the overall performance of the conventional airfoil, uppercut and lowercut J-shaped airfoils with different ORs for λ of 1.6 and 1.5. It is observed from Fig. 5.13 that the C_p and C_T values of uppercut J-shaped airfoils are better than the lowercut J-shaped airfoils and the conventional NACA 4415 airfoil for both the λ values. Opening ratios play a vital role in this comparison; as the ORs increase from 0.1 to 0.8, the C_p and C_T values of both the J-shaped airfoils also increase gradually. The conventional NACA 4415 airfoil in Fig. 5.13 is represented

at a zero OR. Therefore, the C_p and C_T values of this airfoil show the same values for uppercut and lowercut J-shaped airfoil at both the λ values (Fig. 5.13). The absolute and relative values of C_p and C_T for J-shaped airfoils with different ORs with respect to the conventional NACA 4415 airfoil are exhibited in Table 5.2. These outcomes are displayed for two different λ values of 1.5 and 1.6. The uppercut J-shaped airfoil with ORs of 0.8, 0.7, 0.6, 0.5 and 0.4 illustrated higher absolute and relative performance than the conventional NACA 4415 airfoil for both λ values. Further, the J_{lc} (OR=0.8) and J_{lc} (OR=0.7) airfoils depict better absolute performance compared to the conventional NACA 4415 airfoil.

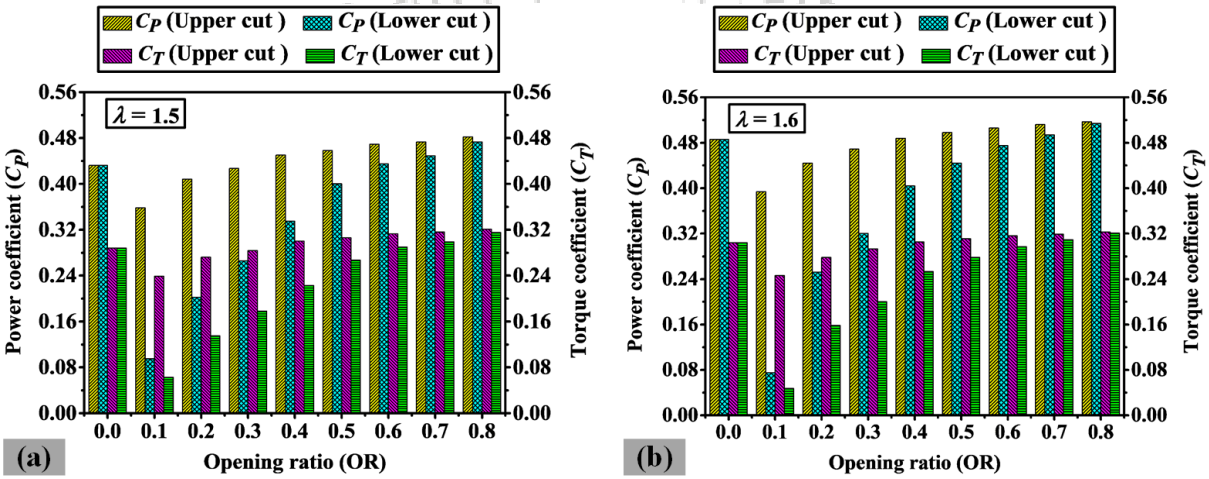

Fig. 5.13. Overall performance of airfoils at different opening ratios: (a) λ =1.6, (b) λ =1.5

More superior performance is found from the uppercut J-shaped airfoils than the lowercut J-shaped airfoils and their improved absolute and relative values for respective ORs are presented in Table 5.2. This comparison demonstrates that the Darrieus-type SB-VAWTs generated higher C_p and C_T values when they used the uppercut J-shaped airfoils with the abovementioned ORs. It is observed that the lowercut J-shaped airfoils generated lower C_P and C_T performance at λ of 1.5 and 1.6 (Fig. 5.13) compared to other configurations due to lower lift generation. The production of low lift is due to the lower pressure difference generated by this airfoil. This happens as these configurations reduce the higher pressure region because of the cut on its lower surface. From the aerodynamic perspective, such a condition is not favourable for potential lift generation. And in the present study, this analogy has been observed with lesser C_P and C_T for the rotor having lowercut J-shaped airfoils.

Table 5.2 Comparison between the conventional NACA 4415 airfoil and J-shaped airfoils

Airfoils	Performance indicator			
	λ =1.6		λ =1.5	
	C_T	C_P	C_T	C_P
(OR=0)	0.304	0.486	0.287	0.431
	Absolute performance			
J_{uc} (OR=0.8)	0.323	0.517	0.321	0.481
J_{uc} (OR=0.7)	0.320	0.512	0.315	0.473
J_{uc} (OR=0.6)	0.316	0.506	0.313	0.469
J_{uc} (OR=0.5)	0.311	0.498	0.305	0.458
J_{uc} (OR=0.4)	0.305	0.488	0.300	0.450
J_{lc} (OR=0.8)	0.321	0.514	0.314	0.471
J_{lc} (OR=0.7)	0.309	0.494	0.299	0.449
	Relative performance (%)			
J_{uc} (OR=0.8)	6.3	6.4	11.8	11.6
J_{uc} (OR=0.7)	5.3	5.3	9.8	9.7
J_{uc} (OR=0.6)	3.9	4.1	9.1	8.8
J_{uc} (OR=0.5)	2.3	2.5	6.3	6.3
J_{uc} (OR=0.4)	0.3	0.4	4.5	4.4
J_{lc} (OR=0.8)	5.6	5.8	9.4	9.3
J_{lc} (OR=0.7)	1.6	1.6	4.2	4.2

The J-shaped SB-VAWTs fall under the small wind turbines (SWTs) category due to their low λ values and *Re* (Siram et al., 2022b). Though such rotors have a lesser generation capacity compared to large wind turbines (LWTs), such turbines are noted for their potential applications in places where the implications of LWTs are not economical or feasible. The cost of installation, operation and maintenance of such turbines are relatively lower than LWTs, making it one of the most reliable and affordable standalone or off-grid renewable energy systems. Such turbines can be installed as an off-grid power source for individual households, the agricultural field, small wind farms or multirotor configurations and offshore VAWT applications (Pan et al., 2021; Siram et al., 2022b).

5.4. Summary

In this study, a series of 2D numerical simulations has been carried out on Darrieus-type SB-VAWTs using J-shaped airfoils with different opening ratios (ORs). The J-shaped airfoils are created by removing some part either from the upper or lower surface of a conventional NACA 4415 airfoil. This work investigates two types of J-shaped airfoils: uppercut J-shaped airfoils and lowercut J-shaped airfoils. A total of sixteen different ORs are examined; eight for uppercut J-shaped airfoils and the remaining eight for the lowercut J-shaped airfoils. A thorough comparison is presented between both J-shaped airfoils and conventional NACA 4415 airfoils. The uppercut J-shaped airfoils are depicted better performance than the lowercut J-shaped airfoils and the conventional NACA 4415 airfoils. The uppercut J-shaped airfoils with ORs of 0.8, 0.7, 0.6, 0.5 and 0.4 displayed a maximum power coefficient (C_p) of 0.517, 0.512, 0.506, 0.498 and 0.488, respectively at tip speed ratio (λ) =1.6. At the same λ and same ORs, the lowercut J-shaped airfoils show maximum C_p of 0.514, 0.494, 0.475, 0.444 and 0.404. Further, the conventional NACA 4415 airfoil depicted a maximum C_p of 0.486 at the same λ value. The lowercut J-shaped airfoils with ORs of 0.8 and 0.7 produce better performance than the conventional NACA 4415 airfoil. The C_p and torque coefficient (C_T) values of SB-VAWTs are enhanced by about 31% when uppercut J-shaped ORs are varied from 0.1 to 0.8. Due to the larger torque generation, the instantaneous torque coefficient (IC_T) values are not affected by the ORs of the uppercut J-shaped airfoils. Further, poor IC_T values are noticed in the upwind region because of the lowercut J-shaped airfoils. The J-shaped airfoils improved the starting characteristics of the Darrieus-type SB-VAWTs compared to the conventional airfoils. The novel profile geometry of J-shaped airfoils trapped the vortices in their geometry and lessened the backside wake.

CHAPTER 6

Experimental and Numerical Investigations of Small-Scale Darrieus-Type SB-VAWTs using J-Shaped Airfoils

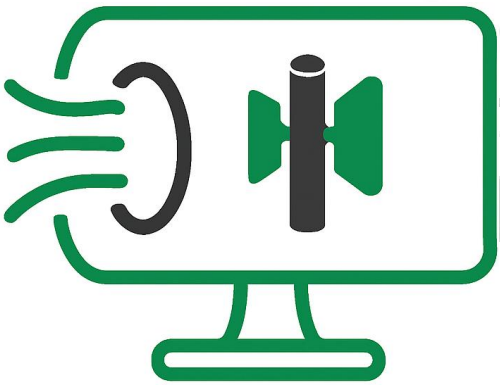

Chapter Layout

Overview

In this chapter, the numerical simulations on conventional cambered airfoil families and their J-shaped airfoils are carried out to find the optimum airfoil for small-scale Darrieus-type SB-VAWTs. Thereafter, optimum blades are fabricated through a 3D printer to design the Darrieus-type SB-VAWT prototype models for experimental investigations. The Darrieus-type SB-VAWTs models with uppercut J-shaped airfoils with three different opening ratios are experimented in a wind tunnel and compared with the SB-VAWTs models consisting of conventional airfoils. This study is conducted only for the 3-bladed SB-VAWTs. The experimental average torque and power characteristics are presented for different Reynolds numbers for each airfoil. Further, experimental static torque coefficient is demonstrated concerning the azimuthal angle for different airfoils and velocities. The numerical instantaneous torque coefficients are plotted for each blade of every airfoil. The numerical results are validated with the experimental outcomes. Moreover, velocity magnitude superimposed streamlines and vorticity magnitude are manifested for J-shaped and conventional blades.

6.1. Introduction

The current investigation aims to perform a detailed systematic study analysis with uppercut J-shaped straight blades suitable for self-starting and better aerodynamic performance for the small-scale Darrieus-type SB-VAWTs. Therefore, multiple numerical and experimental investigation is carried out, especially at lower λ values, to find the optimum camber airfoil and address the gap in understanding the starting behaviour of SB-VAWTs. The details of numerical methodologies used for this study are described in Chapter 3 (Section 3.2). Further, the experimental methodologies such as experimental setup, blade fabrication, prototype models design, torque measurement setup, error analysis and blockage correction are discussed in Chapter 4. The aerodynamics of the airfoil configurations and new blade designs play an essential role in the improvement of the aerodynamic performance as well as the starting torque of SB-VAWTs (Al Hamad et al., 2022). From this perspective, a detailed literature survey has been carried out in Chapter 2 (Sections 2.1 and 2.7). In this study, the cambered airfoil families (NACA 44XX) are selected to create J-shaped blade profiles due to their many benefits (B. K. Kirke and Lazauskas, 1991). Moreover, this study discusses the influence of uppercut opening ratios (ORs) and airfoil thickness on several designed parameters of the SB-VAWTs. In addition, a thorough comparative analysis is presented to compare the output power and flow characteristics between the conventional camber airfoils and their J-shaped airfoils. This study can provide clear guidelines for designing small-scale Darrieus-type SB-VAWTs in order to justify and promote the applications of SB-VAWTs, which can self-start in areas with low wind speed and urban environments. The numerical and experimental methodologies of this investigation are described in terms of a flowchart and are displayed in Fig. 6.1.

6.2. J-shaped Blade Profiles

The conventional cambered airfoils (NACA 44XX) displayed in Fig. 6.2 (a, c, e, i and k) are chosen as the blade profiles of Darrieus-type SB-VAWTs for the present investigation. The "XX" denotes the maximum thickness as a percentage (%) of the c from the LE (leading edge). The conventional cambered airfoils are of constant camber, but their thicknesses are different. In these types of airfoils, the upper surface curvature is higher compared to that of their lower surface. The conventional cambered airfoils provide many additional benefits and enhance the C_P (B K Kirke and Lazauskas, 1991; Naik and Sahoo, 2023) of WTs. These airfoils have the ability to increase the self-starting of SB-VAWTs at low to medium λ values and generally have positive C_L at zero and other α unless a stall occurs. On the other hand, the symmetrical airfoils

are unable to self-start the SB-VAWTs (Bausas and Danao, 2015) and these airfoils have zero C_L at zero α. The shape of the blade profile is the primary cause of the origination of the pressure difference on the airfoil surface that ultimately develops F_L and F_D on airfoils.

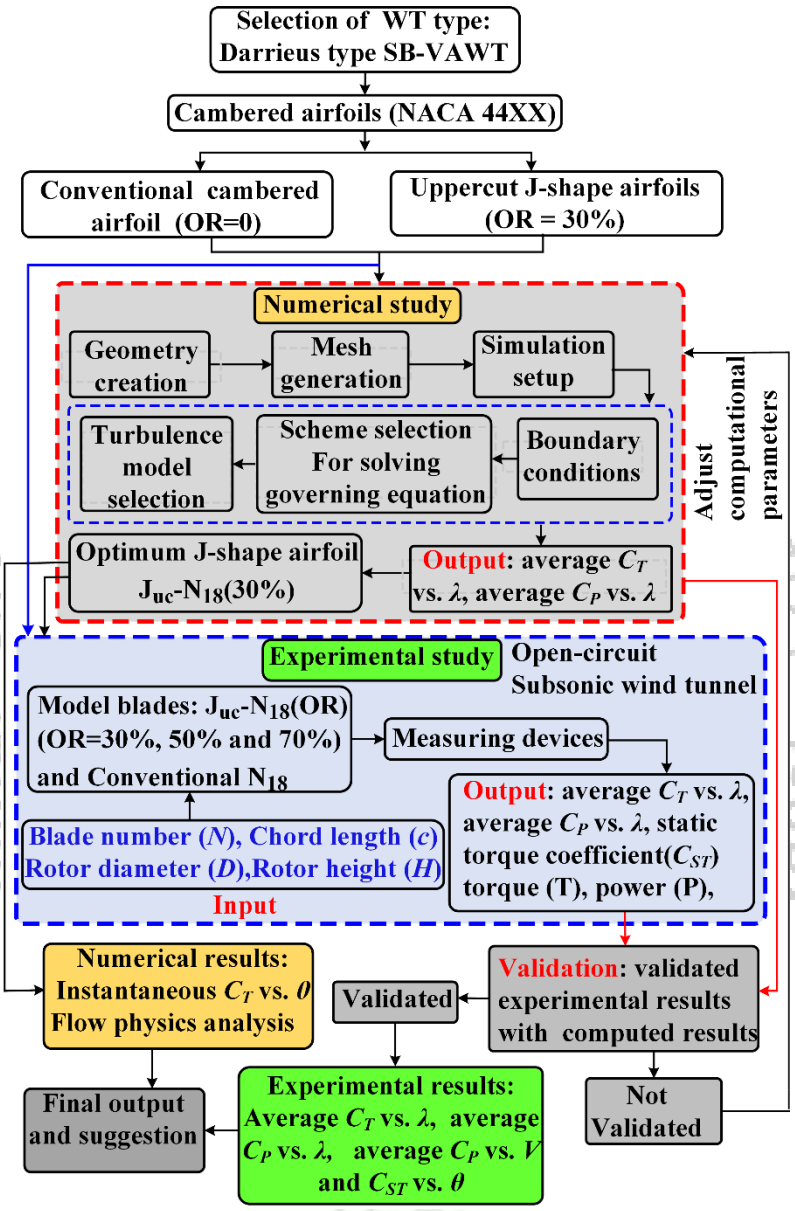

Fig. 6.1. Schematic of methodology flowchart

The J-shaped airfoil structure is formed by removing a part from its upper surface towards the TE of the conventional cambered airfoil, as illustrated in Fig. 6.2 (b, d, f-h, j and l). The aerodynamics of J-shaped airfoil configurations are described in Chapter 1 (Section 1.6). The current work has examined five different conventional cambered airfoils, such as NACA 4412, NACA 4415, NACA 4418, NACA 4421 and NACA 4424 airfoils and their uppercut J-shaped

airfoils (Fig. 6.2). The abbreviations for these airfoils are presented in Table 6.1. These cambered airfoils and their J-shaped airfoils are designated as N_{XX} and J_{YY}-N_{XX} (OR). The "YY" means the uppercut (uc) and the "OR" is the opening ratio. This study does not include the lowercut J-shaped airfoils due to their lower performance than the uppercut J-shaped airfoils (Naik and Sahoo, 2023). The J-shaped airfoil is called uppercut or lowercut when a portion is removed from its upper and lower surfaces, respectively.

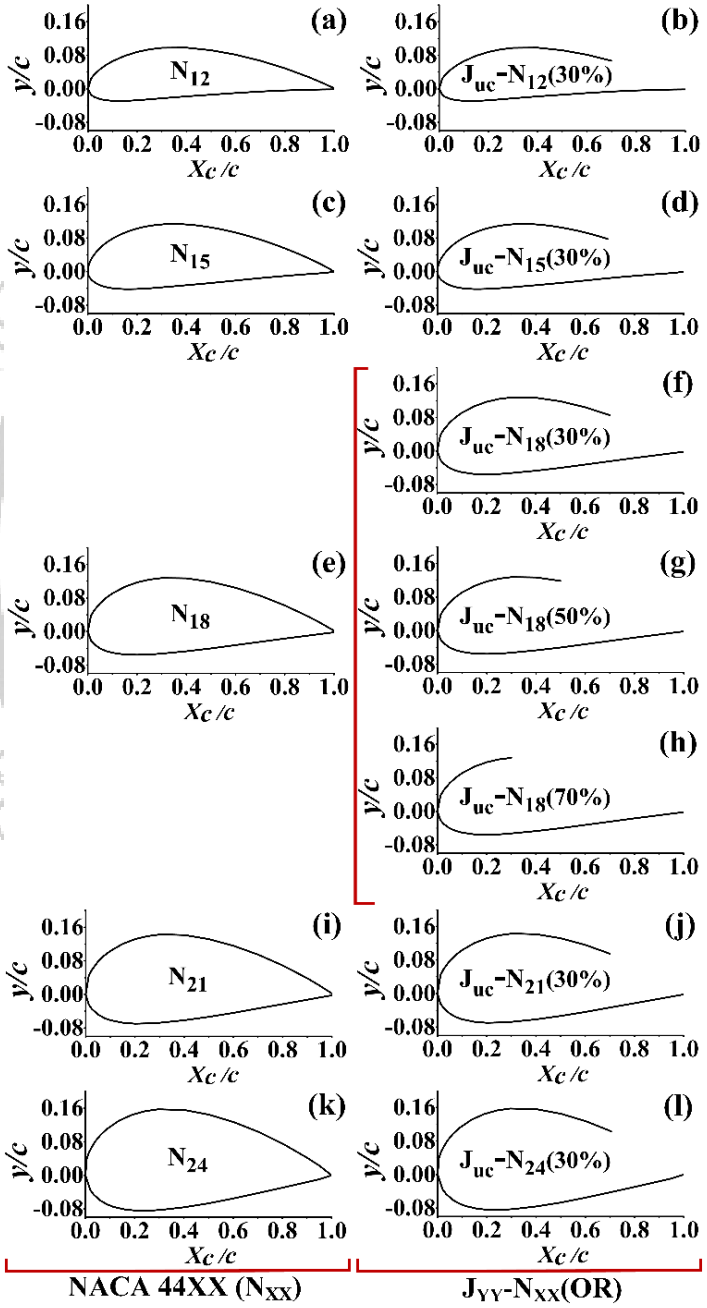

Fig. 6.2. Schematic of different conventional cambered airfoils and their J-shaped airfoils

Table 6.1 Abbreviations for the airfoils

Conventional cambered airfoils name		Uppercut J-shaped airfoil name
NACA 44XX	N_{XX}	J_{YY}-N_{XX} (OR)
NACA 4412	N_{12}	J_{uc}-N_{12} (30%)
NACA 4415	N_{15}	J_{uc}-N_{15} (30%)
NACA 4418	N_{18}	J_{uc}-N_{18} (30%)
NACA 4421	N_{21}	J_{uc}-N_{21} (30%)
NACA 4424	N_{24}	J_{uc}-N_{24} (30%)

6.3. Results and Discussions

6.3.1. Effect of cambered airfoil thicknesses on numerical average C_T and C_P

In this subsection, the impact of the five different cambered airfoil thicknesses is analysed numerically and compared their outcomes with their J-shaped airfoils (OR=30%) at Re=1.71×10^5. Figures 6.3 (a) and (b) display the average C_T (AC_T) and average C_P (AC_P) variation of conventional cambered and their J-shaped airfoils with OR = 30% at different λ values. It is observed that the AC_T and AC_P values of all airfoils increase with an increase in λ values, then rise to a peak value and decrease gradually with any further growth of λ values. The increment in AC_T and AC_P values is mainly because of a rise in the dynamic stall peak and the reduction in those values after the optimum point. This is due to the decrement in the amplitude peak of the dynamic stall (Zamani et al., 2016a). It was found that the Darrieus-type SB-VAWTs perform better when a thicker cambered airfoil with a thickness of 24% c is used in the case of conventional cambered airfoils. That means when the thickness of the cambered airfoil increases from 12% c to 24% c, its AC_T and AC_P values also increase. The better performance is found by the conventional N_{21} and N_{24} airfoils for λ ranges from 0.8 to 1.2, as compared to their J-shaped airfoils (J_{uc}-N_{21} (30%) and J_{uc}-N_{24} (30%)). That means the J_{uc}-N_{21} (30%) and J_{uc}-N_{24} (30%) airfoils are not performing well at most of the λ values. On the other hand, the J_{uc}-N_{12} (30%), J_{uc}-N_{15} (30%) and J_{uc}-N_{18} (30%) airfoils demonstrated superior AC_T and AC_P results as compared to their conventional N_{12}, N_{15} and N_{18} airfoils at the majority of the λ values. Among these three J-shaped airfoils, the J_{uc}-N_{18} (30%) airfoil depicted higher AC_T and AC_P values compared to the other two J-shaped airfoils, as shown in Fig. 6.3.

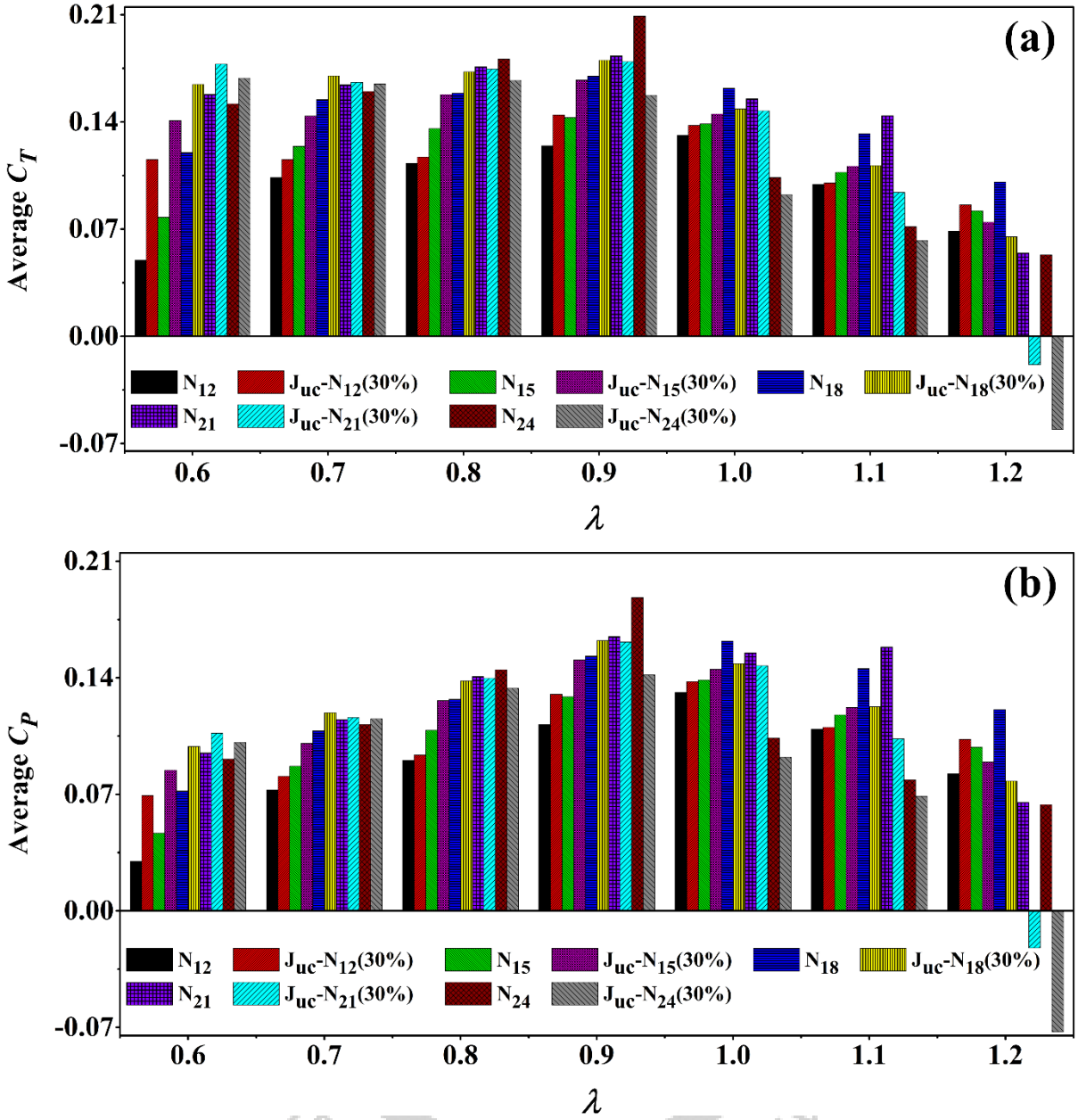

Fig. 6.3. Comparison of airfoil thicknesses: (a) average C_T vs λ and (b) average C_P vs λ

The optimum average C_T ($AC_{T,opt}$) of 0.124, 0.143, 0.169, 0.183 and 0.209 is found at λ = 0.9 by the conventional N_{12}, N_{15}, N_{18}, N_{21} and N_{24} airfoils, respectively. Furthermore, the J_{uc}-N_{12} (30%), J_{uc}-N_{15} (30%), J_{uc}-N_{18} (30%), J_{uc}-N_{21} (30%) and J_{uc}-N_{24} (30%) airfoils obtained an $AC_{T,opt}$ of 0.145, 0.167, 0.180, 0.179 and 0.157, respectively, at λ = 0.9. At the same λ value, an optimum average C_P ($AC_{P,opt}$) of 0.112, 0.129, 0.152, 0.164 and 0.183 is acquired by the conventional N_{12}, N_{15}, N_{18}, N_{21} and N_{24} airfoils, respectively. However, an optimum $AC_{P,opt}$ of 0.130, 0.150, 0.162, 0.161 and 0.141 is procured at λ = 0.9 from the J_{uc}-N_{12} (30%), J_{uc}-N_{15} (30%), J_{uc}-N_{18} (30%), J_{uc}-N_{21} (30%) and J_{uc}-N_{24} (30%) airfoils, respectively. The above comparison showed that the J_{uc}-N_{18} (30%) airfoil displayed a higher $AC_{P,opt}$ value than the other airfoils. Further,

lower performance is found by the J-shaped cambered airfoils with thicknesses of 21% c and 24% c when λ values increased, as demonstrated in Figs. 6.3 (a) and (b). Additionally, these airfoils presented inferior results as compared to their conventional airfoils at large λ values. Based on the above numerical comparison, the J_{uc}-N_{18} (30%) airfoil and its conventional shape (N_{18}) are selected for experimental testing because of their enhanced outcomes compared to the other J-shaped cambered airfoils at all λ values.

6.3.2. Effect of J-shaped airfoil on experimental average C_T and C_P characteristics

The wind tunnel tests are conducted on the conventional cambered airfoil (N_{18}) and its J-shaped airfoils with different ORs (30%, 50% and 70%) to analyse the performance of the Darrieus-type SB-VAWTs. Figure 6.4 displays the performance of the above airfoils in the form of average C_T vs λ and average C_P vs λ at various Re of 1.71×10^5, 1.54×10^5, 1.37×10^5 and 1.19×10^5, respectively. The plots presented in Fig. 6.4 are not addressed with blockage corrections. The uncorrected AC_T and AC_P values are plotted in Fig. 6.4 for each Re. The performance trends of both AC_T and AC_P with respect to λ values are almost similar for all types of airfoils at each Re. As observed from every plot, the conventional N_{18} airfoil shows lower AC_T and AC_P values than J_{uc}-N_{18} (30%) for all four Re. However, it is viewed from Fig. 6.4 that the conventional N_{18} airfoil illustrated a slightly good performance compared to J_{uc}-N_{18} (30%) airfoils at $\lambda > 1.0$ for $Re = 1.54\times10^5$. The J_{uc}-N_{18} (30%) airfoil depicted higher AC_T and AC_P performance at λ ranging from 0.8 - 1.15 and 0.73 - 1.04 at Re of 1.71×10^5 and 1.54×10^5, respectively, compared to the J_{uc}-N_{18} (50%) and J_{uc}-N_{18} (70%) airfoils. Further, its AC_T and AC_P are found to be better for $0.66 \leq \lambda \leq 0.92$ and $0.62 \leq \lambda \leq 0.8$ than the above two J-shaped airfoils at $Re = 1.37\times10^5$ and $Re = 1.19\times10^5$. However, the J_{uc}-N_{18} (50%) and J_{uc}-N_{18} (70%) airfoils show larger AC_T and AC_P characteristics at low λ and optimum λ (λ_{opt}). The outcomes of J_{uc}-N_{18} (50%) and J_{uc}-N_{18} (70%) airfoils exhibit lower AC_T and AC_P performance than N_{18} airfoil within the λ ranges of 1.04 - 1.15, 0.91 - 1.03, 0.75 - 0.92 and 0.69 - 0.8 at Re of 1.71×10^5, 1.54×10^5, 1.37×10^5 and 1.19×10^5, respectively. In these λ ranges, the N_{18} airfoil is more resistant to stall due to high α than the J_{uc} airfoils. The uppercut J-shaped airfoils attain improved aerodynamic performance than the conventional N_{18} airfoil and their $AC_{P,opt}$ values for various Re are presented in Table 6.2. An improvement of 21%, 22% and 25% is achieved in AC_P by the SB-VAWTs with J_{uc}-N_{18} (30%), J_{uc}-N_{18} (50%) and J_{uc}-N_{18} (70%) airfoil, respectively, as compared to the conventional N_{18} airfoil at $Re = 1.71\times10^5$. The $AC_{P,opt}$ increases with the OR of the uppercut J-shaped airfoils.

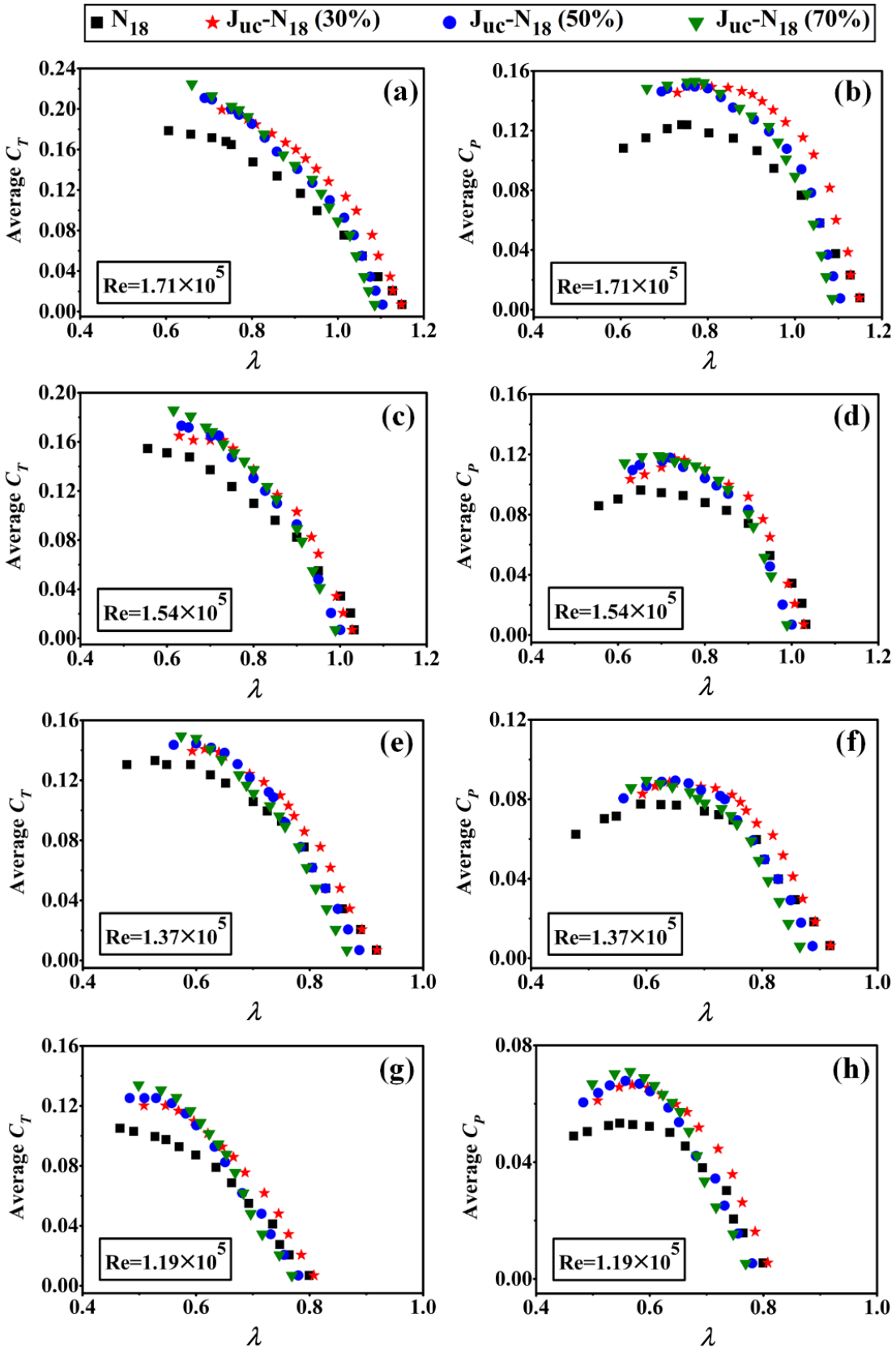

Fig. 6.4. Experimental average C_T and C_P characteristics at different *Re* values: (a, b) *Re* =1.71×10^5, (c, d) *Re* = 1.54×10^5, (e, f) *Re* = 1.37×10^5 and (g, h) *Re* = 1.19×10^5

Table 6.2 Optimum AC_P performance of Darrieus-type SB-VAWTs

Operating conditions		Types of airfoils							
		Conventional N_{18}		J_{uc}-N_{18} (30%)		J_{uc}-N_{18} (50%)		J_{uc}-N_{18} (70%)	
Re	*V* (m/s)	λ_{opt}	$AC_{P,opt}$	λ_{opt}	$AC_{P,opt}$	λ_{opt}	$AC_{P,opt}$	λ_{opt}	$AC_{P,opt}$
1.19×10^5	7	0.55	0.053	0.57	0.066	0.56	0.067	0.57	0.071
1.37×10^5	8	0.59	0.078	0.64	0.088	0.65	0.089	0.60	0.089
1.54×10^5	9	0.65	0.096	0.73	0.117	0.72	0.118	0.69	0.119
1.71×10^5	10	0.74	0.124	0.79	0.150	0.75	0.150	0.77	0.153

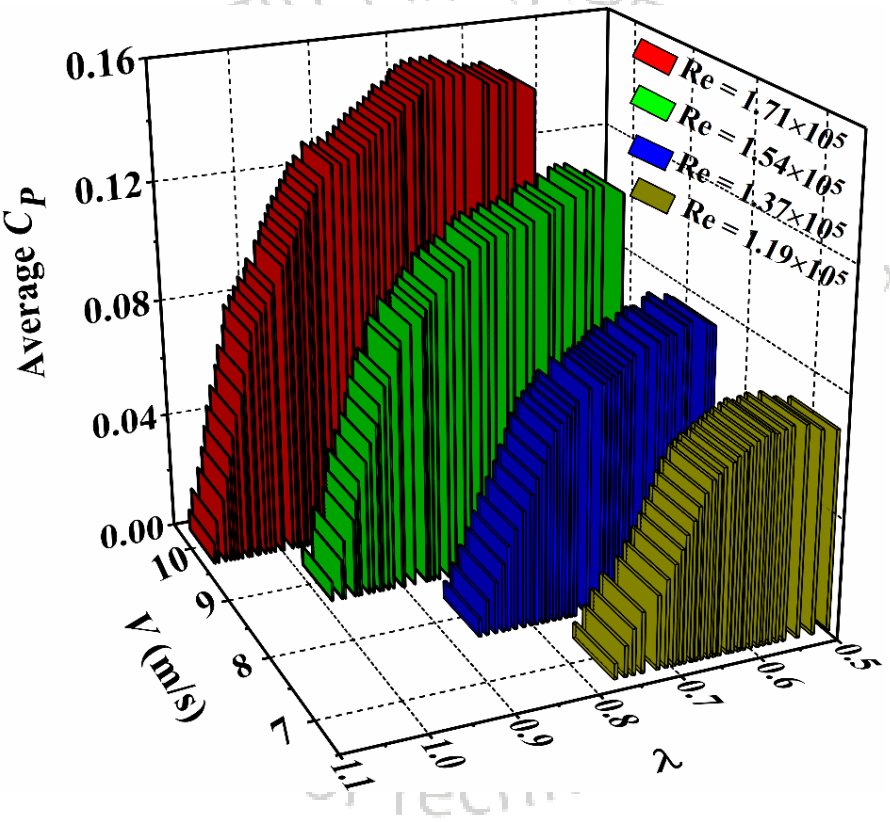

Fig 6.5. Effect of wind velocities on average C_P

The experimental variation of AC_P vs λ for SB-VAWTs with J_{uc}-N_{18} (70%) airfoil at *V* ranging from 7-10 m/s is displayed in Fig. 6.5. As observed, the AC_P increases with growth in *V*. It is worth to notice that $AC_{P,opt}$ for different *V* ranging from 7-10 m/s are generated at an increasing λ values and these values are listed in Table 6.2. The $AC_{P,opt}$ values of J-shaped airfoils are attained at low λ values; thus, these can be used in small-scale SB-VAWTs operating at low λ values.

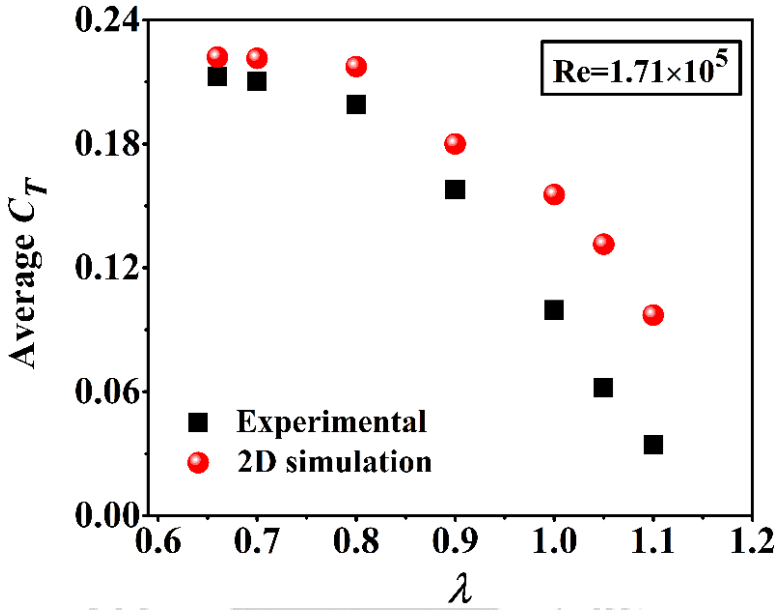

Fig 6.6. Validation of the numerical results with experimental data

The experimental data is also validated with its numerical results and the validation of experimental outcomes for the J_{uc}-N_{18} (70%) airfoil with its numerical simulation is plotted in Fig. 6.6 at *Re* =1.71×10^5. The trend of AC_T for the experiment is found to be almost identical to the numerical 2D simulation. However, the numerical AC_T is overestimated compared to the experimental values. Analogous to this study, the same discrepancies are reported between the experimental and numerical outcomes from previous research (Raciti Castelli et al., 2011a). The differences in these two curves are due to the negligence of the 2D numerical model height. It considers only the aerodynamic forces; hence, its torque does not consider the mechanical losses. Further, the experimental outcomes are less than the numerical results because of 3D wall effects, losses due to structs and blockage effects. The numerical simulations still show almost linear characteristics in AC_T vs λ. The trend between the numerical and experimental data remains unchanged even if the overprediction values exist. Thus, the simulations are employed for the analysis of rotor flow physics and actual performance results are considered from the wind tunnel experimental outcomes.

6.3.3. Effect of J-shaped airfoil on experimental static torque characteristics

The optimal performance for all blades is achieved at a *Re* of 1.71 × 10^5. As a result, experiments on static torque characteristics have been conducted specifically at this *Re*. Figure 6.7 (a) illustrates the static torque characteristics, represented by the static torque coefficient (C_{ST}) and θ, for the N_{18}, J_{uc}-N_{18} (30%), J_{uc}-N_{18} (50%) and J_{uc}-N_{18} (70%) airfoil at a *V* of 10 m/s. The C_{ST} values for each airfoil initially rise and then decline, and this pattern is repeated six times within

a complete revolution of the three-bladed SB-VAWTs. The C_{ST} curve of a three-bladed SB-VAWT displayed six peaks for a whole θ range (0º-360º). According to the theory, the C_{ST} curve within the range of 0º-120º is adequate for describing the C_{ST} curve across the entire θ range (Chen et al., 2016). Therefore, the present work has discussed the comparison of the C_{ST} value for the SB-VAWTs with four different airfoils for the θ value range from 0º-180º. The J-shaped airfoils (J_{uc}-N_{18} (30%), J_{uc}-N_{18} (50%) and J_{uc}-N_{18} (70%)) depicted higher C_{ST} compared to the conventional N_{18} airfoil, which we can observe from Fig. 6.7 (a). This is mainly due to the configuration of J-shaped airfoils, which take advantage of both F_L and F_D and the benefits of J-shaped airfoils are clearly described in Chapter 1 (Section 1.6). The J_{uc}-N_{18} (70%) airfoil displays three peaks in C_{ST} value at θ of 25º, 65º and 145º for the θ range of 0º-180º. Among these three peaks, the highest peak is found at θ = 25º and at this point, a C_{ST} of 0.218 is obtained by the J_{uc}-N_{18} (70%) airfoil. On the other hand, the J_{uc}-N_{18} (30%), J_{uc}-N_{18} (50%) and N_{18} airfoils displayed their highest C_{ST} peak at θ of 5º, 10º and 0º, respectively. These airfoils generated a C_{ST} of 0.123, 0.111 and 0.079 at the same θ values. Based on the aforementioned comparison, the highest C_{ST} value is found for the J_{uc}-N_{18} (70%) airfoil among the other airfoils. The C_{ST} performance of SB-VAWT is not good for the conventional N_{18} airfoil compared to the J-shaped airfoils. The C_{ST} values of SB-VAWTs equipped with a J-shaped airfoil rise when their ORs increase.

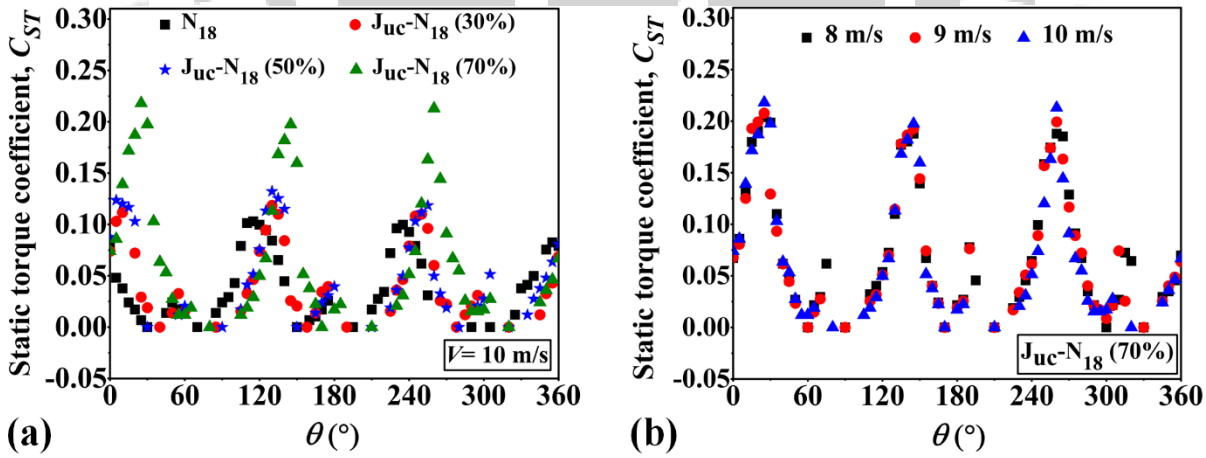

Fig. 6.7. Experimental C_{ST} variation with respect to θ: (a) different airfoils and (b) different velocities

In accordance with both prior research and our experiments, it is anticipated that the C_{ST} will remain unaffected by changes in wind speed (Chen et al., 2012). Figure 6.7 (b) demonstrates the C_{ST} of the J_{uc}- N_{18} (70%) airfoil at three different wind speeds. This figure illustrates that the C_{ST}

curves maintain a similar trend across three distinct wind speeds (Chen et al., 2012). The only difference in C_{ST} values is observed in the θ varied from 80º-100º, 185º-210º and 300º-330º. In addition to this, no significant changes in C_{ST} values are visible for all three wind speeds at other θ values. Three peaks in C_{ST} values are viewed for a three-bladed SB-VAWT within the θ value varied from 0º-180 (Chen et al., 2016, 2016; Feng et al., 2021). The conventional N_{18} airfoil displayed lower C_{ST} values than all J-shaped airfoils. Based on the information presented above, it is viewed that the J-shaped airfoil with a higher OR provides an improved C_{ST}. This augmentation enhances the static torque characteristics of the Darrieus-type SB-VAWTs.

6.3.4. Effect of J-shaped blades on numerical IC_T

The instantaneous C_T (IC_T) variation of Darrieus-type SB-VAWTs with uppercut J-shaped and conventional blades at $\lambda = 0.8$ for one complete rotation of the rotor is illustrated in Fig. 6.8. The above plots display the IC_T variation of blade 1, blade 2, blade 3 and all blades for the SB-VAWTs. The numerical variation of IC_T is examined particularly at $Re = 1.71\times10^5$ as this Re procured the optimum performance. It is observed that blade1, blade 2 and blade 3 follow almost similar types of IC_T curve patterns. The SB-VAWTs with J-shaped blades displayed higher IC_T values than the conventional N_{18} blades. Furthermore, the J_{uc}-N_{18} (70%) blade generated greater IC_T values than the other two J-shaped blades, as shown in Fig. 6.8 (d). The IC_T values of SB-VAWTs are enhanced when the ORs of the J-shaped blades increase, which we can clearly observe from Fig. 6.8 (b)-(d) in both the upwind region ($0^\circ \leq \theta \leq 180^\circ$) and downwind region ($180^\circ < \theta \leq 360^\circ$).

The SB-VAWTs with J-shaped blades displayed IC_T peaks at θ of 79°, 319° and 199° for blade1, blade 2 and blade 3, respectively, whereas the conventional SB-VAWT with N_{18} blade showed these peaks for blade1, blade 2 and blade 3 at θ of 67°, 307° and 187°. Further, the IC_T peaks for all blades of J-shape SB-VAWTs are found at θ of 79°, 193° and 313°, while these peaks of the conventional SB-VAWT are obtained at θ of 67°, 181° and 307° for all blades. The primary reason behind the larger positive IC_T values for the SB-VAWTs with J-shaped blades is the increased torque production due to the structure of J-shaped blades. More importantly, most of the IC_T values are higher for the J-shaped SB-VAWTs than the conventional SB-VAWTs, demonstrating their more remarkable performance in overall torque. Thus, the starting torque of SB-VAWTs is enhanced due to the J-shaped straight blades.

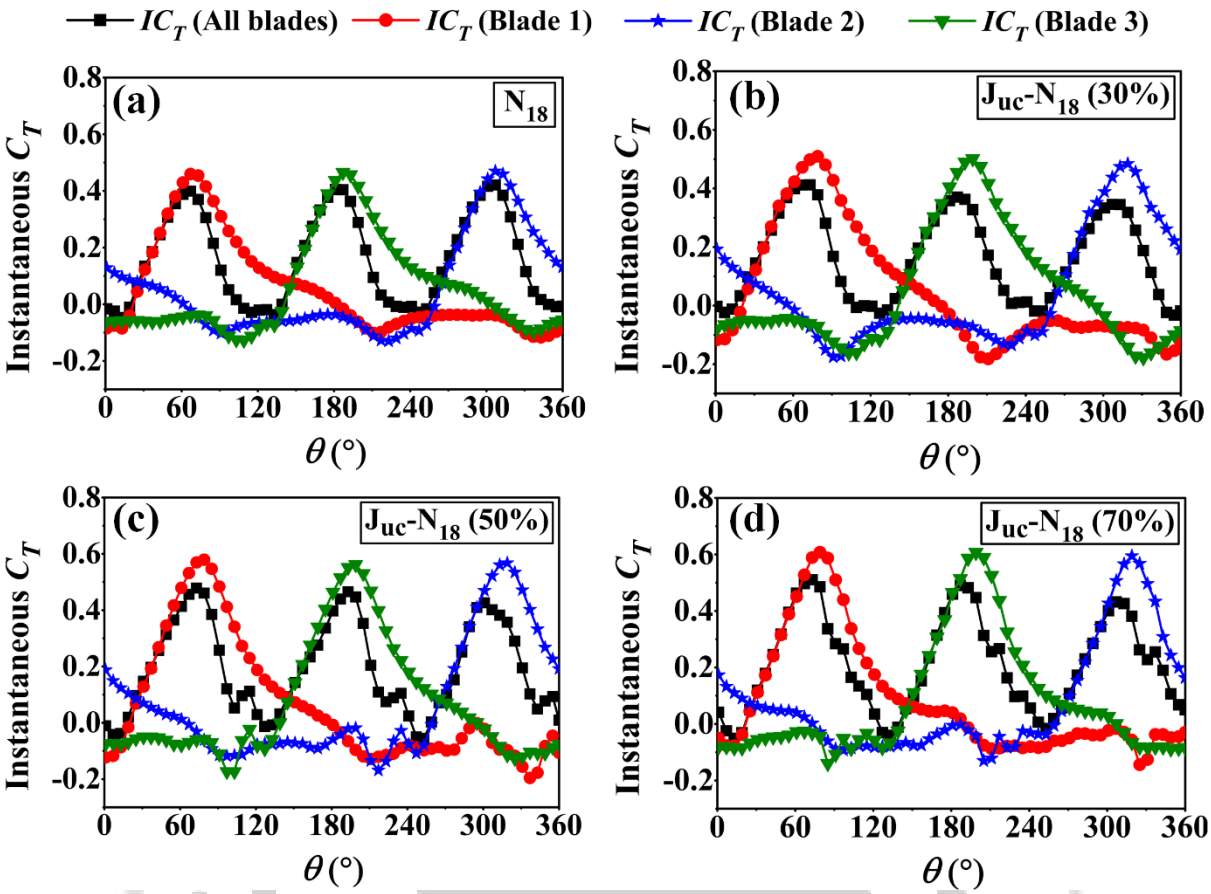

Fig. 6.8. Numerical IC_T variation with respect to θ at Re =1.71×10^5

6.3.5. Instantaneous flow behaviour around the Darrieus-type SB-VAWTs with J-shaped blades

The flow dynamics around the Darrieus-type SB-VAWTs with J-shaped and conventional blades are presented in Figs. 6.9 and 6.10. In this analysis, the instantaneous flow behaviour of the J-shaped SB-VAWTs is examined with three different J-shaped airfoils, such as J_{uc}-N_{18} (30%), J_{uc}-N_{18} (50%) and J_{uc}-N_{18} (70%). Their results are compared with the SB-VAWT with a conventional N_{18} airfoil. In order to understand the behaviour of the J-shaped profile, it is significant to examine the flow field physics around its SB-VAWTs. Figure 6.9 illustrates the comparison of velocity magnitude with superimposed streamlines surrounding the SB-VAWTs for a complete revolution after a steady state is reached. On the other hand, Fig. 6.10 depicts the vorticity magnitude around the SB-VAWTs for one revolution succeeding a steady state. These plots are shown for six different rotational angles at a phase difference of 60º at λ = 0.8. From these contour plots, three different flow regions are recognizable around the SB-VAWTs, such as (1) a high-pressure region on the LS of the airfoil, (2) a low-pressure region on the US of the airfoil and (3) a wake region towards the downstream of the SB-VAWTs.

In the upstream region ($0^{\circ} \leq \theta \leq 180^{\circ}$), the recirculation zone (or vortex) shape and separation length are reduced on the LS of the J_{uc}-N_{18} (30%), J_{uc}-N_{18} (50%) and J_{uc}-N_{18} (70%) airfoil located at θ = 0º, 120º and 240º as compared to the conventional N_{18} airfoil (Fig. 6.9). Further, the recirculation zone generated on the J-shaped airfoils is smaller as compared to the conventional N_{18} airfoil in the downstream region ($180^{\circ} < \theta \leq 360^{\circ}$) as observed from θ = 60º, 180º and 300º. The downstream flow produces more vortices in the conventional case; thus, the flow behind the conventional SB-VAWTs remains more chaotic. Accordingly, a greater amount of power is lost to the flow and less is procured from the SB-VAWTs with conventional blades. The streamlined pattern clearly illustrates that the pressure and velocity distribution on both LS and US and are affected by the conventional N_{18} airfoil. The fully attached flow is observed on the LS of the J-shaped airfoils, which forms a pressure and low velocity region. In the case of J-shaped SB-VAWTs, the pressure difference across the LS and US airfoils is larger, generating more drag. The majority of drag is used for energy conversion and the start-up torque of the SB-VAWTs can be enhanced because of this drag. Additionally, more positive torque is developed by the J-shaped airfoils due to the higher lift as compared to the conventional N_{18} airfoil. The performance of the SB-VAWTs with J_{uc}-N_{18} (70%) airfoil is better among the other two J-shaped airfoils as a result of a larger pressure difference.

Looking at Fig. 6.10, we can observe that vortices are produced at θ = 0º in the upstream of the flow and maximum vortices are obtained at θ = 60º. When θ = 180º, these vortices start to separate from the blade surface and completely separate at θ = 270º from the blade surface. The generated vortices are more in the downstream region than the upstream, where the blades are closer to stall. The extracted power is more in the upstream region as blades are faced with the incoming flow and produce more kinetic energy from the wind energy. In the downstream region, less power is developed because of low wind speed and increased α of blades. It is noticed that more shed vortices are convected to the downstream area because of their low-pressure cores. However, the large shape of vortex structures is seen in the upstream area and shifted to the downstream area at a speed equal to the speed of the blade.

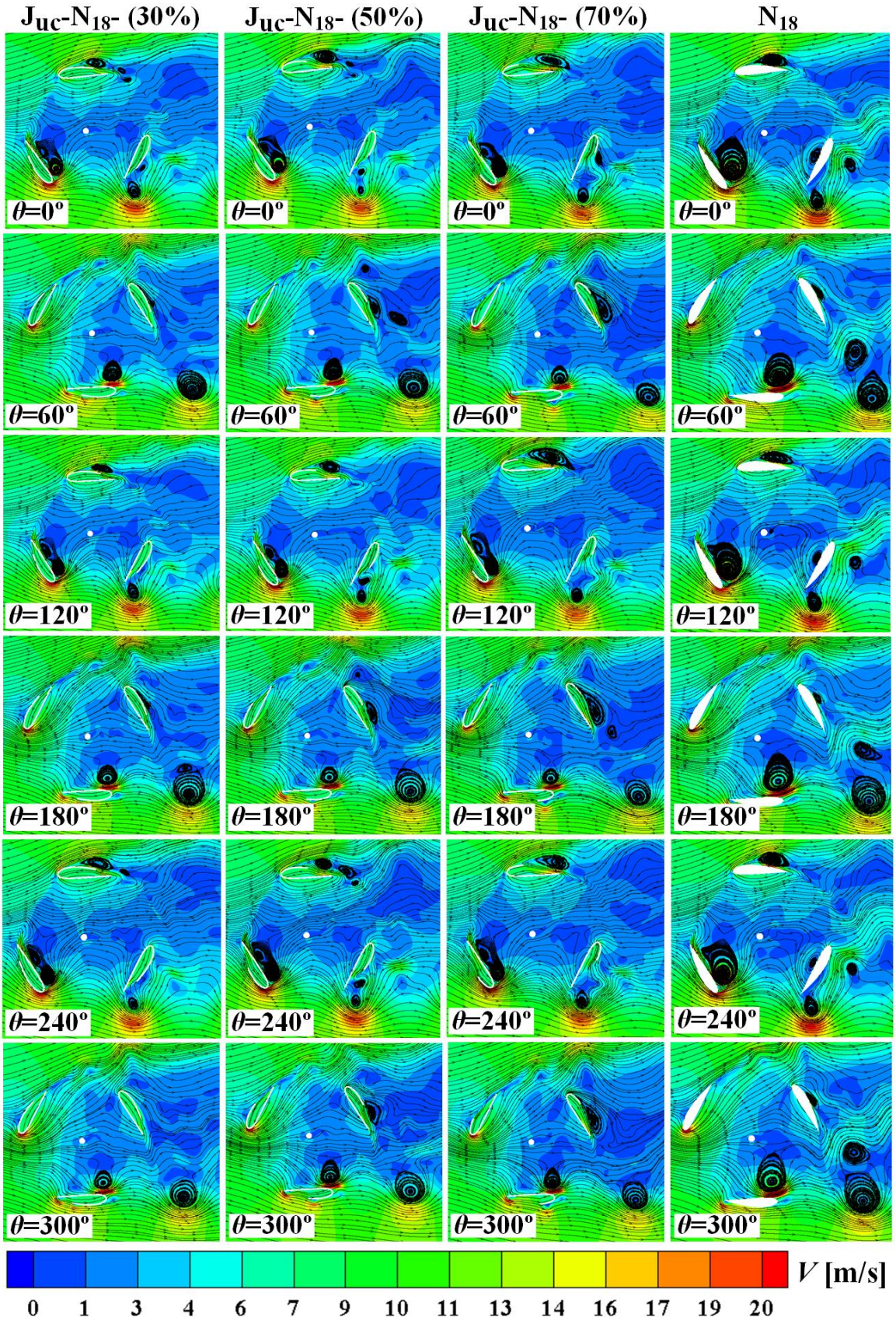

Fig. 6.9. Velocity magnitude comparison with superimposed streamlines for J-shaped and conventional blades at λ = 0.8

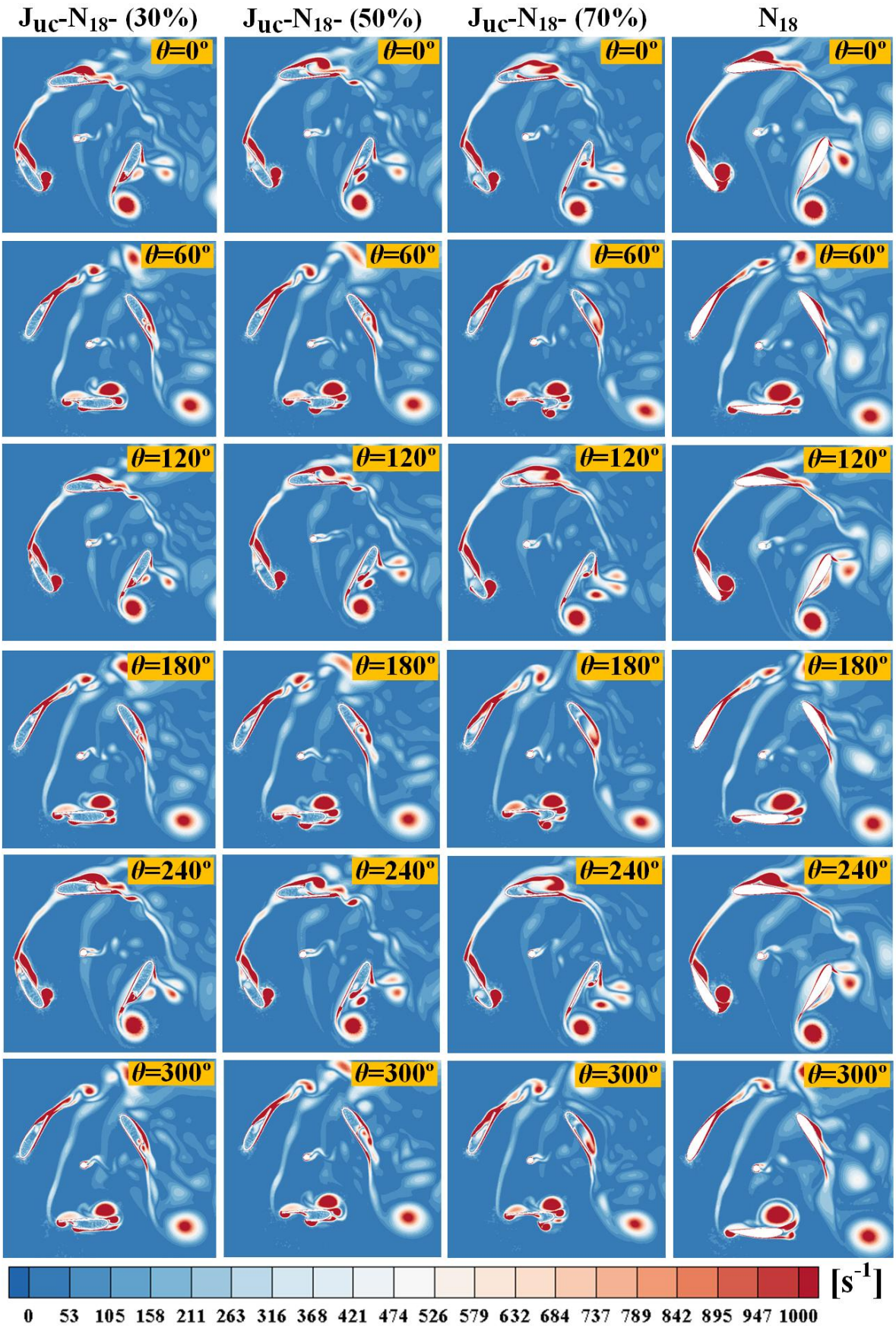

Fig. 6.10. Vorticity contour comparison for J-shaped and conventional blades at λ = 0.8

More importantly, a very less number of separated vortexes with small sizes are generated by the J_{uc}-N_{18} (30%), J_{uc}-N_{18} (50%) and J_{uc}-N_{18} (70%) airfoils, as viewed from Fig. 6.10, than the conventional N_{18} airfoils at θ = 0º, 60º, 120º, 180º, 240º, 300º. Therefore, the flow surrounding the SB-VAWTs becomes more stable, which lowers the vibrations generated from the various parts of the SB-VAWTs. The J-shaped airfoil dissipates these smaller vortices at a faster rate towards the wake area of SB-VAWTs on the downstream side. Most vortices can be trapped by the J-shaped blades, transferred with a revolutionary speed of blades to the downstream area, and then eventually released. This phenomenon can't happen in the case of conventional blades with N_{18} airfoils due to the lack of a geometrical blade shape for the support. As per the blade motion and wind direction, vorticities are developed upstream of the conventional blade and probably another region and instantly released because they are generated and spread inside the turbine downstream.

6.3.6. Comparison of average C_T and instantaneous C_T with existing literatures

The present experimental test results are compared with the experimental findings of Scungio et al. (2016) for the same velocity (V) value and λ range, as presented in Fig. 6.11 (a). Scungio et al. (2016) have adopted auxiliary airfoils in Darrieus-style VAWT to improve the aerodynamic performance and self-starting capability at lower wind speeds. It can be observed from Fig. 6.11 (a) that present experimental plots (N_{18} and J_{uc}-N_{18} (70%) airfoils) follow the almost similar type of average C_T (AC_T) trend with previous data. However, the present AC_T of Darrieus-type SB-VAWT with J_{uc}-N_{18} (70%) airfoil is higher at lower λ than the Darrieus-style VAWT with auxiliary airfoils. For this reason, the self-starting ability of SB-VAWT increases with J_{uc}-N_{18} (70%) airfoil at low λ than the auxiliary airfoils. It is to be noted that the operating range of λ values for VAWT with auxiliary airfoils are different from present research and this is mainly due to the different Ω, α, R of VAWT and cross-sectional area of wind tunnel.

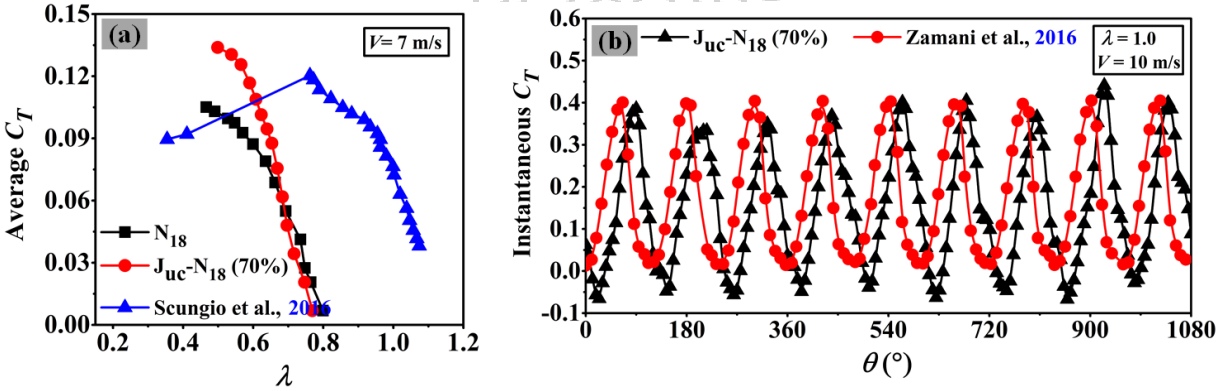

Fig. 6.11. (a) Comparison of average C_T vs λ and (b) comparison of instantaneous C_T vs θ

Furthermore, the present two-dimensional (2D) numerical simulation outcomes are also compared with the three-dimensional 3D numerical results of Zamani et al. (2016), as shown in Fig. 6.11 (b). This comparison is based on same λ, V and θ ranges. The current work created the J-shaped airfoil from an unsymmetrical NACA 4418 airfoil, whereas Zamani et al. (2016) made this design from a symmetrical NACA 0015 airfoil. They investigated a three-bladed Darrieus VAWT with a diameter of 2.5m, a chord length of 0.4m and a height of 3m. However, these dimensions are higher than those used in the current research. The present work employed a SB-VAWT with a diameter of 0.25m, a chord length of 0.1m and a height of 0.25m. The instantaneous C_T (IC_T) values for both J-shaped designs are calculated along with the above respective dimensions and presented their results in Fig. 6.11 (b). This comparison shows that both IC_T curves follow identical patterns even with different turbine dimensions. Therefore, the Darrieus-type SB-VAWT benefit from the present J-shaped (J_{uc}-N_{18} (70%) airfoil) design at low λ values due to the better IC_T values.

6.4. Summary

In this work, numerical and experimental investigations of small-scale Darrieus-type SB-VAWTs have been carried out with uppercut J-shaped airfoils at lower Reynolds numbers (*Re*) and lower tip speed ratios (λ). At first numerical simulations are conducted on SB-VAWTs with five different cambered NACA 44XX airfoils and their corresponding J-shaped airfoils with OR=30%. The main aim of this numerical comparison is to find the optimum airfoils for the SB-VAWTs. In accordance with this, wind tunnel tests are performed on Darrieus-type SB-VAWTs using optimum J-shaped blades with ORs of 30%, 50% and 70% for different *Re* and velocity (V). The J_{uc}-N_{18} (30%) airfoil demonstrated superior numerical average torque coefficient (AC_T) and average power coefficient (AC_P) performance at lower λ than the other uppercut J-shaped airfoils. The experimental tests disclosed that the J_{uc}-N_{18} (30%), J_{uc}-N_{18} (50%) and J_{uc}-N_{18} (70%) airfoil raises the aerodynamic performance of SB-VAWTs at each *Re*. The conventional N_{18} airfoil presented poor results compared to the uppercut J-shaped airfoils. An enhancement of 21%, 22% and 25% is found in AC_P at $Re = 1.71\times10^5$ by the J_{uc}-N_{18} (30%), J_{uc}-N_{18} (50%) and J_{uc}-N_{18} (70%) airfoils, respectively as compared to the conventional N_{18} airfoil. The J-shaped airfoils enhance the self-starting ability of SB-VAWTs compared to the conventional N_{18} airfoil. The optimum AC_P ($AC_{P,opt}$) values of the SB-VAWTs with J_{uc}-N_{18} (70%) airfoils increase with V. The J-shaped airfoils presented notably superior static torque characteristics than conventional cambered blades.

CHAPTER 7

Effect of J-shaped Blade Numbers on the Performance and Starting Characteristics of the Small-Scale Darrieus-type SB-VAWTs for Low Wind Regimes

Chapter Layout

Overview

This chapter described the effect of J-shaped blade numbers on the small-scale Darrieu-type SB-VAWTs for low wind regimes. Small-scale Darrieus-type SB-VAWTs have recently been proven to be a relevant field of research in the wind energy community. In urban environments, the selection of blade number along with the blade configuration plays a vital role in designing the SB-VAWTs for low wind regimes. The present work is carried out to study the effect of J-shaped blade numbers (i.e. 2,3 and 4) on the aerodynamic performance and starting characteristics of small-scale Darrieus-type SB-VAWTs. The J-shaped blade numbers with opening ratios (ORs) of 30%, 50% and 70% are experimented in a wind tunnel to determine the overall performance of SB-VAWTs at lower tip speed ratios ranging between 0.4 to 1.5. Also, numerical simulations have been performed to understand the aerodynamic behaviour of the SB-VAWTs. A validation is presented between the numerical and experimental results for each blade number. Finally, a thorough comparison is presented between the conventional and J-shaped airfoils.

7.1. Introduction

The primary focus of this study is to examine how the J-shaped blade number and solidity influence the aerodynamic performance and self-starting ability of small-scale Darrieus-type SB-VAWTs. In order to accomplish this, a series of experimental and numerical investigations has been conducted on Darrieus-type SB-VAWTs with 2, 3, and 4 blades, both with J-shaped and conventional blade designs, specifically at low λ values. The experimental methodology is described in Chapter 4 and the numerical methodology is discussed in Chapter 3 (Section 3.2). A brief literature survey based on blade numbers (Section 2.6), their self-starting ability (Section 2.7) and various blade profiles (Section 2.1) is described in Chapter 2. Three different types of J-shaped blades with ORs of 30%, 50%, and 70% are tested in this work for each blade number (N_b), and their outcomes are compared with those of the conventional blade with zero OR. Consequently, this study investigates the impacts of N_b on various parameter variations, including θ, λ, σ and Reynolds number (Re). Additionally, this paper identifies the parameter combinations that yield optimal performance based on different performance criteria. This approach holds significant importance in the context of designing and optimizing blades of small-scale Darrieus-type SB-VAWTs for low wind regimes. Furthermore, the Darrieus-type SB-VAWTs with J-shaped blades fall under the small-scale VAWTs. Such SB-VAWTs are installed as an off-grid renewable power source for small wind farms, multirotor configuration and offshore VAWT applications. Figure 7.1 illustrates the methodological process employed in this investigation.

7.2. Design and aerodynamics of J-shaped blades

The J-shaped blade profile is made from the conventional cambered NACA 4418 blade profile by removing some parts either from its upper surface (US) or lower surface (LS) near the trailing edge (TE). (Naik and Sahoo, 2024). The cambered NACA 4418 blade profile has been chosen for the creation of the J-shaped blade because it has the ability to enhance the C_P and starting torque, particularly in the low to medium λ range (B. K. Kirke and Lazauskas, 1991). This is due to the larger lift-drag ratios and more preferable stall behaviour (Sengupta et al., 2019). In the present work, uppercut J-shaped blade profiles are selected for experimental and numerical investigations due to their higher performance than the lowercut (Naik and Sahoo, 2023). The conventional camber NACA 4418 blade profiles and their uppercut J-shaped blade profiles with three different opening ratios (such as 30%, 50% and 70%) are examined in the current study, as depicted in Fig. 7.2 (a-d). The NACA 4418 airfoil is named $N_{18,}$ while the J-shaped airfoils

are designated as J_{uc}-N_{18} (OR). The "uc" is the uppercut and "OR" means the opening ratio in percentage. The OR is the ratio of opening size (X_c) to chord length (c). The J-shaped blade structure is a lift plus drag-based design because it operates by combining the blade functions of Giromill-type (lift-based) and Savonius-type (drag-based) models. The J-shaped three-dimensional (3D) models formed of 2, 3 and 4 blades are shown in Fig. 7.3 (a-c), which is the central point of interest in the current investigation. In Chapter 1 (Section 1.6), the aerodynamics of the J-shaped blades are discussed elaborately.

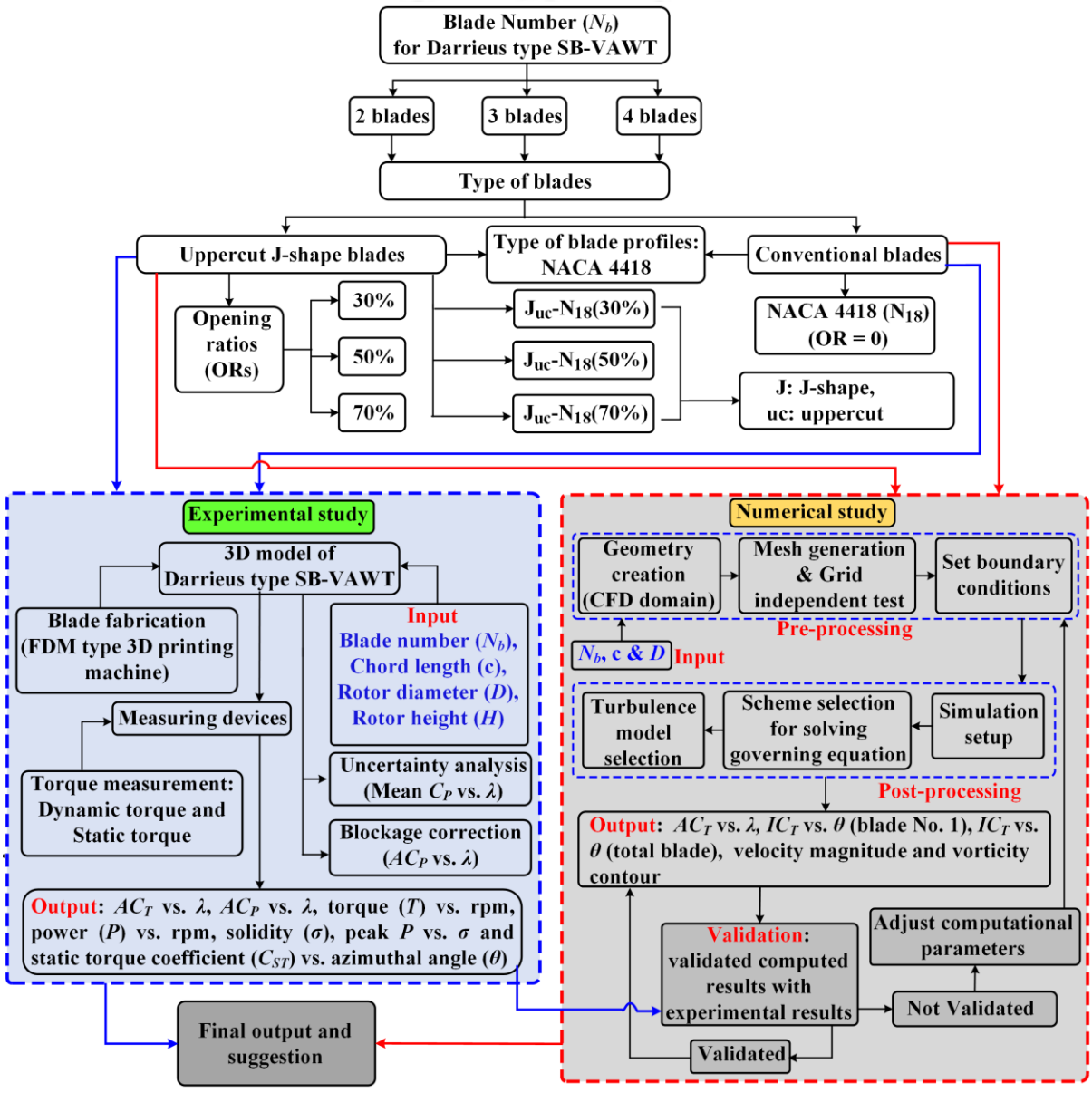

Fig. 7.1. Diagram illustrating the flow of the methodology

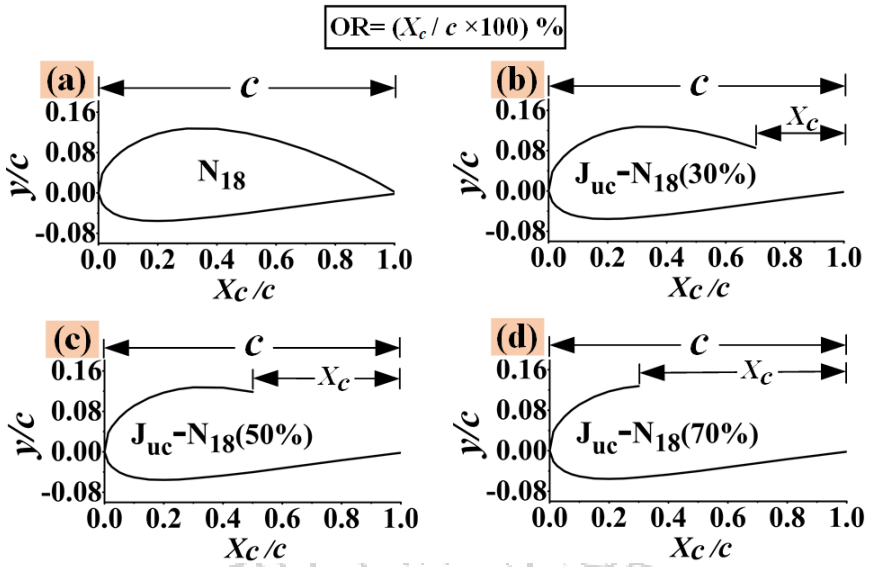

Fig. 7.2. (a) Conventional camber N_{18} blade profile, (b) J_{uc}-N_{18} (30%) blade profile, (c) J_{uc}-N_{18} (50%) blade profile and (e) J_{uc}-N_{18} (70%) blade profile

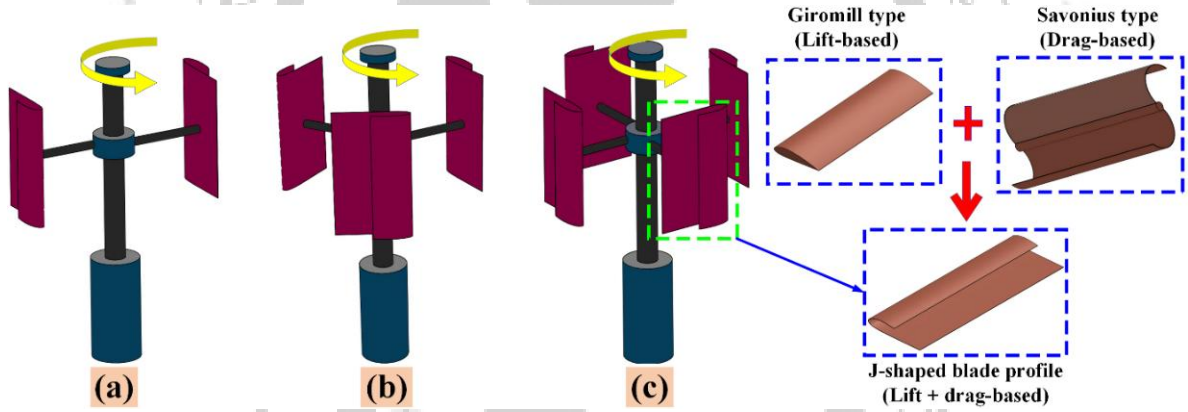

Fig. 7.3. Three-dimensional modelling of the J-shaped model (a) Two-bladed J-shaped rotor, (b) Three-bladed J-shaped rotor and (c) Four-bladed J-shaped rotor

7.3. Results and discussions

7.3.1. Effect of J-shaped blade numbers on experimental AC_T and AC_P performance

The experimental tests are performed on Darrieus-type SB-VAWTs with different J-shaped blades (2, 3 and 4) within a wind tunnel to examine the effect of N_b on AC_T and AC_P performance. This analysis used three different types of J-shaped blades (J_{uc}-N_{18} (30%), J_{uc}-N_{18} (50%) and J_{uc}-N_{18} (70%)) and a single conventional blade (N_{18}).

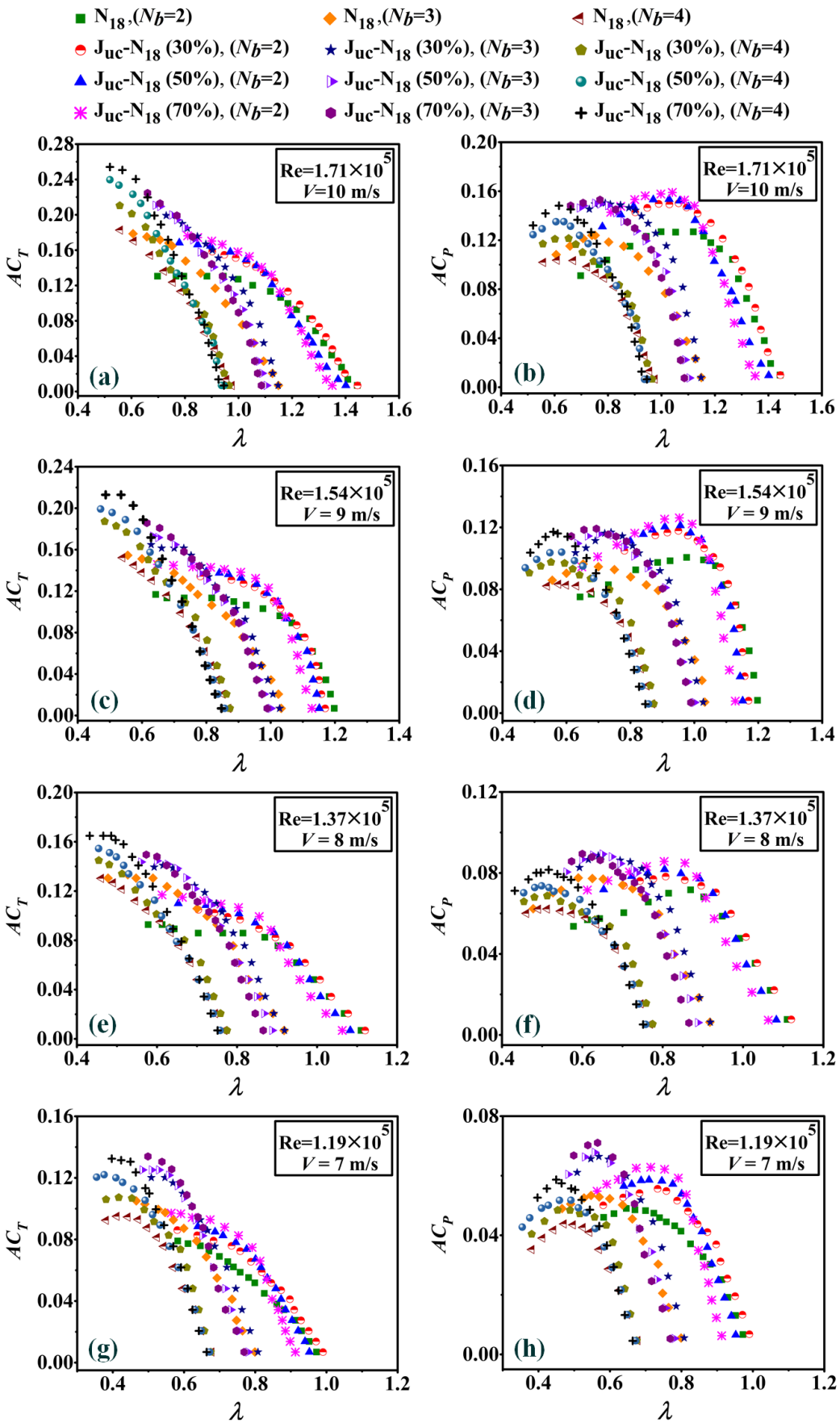

Fig. 7.4. Experimental AC_T and AC_P variation based on the N_b at different V: (a-b) V=10 m/s, (c-d) V=9 m/s, (e-f) V=8m/s and (g-h) V=7 m/s

The experimental AC_T and AC_P variation based on the N_b are presented in Fig. 7.4 by means of AC_T vs λ and AC_P vs λ at different V and Re. In these plots, the blockage corrections are not included and theses plots are depicted the uncorrected AC_T and AC_P values. Figure 7.4 (a, c, e and g) displayed the variation of AC_T with respect to λ at four different V (10 m/s, 9 m/s, 8 m/s and 7 m/s) and Re (1.71×10^5, 1.54×10^5, 1.37×10^5 and 1.19×10^5). At each V and Re, the AC_T performance curves with λ values follow almost identical trends for every N_b. At λ values ranging from 0.81 to 1.12, the 2-bladed J_{uc}-N_{18} (70%) depicted higher AC_T performance at V =10 m/s than the other 2-bladed models. Further, the 2-bladed J_{uc}-N_{18} (30%) displayed higher AC_T values for $1.13 < \lambda < 1.45$ compared to the rest of the 2-bladed SB-VAWTs. For the $1.22 < \lambda < 1.45$, the 2-bladed N_{18} presented higher AC_T performance than the 2-bladed J-shaped SB-VAWTs with 50% and 70% ORs. In these λ ranges, the AC_T values of 2-bladed J_{uc}-N_{18} (50%) are greater compared to 2-bladed J_{uc}-N_{18} (70%). Furthermore, the 3-bladed J_{uc}-N_{18} (70%) illustrated higher AC_T performance for $0.66 < \lambda < 0.8$ than the other 3-bladed SB-VAWTs. The AC_T performance of 3-bladed J_{uc}-N_{18} (30%) is better for $0.82 < \lambda < 1.15$ when compared to its outcomes to the 3-bladed J_{uc}-N_{18} (50%), J_{uc}-N_{18} (70%) and conventional N_{18}. All 3-bladed J-shaped SB-VAWTs show superior AC_T values for λ ranging from 0.66 to 1.03 than the 3-bladed conventional N_{18}. While the 3-bladed conventional N_{18} displayed higher AC_T values than the 3-bladed J_{uc}-N_{18} (50%) and J_{uc}-N_{18} (70%) when $\lambda > 1.03$. Moreover, a higher AC_T performance is observed by 4-bladed J_{uc}-N_{18} (70%) for $0.52 < \lambda < 0.82$ than other 4-bladed SB-VAWTs. In these λ ranges, the 4-bladed conventional N_{18} displayed lower AC_T values in comparison to all 4-bladed J-shaped SB-VAWTs. Additionally, the 4-bladed J_{uc}-N_{18} (30%) demonstrated lower AC_T values than the 4-bladed J_{uc}-N_{18} (50%) for the same λ ranges ($0.52 < \lambda < 0.82$). However, the 4-bladed J_{uc}-N_{18} (30%) display larger AC_T values at λ ranges between 0.84 and 0.97 as compared to the other 4-bladed SB-VAWTs.

The variations of AC_P with respect to λ are presented in Fig. 7.4 (b, d, f and h) at four different V and Re. The 2-bladed, 3-bladed and 4-bladed J-shaped SB-VAWTs (J_{uc}-N_{18} (30%), J_{uc}-N_{18} (50%) and J_{uc}-N_{18} (70%)) and conventional N_{18} SB-VAWTs demonstrated almost identical AC_P curves pattern for each V and Re. The AC_P values of 2-bladed J_{uc}-N_{18} (70%) at V =10 m/s are higher among the other 2-bladed SB-VAWTs for $0.8 < \lambda < 1.12$. For these λ ranges, the 2-bladed J_{uc}-N_{18} (30%) and J_{uc}-N_{18} (50%) show larger AC_P values than the 2-bladed conventional N_{18}. Moreover, the 2-bladed J_{uc}-N_{18} (30%) at λ ranges between 1.13 and 1.44 depicted better AC_P values than the rest of the 2-bladed SB-VAWTs. Further, the 2-bladed conventional N_{18} presented higher AC_P values compared to the 2-bladed J_{uc}-N_{18} (50%) and J_{uc}-N_{18} (70%) for 1.18

$< \lambda <$ 1.44. When the AC_P performance of the 3-bladed SB-VAWTs is compared for V equal to 10 m/s, it is found that the 3-bladed J-shaped SB-VAWTs displayed higher AC_P values for 0.67 $< \lambda <$ 1.12 than the 3-bladed conventional N_{18} SB-VAWT. The 3-bladed J_{uc}-N_{18} (70%) and J_{uc}-N_{18} (50%) show larger AC_P values for 0.67 $< \lambda <$ 0.77 than the 3-bladed J_{uc}-N_{18} (30%). Moreover, the 3-bladed J_{uc}-N_{18} (30%) display greater AC_P values for 0.81 $< \lambda <$ 1.15 compared to the remaining 3-bladed SB-VAWTs. For the 4-bladed case, higher AC_P values are obtained from 4-bladed J-shaped SB-VAWTs than the 4-bladed conventional N_{18} SB-VAWT for 0.52 $< \lambda <$ 0.89. In those λ ranges, the 4-bladed J_{uc}-N_{18} (70%) depicted higher AC_P values among the other 4-bladed J-shaped SB-VAWTs. Furthermore, larger AC_P values are found by 4-bladed J_{uc}-N_{18} (50%) than the 4-bladed J_{uc}-N_{18} (30%) for λ ranges from 0.52 to 0.8. However, the 4-bladed J_{uc}-N_{18} (30%) illustrated greater AC_P values for 0.84 $< \lambda <$ 0.97 in comparison to other 4-bladed SB-VAWTs.

Table 7.1 Absolute performance of SB-VAWTs with J-shaped and conventional N_b

		Operating conditions (V and Re)							
		10 m/s 1.71×10^5		9 m/s 1.54×10^5		8 m/s 1.37×10^5		7 m/s 1.19×10^5	
Types of blade	N_b	λ_{opt}	$AC_{P,opt}$	λ_{opt}	$AC_{P,opt}$	λ_{opt}	$AC_{P,opt}$	λ_{opt}	$AC_{P,opt}$
Conventional N_{18}	2	1.00	0.127	0.92	0.098	0.81	0.070	0.70	0.048
J_{uc}-N_{18} (30%)		1.03	0.149	0.95	0.118	0.85	0.076	0.73	0.055
J_{uc}-N_{18} (50%)		1.03	0.153	0.95	0.121	0.85	0.079	0.74	0.058
J_{uc}-N_{18} (70%)		1.04	0.159	0.95	0.126	0.86	0.085	0.75	0.063
Conventional N_{18}	3	0.74	0.124	0.65	0.096	0.59	0.078	0.55	0.053
J_{uc}-N_{18} (30%)		0.79	0.150	0.74	0.117	0.64	0.088	0.57	0.066
J_{uc}-N_{18} (50%)		0.75	0.150	0.72	0.118	0.65	0.089	0.56	0.068
J_{uc}-N_{18} (70%)		0.77	0.153	0.69	0.119	0.60	0.089	0.57	0.071
Conventional N_{18}	4	0.60	0.104	0.57	0.083	0.51	0.062	0.47	0.044
J_{uc}-N_{18} (30%)		0.60	0.121	0.59	0.097	0.51	0.069	0.49	0.048
J_{uc}-N_{18} (50%)		0.61	0.135	0.59	0.104	0.52	0.073	0.49	0.052
J_{uc}-N_{18} (70%)		0.62	0.148	0.57	0.117	0.52	0.082	0.45	0.059

Table 7.2 Relative performance of SB-VAWTs with J-shaped and conventional N_b

Types of blades	N_b	Operating conditions (V and Re)							
		10 m/s 1.71×10^5		9 m/s 1.54×10^5		8 m/s 1.37×10^5		7 m/s 1.19×10^5	
		λ_{opt}	$AC_{P,opt}$ (%)	λ_{opt}	$AC_{P,opt}$ (%)	λ_{opt}	$AC_{P,opt}$ (%)	λ_{opt}	$AC_{P,opt}$ (%)
J_{uc}-N_{18} (30%)	2	1.03	17	0.95	20	0.85	9	0.73	15
J_{uc}-N_{18} (50%)		1.03	21	0.95	24	0.85	13	0.74	21
J_{uc}-N_{18} (70%)		1.04	25	0.95	29	0.86	21	0.75	31
J_{uc}-N_{18} (30%)	3	0.79	21	0.74	22	0.64	13	0.57	25
J_{uc}-N_{18} (50%)		0.75	21	0.72	23	0.65	14	0.56	28
J_{uc}-N_{18} (70%)		0.77	23	0.69	24	0.60	14	0.57	34
J_{uc}-N_{18} (30%)	4	0.60	16	0.59	17	0.51	11	0.49	9
J_{uc}-N_{18} (50%)		0.61	30	0.59	25	0.52	18	0.49	18
J_{uc}-N_{18} (70%)		0.62	42	0.57	41	0.52	32	0.45	34

As can be clearly seen from Fig. 7.4 (a, c, e and g), the 4-bladed J-shaped SB-VAWTs presented higher AC_T performance than the 2-bladed and 3-bladed J-shaped SB-VAWTs at each V and Re. The higher AC_T values are developed due to the more N_b, which easily rotated these SB-VAWTs at lower wind speeds (Ghiasi et al., 2022). Hence, these 4-bladed J-shaped SB-VAWTs perform better at lower λ values because of larger torque values. Further, the larger N_b produces better AC_P performance at lower λ values. However, these 4-bladed SB-VAWTs presented lower AC_P values than 2-bladed and 3-bladed SB-VAWTs at higher λ values. Meanwhile, the 3-bladed J-shaped SB-VAWTs show greater AC_T values than the 2-bladed J-shaped SB-VAWTs and lower AC_T values compared to 4-bladed J-shaped SB-VAWTs. More consistent AC_P performance is obtained through the 3-bladed J-shaped SB-VAWTs than the 2-bladed and 4-bladed J-shaped models. It is because of its low vibration and minimal stress (Suriyawong et al., 2021). The 2-bladed J-shaped SB-VAWTs illustrated better AC_T and AC_P performance at higher λ values than the 3-bladed and 4-bladed J-shaped SB-VAWTs at every V and Re. The 2-bladed J-shaped SB-VAWTs rotated faster because of increased flow speed and less N_b. This higher wind speed in 2 blades creates more vibration and noise (Suriyawong et al., 2021) and operates these SB-

VAWTs at the higher λ values. However, the noise in more N_b decreases because of the lower speed of the blades (Suriyawong et al., 2021). For each N_b, the J-shaped SB-VAWTs depicted a superior AC_T and AC_P performance compared to the conventional N_{18}. This is due to the simultaneous effect of F_D and F_L on the J-shaped blade structure (Zamani et al., 2016a, 2016b). Table 7.1 demonstrates the absolute performance of SB-VAWTs with J-shaped and conventional blades for different V and Re at optimum λ (λ_{opt}). It is noticed from Table 7.1 that the J-shaped blades raise the absolute performance ($AC_{P,opt}$) of SB-VAWTs for every N_b case than the conventional N_b. Among all J-shaped N_b, the J_{uc}-N_{18} (70%) displayed the highest $AC_{P,opt}$ for respective N_b cases, while it was noticed to be lowered for the conventional N_b cases. Furthermore, the absolute performance ($AC_{P,opt}$) of J-shaped SB-VAWTs for respective N_b cases increases with the increment of ORs of J-shaped blades.

Table 7.2 presents the relative performance (in %) of SB-VAWTs with J-shaped N_b for different V and Re at λ_{opt}. These values are calculated using $AC_{P,opt}$ values of the conventional N_b. It is noticed that the uppercut J-shaped N_b showed superior relative performance compared to conventional N_b. The highest relative performance of 42% is found by 4-bladed SB-VAWTs with J_{uc}-N_{18} (70%) at 10 m/s among others. At the same V, the 4-bladed J_{uc}-N_{18} (50%) displayed the second-highest relative performance of 30% compared to other N_b cases. Moreover, the 4-bladed J_{uc}-N_{18} (30%) enhanced $AC_{P,opt}$ performance to 16% at the same V than the 4-bladed conventional N_b. The 2-bladed J_{uc}-N_{18} (30%), J_{uc}-N_{18} (50%) and J_{uc}-N_{18} (70%) illustrated an improved $AC_{P,opt}$ performance of 17%, 21% and 25%, respectively, as compared to the 2-bladed conventional N_b at 10 m/s. While, an improvement of 21%, 21% and 23% is obtained in the performance of 3-bladed SB-VAWTs at 10 m/s through J_{uc}-N_{18} (30%), J_{uc}-N_{18} (50%) and J_{uc}-N_{18} (70%) blades, respectively, than the 3-bladed conventional N_b. In comparison to the conventional N_{18} blades, a similar type of improvement is also found in 2, 3 and 4-bladed SB-VAWTs through J-shaped blades at the rest of the V (9 m/s, 8 m/s and 7 m/s). The $AC_{P,opt}$ values decrease with an increase in N_b values; thus, the performance curves shift towards the lower λ values, as illustrated in Fig. 7.4. Also, it is observed that the operating range of λ_{opt} values decreases when the N_b of SB-VAWTs increases. The performance of both J-shaped and conventional SB-VAWTs with 2, 3 and 4 blades increases if their V and Re increase.

7.3.2. Effect of solidity on performance

Solidity (σ) is one of the significant non-dimensional parameters that combines N_b, c and R and is useful for comparing the performance of Darrieus-type SB-VAWTs with various N_b. This

study determined σ values by changing the N_b. The σ values for 2, 3 and 4-bladed SB-VAWTs are 0.8, 1.2 and 1.6, respectively. Figure 7.5 presents the σ impact of 2, 3 and 4-bladed SB-VAWTs models with conventional (N_{18}) and J-shaped blades (J_{uc}-N_{18} (30%), J_{uc}-N_{18} (50%) and J_{uc}-N_{18} (70%)) at 10 m/s. Further, these curves also discussed the effect of T with respect to the rotational velocity (rpm) of different σ by changing N_b values. At lower rotational velocity, 4-bladed SB-VAWTs depicted higher T because of the higher σ design. After that, 3-bladed SB-VAWTs produced more T at the same rotational velocity. Further, the production of T is less by the 2-bladed SB-VAWTs at lower rotational velocity due to the lower σ and N_b. However, their T generation is better than that of 4-bladed and 3-bladed SB-VAWTs at larger rotational velocities. However, the T of the 2-bladed SB-VAWTs decreases at a lower rate if the rotational speed rises as compared to the 3-bladed and 4-bladed SB-VAWTs, as illustrated in Fig. 7.5. The T of the 3-bladed SB-VAWTs reduces at a slower rate as the rotational speed increases than the 4-bladed SB-VAWTs. This happens because less N_b impeding the other, a lower number of spokes and a less severe wake effect on blades downstream (Edwards et al., 2008). All three SB-VAWTs with different σ values show optimum T (T_{opt}) at different rotational velocities. It is observed that the SB-VAWTs with J-shaped blades displayed higher T than the conventional N_{18} blades for each σ and N_b. Further, the J_{uc}-N_{18} (70%) blades (Fig. 7.5 (d)) demonstrated higher T values for every σ design among other blades. After this, larger T values are obtained by the J_{uc}-N_{18} (50%) blades (Fig. 7.5 (c)) than the J_{uc}-N_{18} (30%) blades (Fig. 7.5 (b)).

Figure 7.6 demonstrates the power (P) variation with rotational velocity of J-shaped and conventional blades at 10 m/s for various σ values. The P is the multiplication of T and rotational velocity. For a given c and R, an increment in N_b leads to a dramatic growth in the σ, which shifts the P curves towards the lower rotational velocity. The SB-VAWTs with larger σ present better performance at the low λ region than those with a lower σ. Further, the P production is larger at the higher λ when SB-VAWTs have lower σ values. The 4-bladed SB-VAWTs developed lower P than 2-bladed and 3-bladed SB-VAWTs. Incorporating more N_b develops more blockage and reduces the entrance velocity of the blade (Wang and Chen, 2008). Moreover, it increases the wake and lowers the rotational velocity (Wang and Chen, 2008). Ultimately, the P generation is degraded in SB-VAWTs with higher σ values. This is mainly due to the increase in drag induced by the resistance to wind flow (Suriyawong et al., 2021). Hence, it appears to be better to lower the N_b in order to improve the efficiency of SB-VAWTs. The 2-bladed SB-VAWTs produced greater P than the 3-bladed and 4-bladed SB-VAWTs at higher rotational velocity. It is all because of their higher T and lower blockage between the

inter-blades (Sun et al., 2022). Moreover, the reduction in σ (with 1 or 2 blades) will decrease the F_L, reducing the maximum efficiency (Mabrouk and Hami, 2019). On the other hand, the 3-bladed SB-VAWTs depicted higher P than the 4-bladed SB-VAWTs and lower P compared to the 2-bladed SB-VAWTs. At lower to medium rotational velocity, 3-bladed SB-VAWTs display superior performance, as presented in Fig. 7.6. Their performance is more consistent than 2-bladed and 4-bladed SB-VAWTs (Suriyawong et al., 2021). The J-shaped blades induced greater P than conventional N_{18} for every σ value. Further, the J_{uc}-N_{18} (70%) blades produced more P for each σ value as compared to others.

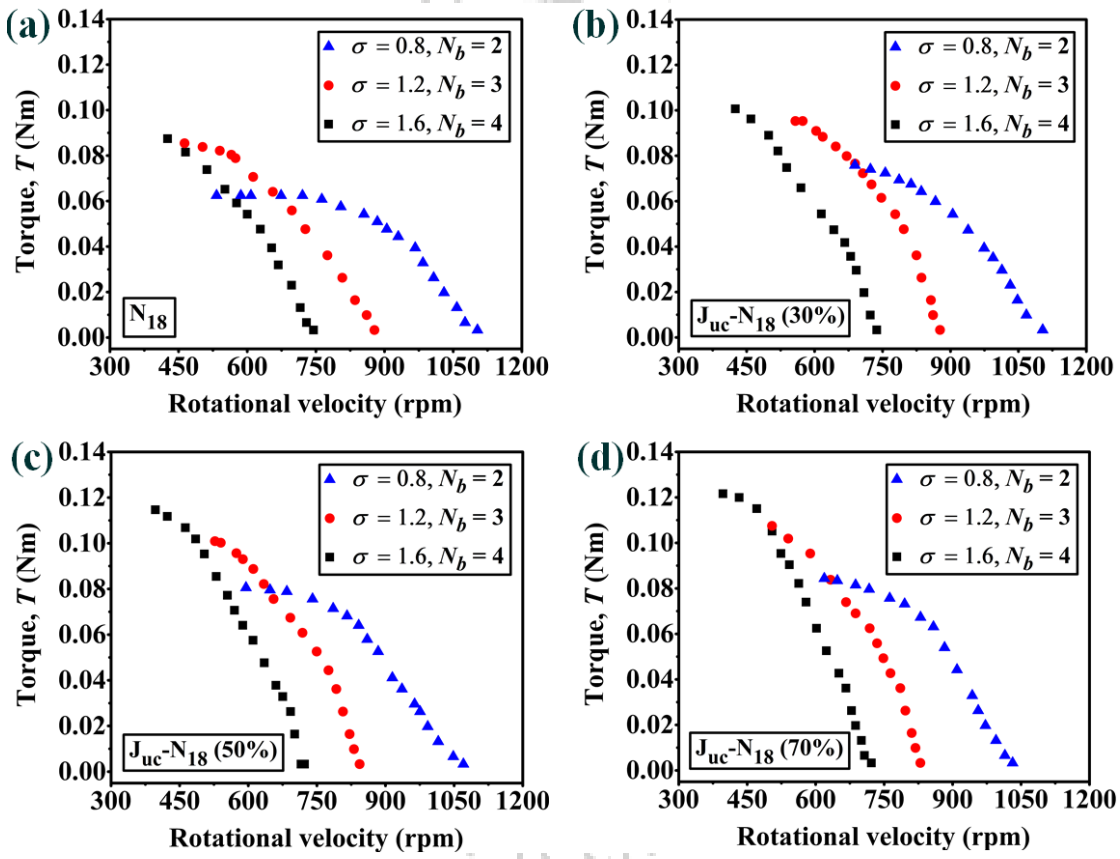

Fig. 7.5. Variation of torque with rotational velocity at 10 m/s: (a) N_{18}, (b) J_{uc}-N_{18} (30%), (c) J_{uc}-N_{18} (50%) and (d) J_{uc}-N_{18} (70%)

Figure 7.7 presents the peak P for each N_b at three different σ values. It is clearly observed that the 2-bladed SB-VAWTs show the highest peak P than the 3-bladed and 4-bladed SB-VAWTs. Further, 3-bladed SB-VAWTs showed larger peak P compared to 4-bladed SB-VAWTs. Additionally, each J-shaped blade displayed a larger peak P than the conventional blade. The

peak in P of SB-VAWT decreases as the σ values increase. This means the SB-VAWT with more N_b depicted lower performance at lower rotational velocity and λ values.

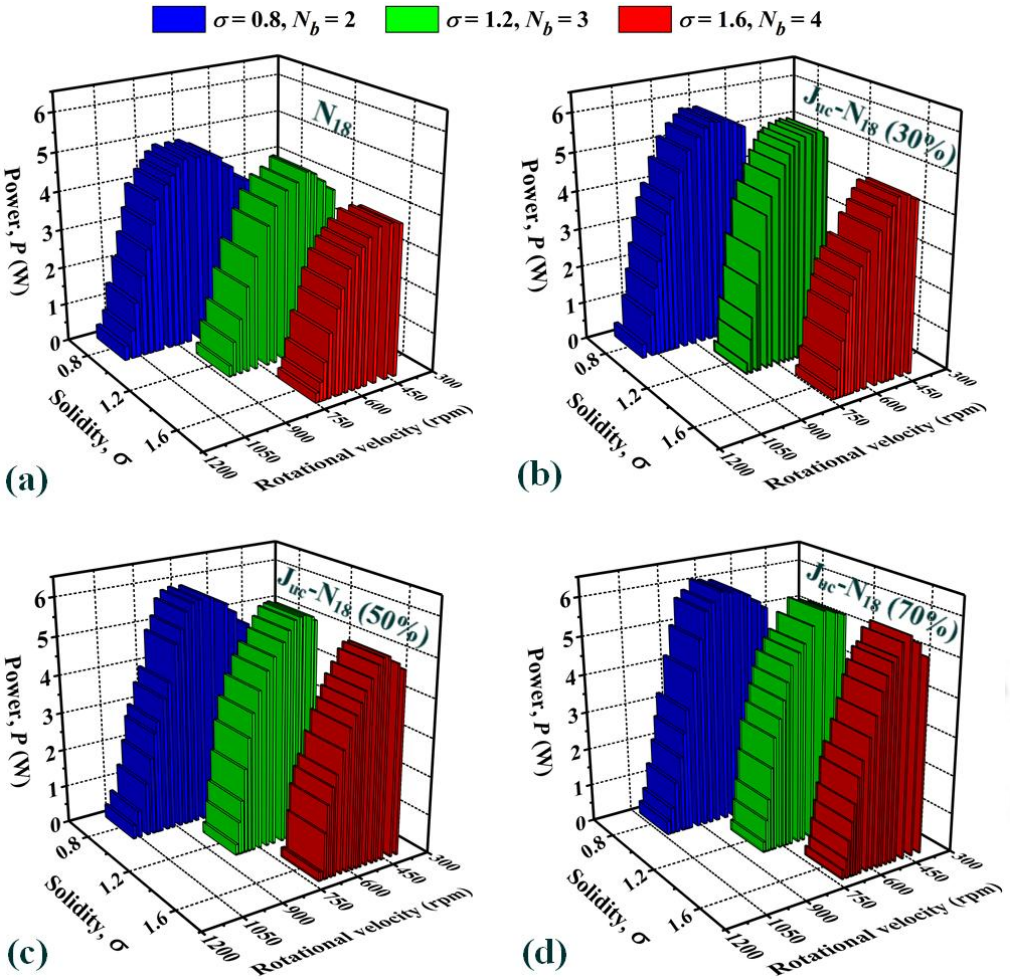

Fig. 7.6. Variation of power with rotational velocity at 10 m/s: (a) N_{18}, (b) J_{uc}-N_{18} (30%), (c) J_{uc}-N_{18} (50%) and (d) J_{uc}-N_{18} (70%)

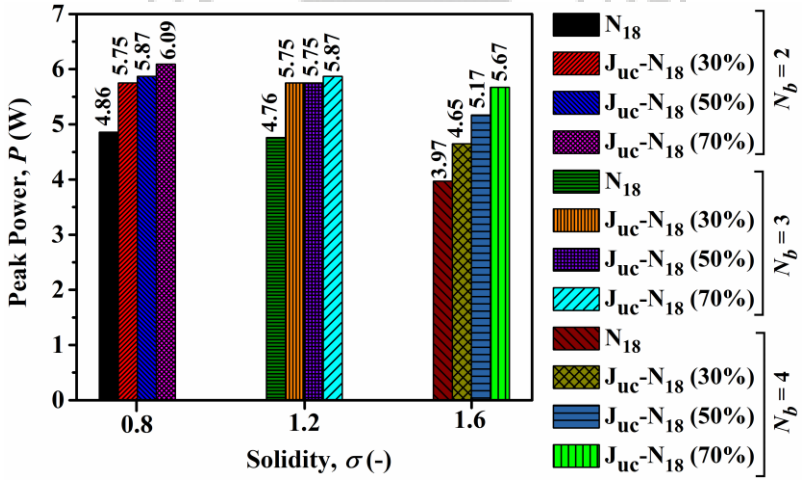

Fig. 7.7. Variation of peak power with solidity at 10 m/s

7.3.3. Effect of J-shaped blade numbers on experimental static torque characteristics

The wind tunnel tests are performed on static torque characteristics at 10 m/s and maximum performance is obtained for all blades at this velocity. The static torque characteristics for different N_b are shown in Fig. 7.8 in terms of static torque coefficient (C_{ST}) at 10 m/s. These plots presented the comparison of C_{ST} between the conventional and J-shaped blades. The 4-bladed J-shaped SB-VAWTs manifested better C_{ST} performance than other N_b because of more N_b values (Sun et al., 2022). Eventually, these SB-VAWTs are rotated easily, even at a lower wind speed than other N_b. However, it is noticed that the 3-bladed J_{uc}-N_{18} (70%) depicted the highest C_{ST} among all N_b, as displayed in Fig. 7.8 (b). Further, the remaining 3-bladed J-shaped blades showed higher C_{ST} than the 2-bladed SB-VAWTs.

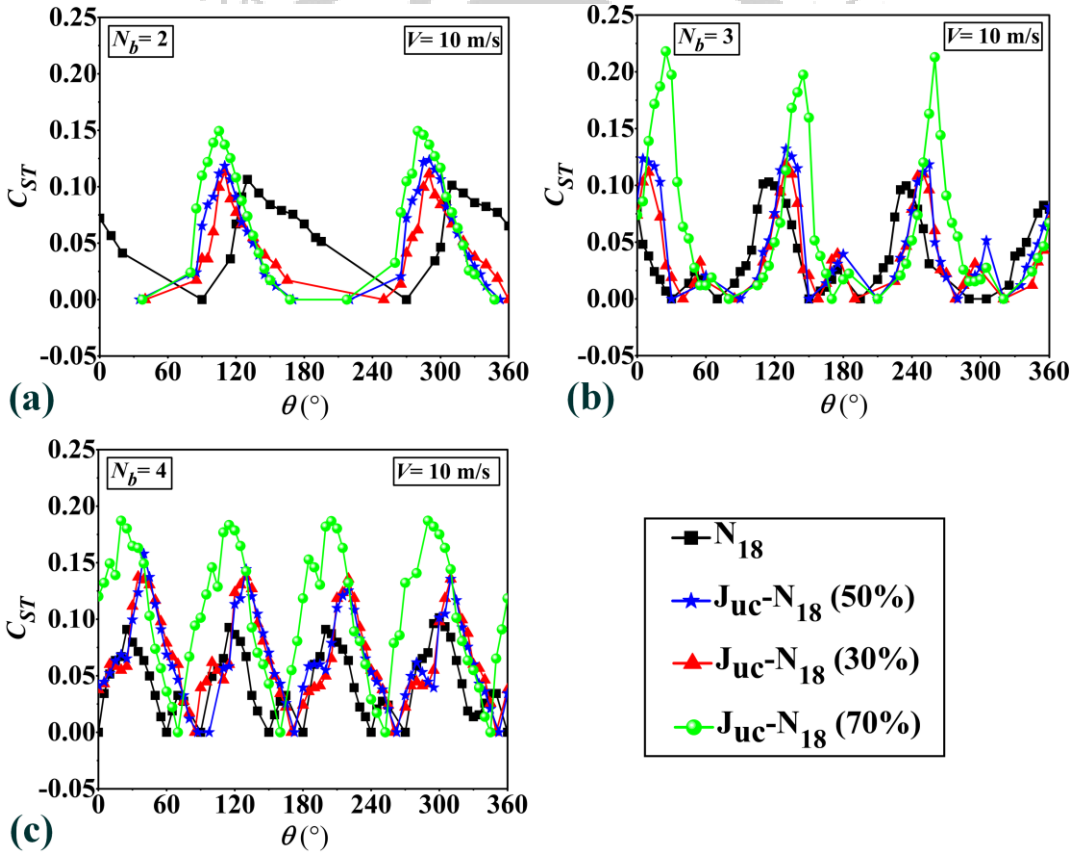

Fig. 7.8. Variation of experimental C_{ST} with the azimuthal angle at 10 m/s: (a) N_b = 2, (b) N_b = 3 and (c) N_b = 4

There is no starting torque at θ of 0º for 2-bladed J-shaped blades as these blades show zero C_{ST} values at this θ. Furthermore, the 2-bladed conventional N_{18} blade has a positive C_{ST} value at this θ. On the other hand, the opposite behaviour is observed for 4-bladed SB-VAWTs at 0º, as

presented in Fig. 7.8 (c). In this case, zero C_{ST} value is found by the 4-bladed conventional N_{18} blade at 0º, while positive C_{ST} values are obtained at this θ by the 4-bladed J-shaped blades. However, conventional and J-shaped blades depicted positive C_{ST} values for the 3-bladed SB-VAWTs. That means 3-bladed SB-VAWTs (Fig. 7.8 (b)) have good self-starting ability when SB-VAWTs start rotating at 0º. A C_{ST} peak of 0.218, 0.197 and 0.213 is found by 3-bladed J_{uc}-N_{18} (70%) at θ of 25º, 145º and 260º, respectively. Meanwhile, the 4-bladed J_{uc}-N_{18} (70%) demonstrated four C_{ST} peaks, among which three same C_{ST} peaks of 0.187 are obtained at θ of 20º, 205º and 290º and another is 0.183, which is found at θ of 115º. On the other hand, the 2-bladed J_{uc}-N_{18} (70%) displayed similar C_{ST} peaks of 0.149 at θ of 105º and 280º. For each N_b case, the static torque characteristics of the conventional N_{18} blade are not good because it shows lower C_{ST} performance in comparison to the J-shaped blades. The J-shaped configurations produce higher static torque performance as they function by both F_L and F_D. It happens because of their blade shape (Zamani et al., 2016a).

7.3.4. Validation of numerical simulation and wind tunnel test

The results acquired from the 2D numerical simulation are validated with the wind tunnel tests data in order to check their level of accuracy. Figure 7.9 depicts the AC_T of the J_{uc}-N_{18} (70%) blade as a function of λ at 10 m/s for different N_b obtained under similar conditions from the numerical simulation and experiment. The numerical simulation outcomes from different N_b presented a similar trend of AC_T with the experimental, despite the minor discrepancy, as illustrated in Fig. 7.9 (a-c). The 2D simulation data of 2-bladed J_{uc}-N_{18} (70%) displayed higher overestimated AC_T values than the experimental values. On the other hand, the 3-bladed and 4-bladed J_{uc}-N_{18} (70%) presented less difference in AC_T values between the 2D simulation and experiment at low λ values compared to the higher λ values. The same inconsistency in the 2D simulation and experiment is stated in the earlier study (Raciti Castelli et al., 2011b).

The experimental results are smaller compared to the 2D simulations. This is because of the rotor axis, model height, structs, flanges, 3D wall effect and blockage effects, which are considered in the wind tunnel experiment and include wind tunnel experimental errors (Li et al., 2018; Sun et al., 2022). Meanwhile, these are not considered in the 2D simulation; it considers the aerodynamic forces and ignores the mechanical losses. Further, the 2D simulation used a larger flow field, while the tests were conducted in a relatively small range of the flow field, which generates certain errors due to this condition (Li et al., 2018). However, a linear characteristic is observed in the AC_T vs λ plots for the case of 2D simulations. Thus, the flow

physics analysis of SB-VAWT used the 2D simulation outcomes because of the similar trend within the simulation and wind tunnel experiment, despite the overprediction values. Furthermore, the results from wind tunnel experimentation are considered as actual performance outcomes. The flow with the SB-VAWT with higher N_b becomes more uniform and guided. Thus, it reduces the 3D tip vortices and spanwise flow elements. The distributed aerodynamic loading observed in higher N_b cases suppresses 3D unsteadiness, which brings the experimental results closer to the 2D simulation results. In contrast, the 3D effects, such as blade tip losses, strong tip vortex shedding, pronounced blade wake interaction and spanwise flow are play a significant role in the experimental results for the lower N_b cases (N_b = 2). These effects produce a larger deviation from the 2D simulation outcomes.

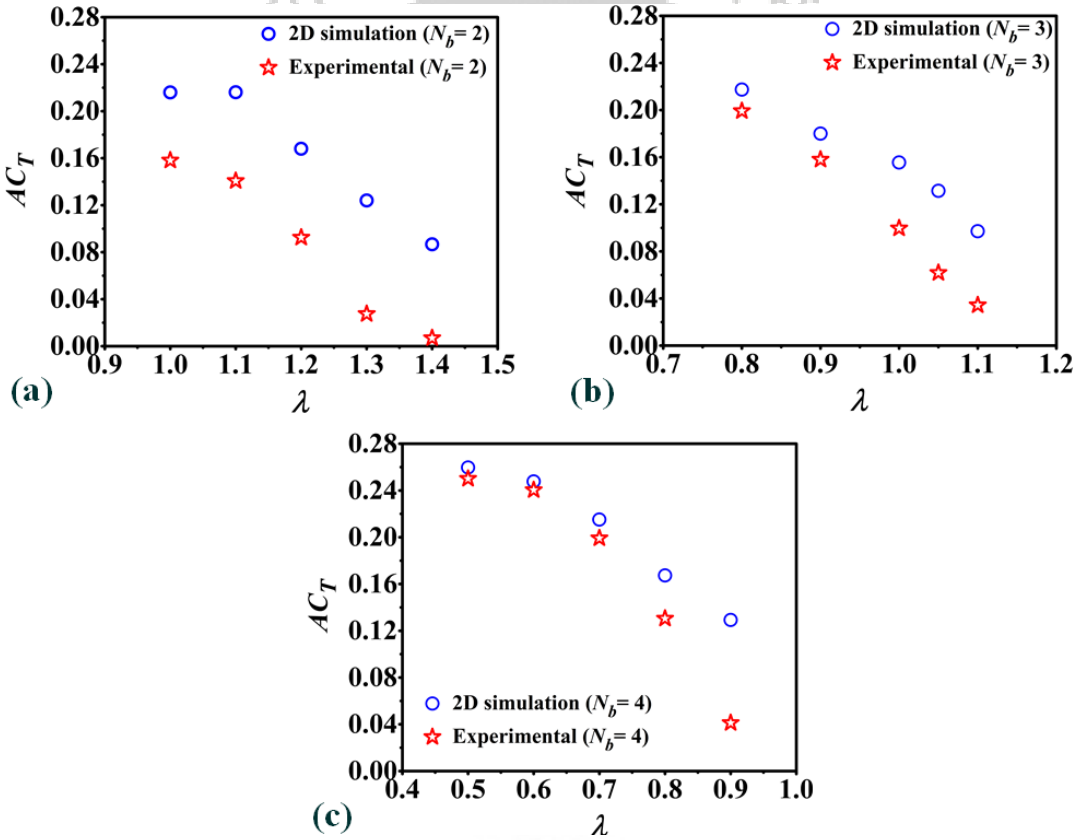

Fig. 7.9. Validation of results between numerical simulations and wind tunnel test at 10 m/s: (a) N_b = 2, (b) N_b = 3 and (c) N_b = 4

7.3.5. Effect of blade numbers on numerical IC_T

The variation of numerical instantaneous C_T (IC_T) of blade No. 1 as a function of θ for different N_b at optimum λ values (λ = 1.0 for N_b = 2, λ = 0.8 for N_b = 3 and λ = 0.6 for N_b = 4) are illustrated in Fig. 7.10 (a-d). These curves are presented as a complete rotation of blade No. 1 for Darrieus-

type SB-VAWTs. In the upwind region, almost identical IC_T patterns are noticed for blade No. 1 for each blade. Furthermore, blade No. 1 of both J-shaped and conventional SB-VAWTs (Fig. 7.10 (b-d)) displayed the maximum IC_T ($IC_{T,max}$) values during the upwind region at the θ ranges between 67º and 86º, where blades have experienced very high relative angles of attack. Blade No. 1 of the J-shaped blades depicted higher IC_T values for each N_b than the conventional blades. The J_{uc}-N_{18} (70%) blades presented larger IC_T values among these J-shaped blades. In IC_T vs. θ plots (Fig. 7.10 (a-d)), blade No. 1 of 2-bladed SB-VAWTs illustrated higher IC_T values in the upwind region compared to 3-bladed and 4-bladed SB-VAWTs. Further, greater IC_T values are obtained by blade No. 1 of 3-bladed SB-VAWTs than by the 4-bladed. The IC_T variation patterns of blade No. 1 for each N_b demonstrated dissimilarity in the downward region, as presented in Fig. 7.10 (a-d). Additionally, every blade in this region has lower IC_T values than the upwind region.

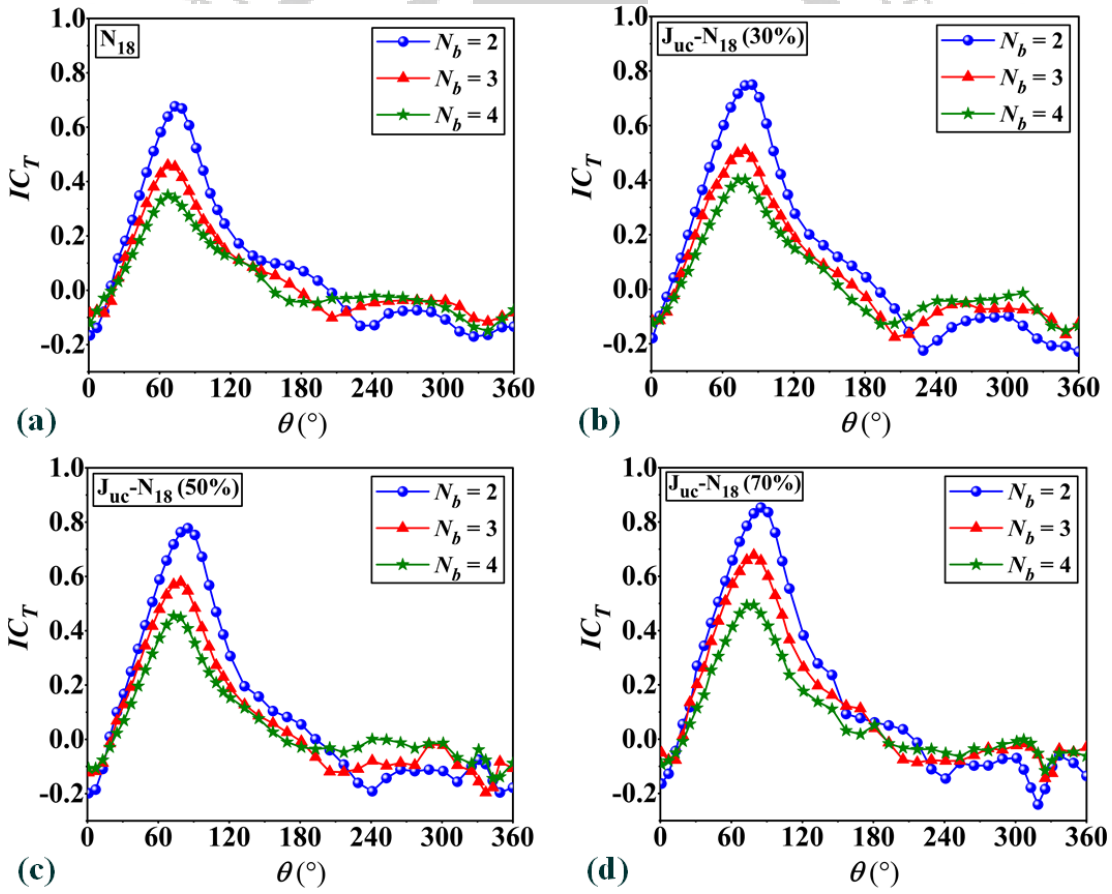

Fig. 7.10. Numerical IC_T variation of blade No. 1 for different N_b at λ_{opt} values (λ = 1.0 for N_b = 2, λ = 0.8 for N_b = 3 and λ = 0.6 for N_b = 4): (a) N_{18}, (b) J_{uc}-N_{18} (30%), (c) J_{uc}-N_{18} (50%) and (d) J_{uc}-N_{18} (70%)

The IC_T curves of all blades as a function of θ are demonstrated in Fig. 7.11 (a-c) at λ = 0.8 to quantitatively address the comparison between different N_b. All blades of 2-bladed SB-VAWTs with J-shaped profiles displayed higher IC_T values compared to the 3-bladed and 4-bladed SB-VAWTs with J-shaped profiles at the same λ values. The IC_T values for all blades of 3-bladed SB-VAWTs are larger than the 4-bladed SB-VAWTs at the same λ value of 0.8. Furthermore, the IC_T values of all blades for J-shaped SB-VAWTs in every N_b case increase with their ORs, which we clearly observed in Fig. 7.11 (a-c). Moreover, all blades of conventional N_{18} SB-VAWTs produced lower IC_T values than the J-shaped SB-VAWTs for each N_b case.

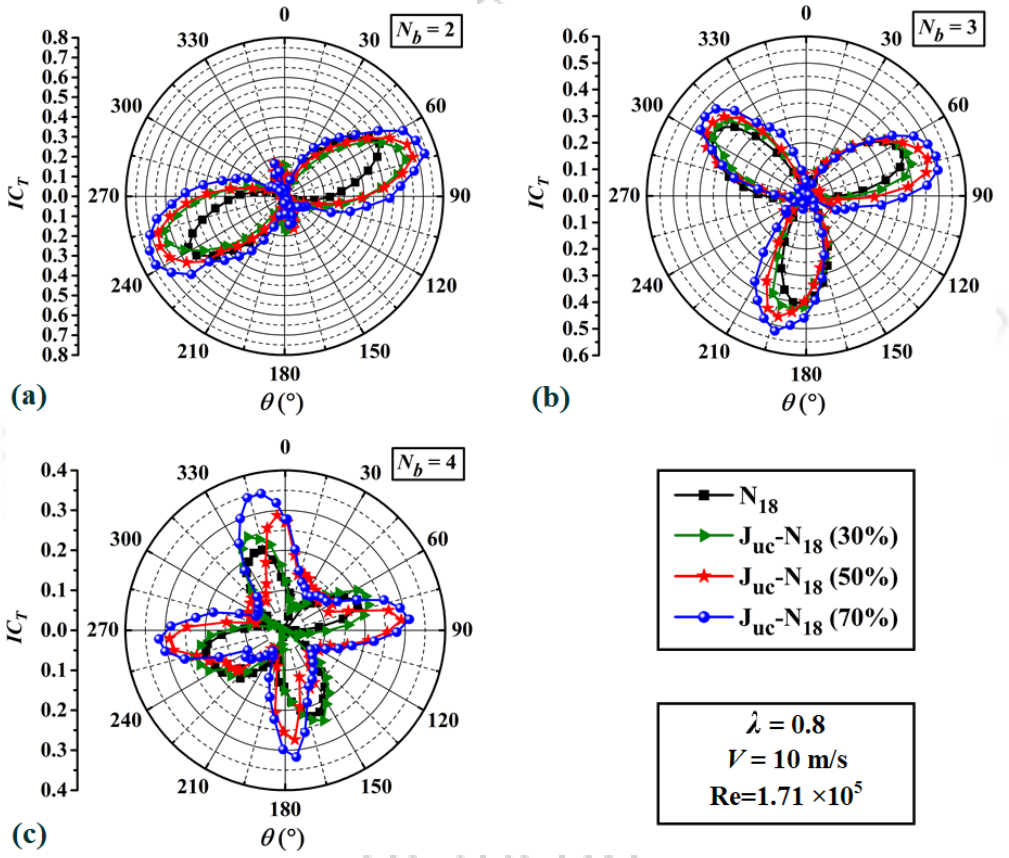

Fig. 7.11. Variation of numerical IC_T for different N_b: (a) N_b = 2, (b) N_b = 3 and (c) N_b = 4

7.3.6. Instantaneous flow behaviour around the J-shaped and conventional blades of Darrieus-type SB-VAWTs

Figures 7.12 - 7.15 illustrate the flow dynamics around the J-shaped and conventional blades of Darrieus-type SB-VAWTs at upwind and downwind zones for 10 m/s under λ = 0.8. These plots are presented for a complete rotation of Darrieus-type SB-VAWTs after accomplishing a steady state at four θ of 0º, 60º, 240º and 300º. Among these four θ, 0º and 60º describe the flow dynamics for the upwind zone, while 240º and 300º describe the downwind zone. The flow field

physics study is carried out to interpret the impact of J-shaped N_b behaviour on Darrieus-type SB-VAWTs and their benefits compared to conventional blades. In these investigations, three different N_b are compared to each other, as shown in Figs. 7.12 – 7.15. Furthermore, three uppercut J-shaped profiles with ORs of 30%, 50% and 70% (J_{uc}-N_{18} (30%), J_{uc}-N_{18} (50%) and J_{uc}-N_{18} (70%)) are examined and compared with the conventional N_{18} profile. The contour plots of the Darrieus-type SB-VAWTs recognize three flow regions: high-pressure, low-pressure and wake. The high-pressure region is visible on airfoil LS and the low-pressure region is recognizable on airfoil US, while the wake region is depicted downstream of the SB-VAWTs.

Figures 7.12 and 7.13 illustrate the instantaneous velocity magnitude with superimposed streamline patterns for different N_b. The direction of fluid flow around the Darrieus-type SB-VAWTs is indicated by the imaginary lines called streamlines. These streamlines can provide background information about the flow behaviour around the SB-VAWTs rotor region. When the wind flows towards the rotor's blades, it encounters the first blade and is deflected upwards. Thus, a low-pressure region is formed due to the upward flow behind the blade, which pulls more air along the sides to fill the space. When the flow continues towards the rotor, it encounters the other blades, deflects the flow upwards and then forms low-pressure regions behind them. Therefore, a circular streamlined series is observed around the rotor at 0º, which rises upwards when it passes every blade before curving back down again because it moves along the next blade. The overall impact of this flow pattern is to establish a rotor rotation because the high-pressure air on the opposite rotor side pushes against the blades and spins the shaft of the rotor.

It is observed that the generated recirculation zones (or vortex) on J-shaped blades are smaller in size than the conventional N_{18} blades in both upstream and downstream zones. The flow behind the conventional blades is more chaotic as these blades form more vortices in their downstream zone. In accordance with this, a large amount of power is wasted in the flow by conventional blades and is recovered in a smaller amount. The J-shaped blades generate more drag because of the higher pressure difference between their LS and US. This drag develops better startup torque in Darrieus-type SB-VAWTs (Zamani et al., 2016a, 2016b) and the majority of the drag is utilized in the conversion of energy. Further, the J-shaped blades generate more positive torque because of higher lift generation. Among the three J-shaped blades, the J_{uc}-N_{18} (70%) blades generated smaller vortexes as compared to the J_{uc}-N_{18} (30%) and J_{uc}-N_{18} (50%) blades in both upstream and downstream zones.

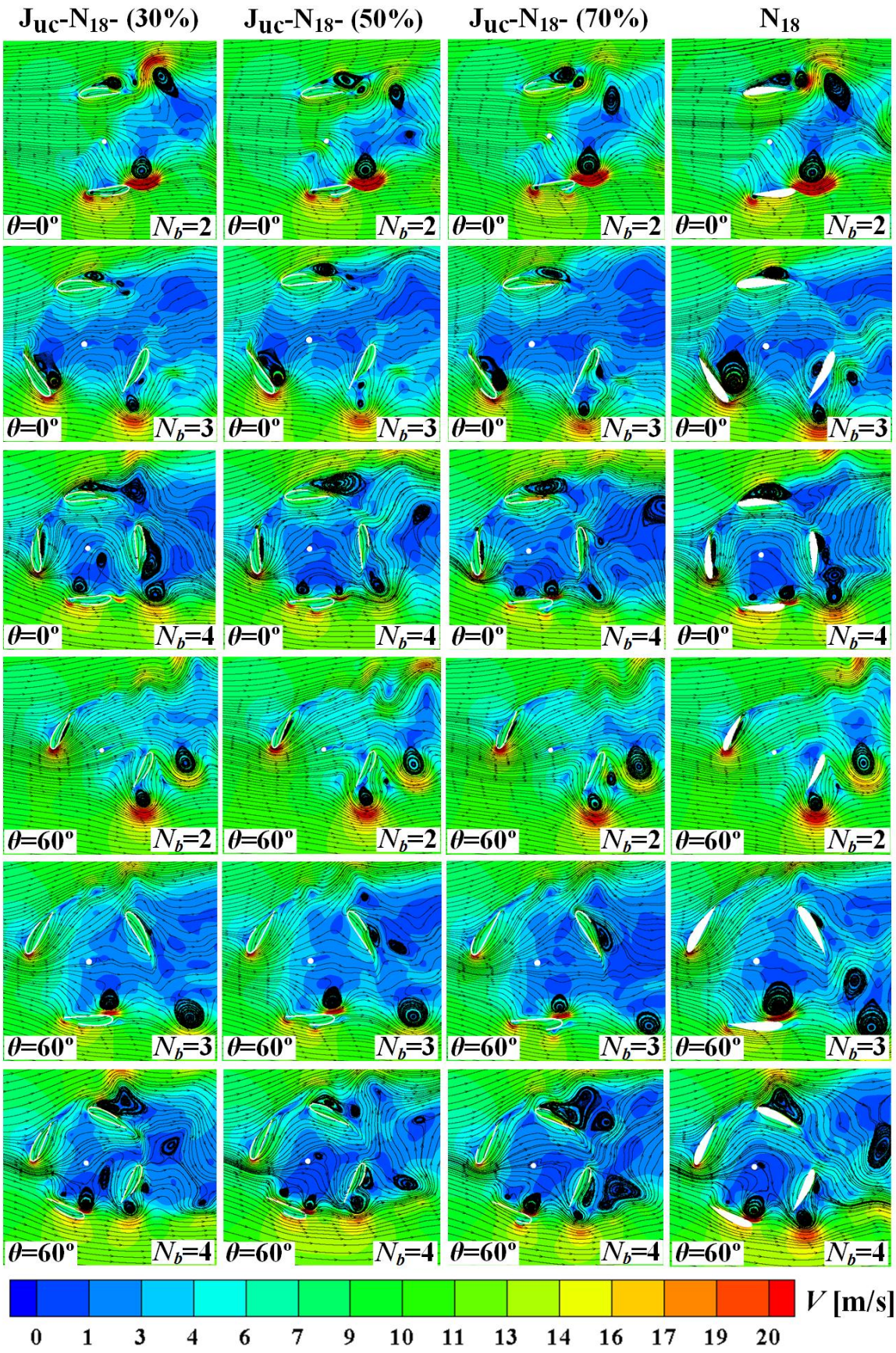

Fig. 7.12. Comparison of simulated velocity magnitude with superimposed streamlines pattern for different N_b in the upwind zone

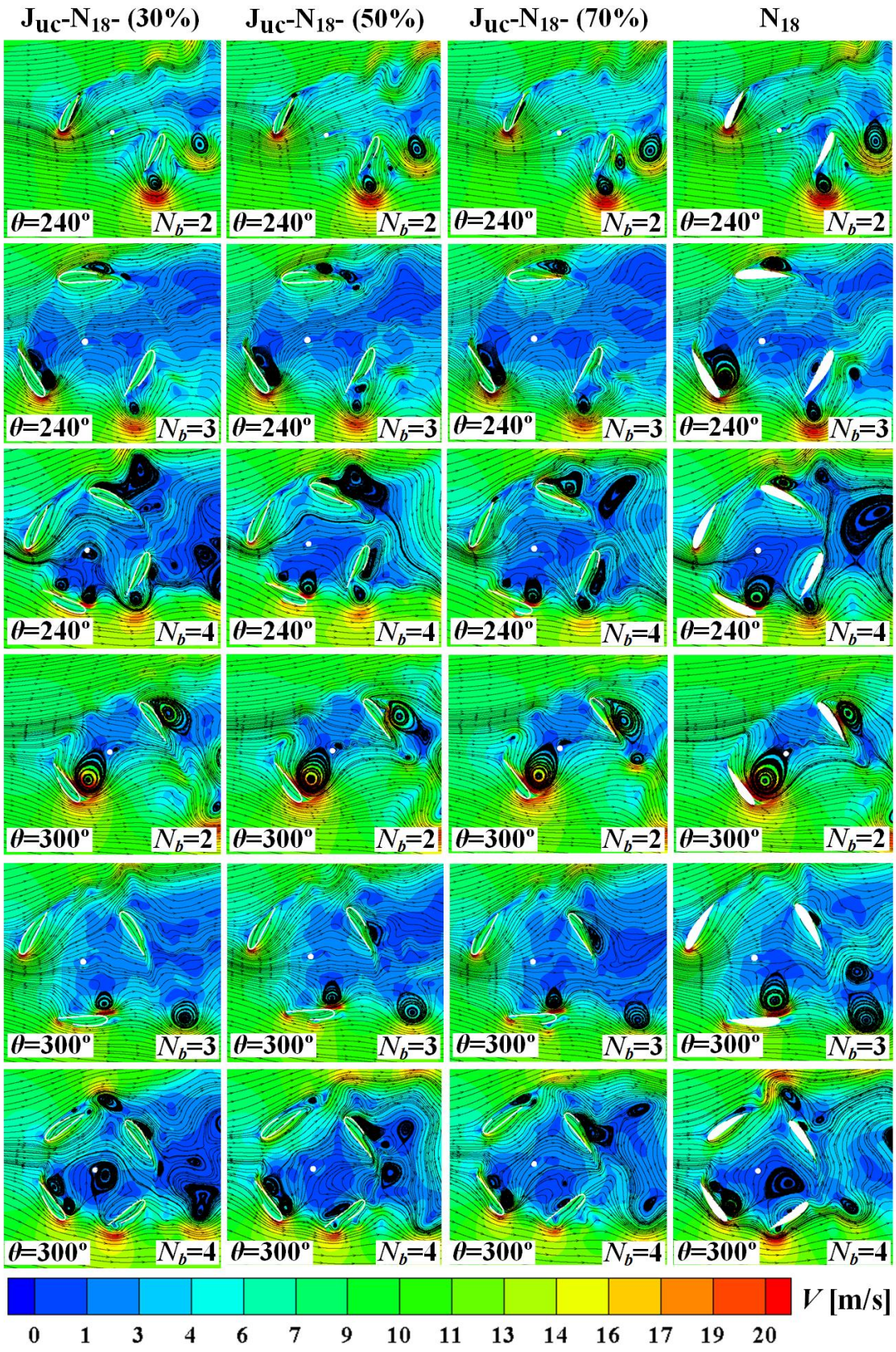

Fig. 7.13. Comparison of simulated velocity magnitude with superimposed streamlines pattern for different N_b in the downwind zone

The blade entrance velocity is increased in 2-bladed J-shaped SB-VAWTs because of lower N_b (Wang and Chen, 2008). It decreases the blockage effect due to the reduced N_b (Wang and Chen, 2008). Hence, the 2-bladed J-shaped SB-VAWTs produced maximum power at higher λ. The 4-bladed J-shaped SB-VAWTs reduce blade entrance velocity due to the increasing N_b and create more blockage (Wang and Chen, 2008). These J-shaped blades increase the C_T of Darrieus-type SB-VAWTs at lower λ. The 4-bladed J-shaped SB-VAWTs develop more vortices because of larger N_b and fewer vortices are produced by the 2-bladed J-shaped SB-VAWTs due to lower N_b. Moreover, the generated vortexes for 3-bladed J-shaped SB-VAWTs are smaller in shape than the 4-bladed J-shaped ones. The internal flow velocity decreases with an increase in the N_b, as illustrated in Figs. 7.12 and 7.13.

The comparison of simulated vorticity contours for different N_b at upstream and downwind zones for four different θ are illustrated in Figs. 7.14 and 7.15. It is noticed that the downstream zone produces more vortices compared to the upstream zone. Further, the power extracted from the upstream zone is higher than the downstream zone because it faces incoming flow at a higher wind speed, while the wind speed decreases when it passes to the downstream zone (Naik and Sahoo, 2024). Additionally, a majority of shed vortices are convected towards the downstream zone as they are of low-pressure cores. However, a vortex structure of a large size is observed in the upstream zone blades, which are passed at the same speed as the SB-VAWT blades towards the downstream zone.

Most importantly, the J-shaped blades (J_{uc}-N_{18} (30%), J_{uc}-N_{18} (50%) and J_{uc}-N_{18} (70%)) generate fewer vortices with a smaller shape and prompt dissipation, making the SB-VAWT wake region in the downstream area shorter. This happens because the J-shaped blade structure can trap more vortices and then transfer them through blade rotational motion towards the upstream area, ultimately releasing them (Zamani et al., 2016a, 2016b). On the other hand, these phenomena are not possible in the case of conventional N_{18} blades due to their geometrical shape. For these blades, the vortices are formed upstream and in other regions, released instantly and spread within the downstream zone of SB-VAWTs. The J-shaped blades produce a more stable flow around the SB-VAWTs and decrease the vibrations generated by the different parts of the SB-VAWTs (Zamani et al., 2016b). Meanwhile, these blades acquired their flow consistency in the downstream area. It is observed from Figs. 7.14 and 7.15, the J_{uc}-N_{18} (70%) blade produces a smaller shape of vortices compared to the other two J-shaped blades. Because of more N_b, the 4-bladed J-shaped SB-VAWTs generated more vortices than the 2-bladed and 3-bladed J-shaped

SB-VAWTs. Moreover, the 2-bladed J-shaped SB-VAWTs developed larger shapes of vortices. However, smaller size of vortices are developed by 3-bladed J-shaped SB-VAWTs than others.

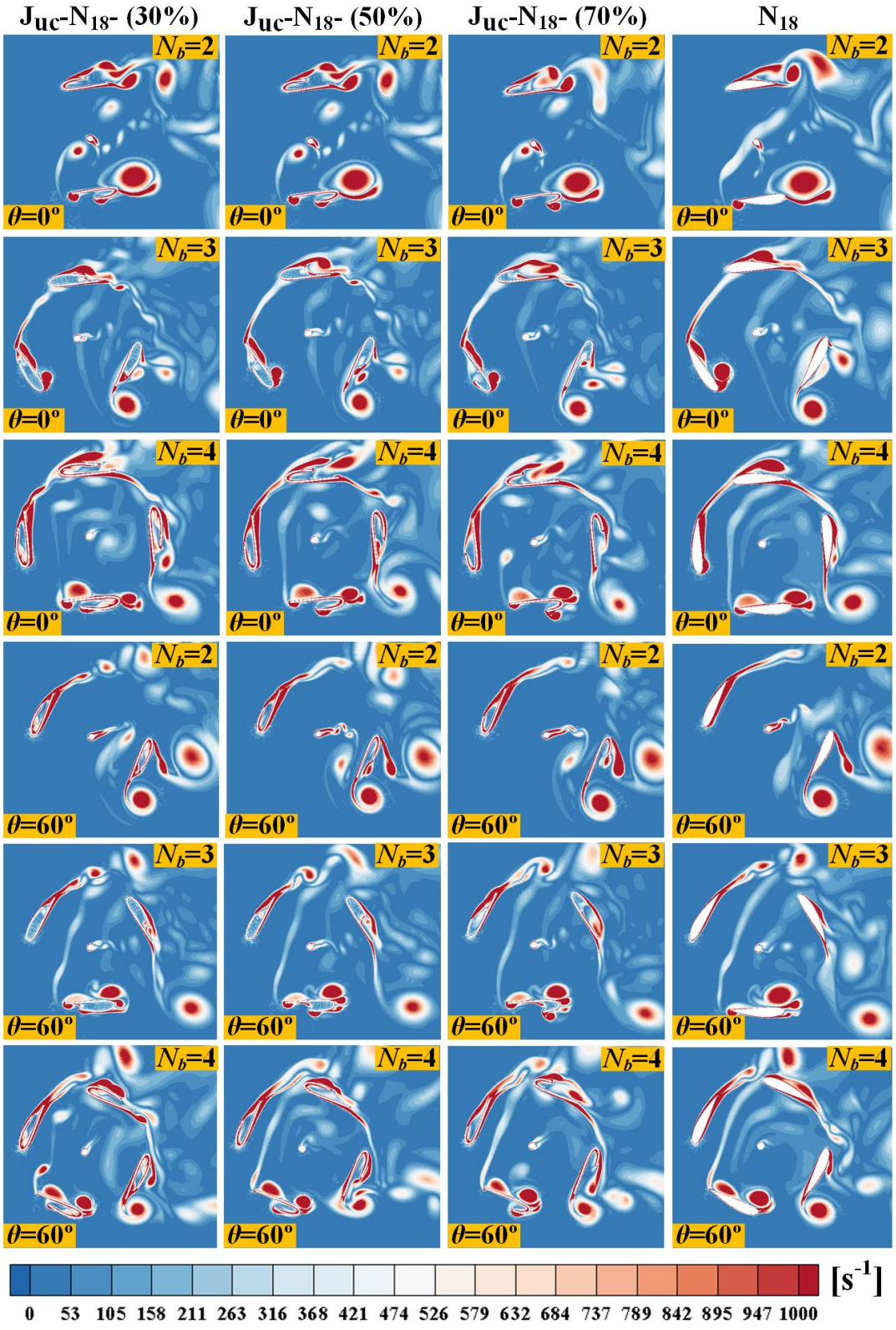

Fig. 7.14. Comparison of simulated vorticity contour for different N_b in the upwind zone

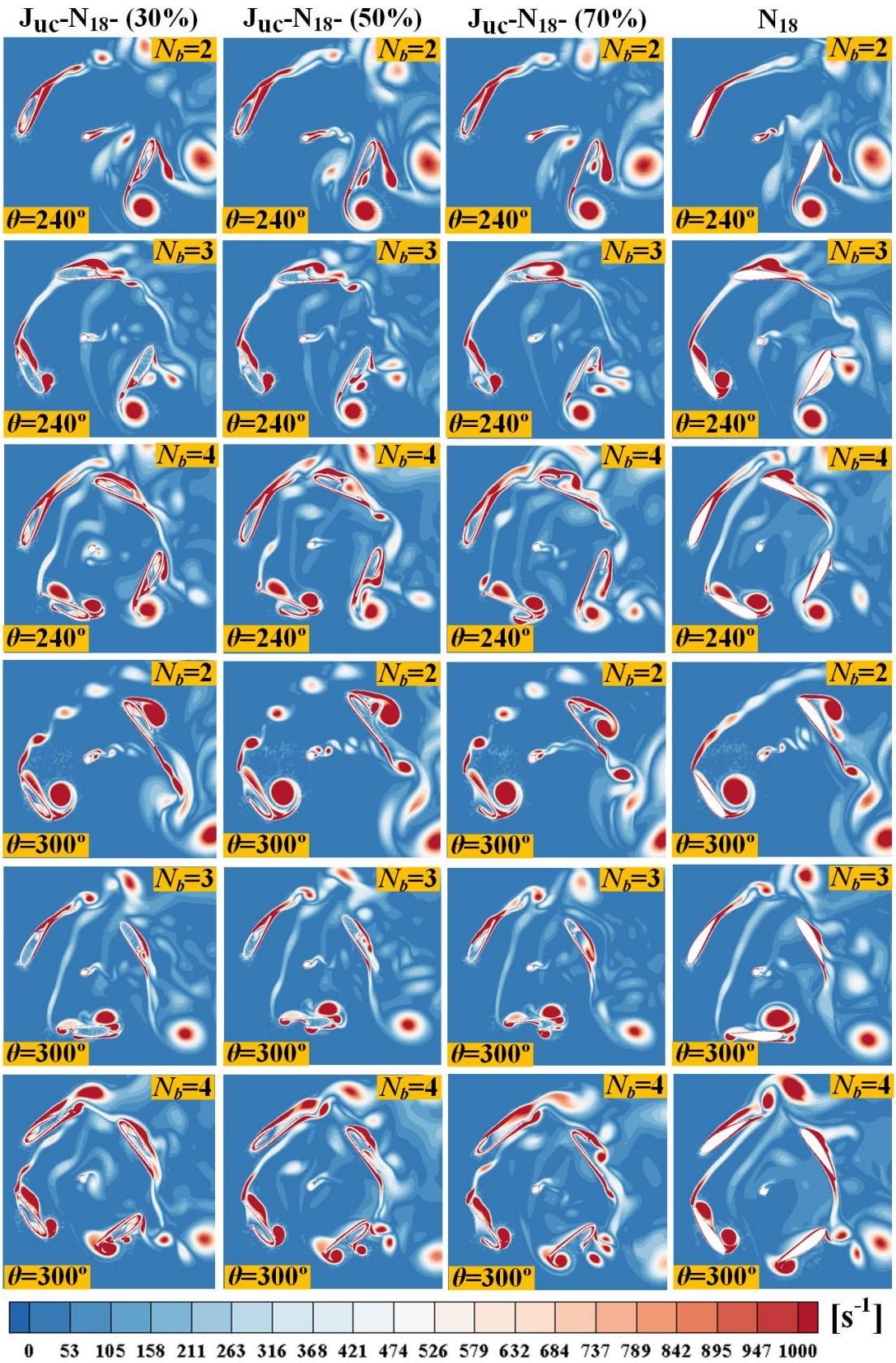

Fig. 7.15. Comparison of simulated vorticity contour for different N_b in the downwind zone

7.4. Summary

This study presented the experimental and numerical analysis of the effect of the J-shaped blade number (N_b) on the aerodynamic performance and self-starting of small-scale Darrieus-type SB-VAWTs for low wind regimes. A comparative analysis is conducted between three different N_b types, such as 2, 3, and 4. The uppercut J-shaped airfoils with opening ratios (ORs) of 30%, 50% and 70% are selected for the present investigations and these airfoils were developed from the conventional NACA 4418 airfoil. The influence of solidity (σ) is also studied in this work by varying N_b. An improved performance is obtained from both experimental and numerical investigations of the J-shaped N_b compared to the conventional N_b for each Reynolds number (*Re*) and velocity (*V*) case. Higher average torque coefficient (AC_T) and average power coefficient (AC_P) values are found by the J-shaped N_b with larger ORs at lower λ values for each N_b case. However, the J-shaped N_b with lower ORs show better AC_T and AC_P values at higher λ values. A poorer AC_T and AC_P performance is obtained from the conventional N_b than the J-shaped N_b at lower λ values for each *V* and *Re*. Due to the larger torque values, the AC_T and AC_P of 3-bladed and 4-bladed J-shaped SB-VAWTs are better at lower λ values than the 2-bladed J-shaped SB-VAWTs at each V and Re. Moreover, the 3-bladed J-shaped SB-VAWTs displayed more consistent AC_T and AC_P performance at low to medium λ values. However, better AC_T and AC_P performance is found from 2-bladed J-shaped SB-VAWTs at higher λ values. The relative performance ($AC_{P,opt}$) of 25%, 23% and 42% is obtained at 10 m/s for 2-bladed, 3-bladed and 4-bladed SB-VAWTs consisting of J-shaped airfoils with 70% OR. The σ of SB-VAWTs increases with N_b. The SB-VAWTs with a larger σ generate higher torque (*T*) at lower rotational velocity and λ values. Meanwhile, higher *T* and power (*P*) are developed by the SB-VAWTs with a smaller σ at larger rotational velocity and λ values. Better starting characteristics are noticed in SB-VAWTs when using J-shaped N_b than the conventional N_b.

CHAPTER 8

Conclusions and Future Scopes

Chapter Layout

Overview

Harnessing wind energy is one of the promising and viable solutions for satisfying the present and future demand for renewable energy. In light of these aspects, the present investigations explore the use of the small-scale Darrieus-type SB-VAWTs with J-shaped blade profiles as a power source for areas with minimal energy requirements. This study analyses the testing of small-scale SB-VAWTs for lower tip speed ratios and Reynolds numbers conditions. A series of 2D numerical simulations and wind tunnel experiments are carried out on SB-VAWTs using J-shaped airfoils with various opening ratios. This study examined the different types of airfoils and blade numbers and thoroughly compared the J-shaped SB-VAWTs and conventional SB-VAWTs. This chapter outlined the key finding of the present investigations and their future scopes for further research.

8.1. Contribution of the present work

The Darrieus-type straight-bladed vertical axis wind turbines (SB-VAWTs) can be a sustainable option for small-scale and low-cost off-grid energy generation. These are suitable especially in tight spaces and areas with low wind speeds where other wind turbines can not function effectively. However, the SB-VAWTs face self-starting, which is one of the major problems for regions with low wind speeds. Further, the aerodynamic performance of SB-VAWTs is not as good as that of horizontal axis wind turbines (HAWTs), even if generating better performance than the other VAWTs. With these aspects, a detailed investigation has been carried out to enhance the aerodynamic performance and the self-starting characteristics of small-scale Darrieus-type SB-VAWTs using a novel shape blade profile referred to as the J-shaped blade profile through a series of numerical simulations and wind tunnel experiments in the present thesis.

Initially, 2D numerical simulations are conducted on Darrieus-type SB-VAWTs with J-shaped airfoils to study their aerodynamic performance and starting characteristics by varying the opening ratios (ORs) of J-shaped airfoils. Further, simulations are carried out on SB-VAWTs with conventional airfoils for comparison. In this context, two types of J-shaped airfoils are selected: uppercut and lowercut J-shaped airfoils. The conventional cambered NACA 4415 airfoil is used for the creation of the J-shaped airfoils. The main motive of this investigation is to find the optimum J-shaped airfoil for the Darrieus-type SB-VAWTs.

Based on the simulation outcomes, further 2D simulations are carried out on small-scale Darrieus-type SB-VAWTs with different cambered airfoils and their uppercut J-shaped airfoils with 30% ORs in order to obtain better cambered airfoils for the fabrication of the J-shaped blades. From the simulation results, the J-shaped blades are designed using conventional cambered NACA 4418 airfoils with three different ORs (such as 30%, 50% and 70%) to conduct experimentation on the Darrieus-type SB-VAWTs at various lower Reynolds numbers (*Re*) and lower tip speed ratios (λ). This study presented an in-depth analyzes of the effect of uppercut J-shaped airfoils on the overall performance and self-starting of the SB-VAWTs, considering the various performance parameters.

Additionally, the effect of the J-shaped blade number (N_b) (i.e., 2, 3 and 4) with ORs of 30%, 50% and 70% has been studied on the performance and starting characteristics of small-scale Darrieus-type SB-VAWTs at lower *Re* and lower λ. Therefore, several experiments have been

conducted in a wind tunnel on the SB-VAWTs using J-shaped N_b and conventional N_b. This test uses cambered NACA 4418 airfoils to create the J-shaped blades. Further, numerical simulations are carried out to investigate the flow characteristics of the J-shaped N_b and for validation purposes. The numerical data also presented the starting torque characteristics and instantaneous flow behaviour around the Darrieus-type SB-VAWTs consisting of different N_b. The key findings of the present thesis are summarized in the following subsections. The application potential and scopes for future work are also presented.

In this work, 2D CFD investigations are carried out to highlight specific biases relative to 3D effects. The 2D models displayed an overestimated absolute performance, which is less robust, as they neglect 3D effects such as tip losses, spanwise flow, variation of dynamic stall along the blade height, and interactions with the end-plate. Accordingly, the reported absolute values should be viewed as theoretical data rather than exact field performance. However, the 2D models capture the relative performance trends effectively; thus, the comparative rankings and design trends are expected to remain robust.

8.1.1. Numerical Investigations of J-shaped airfoils on the Performance of Darrieus-Type SB-VAWTs

The Darrieus-type SB-VAWTs are more suitable for energy production at lower wind speeds in urban regions, but still generate lower torque and power output. The cross-sectional profile of the blade is the crucial parameter which affects the aerodynamic performance of the Darrieus rotor. The present study mainly concentrated on improving the aerodynamic performance and starting torque of the Darrieus-type SB-VAWTs. Therefore, two-dimensional numerical studies have been carried out by using the conventional NACA 4415 airfoil and its J-shaped airfoil with different opening ratios (ORs). Two types of J-shaped airfoils, such as uppercut and lowercut J-shaped airfoils, along with eight different ORs have been examined in the present investigation. The significant results are outlined below:

- The uppercut J-shaped airfoils with ORs of 0.8, 0.7, 0.6, 0.5 and 0.4 displayed higher power coefficient (C_p) and torque coefficient (C_T) values compared to the conventional NACA 4415 and the rest of all J-shaped airfoils.

- The C_p and C_T values of the J-shaped airfoils increase when the opening ratio increases from 0.1 to 0.8. It shows an improvement of 31 % in the C_p and C_T values when ORs rise from 0.1 to 0.8. The ORs of the uppercut J-shaped airfoils perform better than the lowercut.
- The lowercut J-shaped airfoils with ORs of 0.8 and 0.7 exhibited higher C_p and C_T values than the conventional NACA 4415 airfoil. However, the lowercut J-shaped airfoils exhibit poorer aerodynamic performance than the uppercut.
- The self-starting ability and performance of the Darrieus-type SB-VAWTs are enhanced when they use the uppercut J-shaped airfoils, as these airfoils generate higher torque at low λ than the conventional airfoil and lowercut J-shaped airfoils. Therefore, the uppercut J-shaped airfoils can be used in small-scale WTs to improve their start-up torque and performance at low λ values.
- The instantaneous torque coefficient (IC_T) values of the uppercut J-shaped airfoils are not influenced by the ORs due to the higher torque generation in the upwind region compared to the downwind region. The lowercut J-shaped airfoils have demonstrated poorer IC_T values than those with upper openings in the upwind region.
- The J-shaped airfoils minimize the wake region at the backside of the Darrieus-type SB-VAWTs, as the generated vortices are entrapped in their profile geometry. Thus, these airfoils produce less noise and turbulence. Therefore, faster consistency can be revived at the downward of the Darrieus-type SB-VAWTs.
-

8.1.2. Experimental and Numerical Investigations of Small-Scale Darrieus-Type SB-VAWTs using J-Shaped Airfoils

The primary purpose of this investigation is to enhance the aerodynamic performance and starting torque of small-scale Darrieus-type SB-VAWTs. This study initially conducts several numerical simulations on the five different cambered NACA 44XX airfoils and their corresponding J-shaped airfoils with OR=30% to obtain better J-shaped blades with improved performance for the Darrieus-type SB-VAWTs. Subsequently, experimental tests are carried out on Darrieus-type SB-VAWT utilizing specifically chosen J-shaped blades with OR of 30%, 50% and 70%. These tests are performed within a wind tunnel facility characterized by lower turbulence levels at four different Reynolds numbers (*Re*). The Darrieus-type SB-VAWTs with conventional blades are also examined within a wind tunnel for comparative analysis. The results obtained from the experiment are validated and compared with the numerical results. Additionally, the physics of flow behaviours around the Darrieus-type SB-VAWTs with J-

shaped and conventional blades are presented to elucidate the better performance and support the experimental outcomes. The following results are achieved from this study:

- The uppercut J-shaped airfoil with OR of 30% (J_{uc}-N_{18} (30%)) illustrates better numerical average torque coefficient (AC_T) and average power coefficient (AC_P) performance at lower tip speed ratio (λ) values as compared to the other uppercut J-shaped airfoils (J_{uc}-N_{12} (30%), J_{uc}-N_{15} (30%), J_{uc}-N_{21} (30%) and J_{uc}- N_{24} (30%)) with the same OR.
- The experimental investigations have revealed that the J_{uc}-N_{18} (30%), J_{uc}-N_{18} (50%) and J_{uc}-N_{18} (70%) airfoil increases the aerodynamic performance of Darrieus-type SB-VAWT at each *Re* than the conventional N_{18} airfoil.
- The highest experimental AC_T and AC_P performance is obtained from the highest *Re* in each J-shaped airfoil for the tested range of *Re* values.
- The Darrieus-type SB-VAWTs equipped with the J_{uc}-N_{18} (30%), J_{uc}-N_{18} (50%) and J_{uc}-N_{18} (70%) airfoils acquired an improvement of 21%, 22% and 25%, respectively, in AC_P than the conventional N_{18} airfoil at $Re = 1.71\times10^5$.
- The AC_P of the Darrieus-type SB-VAWT with J_{uc}-N_{18} (70%) airfoils increases with a rise of velocity (V) from 7 to 10 m/s and their $AC_{P,opt}$ values are found at an increasing λ for each V, which ranges from 7 to 10 m/s.
- The J-shaped blade profile augments the starting torque of the Darrieus-type SB-VAWTs due to its blade design. The J-shaped blade profile develops higher torque than the conventional cambered blade profile. Therefore, the J-shaped profile can be a viable option for small-scale SB-VAWTs to increase the start-up torque and performance at low λ values.
- The J-shaped blades exhibit notably superior static torque characteristics in comparison to conventional cambered blades. The Darrieus-type SB-VAWTs with J_{uc}-N_{18} (30%), J_{uc}-N_{18} (50%) and J_{uc}-N_{18} (70%) blade profiles yield a larger static torque coefficient (C_{ST}) than the conventional N_{18} blade profile. Moreover, the J_{uc}-N_{18} (70%) blade profile generates higher C_{ST} values among the three J-shaped blade profiles.
- The numerical IC_T values of Darrieus-type SB-VAWTs with J-shaped blades are higher than those of conventional cambered blades.
- The wake region at the back of Darrieus-type SB-VAWTs is lessened by the J-shaped airfoils than the conventional airfoil. This is because of the profile of the J-shaped, as it can entrap the generated vortices. Therefore, minimal turbulence and noise are developed and can be acquired with quicker consistency towards the downstream region of the Darrieus-type SB-VAWTs.

- The numerical outcomes also admired the experimental results and presented credible flow physics, which demonstrates the primary cause behind the improvement in performance by J-shaped blade profiles.

8.1.3. Effect of J-shaped Blade Numbers on the Performance and Starting Characteristics of the Small-Scale Darrieus-type SB-VAWTs for Low Wind Regimes

The effect of J-shaped blade number on the aerodynamic performance and self-starting of small-scale Darrieus-type SB-VAWTs for low wind regimes has been presented in this investigation using experimental measurements and numerical simulations. A comparative analysis is conducted between three different blade numbers (N_b) types, such as 2, 3, and 4, to analyse their effects on performance. For this goal, this investigation examined the uppercut J-shaped blades created from conventional NACA 4418 (N_{18}) airfoil with opening ratios (ORs) of 30%, 50% and 70% within a wind tunnel facility at four different Reynolds numbers (*Re*). These outcomes are also compared with the conventional N_{18} blade results. The experimental results are validated and compared with the numerical findings. Moreover, the flow physics behaviours around the Darrieus-type SB-VAWTs with different N_b with J-shaped and conventional profiles are illustrated to explain the good performance and support the experimental findings. The significant outcomes are outlined below:

- Both experimental and numerical investigations manifest an improved performance of the J-shaped N_b in contrast to the conventional N_b.
- Identical patterns of average torque coefficient (AC_T) and average power coefficient (AC_P) with respect to tip speed ratio (λ) are observed in each Reynolds number (*Re*) and velocity (*V*) case for the tested J-shaped and conventional N_b.
- In each N_b case, the J-shaped N_b with larger ORs depicted higher AC_T and AC_P values at lower λ values. Meanwhile, the J-shaped N_b with lower ORs obtain better AC_T and AC_P values at larger λ values. The J-shaped blades perform better due to the simultaneous effect of drag force (F_D) and lift force (F_L). The conventional N_b presented poorer AC_T and AC_P performance than the J-shaped N_b at lower λ values for each *V* and *Re*. Further, their AC_T and AC_P performance are better at higher λ values.
- The AC_T and AC_P performance of 3-bladed and 4-bladed J-shaped SB-VAWTs is better at lower λ values than the SB-VAWTs with 2 blades at each *V* and *Re* due to the larger torque values. Further, 3-bladed J-shaped SB-VAWTs illustrated the more consistent AC_T and AC_P

performance at low to medium λ values. Meanwhile, the 2-bladed J-shaped SB-VAWTs displayed better AC_T and AC_P performance at larger λ values. The AC_T and AC_P performance curves are moved towards the lower λ values with increments in N_b.

- The absolute performance ($AC_{P,opt}$) of J-shaped SB-VAWTs rises with an increase of ORs for respective N_b cases. Further, a decrement is obtained in the $AC_{P,opt}$ values when increasing the N_b. Also, the operating range of optimum λ (λ_{opt}) values decreases when the N_b increases. An improvement of 25%, 23% and 42% is found in $AC_{P,opt}$ values at 10 m/s for 2-bladed, 3-bladed and 4-bladed SB-VAWTs using J_{uc}-N_{18} (70%) blade compared to conventional N_{18} SB-VAWTs.
- The solidity (σ) of Darrieus-type SB-VAWTs increases with N_b. The 4-bladed SB-VAWTs generated higher torque (T) at lower rotational velocity and λ values due to their larger σ. However, lower rotational velocity produces less power (P) production in 4-bladed SB-VAWTs. At low to medium rotational velocity and λ values, 3-bladed SB-VAWTs presented better T and P. Moreover, larger T and P are developed at larger rotational velocity and λ values by 2-bladed SB-VAWTs with a lower σ. Further, J-shaped blades generate more T and P than conventional blades for each σ and N_b. The J_{uc}-N_{18} (70%) blades produced more P for each σ value than other J-shaped blades.
- The J-shaped N_b depicted better starting performance for Darrieus-type SB-VAWTs compared to the conventional one. The 4-bladed J-shaped SB-VAWTs manifested a superior static torque coefficient (C_{ST}) than other N_b because of more N_b values. Moreover, 3-bladed J_{uc}-N_{18} (70%) illustrated the highest C_{ST} among all N_b. Poor C_{ST} performance is found in the 2-bladed J-shaped SB-VAWTs in comparison to other J-shaped N_b.
- The numerical instantaneous torque coefficient (IC_T) values of J-shaped N_b are superior to those of conventional N_b. The IC_T of J-shaped SB-VAWTs increases with ORs and also rises as N_b values reduce. The J-shaped N_b produced a recirculation zone of a smaller size than the conventional N_b. The conventional N_b procured less P as a vast quantity of P is wasted in their flow due to the more chaotic flow and vortices. Further, the increment in N_b decreases the internal flow velocity and generates more vortices. The J-shaped N_b trapped more vortices because of its blade structure. A more stable flow is developed around the Darrieus-type SB-VAWTs by the J-shaped N_b, which decreases the vibrations produced from different parts of the SB-VAWTs. Therefore, the flow in the downstream area of the J-shaped N_b procured their consistency.

8.2. Application Potential

The implication of large-scale wind turbines (LSWTs) may not be feasible and cost-effective in fulfilling the lower energy demand for various applications, such as isolated individual households, small-scale farms, rural areas, and others. These circumstances highlight the requirement for more effective, affordable and efficient small-scale wind turbines (SSWTs). The Darrieus-type SB-VAWTs using J-shaped blade profiles come under SSWTs. These SB-VAWTs are simpler in design; thus, fabrication is easier and requires less maintenance. Moreover, the SB-VAWTs are highly beneficial in variable wind speed conditions due to their omnidirectional nature. The SB-VAWTs with J-shaped blade profiles can be fitted on building or communication towers and ridge location for localized electricity production. The J-shaped profiles help the SB-VAWTs start easily and can be used to pump water for long periods in agricultural fields.

In the offshore field, the usage of LSWTs occupies a large space and requires more cost for their operation and maintenance. In such conditions, the novel blade structure of J-shaped design integrated in Darrieus-type SB-VAWTs is a viable solution for offshore applications. This blade design can work in different situations in offshore fields and can enhance torque performance and capture rate of wind energy.

The present thesis revealed that uppercut J-shaped airfoils enhance the starting characteristics and aerodynamic performance of the small-scale Darrieus-type SB-VAWTs at lower *Re* and λ values than conventional airfoils. Further, the J-shaped airfoils with higher ORs performed better at lower λ values, while lower ORs function better at medium λ values. Additionally, the 3-bladed SB-VAWTs with J-shaped airfoils presented more consistent performance compared to the 2-bladed and 4-bladed SB-VAWTs. The J-shaped airfoils are vital for cost-effective small-scale SB-VAWTs, which can be considered as candidates for urban and off-grid rural applications.

8.3. Scopes for Future Work

The present thesis investigated the J-shaped airfoils on small-scale Darrieus-type SB-VAWTs through 2D numerical simulations and experimental tests. The self-starting characteristics and aerodynamic performance of the Darrieus-type SB-VAWTs with J-shaped and conventional airfoils have been examined using performance coefficients, static torque coefficient, self-

starting characteristics and flow behaviour. According to the research work carried out in the present thesis, the following recommendations and scopes of future work are summarized below:

- In the present thesis, the 2D CFD simulations have been carried out to study the effect of J-shaped airfoils. However, researchers can investigate the J-shaped airfoils through 3D CFD simulations to gain more insights into the self-startup and overall performance of Darrieus-type SB-VAWTs. With this analysis, they will present a better comparison between conventional and J-shaped airfoils, considering blade span and supporting arms.
- Experimentation of wake analysis behind the Darrieus-type SB-VAWTs with J-shaped airfoils can be conducted using wind tunnel tests. In these tests, more than one SB-VAWT can be used to examine the wake effect on their overall performance.
- Measurement of the flow field over the J-shaped airfoils can also be conducted through the Particle Image Velocimetry (PIV) techniques. This analysis allows researchers to understand the complex flow behaviour around the J-shaped airfoils.
- Wind tunnel tests and CFD simulations can be carried out on the hybrid blade design consisting of both J-shaped and conventional blades to understand the various blade design configurations for Darrieus-type SB-VAWTs.
- Different augmentation techniques can be used on blades of Darrieus-type SB-VAWTs to enhance their self-startup and aerodynamic performance.
- Bioinspired J-shaped blades using different cross-sectional shapes can be examined using CFD simulations and wind tunnel tests to understand their effect on Darrieus-type SB-VAWTs.
- Different data-driven techniques, such as artificial neural network (ANN) and genetic expression programming (GEP) will be explored in future studies for various configurations of Darrieus-type SB-VAWTs using J-shaped blades.

References

Abraham, J.P., Plourde, B.D., Mowry, G.S., Minkowycz, W.J., Sparrow, E.M., 2012. Summary of Savonius wind turbine development and future applications for small-scale power generation. J. Renew. Sustain. Energy 4, 042703. https://doi.org/10.1063/1.4747822

Adaramola, M.S., Krogstad, P.Å., 2011. Experimental investigation of wake effects on wind turbine performance. Renew. Energy 36, 2078–2086. https://doi.org/10.1016/j.renene.2011.01.024

Akwa, J.V., Vielmo, H.A., Petry, A.P., 2012. A review on the performance of Savonius wind turbines. Renew. Sustain. Energy Rev. 16, 3054–3064. https://doi.org/10.1016/j.rser.2012.02.056

Al Hamad, S., Habash, O., Hasan, A., Amano, R.S., 2022. Effect of the J-Shaped Wind Turbine Airfoil Opening Ratio and Thickness on the Performance of Symmetrical Airfoils. J. Energy Resour. Technol. Trans. ASME 144. https://doi.org/10.1115/1.4053743

Almohammadi, K.M., Ingham, D.B., Ma, L., Pourkashanian, M., 2015. Modeling dynamic stall of a straight blade vertical axis wind turbine. J. Fluids Struct. 57, 144–158. https://doi.org/10.1016/j.jfluidstructs.2015.06.003

Amet, E., Maître, T., Pellone, C., Achard, J.L., 2009. 2D numerical simulations of blade-vortex interaction in a darrieus turbine. J. Fluids Eng. Trans. ASME 131, 1111031–11110315. https://doi.org/10.1115/1.4000258

Auyanet, A.G., Santoso, R.E., Verdin, P.G., Mohan, H., Rathore, S.S., Chakraborty, D., 2022. CFD-Based J-Shaped Blade Design Improvement for Vertical Axis Wind Turbines. Sustainability 14, 15343. https://doi.org/10.3390/su142215343

Baker, J R, 1983. Features to aid or enable self starting of fixed pitch low solidity vertical axis wind turbines. J. Wind Eng. Ind. Aerodyn. 15, 369–380. https://doi.org/10.1016/0167-6105(83)90206-4

Baker, J. R., 1983. Features to aid or enable self starting of fixed pitch low solidity vertical axis wind turbines. J. Wind Eng. Ind. Aerodyn. 15, 369–380. https://doi.org/10.1016/0167-6105(83)90206-4

Balduzzi, F., Bianchini, A., Ferrara, G., Ferrari, L., 2016a. Dimensionless numbers for the assessment of mesh and timestep requirements in CFD simulations of Darrieus wind turbines. Energy 97, 246–261. https://doi.org/10.1016/j.energy.2015.12.111

Balduzzi, F., Bianchini, A., Maleci, R., Ferrara, G., Ferrari, L., 2016b. Critical issues in the CFD simulation of Darrieus wind turbines. Renew. Energy 85, 419–435. https://doi.org/10.1016/j.renene.2015.06.048

Batista, N.C., Melício, R., Matias, J.C.O., Catalão, J.P.S., 2011. New blade profile for darrieus wind turbines capable to self-start. IET Conf. Renew. Power Gener. (RPG 2011), Edinburgh, UK, Sept. 6-8 1–5. https://doi.org/10.1049/cp.2011.0219

Bausas, M.D., Danao, L.A.M., 2015. The aerodynamics of a camber-bladed vertical axis wind turbine in unsteady wind. Energy 93, 1155–1164. https://doi.org/10.1016/j.energy.2015.09.120

Bedon, G., Castelli, M.R., Benini, E., 2014. Proposal for an innovative chord distribution in the Troposkien vertical axis wind turbine concept. Energy 66, 689–698. https://doi.org/10.1016/j.energy.2014.01.004

Bedon, G., Schmidt, U., Aagaard, H., Belloni, F., Raciti, M., Benini, E., 2017. Computational assessment of the DeepWind aerodynamic performance with different blade and airfoil configurations q. Appl. Energy 185, 1100–1108. https://doi.org/10.1016/j.apenergy.2015.10.038

Bel Mabrouk, I., El Hami, A., 2019. Effect of number of blades on the dynamic behavior of a Darrieus turbine geared transmission system. Mech. Syst. Signal Process. 121, 562–578. https://doi.org/10.1016/j.ymssp.2018.11.048

Belabes, B., Paraschivoiu, M., 2021. Numerical study of the effect of turbulence intensity on VAWT performance. Energy 233, 121139. https://doi.org/10.1016/j.energy.2021.121139

Benedict, M., Lakshminarayan, V., Pino, J., Chopra, I., 2016. Aerodynamics of a small-scale vertical-axis wind turbine with dynamic blade pitching. AIAA J. 54, 924–935. https://doi.org/10.2514/1.J052979

Beri, H., Yao, Y., 2011. Effect of camber airfoil on self starting of Vertical Axis Wind Turbine. J. Environ. Sci. Technol. 4, 302–312.

Bravo, R., Tullis, S., Ziada, S., 2007. Performance Testing of a Small Vertical-Axis Wind Turbine. Proc. 21st Can. Congr. Appl. Mech. (CANCAM 2007), Toronto, Ontario, (Canada), June 3-7 3–7.

Brusca, S., Lanzafame, R., Messina, M., 2014. Design of a vertical-axis wind turbine: how the aspect ratio affects the turbine's performance. Int. J. Energy Environ. Eng. 5, 333–340. https://doi.org/10.1007/s40095-014-0129-x

Bruun, H, H., 1996. Hot-wire anemometry: principles and signal analysis. Meas. Sci. Technol. 10, 024. https://doi.org/10.1088/0957-0233/7/10/024

Buchner, A.J., Lohry, M.W., Martinelli, L., Soria, J., Smits, A.J., 2015. Dynamic stall in vertical axis wind turbines: Comparing experiments and computations. J. Wind Eng. Ind. Aerodyn. 146, 163–171. https://doi.org/10.1016/j.jweia.2015.09.001

Buechler, E., Powell, S., Sun, T., Astier, N., Zanocco, C., Bolorinos, J., Flora, J., Boudet, H., Rajagopal, R., 2022. Global changes in electricity consumption during COVID-19. iScience 25, 103568. https://doi.org/10.1016/j.isci.2021.103568

Castelli, M.R., Betta, S. De, Benini, E., 2012. Effect of Blade Number on a Straight-Bladed Vertical-Axis Darreius Wind Turbine. World Acad. Sci. Eng. Technol. 61, 305–3011.

Celik, Y., Ingham, D., Ma, L., Pourkashanian, M., 2022. Design and aerodynamic performance analyses of the self-starting H-type VAWT having J-shaped aerofoils considering various design parameters using CFD. Energy 251, 123881. https://doi.org/10.1016/j.energy.2022.123881

Chen, J., Jan, K., Zhang, L., Lu, L., Yang, H., 2012. Influence of phase-shift and overlap ratio on savonius wind turbine's performance. J. Sol. Energy Eng. Trans. ASME 134, 1–9. https://doi.org/10.1115/1.4004980

Chen, J., Yang, H., Yang, M., Xu, H., 2015. The effect of the opening ratio and location on the performance of a novel vertical axis Darrieus turbine. Energy 89, 819–834. https://doi.org/10.1016/j.energy.2015.05.136

Chen, L., Chen, J., Xu, H., Yang, H., Ye, C., Liu, D., 2016. Wind tunnel investigation on the two- and three-blade Savonius rotor with central shaft at different gap ratio. J. Renew. Sustain. Energy 8. https://doi.org/10.1063/1.4940434

Chen, T.Y., Liou, L.R., 2011. Blockage corrections in wind tunnel tests of small horizontal-axis wind turbines. Exp. Therm. Fluid Sci. 35, 565–569. https://doi.org/10.1016/j.expthermflusci.2010.12.005

Cheng, Z., Aagaard, H., Gao, Z., Moan, T., 2017. Effect of the number of blades on the dynamics of floating straight-bladed vertical axis wind turbines. Renew. Energy 101, 1285–1298. https://doi.org/10.1016/j.renene.2016.09.074

Consul, C. a, Willden, R.H.J., Ferrer, E., McCulloch, M.D., 2009. Influence of Solidity on the Performance of a Cross-Flow Turbine. Proc. 8th Eur. Wave Tidal Energy Conf. Uppsala, Sweden 484–493.

Delafin, P.L., Nishino, T., Wang, L., Kolios, A., 2016. Effect of the number of blades and solidity on the performance of a vertical axis wind turbine. J. Phys. Conf. Ser. 753. https://doi.org/10.1088/1742-6596/753/2/022033

Dominy, R.G., Lunt, P., Bickerdyke, A., Dominy, J., 2007. Self-starting capability of a Darreus turbine. Proc. Inst. Mech. Eng. Part A J. Power Energy 221, 111–120. https://doi.org/10.1243/09576509JPE340

DTU, 2023. Wind Speed atlas of India [WWW Document]. Technol. Univ. Denmark. URL https://globalwindatlas.info/area/India.

Du, L., Ingram, G., Dominy, R.G., 2019. Experimental study of the effects of turbine solidity, blade profile, pitch angle, surface roughness, and aspect ratio on the H-Darrieus wind turbine self-starting and overall performance. Energy Sci. Eng. 7, 2421–2436. https://doi.org/10.1002/ese3.430

Earnest, J., Rachel, S., 2019. Wind power technology, Third Edit. ed. PHI Learning Pvt. Ltd., Delhi.

Eboibi, O., Danao, L.A.M., Howell, R.J., 2016. Experimental investigation of the influence of solidity on the performance and flow field aerodynamics of vertical axis wind turbines at low Reynolds numbers. Renew. Energy 92, 474–483. https://doi.org/10.1016/j.renene.2016.02.028

Edwards, J., Durrani, N., Howell, R., Qin, N., 2008. Wind Tunnel and Numerical Study of a Small Vertical Axis Wind Turbine, in: 46th AIAA Aerospace Sciences Meeting and Exhibit. Reno, Nevada, p. 1316. https://doi.org/10.2514/6.2008-1316

Elkhoury, M., Kiwata, T., Aoun, E., 2015. Experimental and numerical investigation of a three-dimensional vertical-axis wind turbine with variable-pitch. J. Wind Eng. Ind. Aerodyn. 139, 111–123. https://doi.org/10.1016/j.jweia.2015.01.004

Elsakka, M.M., Ingham, D.B., Ma, L., Pourkashanian, M., 2019. CFD analysis of the angle of attack for a vertical axis wind turbine blade. Energy Convers. Manag. 182, 154–165. https://doi.org/10.1016/j.enconman.2018.12.054

Eriksson, S., Bernhoff, H., Leijon, M., 2008. Evaluation of different turbine concepts for wind power. Renew. Sustain. Energy Rev. 12, 1419–1434. https://doi.org/10.1016/j.rser.2006.05.017

Feng, F., Tong, G., Ma, Y., Li, Y., 2021. Numerical simulation and wind tunnel investigation on static characteristics of VAWT rotor starter with lift-drag combined structure. Energies 14, 6167. https://doi.org/10.3390/en14196167

Ghazalla, R.A., Mohamed, M.H., Ha, A.A., 2019. Synergistic analysis of a Darrieus wind turbine using computational fluid dynamics. Energy 189, 116214. https://doi.org/10.1016/j.energy.2019.116214

Ghiasi, P., Najafi, G., Ghobadian, B., Jafari, A., Mazlan, M., 2022. Analytical Study of the Impact of Solidity, Chord Length, Number of Blades, Aspect Ratio and Airfoil Type on H-Rotor DarrieusWind Turbine Performance at Low Reynolds Number. Sustainability 14. https://doi.org/10.3390/su14052623

Gupta, R., Biswas, A., Sharma, K.K., 2008. Comparative study of a three-bucket Savonius rotor with a combined three-bucket Savonius-three-bladed Darrieus rotor. Renew. Energy 33, 1974–1981. https://doi.org/10.1016/j.renene.2007.12.008

GWEC, 2025. Global Wind Report. Lisbon, Portugal.

Healy, J. V., 1978. Influence of Blade Thickness on the Output of Vertical Axis Wind Turbines. Wind Eng. 2, 146–155.

Hill, N., Dominy, R., Ingram, G., Dominy, J., 2009a. Darrieus turbines: The physics of self-starting. Proc. Inst. Mech. Eng. Part A J. Power Energy 223, 21–29. https://doi.org/10.1243/09576509JPE615

Hill, N., Dominy, R., Ingram, G., Dominy, J., 2009b. Darrieus turbines: The physics of self-starting: Proc. Inst. Mech. Eng. Part A J. Power Energy 223, 21–29. https://doi.org/10.1243/09576509JPE615

Howell, R., Qin, N., Edwards, J., Durrani, N., 2010. Wind tunnel and numerical study of a small vertical axis wind turbine. Renew. Energy 35, 412–422. https://doi.org/10.1016/j.renene.2009.07.025

IEA, 2022. World Energy Outlook. International Energy Agency (IEA).

IEA, 2021. . India energy outlook 2021. https://doi.org/https://doi.org/10.1787/ec2fd78d- en

Islam, M., Fartaj, A., Carriveau, R., 2011. Design analysis of a smaller-capacity straight-bladed VAWT with an asymmetric airfoil. Int. J. Sustain. Energy 30, 179–192. https://doi.org/10.1080/1478646X.2010.509496

Jain, S., Saha, U.K., 2020a. On the influence of blade thickness-to-chord ratio on dynamic stall phenomenon in H-type Darrieus wind rotors. Energy Convers. Manag. 218, 113024. https://doi.org/10.1016/j.enconman.2020.113024

Jain, S., Saha, U.K., 2020b. Capturing the Dynamic Stall in H-Type Darrieus Wind Turbines Using Different URANS Turbulence Models. J. Energy Resour. Technol. Trans. ASME 142, 091302. https://doi.org/10.1115/1.4046730

Jin, X., Zhao, G., Gao, K., Ju, W., 2015. Darrieus vertical axis wind turbine: Basic research methods. Renew. Sustain. Energy Rev. 42, 212–225. https://doi.org/10.1016/j.rser.2014.10.021

Joo, S., Choi, H., Lee, J., 2015. Aerodynamic characteristics of two-bladed H-Darrieus at various solidities and rotating speeds. Energy 90, 439–451. https://doi.org/10.1016/j.energy.2015.07.051

Jung, C., Schindler, D., Laible, J., 2018. National and global wind resource assessment under six wind turbine installation scenarios. Energy Convers. Manag. 156, 403–415. https://doi.org/10.1016/j.enconman.2017.11.059

Kamoji, M.A., Kedare, S.B., Prabhu, S. V, 2008. Experimental investigations on single stage , two stage and three stage conventional Savonius rotor. Int. J. Energy Res. 32, 877–895. https://doi.org/10.1002/er

Kirke, B K, Lazauskas, L., 1991. Enhancing the Performance of Vertical Axis Wind Turbine Using a Simple Variable Pitch System. Wind Eng. 15, 187–195. https://doi.org/https://www.jstor.org/stable/43750355

Kirke, B. K., Lazauskas, L., 1991. Enhancing the performance of vertical axis wind turbine using a simple variable pitch system. Wind Eng. 15, 187–195. https://doi.org/https://www.jstor.org/stable/43750355

Kuang, L., Zhang, R., Su, J., Shao, Y., Zhang, K., Chen, Y., Zhang, Z., Tu, Y., Zhou, D., Han, Z., Bao, Y., Cao, Y., 2023. Systematic investigation of effect of rotor solidity on vertical-axis wind turbines: Power performance and aerodynamics analysis. J. Wind Eng. Ind. Aerodyn. 233. https://doi.org/10.1016/j.jweia.2022.105284

Kumar, P.M., Sivalingam, K., Narasimalu, S., Lim, T.-C., Ramakrishna, S., Wei, H., 2019. A Review on the Evolution of Darrieus Vertical Axis Wind Turbine: Small Wind Turbines. J. Power Energy Eng. 7, 27–44. https://doi.org/10.4236/jpee.2019.74002

Kyozuka, Y., 2008. An Experimental Study on the Darrieus-Savonius Turbine for the Tidal Current Power Generation 3, 439–449. https://doi.org/10.1299/jfst.3.439

Lam, H.F., Peng, H.Y., 2016. Study of wake characteristics of a vertical axis wind turbine by two- and three-dimensional computational fluid dynamics simulations. Renew. Energy 90, 386–398. https://doi.org/10.1016/j.renene.2016.01.011

Lanzafame, R., Mauro, S., Messina, M., 2014. 2D CFD modeling of H-Darrieus Wind Turbines using a transition turbulence model. Energy Procedia 45, 131–140. https://doi.org/10.1016/j.egypro.2014.01.015

Lazauskas, L., Kirke, B.K., 1992. Performance optimisation of a self-acting variable pitch vertical axis wind turbine. Wind Eng. 16, 10–26.

Li, Q., Maeda, T., Kamada, Y., Hiromori, Y., Nakai, A., Kasuya, T., 2017a. Study on stall behavior of a straight-bladed vertical axis wind turbine with numerical and experimental investigations. J. Wind Eng. Ind. Aerodyn. 164, 1–12. https://doi.org/10.1016/j.jweia.2017.02.005

Li, Q., Maeda, T., Kamada, Y., Murata, J., Furukawa, K., Yamamoto, M., 2015. Effect of number of blades on aerodynamic forces on a straight-bladed Vertical Axis Wind Turbine. Energy 90, 784–795. https://doi.org/10.1016/j.energy.2015.07.115

Li, Q., Maeda, T., Kamada, Y., Murata, J., Shimizu, K., Ogasawara, T., Nakai, A., Kasuya, T., 2016a. Effect of solidity on aerodynamic forces around straight-bladed vertical axis wind turbine by wind tunnel experiments (depending on number of blades). Renew. Energy 96, 928–939. https://doi.org/10.1016/j.renene.2016.05.054

Li, Q., Maeda, T., Kamada, Y., Murata, J., Yamamoto, M., Ogasawara, T., Shimizu, K., Kogaki, T., 2016b. Study on power performance for straight-bladed vertical axis wind turbine by field and wind tunnel test. Renew. Energy 90, 291–300. https://doi.org/10.1016/j.renene.2016.01.002

Li, Q., Maeda, T., Kamada, Y., Murata, J., Yamamoto, M., Ogasawara, T., Shimizu, K., Kogaki, T., 2016c. Study on power performance for straight-bladed vertical axis wind turbine by field and wind tunnel test. Renew. Energy 90, 291–300. https://doi.org/10.1016/j.renene.2016.01.002

Li, Q., Maeda, T., Kamada, Y., Shimizu, K., Ogasawara, T., Nakai, A., Kasuya, T., 2017b. Effect of rotor aspect ratio and solidity on a straight-bladed vertical axis wind turbine in three-dimensional

analysis by the panel method. Energy 121, 1–9. https://doi.org/10.1016/j.energy.2016.12.112

Li, S., Li, Y., 2010. Numerical study on the performance effect of solidity on the straight-bladed vertical axis wind turbine. Asia-Pacific Power Energy Eng. Conf. APPEEC 1–4. https://doi.org/10.1109/APPEEC.2010.5449269

Li, Y., Zhao, S., Tagawa, K., Feng, F., 2018. Starting performance effect of a truncated-cone-shaped wind gathering device on small-scale straight-bladed vertical axis wind turbine. Energy Convers. Manag. 167, 70–80. https://doi.org/10.1016/j.enconman.2018.04.062

Li, Z., Gao, M., Cao, X., Cheng, L., Wang, X., An, G., Sun, H., 2022. Structural optimal design and power generation characteristics of a bionic type nautilus vertical axis wind turbine. J. Eng. 2022, 64–75. https://doi.org/10.1049/tje2.12095

Liu, J., Lin, H., Zhang, J., 2019. Review on the technical perspectives and commercial viability of vertical axis wind turbines. Ocean Eng. 182, 608–626. https://doi.org/10.1016/j.oceaneng.2019.04.086

López, O., Meneses, D., Quintero, B., Laín, S., 2016. Computational study of transient flow around Darrieus type cross flow water turbines. J. Renew. Sustain. Energy 8, 014501. https://doi.org/10.1063/1.4940023

M. El-Samanoudy, Ghorab, A.A.E., Youssef, S.Z., 2010. Effect of some design parameters on the performance of a Giromill vertical axis wind turbine. Ain Shams Eng. J. 1, 85–95. https://doi.org/10.1016/j.asej.2010.09.012

Mabrouk, I.B., Hami, A. El, 2019. Effect of number of blades on the dynamic behavior of a Darrieus turbine geared transmission system. Mech. Syst. Signal Process. 121, 562–578. https://doi.org/10.1016/j.ymssp.2018.11.048

Mackay, D., 2009. Sustainable energy-without the hot air,1st ed, UIT Cambridge Ltd. UIT Cambridge Ltd., Cambridge.

Menter, F.R., 1994. Two-equation eddy-viscosity turbulence models for engineering applications. AIAA J. 32, 1598–1605. https://doi.org/10.2514/3.12149

MNRE, 2023. Annual Report 2022-23. Delhi, India.

Mo, J.O., Choudhry, A., Arjomandi, M., Kelso, R., Lee, Y.H., 2013. Effects of wind speed changes on wake instability of a wind turbine in a virtual wind tunnel using large eddy simulation. J. Wind Eng. Ind. Aerodyn. 117, 38–56. https://doi.org/10.1016/j.jweia.2013.03.007

Moffat, R.J., 1988. Describing the Uncertainties in Experimental Results. Exp. Therm. Fluid Sci. 1, 3–17. https://doi.org/10.1016/0894-1777(88)90043-X

Mohamed, M.H., 2019. Criticism study of J-Shaped darrieus wind turbine : Performance evaluation and noise generation assessment. Energy 177, 367–385. https://doi.org/10.1016/j.energy.2019.04.102

Mohamed, M.H., 2013. Impacts of solidity and hybrid system in small wind turbines performance. Energy. https://doi.org/10.1016/j.energy.2013.06.004

Mohamed, M.H., 2012. Performance investigation of H-rotor Darrieus turbine with new airfoil shapes. Energy 47, 522–530. https://doi.org/10.1016/j.energy.2012.08.044

Mohamed, M.H., Dessoky, A., Alqurashi, F., 2019. Blade shape effect on the behavior of the H-rotor Darrieus wind turbine: Performance investigation and force analysis. Energy 179, 1217–1234.

https://doi.org/10.1016/j.energy.2019.05.069

Mohamed, M.H., Janiga, G., Pap, E., Thévenin, D., 2011. Optimal blade shape of a modified Savonius turbine using an obstacle shielding the returning blade. Energy Convers. Manag. 52, 236–242. https://doi.org/10.1016/j.enconman.2010.06.070

Naik, K., Sahoo, N., 2024. Aerodynamic performance and starting torque enhancement of small-scale Darrieus type straight-bladed vertical axis wind turbines with J-shaped airfoil. J. Renew. Sustain. Energy 16. https://doi.org/10.1063/5.0203557

Naik, K., Sahoo, N., 2023. Synergistic Effect of J-Shape Airfoil on the Performance of Vertical Axis Wind Turbine. J. Energy Resour. Technol. 145, 1–13. https://doi.org/10.1115/1.4062082

Pan, L., Zhu, Z., Xiao, H., Wang, L., 2021. Numerical analysis and parameter optimization of j-shaped blade on offshore vertical axis wind turbine. Energies 14, 1–29. https://doi.org/10.3390/en14196426

Parker, C.M., Leftwich, M.C., 2016. The effect of tip speed ratio on a vertical axis wind turbine at high Reynolds numbers. Exp. Fluids 57, 1–11. https://doi.org/10.1007/s00348-016-2155-3

Peng, J., 2018. Effects of aerodynamic interactions of closely-placed vertical axis wind turbine pairs. Energies 11, 1–13. https://doi.org/10.3390/en11102842

Peng, Y.X., Xu, Y.L., Zhu, S., Li, C., 2019. High-solidity straight-bladed vertical axis wind turbine: Numerical simulation and validation. J. Wind Eng. Ind. Aerodyn. 193, 103960. https://doi.org/10.1016/j.jweia.2019.103960

Pérez-Lombard, L., Ortiz, J., Pout, C., 2008. A review on buildings energy consumption information. Energy Build. 40, 394–398. https://doi.org/10.1016/j.enbuild.2007.03.007

Pope, A., Harper, J.J., 1966. Low Speed Wind Tunnel Testing. John Wiley and Sons, New York.

Posa, A., 2020. Influence of Tip Speed Ratio on wake features of a Vertical Axis Wind Turbine. J. Wind Eng. Ind. Aerodyn. 197, 104076. https://doi.org/10.1016/j.jweia.2019.104076

Posa, A., Parker, C.M., Leftwich, M.C., Balaras, E., 2016. Wake structure of a single vertical axis wind turbine. Int. J. Heat Fluid Flow 61, 75–84. https://doi.org/10.1016/j.ijheatfluidflow.2016.02.002

Qamar, S.B., Janajreh, I., 2017a. Investigation of Effect of Cambered Blades on Darrieus VAWTs. Energy Procedia 105, 537–543. https://doi.org/10.1016/j.egypro.2017.03.353

Qamar, S.B., Janajreh, I., 2017b. A comprehensive analysis of solidity for cambered darrieus VAWTs. Int. J. Hydrogen Energy 42, 19420–19431. https://doi.org/10.1016/j.ijhydene.2017.06.041

Raciti Castelli, M., Englaro, A., Benini, E., 2011a. The Darrieus wind turbine: Proposal for a new performance prediction model based on CFD. Energy 36, 4919–4934. https://doi.org/10.1016/j.energy.2011.05.036

Raciti Castelli, M., Englaro, A., Benini, E., 2011b. The Darrieus wind turbine: Proposal for a new performance prediction model based on CFD. Energy 36, 4919–4934. https://doi.org/10.1016/j.energy.2011.05.036

Rathod, U.H., Talukdar, P.K., Kulkarni, V., Saha, U.K., 2019. Effect of Capped Vents on Torque Distribution of a Semicircular-Bladed Savonius Wind Rotor. J. Energy Resour. Technol. Trans. ASME 141, 1–15. https://doi.org/10.1115/1.4043791

Reddy, K.B., Bhosale, A.C., 2024. Effect of number of blades on performance and wake recovery for a vertical axis helical hydrokinetic turbine. Energy 299, 131520. https://doi.org/10.1016/j.energy.2024.131520

Rezaeiha, A., Montazeri, H., Blocken, B., 2018a. Towards accurate CFD simulations of vertical axis wind turbines at different tip speed ratios and solidities: Guidelines for azimuthal increment, domain size and convergence. Energy Convers. Manag. 156, 301–316. https://doi.org/10.1016/j.enconman.2017.11.026

Rezaeiha, A., Montazeri, H., Blocken, B., 2018b. Towards optimal aerodynamic design of vertical axis wind turbines: Impact of solidity and number of blades. Energy 165, 1129–1148. https://doi.org/10.1016/j.energy.2018.09.192

Rezaeiha, A., Montazeri, H., Blocken, B., 2018c. Characterization of aerodynamic performance of vertical axis wind turbines: Impact of operational parameters. Energy Convers. Manag. 169, 45–77. https://doi.org/10.1016/j.enconman.2018.05.042

Roh, S., Kang, S., 2013. Effects of a blade profile , the Reynolds number , and the solidity on the performance of a straight bladed vertical axis wind turbine. J. Mech. Sci. Technol. 27, 3299–3307. https://doi.org/10.1007/s12206-013-0852-x

Roshan, A., Sagharichi, A., Maghrebi, M.J., 2020. Nondimensional parameters' effects on hybrid darrieus-savonius wind turbine performance. J. Energy Resour. Technol. Trans. ASME 142, 1–12. https://doi.org/10.1115/1.4044517

Roy, S., Ducoin, A., 2016. Unsteady analysis on the instantaneous forces and moment arms acting on a novel Savonius-style wind turbine. Energy Convers. Manag. 121, 281–296. https://doi.org/10.1016/j.enconman.2016.05.044

Saad, A.S., Ahmed, M., 2023. Impact of Number of Blades and Solidity on the Performance of a Darrieus Vertical Axis Wind Turbine With Helical Blades, in: International Mechanical Engineering Congress and Exposition. https://doi.org/10.1115/IMECE2023-113651

Sagharichi, A., Zamani, M., Ghasemi, A., 2018. Effect of solidity on the performance of variable-pitch vertical axis wind turbine. Energy 161, 753–775. https://doi.org/10.1016/j.energy.2018.07.160

Satrio, D., Utama, I.K.A.P., Mukhtasor, 2018. Numerical Investigation of Contra Rotating Vertical-Axis Tidal-Current Turbine. J. Mar. Sci. Appl. 17, 208–215. https://doi.org/10.1007/s11804-018-0017-5

Schönborn, A., Chantzidakis, M., 2007. Development of a hydraulic control mechanism for cyclic pitch marine current turbines. Renew. Energy 32, 662–679. https://doi.org/10.1016/j.renene.2006.02.004

Schuerich, F., Brown, R.E., 2011. Effect of dynamic stall on the aerodynamics of vertical-axis wind turbines. AIAA J. 49, 2511–2521. https://doi.org/10.2514/1.J051060

Scungio, M., Arpino, F., Focanti, V., Profili, M., and Rotondi, M., 2016. Wind tunnel testing of scaled models of a newly developed Darrieus-style vertical axis wind turbine with auxiliary straight blades. Energy Convers. Manag. 130, 60–70.

Sengupta, A.R., Biswas, A., Gupta, R., 2019. Comparison of low wind speed aerodynamics of unsymmetrical blade H-Darrieus rotors-blade camber and curvature signatures for performance improvement. Renew. Energy 139, 1412–1427. https://doi.org/10.1016/j.renene.2019.03.054

Simão Ferreira, C., Van Kuik, G., Van Bussel, G., Scarano, F., 2009. Visualization by PIV of dynamic stall on a vertical axis wind turbine. Exp. Fluids 46, 97–108. https://doi.org/10.1007/s00348-008-0543-z

Singh, M.A., Biswas, A., Misra, R.D., 2015. Investigation of self-starting and high rotor solidity on the performance of a three S1210 blade H-type Darrieus rotor. Renew. Energy 76, 381–387. https://doi.org/10.1016/j.renene.2014.11.027

Siram, O., Kumar, R., Saha, U.K., Sahoo, N., 2022a. Wind Tunnel Probe Into an Array of Small-Scale Horizontal-Axis Wind Turbines Operating at Low Tip Speed Ratio Conditions. J. Energy Resour. Technol. 144, 1–13. https://doi.org/10.1115/1.4053579

Siram, O., Saha, U.K., Sahoo, N., 2022b. Blade design considerations of small wind turbines: From classical to emerging bio-inspired profiles/shapes. J. Renew. Sustain. Energy 14. https://doi.org/10.1063/5.0096402

Siram, O., Sahoo, N., Saha, U.K., 2022c. Wind Tunnel Tests of a Model Small-Scale Horizontal-Axis Wind Turbine Developed From Blade Element Momentum Theory. J. Energy Resour. Technol. Trans. ASME 144, 1–10. https://doi.org/10.1115/1.4052774

Sørensen, J.N., Shen, W.Z., 2002. Numerical modeling of wind turbine wakes. J. Fluids Eng. Trans. ASME 124, 393–399. https://doi.org/10.1115/1.1471361

Subramanian, A., Yogesh, S.A., Sivanandan, H., Giri, A., Vasudevan, M., Mugundhan, V., Velamati, R.K., 2017. Effect of airfoil and solidity on performance of small scale vertical axis wind turbine using three dimensional CFD model. Energy 133, 179–190. https://doi.org/10.1016/j.energy.2017.05.118

Sun, K., Yi, Y., Zhang, Jisheng, Zhang, Jianhua, Haider Zaidi, S.S., Sun, S., 2022. Influence of blade numbers on start-up performance of vertical axis tidal current turbines. Ocean Eng. 243. https://doi.org/10.1016/j.oceaneng.2021.110314

Sun, X., Wang, Y., An, Q., Cao, Y., Wu, G., Huang, D., 2014. Aerodynamic performance and characteristic of vortex structures for Darrieus wind turbine. I. Numerical method and aerodynamic performance. J. Renew. Sustain. Energy 6. https://doi.org/10.1063/1.4893775

Sun, X., Zhu, J., Hanif, A., Li, Z., Sun, G., 2020. Effects of blade shape and its corresponding moment of inertia on self-starting and power extraction performance of the novel bowl-shaped floating straight-bladed vertical axis wind turbine. Sustain. Energy Technol. Assessments 38, 100648. https://doi.org/10.1016/j.seta.2020.100648

Sun, X., Zhu, J., Li, Z., Sun, G., 2021. Rotation improvement of vertical axis wind turbine by offsetting pitching angles and changing blade numbers. Energy 215, 119177. https://doi.org/10.1016/j.energy.2020.119177

Suriyawong, A., Saisorn, S., Sule, L., Rompas, P.T.D., 2021. The Effect of the Number of Blades on the Efficiency of A Wind Turbine. IOP Conf. Ser. Earth Environ. Sci. 801, 012020. https://doi.org/10.1088/1755-1315/801/1/012020

Tabassum, S.A., Probert, S.D., 1987. Vertical-axis wind turbine: A modified design. Appl. Energy 28, 59–67. https://doi.org/10.1016/0306-2619(87)90041-9

Tirkey, A., Sarthi, Y., Patel, K., Sharma, R., Sen, P.K., 2014. Study on the effect of blade profile, number of blade, Reynolds number, aspect ratio on the performance of vertical axis wind turbine. Int. J.

Sci. Eng. Technol. Res. 3, 3183–3187.

Tjiu, W., Marnoto, T., Mat, S., Ruslan, M.H., Sopian, K., 2015. Darrieus vertical axis wind turbine for power generation I: Assessment of Darrieus VAWT configurations. Renew. Energy 75, 50–67. https://doi.org/10.1016/j.renene.2014.09.038

Toja-Silva, F., Colmenar-Santos, A., Manuel Castro-Gil, 2013. Urban wind energy exploitation systems: Behaviour under multidirectional flow conditions - Opportunities and challenges. Renew Sustain Energy Rev 24, 364–378. https://doi.org/https://doi.org/10.1016/j.rser.2013.03.052

Van Treuren, K.W., 2015. Small-scale wind turbine testing in wind tunnels under low reynolds number conditions. J. Energy Resour. Technol. Trans. ASME 137, 1–11. https://doi.org/10.1115/1.4030617

Wang, S.H., Chen, S.H., 2008. Blade number effect for a ducted wind turbine. J. Mech. Sci. Technol. 22, 1984–1992. https://doi.org/10.1007/s12206-008-0743-8

Wang, Y., Sun, X., Dong, X., Zhu, B., Huang, D., Zheng, Z., 2016. Numerical investigation on aerodynamic performance of a novel vertical axis wind turbine with adaptive blades. Energy Convers. Manag. 108, 275–286. https://doi.org/10.1016/j.enconman.2015.11.003

Wang, Z., Wang, Y., Zhuang, M., 2018. Improvement of the aerodynamic performance of vertical axis wind turbines with leading-edge serrations and helical blades using CFD and Taguchi method. Energy Convers. Manag. 177, 107–121. https://doi.org/10.1016/j.enconman.2018.09.028

Watson, S., Moro, A., Reis, V., Baniotopoulos, C., Barth, S., Bartoli, G., Bauer, F., Boelman, E., Bosse, D., Cherubini, A., Croce, A., Fagiano, L., Fontana, M., Gambier, A., Gkoumas, K., Golightly, C., Latour, M.I., Jamieson, P., Kaldellis, J., Macdonald, A., Murphy, J., Muskulus, M., Petrini, F., Pigolotti, L., Rasmussen, F., Schild, P., Schmehl, R., Stavridou, N., Tande, J., Taylor, N., Telsnig, T., Wiser, R., 2019. Future emerging technologies in the wind power sector: A European perspective. Renew. Sustain. Energy Rev. 113. https://doi.org/10.1016/j.rser.2019.109270

WWEA, 2025. WWEA Annual Report 2024. Bonn, Germany.

Zamani, M., Maghrebi, M.J., Varedi, S.R., 2016a. Starting torque improvement using J-shaped straight-bladed Darrieus vertical axis wind turbine by means of numerical simulation. Energy 95, 109–126. https://doi.org/10.1016/j.renene.2016.03.069

Zamani, M., Nazari, S., Moshizi, S.A., Javad, M., 2016b. Three dimensional simulation of J-shaped Darrieus vertical axis wind turbine. Energy 116, 1243–1255. https://doi.org/10.1016/j.energy.2016.10.031

Zanforlin, S., Deluca, S., 2018. Effects of the Reynolds number and the tip losses on the optimal aspect ratio of straight-bladed Vertical Axis Wind Turbines. Energy 148, 179–195. https://doi.org/10.1016/j.energy.2018.01.132

Zhu, H., Hao, W., Li, C., Ding, Q., 2019. Numerical study of effect of solidity on vertical axis wind turbine with Gurney flap. J. Wind Eng. Ind. Aerodyn. 186, 17–31. https://doi.org/10.1016/j.jweia.2018.12.016

List of Publications

Refereed Journals

1. Naik, K., Sahoo, N., 2023, "Synergistic Effect of J-Shape Airfoil on the Performance of Vertical Axis Wind Turbine," J. Energy Resour. Technol. 145, 1–13. https://doi.org/10.1115/1.4062082.

2. Naik, K., Sahoo, N., 2024, "Aerodynamic performance and starting torque enhancement of small-scale Darrieus type straight-bladed vertical axis wind turbines with J-shaped airfoil," J. Renew. Sustain. Energy 16. https://doi.org/10.1063/5.0203557.

3. Naik, K., Sahoo, N., 2026, "Effect of J-shaped Blade Number on Small-Scale Darrieus-type Straight Bladed Vertical Axis Wind Turbine for Low Wind Regime," Ocean Eng., 343. https://doi.org/10.1016/j.oceaneng.2025.123500

Refereed Conferences

1. Naik, K. and Sahoo, N., 2021, "Dimple Shape Effect on the Aerodynamic Performance of H-Rotor Darrieus Vertical Axis Wind Turbine", In *Gas Turbine India Conference* (Vol. 85536, p. V001T09A006). American Society of Mechanical Engineers. (doi: https://doi.org/10.1115/GTINDIA2021-76017)

2. Naik, K. and Sahoo, N., 2022, "On the use of cavity for the power augmentation of straight-bladed Darrieus vertical axis wind turbines", In *Indo-German International Conference on Metrology for the Deployment of Green Hydrogen and Renewable Fuels* (IMEKO-TC20), April 4-6.

3. Naik, K. and Sahoo, N., 2022, "Numerical Study of the Effect of Gurney Flaps on the Aerodynamic Performance Augmentation of the H-type Darrieus Wind Rotors", In *North-East research Conclave* (NERC), IIT Guwahati, May 20-22.

4. Naik, K. and Sahoo, N., 2022, "Aerodynamic Performance Improvements of the Darrieus type Straight-Bladed Vertical Axis Wind Turbine with Gurney Flaps", In *67th Congress of the Indian Society of Theoretical and Applied Mechanics* (ISTAM)), IIT Mandi, Dec 14-16, Paper ID: ISTAM/2022/0235.

5. Naik, K. and Sahoo, N., 2023, "Diameter-to-chord ratio Effect on the Aerodynamic Performance of Small-scale Darrieus type Straight-Bladed Vertical Axis Wind Turbine", In *Gas Turbine India Conference,* (Vol. 118458, p. V001T06A002). American Society of Mechanical Engineers. (doi: https://doi.org/10.1115/GTINDIA2023-118458)

6. Naik, K., Biswal SK., and Sahoo, N., 2026, "Effect of drag and lift-based blade on aerodynamic performance and starting torque of small-scale Darrieus-type straight-bladed vertical axis wind turbine", *In International Conference on Advances in Aerospace and Energy Systems* (p. 471-483), Singapore: Springer Nature Singapore.

7. Naik, K., Biswal SK., and Sahoo, N., 2026, "Comparative performance analysis of Darrieus-type straight-bladed vertical axis wind turbine using conventional and J-Shaped airfoils", I*n Conference on Research and Industrial Conclave-Integration* (p. 93-106), Singapore: Springer Nature Singapore.